Title
Radiative and climate impacts of absorbing aerosols

Author
Zhu, Aihua

Publication Date
2010

Peer reviewed|Thesis/dissertation

UNIVERSITY OF CALIFORNIA, SAN DIEGO

Radiative and Climate Impacts of Absorbing Aerosols

A dissertation submitted in partial satisfaction of the

requirements for the degree Doctor of Philosophy

in

Earth Sciences

by

Aihua Zhu

Committee in charge:

V. Ramanathan, Chair
Dan Lubin
Joel Norris
Kimberly Prather
Lynn Russell
Mark Thiemens
Guang J. Zhang

2010

The Dissertation of Aihua Zhu is approved, and it is acceptable in quality and form for publication on microfilm and electronically:

_____

_____

_____

_____

_____

_____

_____

Chair

University of California, San Diego

2010

DEDICATION

To

My beloved Families

TABLE OF CONTENTS

LIST OF ABBREVIATIONS

AAE	Absorption *Angström* Exponent
ABC	Atmospheric Brown Clouds
ACE	Aerosol Characterization Experiment
ADEC	Aeolian Dust Experiment on Climate impacts
AERONET	AErosol RObotic NETwork
AGCM	Atmospheric General Circulation Model
ANG	Ångström exponent
AOD	Aerosol Optical Depth
APMEX	ABC Post Monsoonal Experiment
APS	Aerodynamic particle sizer
ARF	aerosol radiative forcing
AS	Arabian Sea
ASD	Analytical Spectral Devices
ASTEX	Atlantic Stratocumulus Transition Experiment
ASY	asymmetry factor
ATOFMS	Aerosol Time-of-Flight Mass Spectrometry
AVHRR	Advanced Very High Resolution Radiometer
BB	brown carbon
BC	black carbon
BL	boundary layer
BOB	Bay of Bengal
BOMEX	Barbados Oceanographic and Meteorological Experiment
BRDF	Bidirectional Reflectance Distribution Functions
C^4	Center for Clouds, Chemistry and Climate
CAM	Community Atmosphere Model
CCN	cloud condensation nuclei
CCSM	Community Climate System Model
CDP	cloud drop size distribution

CERES	the Clouds and the Earth's Radiant Energy System
CKD	Clough–Kniezys–Davies
CPC	total particle counter
DISORT	Discrete Ordinates Radiative Transfer model
DU	dust aerosol
EC	elemental carbon
ECMWF	European Centre for Medium-Range Weather Forecasts
EOS	Earth Observing System
ERBS	the Earth Radiation Budget Satellite
GOCART	Goddard Global Ozone Chemistry Aerosol Radiation and Transport model
HITRAN	high-resolution transmission molecular absorption database
HYSPLIT	Hybrid Single-Particle Lagrangian Integrated Trajectory
ICE-L	Ice in Clouds Experiment-Layer Clouds
ICESat	Ice, Cloud, Land Elevation Satellite
INDOEX	Indian Ocean Experiment
IPCC	Intergovernmental Panel on Climate Change
IR	infrared
ISCCP	International Satellite Cloud Climatology Project
ITCZ	Intertropical Convergence Zone
JJA	June-July-August
LAP	light-absorbing particles
LTS	lower-tropospheric stability
LUT	look-up-table
LW	longwave
LWC	liquid water content probe
MAC	Maldives Autonomous unmanned aerial vehicle Campaign
MACR	Monte Carlo Aerosol-Cloud-Radiation model
MAM	March-April-May
MBL	marine boundary layer

MCOH	Maldives Climate Observatory in Hanimaadhoo
MILAGRO	Megacity Initiative: Local and Global Research Observations
MISR	Multiangle Imaging Spectroradiometer
MODIS	Moderate Imaging Spectroradiometer
MODTRAN	MODerate spectral resolution atmospheric TRANSsmittance model
MPL	Micro-Pulse Lidar
NASA	National Aeronautics and Space Administration
NCEP/NCAR	National Centers for Environmental Prediction / National Center for Atmospheric Research
NH	Northern Hemisphere
NOAA	National Oceanic and Atmospheric Administration
OC	organic carbon
OMI	Ozone Monitoring Instrument
OPAC	Optical Properties of Aerosols and Clouds
OPC	optical particle counter
PAR	Photo-synthetically Active Radiation
PRIDE	the Puerto Rico Dust Experiment
PSL	polystyrene latex
RH	relative humidity
RTM	radiative transfer model
SAGE	Stratospheric Aerosol and Gas Experiment
SAM	Stratospheric Aerosol Measurement
SC	Saharan Coast
SH	Southern Hemisphere
SHADE	the Saharan Dust Experiment
SOFIA	Surface of the Ocean, Fluxes and Interactions with the Atmosphere
SS	sea salt
SSA	single scattering albedo
SST	sea surface temperature
SU	sulfate

SW	shortwave
SZA	solar zenith angle
TEM	transmission electron microscope
TOA	top-of-the-atmosphere
TOMS	Total Ozone Mapping Spectrometer
TOVS	Tiros Operational Vertical Sounder
UAV	unmanned aerial vehicle
UV	ultraviolet
VOC	volatile organic compounds
YS	Yellow Sea

LIST OF FIGURES

LIST OF TABLES

ACKNOWLEDGEMENTS

First and foremost, I would like to thank my advisor, Professor V. Ramanathan, who supported and guided my research from in-depth discussion to broader vision in science, shared his ideas covering a wide range of topics, and brought clarity to my research over the years. I have always appreciated his inspiration, patience, wisdom, and passion on climate sciences, which helped me to be creative and independent in research. I'm very grateful that he provided me with many precious opportunities to participate in conferences and workshops, and to corporate with other outstanding scientists.

I also acknowledge my doctoral committee member, Drs. Dan Lubin, Joel Norris, Kimberly Prather, Lynn Russell, Mark Thiemens, and Guang J. Zhang for their valuable advice and support on various stages of my Ph.D. study.

Great thanks to my colleagues in C^4 group for their wonderful support and thoughtful advice: Dohyeong Kim, Yan Feng, Muvva Ramana, Craig Corrigan, Hung Nguyen, Greg Roberts, Katrin Lehmann, Fang Li, Eddy Chung, Steph Weidemann, Martin Olivera, Rocky Issa, Sean Cole, Richard Thomas, and my great officemate and fellow student Odelle Hadley.

I acknowledge NSF, NASA and NOAA for their funding support for my research. I am grateful to Professor Kim Prather and her grad students: Andy Ault, Matt Spencer, and Ryan Moffet for their help with ATOFMS data analysis. I also thank my collaborators in Korea for their great support and help during ABC-EAREX 2007 and PACDEX campaign: Professor Soon-Chang Yoon, B. J. Sohn, grad students

Man-Hae Kim, Ji-Hyung Kim, Hyoung-wook Chun, Jong Hwan Kim, and scientists and staffs in Gosan observatory.

I would like to acknowledge my fellow students in the SIO department: Guillaume Mauger, Hyodae Seo, Hey-Jin Kim, Theresa Carpenter, David Mansbach, Dian Putrasahan, Anais Orsi, Guoqing Lin, Shang Liu, and Vas Petrenko. I am grateful to staffs in SIO department for their help and support: Joshua Reeves, Dawn Huffman, Kharyn Loteyro, Becky Burrola, and Alice Zheng. I also want to thank my friends Huiling Yuan, Cheng Huang, Shenfu Dong, Doris Chan, Wanting Wang, Yanan Zheng, Shuqing Zhao, Lei Xu, Guiqing Liu, Yong Jia, Qihui Jin, Fei Huang and Na Yang.

I am grateful to my family for all their support, my parents for their love and understanding, my brother for always believing in me. Lastly and most importantly, I thank my husband, Fengpeng Sun, with all my heart, for his love, encouragement, patience, encouragement, and scientific discussions. I could have done none of this without him.

The text of Chapter 2, in full, is a reprint of a published paper entitled “Dust Plumes over the Pacific, Indian, and Atlantic Oceans: Climatology and Radiative Impacts” in an August 2007 issue of Journal of Geophysical Research-Atm. The dissertation author was the primary researcher and author of this paper. Co-authors on this paper are Dr. V. Ramanathan, Fang Li, and Dohyeong Kim.

VITA

1996-2000 Bachelor of Science, Nanjing University, China

2000-2003 Master of Science, Peking University, China

2003-2010 Doctor of Philosophy, University of California, San Diego

PUBLICATIONS

Corrigan, C. E., M. V. Ramana, **A. Zhu**, K. Lehmann, O. Hadley, and V, Ramanathan (2010), Enhancement of Atmospheric Solar Heating from Forest Fires as Measured by Unmanned Aircraft, submitted.

Ault, A.P., **A. Zhu**, V. Ramanathan, and K.A. Prather (2010), Analysis of regionally transported particles in Gosan, Korea by single particle mass spectrometry. Atmospheric Environment, 2010, in preparation.

Ramanathan, V., H. Akimoto, P. Bonasoni, M. Brauer, G. Carmichael, C.E. Chung, Y. Feng, S. Fuzzi, S. I. Hasnain, M. Iyngararasan, A. Jayaraman, M. Lawrence, T. Nakajima, T. Panwar, M.V. Ramana, M. Rupakheti, S. Weidemann, S.C. Yoon and **A. Zhu** (2008), Atmospheric Brown Clouds and Regional Climate Change, Part I of Atmospheric Brown Clouds: Regional Assessment Report with Focus on Asia. Published by the Project Atmospheric Brown Cloud, United Nations Environment Programme, Nairobi, Kenya.

Zhu, A., V. Ramanathan, F. Li, and D. Kim (2007), Dust Plumes over the Pacific, Indian, and Atlantic Oceans: Climatology and Radiative Impact, J. Geophys. Res., 112, D16208, doi:10.1029/2007JD008427.

Zhu, A., C. Li, G. Liu, and J. Mao (2004), Validation and Application of MODIS Remote Aerosol Information in Beijing, Acta Scientiae Circumstantiae (in Chinese), 24(1), 86-90.

Yan, P., J. Mao, D. Yang, G. Liu, **A. Zhu**, X. Yu, and G. Liu (2004), The Characterization of Aerosol Physical and Chemical Properties at Linan Station during the Transport of a Sandstorm, Quaternary Sciences (in Chinese), 24(4), 421.

Liu, G., C. Li, **A. Zhu**, and J. Mao (2003), Optical Depth Research of Atmospheric Aerosol in the Yangtze River Delta Region, Environmental Protection (in Chinese), 2003(8), 58-63.

Li, C., J. Mao, Q. Liu, X. Liu, G. Liu, and **A. Zhu** (2003), Research on the Air Pollution in Beijing and its Surroundings with MODIS AOD Products, Chinese Journal of Atmospheric Sciences (in Chinese), 27(5).

Li, C., J. Mao, Q. Liu, J. Chen, Z. Yuan, X. Liu, **A. Zhu**, and G. Liu (2003), Characteristics of Distribution and Seasonal Variation of Aerosol Optical Depth in Eastern China with MODIS Products, Chinese Science Bulletin (in Chinese), 48(19): 2094-2100.

ABSTRACT OF THE DISSERTATION

Radiative and Climate Impacts of Absorbing Aerosols

By

Aihua Zhu

Doctor of Philosophy in Earth Sciences

University of California, San Diego, 2010

Professor V. Ramanathan, Chair

By integrating experimental data, radiative transfer theory, and numerical modelling, this dissertation aims to improve our understanding of the radiative and the climate impacts of the major absorbing aerosols: mineral dust, black carbon (BC) and brown carbon. The research presented here combines existing surface, satellite and aircraft measurements and develops self-consistent models for aerosol mixing state, global and regional radiative forcing of absorbing aerosols and their climate effects.

The first part of this dissertation presents the climatology and radiative impacts of dust plumes over the Pacific, the Indian and the Atlantic Oceans using multiple satellite datasets in conjunction with MACR (Monte Carlo Aerosol-Cloud-Radiation) model. A core-shell internally mixed aerosol model has been developed using the

microphysical, chemical, and radiative observations as constraints. It is shown that internal mixing enhances the aerosol absorption and contributes to over 20% increase of radiative forcing. The aerosol mixing model is validated by comparing model simulated spectrally-resolved irradiance with observations. The results show that aerosol induced forcing is mainly confined in the visible band and the largest forcing occurs in the blue channel.

Having validated the modelling of the mixing-state of absorbing aerosols with broadband and high-resolution spectral radiation data, global three-dimensional distribution of the spectral radiative forcing is obtained. The aerosol forcing is used to drive a general circulation model (GCM) with prescribed sea surface temperature to investigate the impact of absorbing aerosols on regional climate. One of the main model findings is that heating of the atmosphere by absorbing aerosols can contribute to significant reductions in low level clouds, which in turn amplifies the warming. The simulated cloudiness reduction is particularly strong over the Arctic and China and the simulated warming over the Arctic exceeds 1.5°C. The findings of cloud reduction over China and the warming over the Arctic are consistent with observations. The above effects are relatively weak or negligible when absorbing aerosols are treated as externally mixed which is used as the assumption by most GCM studies thus far. This study reveals the fundamental importance of accounting for the observed chemical and physical properties of absorbing aerosols.

Chapter 1

Introduction

1.1 Atmospheric aerosols

A result of rapid industrialization and population growth, environmental deterioration and the climate change caused by anthropogenic activities are the major challenges facing to the next generation. The effects of atmospheric aerosols on the Earth-Atmosphere radiative balance, clouds and precipitation are major sources of uncertainty in quantifying the impact of human activities on climate change [IPCC, 2007]. Atmospheric aerosols are suspensions of tiny solid or liquid particles in the air with varying origins, sizes, chemical composition, and atmospheric loading. Aerosols originate from both natural and anthropogenic sources and can be directly emitted as particles (primary aerosols) or formed as the result of chemical reactions (secondary aerosols). Some aerosol particles are directly emitted to the air through natural processes such as: originating from volcanic eruption, soil and rock debris, sea spray, dust storms, and forest fires. Human activities, including fossil fuel combustion, power generation, residential heating and cooking, biomass burning, slash and deforestation, construction and various industrial processes, also generate large amount of aerosols. Secondary aerosols are often produced by atmospheric gases reacting and condensing, or by 'gas-to-particle-conversion' process [*Seinfeld and Pandis*, 1998].

The sizes of atmospheric aerosols vary from a few nanometers to 100 microns. Combustion and chemical reactions of sulfate, nitrate, ammonium and secondary

organics generate small particles (submicron), while coarse particles are products of mechanical processes consisting of sea salt, dust, ashes, and biological debris [*Penner et al.*, 2001]. The average lifetime of atmospheric aerosols is on the order of a few days to weeks and primarily depends on their size and location. Some volcanic aerosols are transported to the stratosphere where they can remain in the atmosphere for over a year. Both dry (gravitational settling and turbulent deposition) and wet (rainout, washout, and sweepout) mechanisms clear aerosols from the atmosphere [*Seinfeld and Pandis*, 1998]. All these removal mechanisms are very efficient at removing coarse particles; however, there are no effective pathways for fine particle removal unless they grow to larger size by coagulation, condensation, and cloud processing.

The chemical composition of aerosols depends on their sources and geographical location and can be extremely variable. Sea salt aerosols, originating from sea spray, mainly consist of sodium chloride, magnesium, sulfate, calcium, potassium etc, while the constituents of dust aerosols are primarily mineral oxides, reflecting the composition of soil and the Earth's crust [*Seinfeld and Pandis*, 1998]. Biomass burning aerosols are dominated by carbonaceous components, mainly black carbon (BC) and organic carbon (OC) with lesser contributions from inorganic species (potassium, calcium, and iron etc). Secondary aerosols are the result of the oxidation of primary gases such as sulfuric acid, volatile organic compounds (VOCs), and nitrogen oxides, and take the form of salts or acid [*Penner et al.*, 2001]. Atmospheric loading of aerosols associated with industrialization and urbanization tends to increase

rapidly due to increased anthropogenic emissions of particles and their precursor gases from pre-industrial [IPCC, 2007].

Aerosol particles affect electromagnetic radiation through scattering and absorption. The radiative properties of atmospheric aerosols are critically dependent on their size and complex refractive index ($n=n_r+ik$), where n_r is the real part responsible for scattering, and k is the imaginary part representing absorption. The refractive index is strongly dependent on the chemical composition of the particle and varies with wavelength. The relative importance of scattering and absorption due to aerosols, is assessed through the single scattering albedo (SSA), defined as the ratio of scattering alone to total extinction (the sum of scattering and absorption) by a particle. For 'scattering' aerosols such as sulfate and sea salt, SSA in the visible band is close to 1, and scattering dominates the extinction of radiation. As to 'absorbing' aerosols like BC (or soot), SSA at ~550 nm is as low as about 0.2-0.3, indicating a strong absorption of solar radiation by this type of aerosol.

1.2 Aerosol radiative effects

Atmospheric aerosols play an important role in the radiative budget of the Earth-Atmosphere system through several different mechanisms as illustrated in Figure 1.1 [*Forster et al.*, 2007]. 1) Aerosols scatter and absorb solar and terrestrial radiation and hence directly modulate the way radiation is transmitted through the atmosphere. 2) Aerosols can also modify the microphysical and radiative properties of clouds; indirectly changing their albedo and lifetime. Serving as cloud condensation nuclei, atmospheric aerosols increase the cloud droplet number concentration and

decrease the effective cloud droplet size when cloud liquid water content is fixed. This indirect effect is also called as the 'first indirect effect' [*Ramaswamy et al.,* 2001], 'Twomey effect' [*Twomey*, 1977], or the 'cloud albedo effect' [*Lohman and Feichter*, 2005]. The influence of aerosols on cloud height, liquid water content, and lifetime has been termed as the 'second indirect effect' [*Ramaswamy et al.,* 2001], 'Albrecht effect' [*Albrecht*, 1989], or 'cloud lifetime effect' [*Lohman and Feichter*, 2005]. 3) Some aerosols also have the so-called 'semi-direct' effect [*Hansen et al.,* 1997], which describes the evaporation of clouds due to the absorption of solar radiation by dark aerosols such as BC. The heating induced by the absorbing aerosols changes the relative humidity and stability of troposphere and in turn modifies cloud amount, thickness, and lifetime [*Ackerman et al.,* 2000; *Johnson et al.,* 2004]. 4) The deposition of dark aerosols such as BC on snow/ice greatly darkens the surface and aggravates the retreat of glaciers and melting of sea ice by changing surface albedo [*Hansen and Nazarenko*, 2004; *Flanner et al.,* 2007].

Major modeling efforts have been initiated to accurately estimate the radiative effects of atmospheric aerosols. Observational efforts have also been mounted to aid modeling studies. During the Indian Ocean Experiment (INDOEX), comprehensive, detailed, and direct observations of the aerosol radiative forcing were made using aircraft, ship and ground-based observations of aerosol chemistry, microphysics, and radiative flux [*Ramanathan et al.,* 2001a]. These measurements allowed the aerosol radiative forcing efficiency at the surface (decrease in solar radiative flux at the surface per unit aerosol optical depth) and at the top-of-the-atmosphere (TOA)

[*Satheesh and Ramanathan*, 2000] to be evaluated. In addition, by constraining models with observations, the aerosol indirect forcing and semi-direct forcing [*Ramanathan et al.*, 2001a] were derived. The Maldives Autonomous unmanned aerial vehicle (UAV) Campaign (MAC) directly measured the atmospheric solar absorption and heating rates using three lightweight UAVs that were vertically stacked between 0.5 and 3 km over the polluted Indian Ocean [*Ramanathan et al.*, 2007]. The miniaturized instruments onboard these UAVs measured aerosol concentration, BC amount, clouds, humidity, temperature and solar fluxes. The synchronization of these measurements from UAVs above-cloud, in-cloud, and below-cloud with a horizontal separation of tens of meters or less and a temporal separation of less than ten seconds made it possible to measure the vertical heating rate directly and assess the contribution of atmospheric brown clouds in warming the atmosphere. More recently, pioneering efforts to determine radiative properties of aerosols at the single particle level have been initiated [*Moffet and Prather*, 2009].

The major goal of this dissertation is to take advantage of these observational efforts and develop a new modeling study to understand the role of aerosols on the radiation budget of the entire atmospheric column, and use this model to understand the impact of aerosols on climate. The model developed in this study makes a detailed attempt to meet the chemical and physical constraints imposed by these observations.

A large effort has been invested in accurately evaluating the radiative effects of atmospheric aerosols. A summary of the radiative forcing of anthropogenic aerosols from various studies was well documented in *the 4th report of Intergovernmental*

Panel on Climate Change [IPCC, 2007]. Radiative forcing is a measure of how the energy balance of the Earth-Atmosphere system is changed when factors that affect climate are altered. It is defined as the net irradiance change at the tropopause resulting from an applied perturbation, after allowing for stratospheric temperatures to readjust to radiative equilibrium while holding all other atmospheric variables fixed. Radiative forcing is a simple measure of climate change and does not represent the climate response. When applied to aerosols, radiative forcing normally refers to the forcing at the TOA, because the difference of radiative forcing at tropopause and the TOA is negligible. A positive value of radiative forcing indicates that the energy of the Earth-Atmosphere system will ultimately increase, which leads to a warming of the system. A negative radiative forcing will result in a cooling of the system. Another term 'surface forcing' [*Ramanathan et al.*, 2001a] is also frequently used to characterize aerosol radiative effect, which is a diagnostic quantity referring to the instantaneous perturbation of the surface radiative balance by atmospheric aerosols.

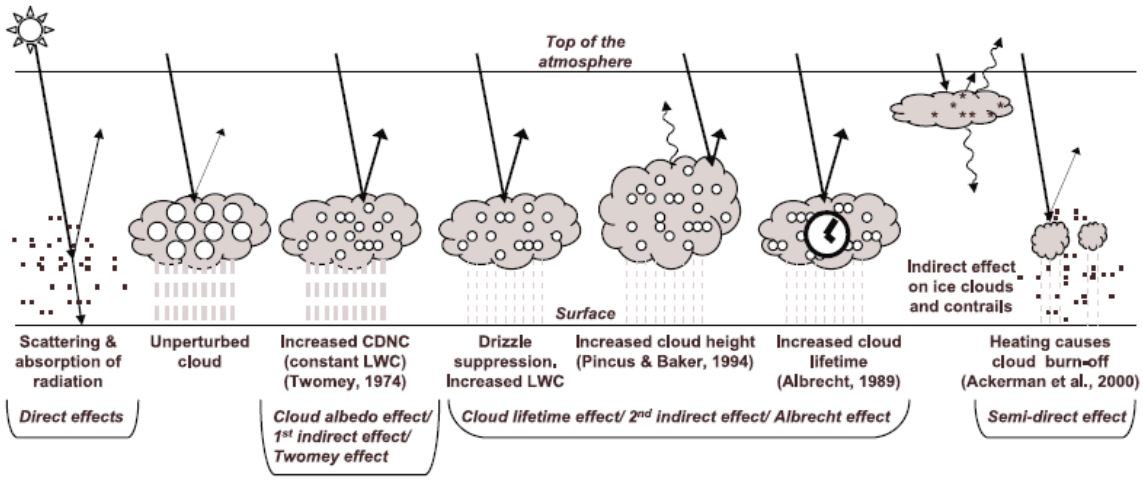

Figure 1.1: Schematic diagram of various radiative mechanisms associated with atmospheric aerosols. (figure from IPCC AR4 report chapter 2 Figure 2.10).

Figure 1.2 shows the radiative forcing by different aerosol components summarized by IPCC AR4 report. The direct radiative forcing by atmospheric sulfate aerosol is approximately -0.4±0.2 Wm^{-2} and the surface forcing is similar to that estimated at the TOA because sulfate aerosol is essentially a scattering aerosol in the solar spectrum with a SSA=1 and only a small degree of absorption in the near-infrared. A complex mixture of chemical compounds containing organic or elemental carbon species generated from fossil fuel, biofuel and biomass combustion, organic carbon has relatively different optical properties. OC aerosols are predominantly scattering; however some OC from fossil fuel combustion absorbs weakly in the ultraviolet and shorter wavelength range of the visible spectrum [*Bond*, 2001], and OC generated from less efficient combustion processes such as biomass burning have even greater absorption properties [*Kirchstetter et al.*, 2004]. The direct radiative forcing by total OC (fossil fuel, biofuel and biomass burning) is -0.19±0.20 Wm^{-2}. Black carbon aerosol is directly emitted from incomplete combustion of fossil fuel and biomass burning. BC absorbs strongly at all wavelengths of the solar spectrum and therefore exerts a positive radiative forcing. The mean direct radiative forcing by total BC is +0.34±0.25 Wm^{-2}. Estimates of the direct radiative forcing of anthropogenic mineral dust have high uncertainties due to the difficulties in determining the contribution from human activity (land use change and industrial practice) and the optical properties of dust particle in both shortwave and longwave spectrum. The direct radiative forcing of anthropogenic dust aerosols ranges from -0.3 Wm^{-2} to +0.1 Wm^{-2} assuming a 20% anthropogenic dust fraction.

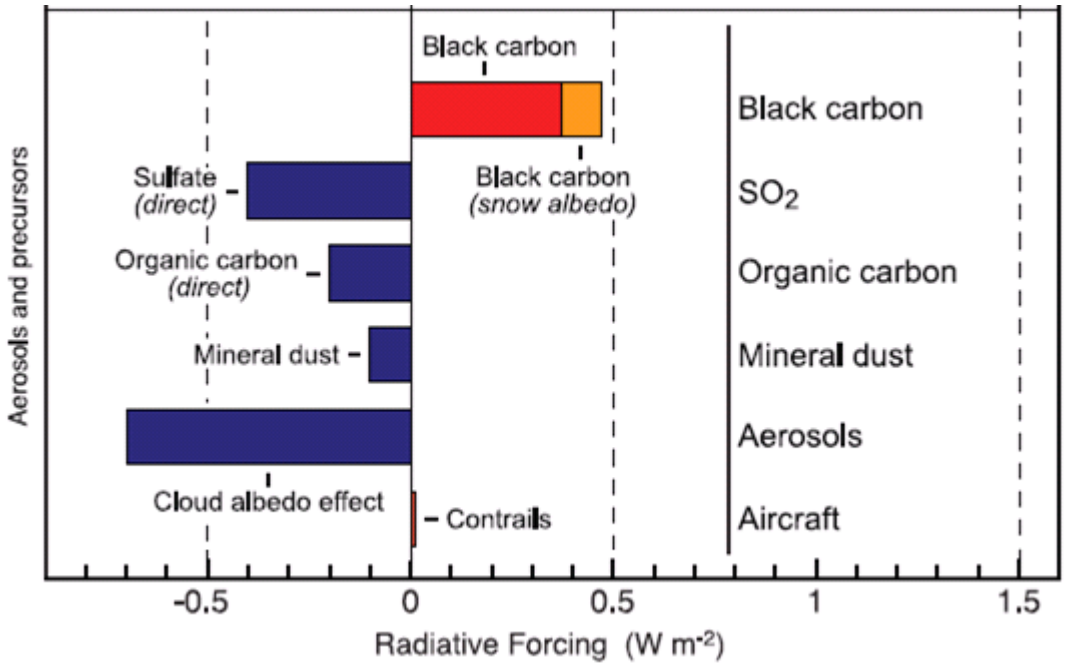

Figure 1.2: Radiative forcing for different aerosol components (figure from IPCC 2007, Figure 2.21).

Estimates of direct radiative forcing by individual aerosol components do not represent the overall forcing from aerosols because of nonlinear processes that include aerosol dynamics and interactions between the aerosols and the radiation field. The radiative properties of the combined aerosols change due to the mixing of various aerosol components. The mixing modifies chemical composition, state, size and shape of aerosols which leads to further changes of aerosol formation and removal processes. The development of new aerosol measurement techniques onboard satellite platforms along with improved, more frequent in situ observations provides better constraints for numerical models to estimate radiative forcings of total aerosols. *Yu et al.* [2006] reported a mean global clear-sky direct radiative forcing of -5.4±0.9 Wm^{-2} imposed by all aerosols (both anthropogenic and natural) over the oceans, which is consistent with

similar studies. Using integrated global data sets for aerosols, clouds, radiation fluxes, and radiative transfer model, *Kim and Ramanathan* [2008] showed that in the presence of clouds, the aerosol induced radiative forcing is -3.0±1 Wm^{-2} at the TOA and -7.0±2 Wm^{-2} at the surface.

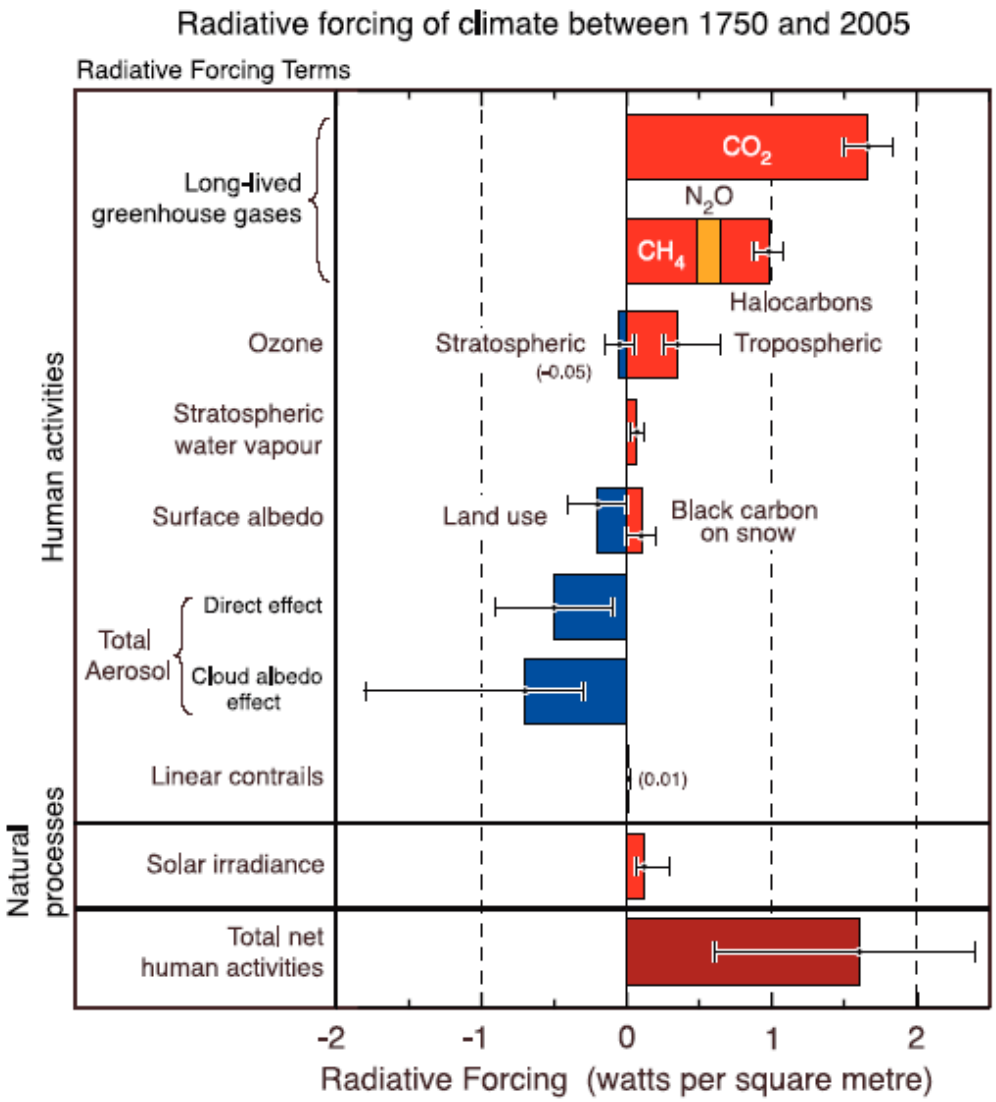

Figure 1.3: Summary of the principal components of the radiative forcing of climate change. The values represent the forcings in 2005 relative to the start of the industrial era (about 1750). (Note: figure from IPCC AR4 report chapter 2 FAQ 2.1 Figure 2).

An accurate estimate of the anthropogenic fraction of aerosols is vital to properly evaluate the aerosol radiative forcing from only the anthropogenic components. *Chung et al.* [2005] merged the modeled and observed fields of aerosol parameters using assimilation methods and estimated the direct forcing by anthropogenic aerosols with the employment of satellite, AERONET (AErosol RObotic NETwork), and model analysis. Their results show that the global annual mean direct radiative forcing by anthropogenic aerosols is -0.35 Wm^{-2} at the TOA and -3.4 Wm^{-2} at the surface with an overall uncertainty range of -0.1 to -0.6 Wm^{-2}. The study by *Bellouin et al.* [2005] estimated the anthropogenic aerosol forcing at -0.8±0.1 Wm^{-2} and *Yu et al.* [2006] reported a value of -0.5±0.33 Wm^{-2}. As indicated in Figure 1.3, the direct radiative forcing summed over all anthropogenic aerosol types (together with the estimation of nitrate and mineral dust) is -0.5 ±0.4 Wm^{-2} [IPCC, 2007].

Aerosols cause a negative radiative forcing indirectly through changing cloud albedo. All IPCC AR4 models estimate a negative global mean radiative forcing associated with cloud albedo effect and the median of the model results is -0.7 Wm^{-2} and much complex aerosol-cloud interactions are able to be captured by models. The presence of BC particles on snow/ice via precipitation and dry deposition can modify the reflective properties and emissivity of the surface and induce a positive radiative forcing. The best estimate of this forcing is +0.1±0.10 Wm^{-2} [IPCC, 2007] with a low level of scientific understanding. The global annual mean forcing (direct plus indirect) by anthropogenic aerosols is -1.2 Wm^{-2} (90% confidence interval of -2.7 to -0.4 Wm^{-2})

at the TOA, which masked 20-80% of greenhouse gases warming of ~3 Wm^{-2} in the past century [IPCC, 2007].

1.3 Climate impacts of aerosols

The build-up of aerosols not only affects the long term radiation balance, but also alters the monsoon circulation and regional water cycle [*Ramanathan et al., 2001b*]. A model study by *Menon et al.* [2002] showed that absorbing aerosols like BC may be responsible for the decrease of precipitation over the northern region of India and the north-south shift of rainfall patterns in East China (south flood, north drought). *Meehl et al.* [2008] employed Community Climate System Model (CCSM3) and performed model experiments with varying BC aerosols in order to study the effect of BC on the Indian summer monsoon. Their results showed that the radiative effects of BC are significant during the premonsoon months (March-April-May) and the dimming effect decreases of the surface temperature over most of India, the Bay of Bengal, and the Arabian Sea. BC induced shortwave heating warms the lower troposphere and the warmer air is advected northward, creating an elevated heat source over the Tibetan Plateau. This produces an anomalously strengthened meridional temperature gradient through the troposphere and enhances rainfall over most of India. At the onset of the monsoon, BC concentration decreases and the elevated heat source and meridional temperature gradient decrease. Combined with the anomalously cool SST (sea surface temperature) in the Arabian Sea and Bay of Bengal, this causes a reduction in precipitation over much of India during June-July-August. Using a coupled ocean-atmosphere model over South Asia with aerosol properties

prescribed according to observations, *Ramanathan et al.* [2005 and 2007] showed that anthropogenic aerosols increased atmospheric stability, weakened the latitudinal SST gradients in the Northern Indian Ocean, and led to a weakening of the monsoon circulation and a reduction of rainfall over India during the summer monsoon. *Bollasian et al.* [2008] investigated the influence of aerosol variability on the South Asian summer monsoon and found that anomalously high aerosols in May led to the reduction of cloud amount and precipitation and increased surface shortwave radiation and land surface warming. In June and July, the monsoon intensified as a result of the increased thermal contrast. This suggests that although excessive aerosols are associated with the decline of precipitation over India in early spring, internal atmosphere-land surface feedback actually strengthens the monsoon in subsequent summer months and land surface processes play an important role in mediating monsoon evolution. Given the complexity of the radiative, cloud-microphysics, dynamic responses, and hydrometeorological processes involved with aerosols, thoroughly understanding the influence of aerosols on monsoon rainfall is challenging.

1.4 Statement of problems and motivation

In spite of intense efforts to improve the understanding of the radiative and climate impacts of atmospheric aerosols, certain chronic and major problems remain in current studies. This study addresses these issues and attempts to rectify them.

The first issue is the mixing state of different aerosols. Most studies treat different aerosol chemical species as externally mixed. Surface observations show that this assumption is mostly incorrect. Freshly emitted particles coagulate with other

preexisting aerosols, or become coated by gaseous species. This atmospheric processing of aerosol chemical composition changes the radiative properties of the particles. Single particle chemistry analysis during INDOEX indicated that sulfates were nearly always associated with other materials and that single particles containing pure sulfuric acid, sodium sulfate, or ammonium sulfate were rare [*Guazzotti et al.*, 2001]. *Naoe and Okada* [2001] examined the aerosol samples collected in the urban air of Japan and found a dominant number fraction (75%) of internally mixed soot-particles in a "polluted" case in the radius range of 0.01-0.2 μm.

External mixing is widely used in many studies, which assumes that aerosol particles have had no physical interaction with each other, and therefore chemical composition, optical properties and radiative forcing of each aerosol component can be determined separately. Other studies treat interaction among different aerosol components by simply assuming that all aerosol species are perfectly mixed with each other at the molecular level. In this scenario, also known as the perfect internal mixing (or volume mixing) all particles have the same composition. Another mixing assumption is core-shell internal mixing (or coated mixing), in which solid particles such as BC and mineral dust serve as the core and are encapsulated by well-mixed non-absorbing materials. Many in situ measurements showed that the coated mixing assumption is closest to reality. *Okada et al.* [2001] found that organic material from biomass burning was internally mixed with inorganic salts such as sulfate, nitrate and soot. Field observation at Mexico City and Riverside showed that the majority of soot particles were associated with sulfate, organics, nitrate, and water [*Moffet and Prather*,

2009]. Accurate aerosol absorption properties are crucial for quantitative radiation budget estimates. *Bond et al.* [2006] suggested that absorption by aged soot particles mixed with other aerosols is about 1.5 times greater than that of fresh aerosols. A model study [*Jacobson*, 2000 and 2001] reported that the globally averaged direct radiative forcing of soot aerosols is 0.27 Wm^{-2} for externally mixed aerosols and 0.58 Wm^{-2} for a core-shell mixture, but is enhanced to 0.78 Wm^{-2} when aerosols are internally mixed. This clearly illustrates that the magnitude of direct aerosol radiative forcing largely depends on the mixing state of BC with other aerosols. Theoretically, absorption is always increased when light-absorbing particles are internally mixed with other materials [*Bond et al.*, 2006].

Next, organic carbon has been regarded by most if not all studies to have negligible absorption and simply treated as scattering aerosols. Recent studies suggested that certain organic carbon originating from biomass burning, called “brown carbon” [*Andreae and Gelenser*, 2006], absorbs strongly in the ultraviolet and blue band, with absorption decreasing at longer wavelength. The radiative and climate impacts of this absorbing organic carbon have been missed in most previous model studies.

Despite many studies aims at assessing the role of atmospheric aerosols in climate system, the net effect of aerosols on climate still represents one of the greatest uncertainties in our ability to predict and simulate climate change. The conclusions regarding the impact of absorbing aerosols on monsoon rainfall over the Indian subcontinent remain controversial and show heavy reliance on model settings used by

different studies. For example, the coupling of the ocean with atmosphere or using the prescribed SSTs leads to quite different model results on monsoon rainfall associated with aerosol effects [*Ramanathan et al.*, 2005; *Lau et al.*, 2006]. This is mainly because the former includes responses of the ocean to aerosol induced cooling at the surface while the latter does not.

1.5 Scope of the dissertation

The research presented in this dissertation integrates experimental observations and numerical modeling with the aim to improve the understanding of radiative and climate impacts of atmospheric aerosols. Chapter 2 presents the climatological distributions and radiative impacts of dust plumes over the Pacific, the Indian and the Atlantic Oceans. Chapter 3 integrates available observations to explore the importance of mixing state and radiative impacts of light-absorbing aerosol particles over the tropical Indian Ocean. Detailed investigation on the spectral signature of aerosol radiative forcing over the tropical Indian Ocean is described in Chapter 4. Chapter 5 presents the results of a model study of the radiative and climatic impact of absorbing aerosol. A brief summary and short discussion regarding the direction of further research are presented in Chapter 6.

Reference:

Ackerman, A. S., O.B. Toon, D.E. Stevens, A.J. Heymsfield, V. Ramanathan and E.J. Welton (2000), Reduction of tropical cloudiness by soot, *Science*, 288: 1042-1047.

Albrecht, B. (1989), Aerosols, cloud microphysics and fractional cloudiness, *Science*, **245**, 1227–1230.

Andreae, M. O., and A. Gelencser (2006), Black carbon or brown carbon? The nature of light-absorbing carbonaceous aerosols, *Atmos Chem Phys*, 6, 3131-3148.

Bellouin, N., O. Boucher, J. Haywood, and M. S. Reddy (2005), Global estimate of aerosol direct radiative forcing from satellite measurements, *Nature*, **438**, 1138–1141.

Bollasian, M., S. Nigam, and K.-M. Lau (2008), Absorbing aerosols and summer monsoon evolution over South Asia: an observational portrayal, *J. Climate*, 21, 3221-3239.

Bond, T. C. (2001), Spectral dependence of visible light absorption by carbonaceous particles emitted from coal combustion, *Geophys. Res. Lett.*, 28(21), 4075-4078.

Bond, T. C., G. Habib, and R. W. Bergstrom (2006), Limitations in the enhancement of visible light absorption due to mixing state, *J. Geophys. Res.*, 111, D20211, doi:10.1029/2006JD007315.
Chung, C. E., V. Ramanathan, D. Kim, and I. A. Podgorny (2005), Global anthropogenic aerosol direct forcing derived from satellite and ground-based observations, *J. Geophys. Res.*, 110, D24207, doi:10.1029/2005JD006356.

Forster, P., V. Ramaswamy, P. Artaxo, T. Berntsen, R. Betts, D.W. Fahey, J. Haywood, J. Lean, D.C. Lowe, G. Myhre, J. Nganga, R. Prinn, G. Raga, M. Schulz and R. Van Dorland (2007), Changes in Atmospheric Constituents and in Radiative Forcing. In: Climate Change 2007: The Physical Science Basis. Contribution of Working Group I to the Fourth Assessment Report of the Intergovernmental Panel on Climate Change [Solomon, S., D. Qin, M. Manning, Z. Chen, M. Marquis, K.B. Averyt, M.Tignor and H.L. Miller (eds.)]. Cambridge University Press, Cambridge, United Kingdom and New York, NY, USA.

Flanner, M. G., C. S. Zender, J. T. Randerson, and P. J. Rasch (2007), Present-day climate forcing and response from black carbon in snow, *J. Geophys. Res.*, 112, D11202, doi:10.1029/2006JD008003.

Guazzotti, S.A., K.R. Coffee, and K.A. Prather (2001), Continuous measurements of size-resolved particle chemistry during INDOEX-Intensive Field Phase 99, *J. Geophys. Res., 106* (D22), 28607-28627.

Hansen, J., and L. Nazarenko (2004), Soot climate forcing via snow and ice albedos, *Proc. Natl. Acad. Sci., 101*(2), 423–428.

Hansen, J., M. Sato, and R. Ruedy (1997), Radiative forcing and climate response. *J. Geophys. Res.*, **102,** 6831–6864.

Intergovernmental Panel on Climate Change (IPCC) (2007), Climate change 2007: the scientific basis. In: Solomon, S. (Ed.), Contribution of Working Group I to the Fourth Assessment Report of the Intergovernmental Panel on Climate Change. Cambridge Univ. Press, New York.

Jacobson, M. Z. (2000), A physically-based treatment of elemental carbon optics: Implications for global direct forcing of aerosols, *Geophys. Res. Lett.*, *27*(2), 217–220.

Jacobson, M. Z. (2001), Strong radiative heating due to the mixing state of black carbon in atmospheric aerosols, *N*ature, 409, 695-697.

Johnson, B.T., K.P. Shine, and P.M. Forster (2004), The semi-direct aerosol effect: Impact of absorbing aerosols on marine stratocumulus. *Q. J .R.Meteorol. Soc.*, **130**, 1407–1422.

Kim, D., and V. Ramanathan (2008), Solar radiation budget and radiative forcing due to aerosols and clouds, *J. Geophys. Res.*, 113, D02203, doi:10.1029/2007JD008434.

Kirchstetter, T. W., T. Novakov, and P. V. Hobbs (2004), Evidence that the spectral dependence of light absorption by aerosols is affected by organic carbon, *J. Geophys. Res.*, 109, D21208, doi:10.1029/2004JD004999.

Lau, K. M., M. K. Kim, and K. M. Kim (2006), Asian summer monsoon anomalies induced by aerosol direct forcing: The role of the Tibetan Plateau, *Climate Dyn.*, 26, 855–864.

Lohmann, U., and J. Feichter (2005), Global indirect aerosol effects: A review. *Atmos. Chem. Phys.*, **5**, 715–737.

Meehl, G. A., J. M. Arblaster, and W. D. Collins (2008), Effects of black carbon aerosols on the Indian monsoon. *J. Climate*, 21, 2869–2882.

Menon, S., J. Hansen, L. Nazarenko, and Y. Luo (2002), Climate effect of black carbon aerosols in China and India, *Science*, 297, 2250– 2252.

Moffet, R. C. and K. A. Prather (2009), In-situ measurements of the mixing state and optical properties of soot with implications for radiative forcing estimates, *Proceedings of the National Academy of Sciences*, 106(29),11872-11877.

Naoe, H., and K. Okada (2001), Mixing properties of submicrometer aerosol particles in the urban atmosphere - with regard to soot particles, *Atmospheric Environment*, 35, 5765-5772.

Okada, K., M. Ikegami, Y. Zaizen, Y. Makino, J. B. Jensen, J. L. Gras (2001), The mixture state of individual aerosol particles in the 1997 Indonesian haze episode, *Journal of Aerosol Science*, 32, 1269–1279.

Penner, J.E., et al. (2001), Aerosols, their direct and indirect effects. In: Climate Change 2001: The Scientific Basis. Contribution of Working Group I to the Third Assessment Report of the Intergovernmental Panel on Climate Change [Houghton, J.T., et al. (eds.)]. Cambridge University Press, Cambridge, United Kingdom and New York, NY, USA, pp. 289–348.

Ramanathan, V. et al. (2001a), Indian Ocean EXperiment: An integrated analysis of the climate forcing and effects of the great Indo-Asian haze, *J. Geophys. Res, 106* (D22): 28371-28398.

Ramanathan, V., P. J. Crutzen, J. T. Kiehl and D. Rosenfeld (2001b), Aerosols, Climate, and the Hydrological Cycle, *Science*, 294, 2119-2124.

Ramanathan et al. (2005), Atmospheric brown clouds: Impacts on South Asian climate and hydrological cycle. *Proceedings of the National Academy of Sciences USA*, **102,** 5326–5333.

Ramanathan, V., M. V. Ramana, G. C. Roberts, D. Kim, D., C. E. Corrigan, C. Chung, and D. Winker (2007), Warming trends in Asia amplified by brown cloud solar absorption, *Nature*, 448, 575–578, doi:10.1038/nature06019.

Ramaswamy, V., et al. (2001), Radiative forcing of climate change. In: Climate Change 2001: The Scientific Basis. Contribution of Working Group I to the Third Assessment Report of the Intergovernmental Panel on Climate Change [Houghton, J.T., et al. (eds.)]. Cambridge University Press, Cambridge, United Kingdom and New York, NY, USA, pp. 349–416.

Satheesh, S. K., and V. Ramanathan (2000), Large differences in tropical aerosol forcing at the top of the atmosphere and Earth's surface, *Nature*, 405, 60– 63.

Seinfeld, J.H. and S.N. Pandis (1998), Atmospheric Chemistry and Physics: From Air Pollution to Climate Change. 2nd Edn., Wiley Interscience, New York, ISBN: 0-471-17816-0, pp: 1326.

Twomey, S. A. (1977), The influence of pollution on the shortwave albedo of clouds, *J. Atmos. Sci*., 34, 1149–1152.

Yu, H., et al. (2006), A review of measurement-based assessments of the aerosol direct radiative effect and forcing. *Atmos. Chem. Phys.*, **6**, 613–666.

Chapter 2

Dust Plumes over the Pacific, Indian, and Atlantic Oceans: Climatology and Radiative Impact

2.1 Introduction

Airborne dust aerosols have been documented extensively [*Harrison et al.*, 2001; *Duce*, 1995; *Mahowald et al.*, 2006; *Tegen et al.*, 1996; *Prospero et al.*, 2002]. The dominance of dust aerosols over anthropogenic aerosols was shown by *Li and Ramanathan* [2002], e.g., for the Arabian Sea, the authors showed that the summer time (Jun-Jul-Aug) aerosol optical depth (AOD) (mainly due to dust) far exceeded the dry season anthropogenic aerosol AODs. Of increasing interest is the climate impact introduced by dust aerosols through regulation of the radiation budget [IPCC, 2001]. Dust aerosols cut down incoming solar radiation reaching the surface via reflection and absorption. Moreover, dust particles also interact with LW flux mainly through the absorption of the outgoing LW radiation originating from the underlying regions [*Sokolik and Toon*, 1999]. The aforementioned effects are the so called direct radiative forcing of dust aerosols. On the other hand, acting as cloud condensation nuclei (CCN) and ice nuclei, dust particles may modify the albedo and lifetime of clouds [*Twomey*, 1977; *DeMott et al.*, 2003; *Sassen et al.*, 2003], defined as the first and second indirect effect, respectively. The additional heating induced by mineral dust can also lead to reduction of liquid water path and cloud cover [*Huang et al.*, 2006], causing a semi-direct effect. The strong radiative forcing by dust aerosols may further lead to

potential impacts to the regional climate and hydrological cycle. The model simulation by *Lau et al.* [2006] indicated that the mixture of dust aerosols and soot can heat the air over the Tibetan Plateau, which may alter the Asian monsoon circulation.

By parameterization of mineral dust within the Hadley Centre AGCM (atmospheric general circulation model), *Woodward* [2001] yielded a global annual mean direct dust radiative forcing of +0.07 Wm^{-2} at the top-of-the-atmosphere (TOA), and -0.82 Wm^{-2} at the surface. However, the peak forcing introduced by dust aerosol can be up to 2 orders of magnitude larger than the global annual mean values, especially downstream of the dust source regions such as the Saharan Desert, Taklamakan Desert, Gobi Desert, and Arabian Desert and so on. The largest and most persistent dust sources are found to be mainly in the Northern Hemisphere extending from North Africa, Middle East, Central and South Asia, and China [*Prospero et al.*, 2002]. Inside this broad 'dust belt', three distinct dust plumes over the oceans can be distinguished, which are East Asian dust plume over the N. Pacific Ocean in the spring time, Saharan dust plume over the Atlantic Ocean and the Arabian dust plume over the Indian Ocean [*Li and Ramanathan*, 2002] during the summer months. Although, impressive progress has been achieved in the development of numerical aerosol models to simulate the emission, deflation, transport, and deposition of atmospheric aerosols on regional and global scales [*Penner et al.,* 2001; *Woodward* 2001; *Perlwitz et al.,* 2001; *Song and Carmichael*, 2001; *Gong et al*., 2003; *Shao* et al., 2003; *Chin et al.,* 2002; *Zender et al.,* 2003], very few models were able to adequately predict dust optical depth when compared with the observations [*Sokolik et al.,* 2001; *Lunt and*

Valdes, 2002]. The deficiency of numerical models to accurately simulate the dust optical depth necessitates the comprehensive use of all kinds of observations for the study of dust radiative forcing.

Various field experiments have been conducted to study the physical and chemical characteristics and radiative impacts of dust aerosols. These include ACE-2 (the 2nd Aerosol Characterization Experiment) [*Raes et al.,* 2000], PRIDE (the Puerto Rico Dust Experiment) [*Colarco et al.*, 2003a, 2003b], SHADE (the Saharan Dust Experiment) [*Haywood et al.*, 2003; *Tanré et al.,* 2003; *Myhre et al.,* 2003], ADEC (Aeolian Dust Experiment on Climate impacts) [*Shi et al.,* 2005], and ACE-Asia [*Seinfeld et al.,* 2004]. However, the systematic comparison of climatology and radiative effects of the aforementioned three major dust plumes have never been done before due to limited observations and scarce data. With the advantages of advanced techniques to monitor large scale atmospheric aerosols over long periods, satellite data help to fill the gap of insufficient observations and significantly improve our understanding of the behaviors of dust plumes [*Kaufman et al.,* 2005; *Husar et al.*, 2001]. *Li et al.* [2004] provided an observationally constrained shortwave radiative forcing of Saharan dust by employing MODIS (Moderate Imaging Spectroradiometer) AOD and CERES (the Clouds and the Earth's Radiant Energy System) flux data. These successful achievements encourage us to apply more satellite data to study the climatology and radiative impacts of dust plumes over the global oceans.

In this study, I will focus on the climatology and radiative impacts of three major dust plumes over the Northern hemisphere: the East Asian dust plume over the

Pacific Ocean, the Arabian dust plume over the Indian Ocean, and the Saharan dust plume over the Atlantic Ocean. For this purpose, five different satellite datasets were combined. Providing the longest observation period (1981~2001), NOAA (National Oceanic and Atmospheric Administration) PathFinder AVHRR (Advanced Very High Resolution Radiometer) aerosol data are appropriate for the analysis of temporal and spatial climatology of dust plumes. Stratospheric Aerosol and Gas Experiment (SAGE) II aerosol extinction coefficient data are used to determine the vertical distribution of dust plumes. MODIS large mode AOD data and aerosol model results derived from Goddard Global Ozone Chemistry Aerosol Radiation and Transport (GOCART) model [*Chin et al.,* 2002; *Ginoux et al.,* 2001] were used to evaluate the dust fraction estimate. TOMS (Total Ozone Mapping Spectrometer) and MISR (Multiangle Imaging Spectroradiometer) AOD data are employed to examine the consistency among different satellite observations. MODIS level-2 AOD data are applied to MACR model to assess the direct radiative forcing, and atmospheric heating rate change introduced by mineral dust.. The single scattering albedo measured at AERONET (Aerosol Robotic NETwork) [*Holben et al.,* 1998] dust-dominated sites and refractive index observed by previous experiments near upstream source regions are employed to represent the optical properties of dust particles.

Section 2 describes the radiative transfer model, satellite aerosol products and other input parameters employed in this study. The climatological results of dust plumes derived from satellite data are presented in Section 3. The radiative impacts induced by dust plumes are shown in Section 4, followed by Section 5 with discussion

about the uncertainties and limitations of this study. Conclusions are summarized in Section 6.

2.2 Model and Data

The MACR radiative transfer model, satellite derived aerosol data, and other input parameters employed in this study are discussed in this section.

2.2.1 Radiative Transfer Model

Monte Carlo Aerosol-Cloud-Radiation (MACR) model is adopted to evaluate the climate impacts introduced by dust aerosols. MACR was first developed at the Center for Clouds, Chemistry and Climate (C^4), Scripps Institution of Oceanography during INDOEX (the Indian Ocean Experiment) [*Ramanathan et al.,* 2001; *Podgorny and Ramanathan,* 2001; *Podgorny et al.*, 1998; *Satheesh et al.*, 1999; *Vogelmann et al.*, 2001]. Using the Maximum Cross-Section Method [*Marchuk et al.*, 1980], MACR computes the photon transport in the media and estimates the radiative flux at each interface. In the current version, a total of 32 shortwave (SW) bands (from 0.25μm to 5.0μm) and 16 longwave (LW) bands (from 3.0μm to 1000.0μm) are used for the solar and terrestrial radiation calculations, respectively. MACR can treat the scattering, absorbing, and emission by gases, clouds, and aerosols. Clouds are classified into low-, mid-, and high-clouds (based on their height), as well as convective clouds. To account for the gaseous absorption, the updated gas absorption database HITRAN2000 (high-resolution transmission) [*Rothman et al.,* 2003] and CKD2.4 [*Clough et al.,* 1989] for water vapor continuum are incorporated with the correlated-*k* distribution method [*Goody et al.,* 1989; *Fu and Liou,* 1992; *Lacis and Oinas,* 1991; *Kato et al.,*

1999], which includes up to 20 correlated-*k* coefficients at each band. The absorption of water vapor, ozone, carbon dioxide, and oxygen are considered in both SW and LW portions. Trace gases, such as CH_4, N_2O, and CO are also contained in the LW absorption calculation.

2.2.2 Satellite Derived Aerosol Data

2.2.2.1 AVHRR

Recognizing the need to improve long time series datasets for global change research, NOAA and NASA initiated the "Early-EOS (Earth Observing System) Pathfinder Data Set Activity" in 1990. The Pathfinder Program focuses on how the existing satellite datasets could be processed and used to study global change. The long time series datasets are applied to the stable calibrations and community consensus algorithms [*Stowe et al*., 1997]. AVHRR Pathfinder atmospheric datasets cover the period from June 1981 to July 2001 and use a quasi-equal area grid (equivalent to the area of a 1° latitude/longitude grid box at the Equator ~110km by 110km) for the computation of statistics and the storage of mapped data. The aerosol retrieval algorithm is based on a simple Junge aerosol size distribution (size parameter, v=3.5) for the non-absorbing aerosols (real part of refractive index is 1.5) [*Stowe et al.,* 1997]. AOD is estimated from backscattering radiation measured at an effective wavelength of 0.63μm for cloud-free days (2nd generation) over the dark oceans (surface reflectance ~1.5%). Cloud screening procedures are based on the fact that the cloud reflectance is high and relatively constant for the most visible and infrared spectrums. In contrast, aerosol backscattering is much stronger in the visible than in

the near and far infrared range. Pixels containing clouds can be identified and removed by comparing the observed signal in near-IR with that in the absence of clouds. This cloud screening approach can not retrieve AOD when its value is larger than 2.0 because the separation between cloud and aerosol becomes ambiguous for remote sensing when AOD exceeds this value [*Stowe et al*., 2002]. With the longest observation period, AVHRR aerosol products are expected to provide the most complete climatological descriptions on the spatial and temporal variations of dust plumes.

2.2.2.2 MODIS

MODIS aerosol products present the ambient AOD over the oceans globally and over a portion of the continents with low surface albedo. There are two MODIS aerosol datasets: one contains data from the Terra platform, and another collects data from the Aqua platform. In this study I chose Terra data, because the observations period exceeds that of the Aqua data by two years. Daily Level-2 AOD data are produced at the spatial resolution of a 10 by 10 km (at nadir) pixel array. The observed TOA reflectance at seven wavelengths (0.47, 0.55, 0.66, 0.87, 1.24, 1.64 and 2.13 m) was compared to a pre-computed look-up table, which contains the reflectance for an array of angles, size distributions and optical depths [*Tanré et al.,* 1997]. The modeled reflectance with the smallest difference from the observed reflectance is retrieved from the look-up table. This best-fit reflectance is associated with a corresponding set of aerosol properties. Currently, nine tropospheric aerosol models are used, including four small mode models and five large mode models. The scattering and absorbing

properties are derived from the analyses of AERONET data and LANDSAT Thematic Mapper (TM) images [*Tanré et al.,* 2001; *Kaufman et al*., 2001]. Aerosol size information is currently derived for ocean areas only. MODIS cloud mask determination combines both SW and LW channels for a total of 13 channels. Additional cloud screening with regard to the neighboring pixels is also considered in the algorithm after the application of cloud mask. Because cirrus cloud can be highly transparent and contaminate the retrieval of aerosol product, MODIS cloud screening algorithm subtracts cirrus effect by rejecting 25-33% of the brightest and darkest pixels at 865 nm within the 10 by10 km box [*Martins et al.,* 2002]. The low reflectance pixels of small signal-to-noise ratio are also excluded to maintain the quality of the results [*Kaufman and Tanre*, 1998]. MODIS AOD data from 2000 to 2004 are used to estimate the optical depths of dust particles, and applied to the MACR radiative model to assess the radiative impacts of dust plumes.

2.2.2.3 TOMS and MISR

TOMS AOD record covers the periods from January 1979 to April 1993 (Nimbus7-TOMS observations), and from July 1996 to December 2000 (Earth Probe TOMS measurements). These datasets are tabulated on a 1° by 1° grid between 89.5°S and 89.5°N. The backscattered radiances (I_λ) measured at two wavelengths λ_1 and λ_2 are used in the aerosol retrieval algorithm, which is based on the theoretical framework presented by *Torres et al*. [1998]. Particles are characterized by comparing measured and pre-computed spectral contrast ($I_{\lambda 1}$/ $I_{\lambda 2}$) and the radiance at the longer wavelength ($I_{\lambda 2}$). Wavelength pairs at 340 and 380 nm are used for Nimbus 7 data and

pairs at 331 and 360nm are for the Earth Probe TOMS data. In this study the Earth Probe TOMS monthly averaged datasets are used due to its good quality control [*Torres et al*., 2002].

The MISR instrument orbits the Earth about 15 times each day and accomplishes the nearly global coverage within 9 days. MISR collects multi-angle as well as multi-spectral data, which are not available from any other satellite instruments. Viewing the sunlit Earth simultaneously at nine widely-spaced angles (0-70.5°), MISR provides radio-metrically and geometrically calibrated images in four spectral bands (446, 558, 672 and 866nm) at each angle. With this particular ability, MISR can retrieve AOD over land with a bright surface [*Diner et al*., 2001]. Three years of MISR AOD data (2000-2002) are analyzed in this study. TOMS and MISR AOD data are employed to examine the consistency of different satellite AOD datasets.

2.2.2.4 SAGE II

The SAGE II sensor was launched into a 57° inclination orbit aboard the Earth Radiation Budget Satellite (ERBS) in October 1984. During each sunrise and sunset encountered by the orbiting spacecraft, the instrument uses the solar occultation technique measuring the attenuated solar radiation through the Earth's limb in seven channels with central wavelengths ranging from 0.385 to 1.02 μm. The transmittance measurements are inverted using the "onion-peeling" approach [*Antuña et al.,* 2002] to retrieve the aerosol extinction coefficient [km^{-1}] as well as the other atmospheric compounds such as ozone, nitrogen dioxide, and water vapor at 0.385, 0.453, 0.525, and 1.02 μm. These data, in conjunction with data from sister instruments

Stratospheric Aerosol Measurement (SAM) II and SAGE I, can be used to estimate long-term constituent trends and to identify responses to episodic events. SAGE II has a horizontal resolution of the order of 200 km and a vertical resolution of 1 km [*Kent et al.,* 1998]. A global climatology of stratospheric aerosol radiative properties has been compiled from SAGE II multi-wavelength extinction measurements [*Thomason et al.,* 1997]. Although SAGE II was initially designed for detecting stratospheric aerosols, its 1.02 μm aerosol extinction coefficient profiles have actually been retrieved reaching down to the boundary layer [*Wang et al*., 1999; *Thomason and Taha* 2003; *Kent et al*., 2003]. Sufficient tropospheric data have been accumulated under cloudless conditions after long observation period. These low level SAGE II data afford a rough but potential way to understand the vertical distributions of tropospheric aerosols. In this study, aerosol extinction coefficient data [km^{-1}] at 1.02 μm was used due to its better quality [*Kent et al*., 1998].

2.2.3 Other Input Parameters for MACR

Three important optical parameters are required in order to estimate direct radiative forcing by aerosol particles using the MACR model, which are single scattering albedo (SSA), asymmetry factor (ASY), and Ångström exponent (ANG). Due to the variety of the mineralogical compositions, dust particles from different regions show quite different optical properties [*Sokolik and Toon*, 1999]. To compare the radiative forcing due to dust particle itself, the optical properties of dust particle sampled near the source regions are considered only. For example, I select aerosol optical properties from desert site upwind of China to model Yellow Sea (YS) dust.

For SW calculation, SSA, ASY, and ANG data are derived from three dust-dominated AERONET sites [*Dubovik et. al.,* 2002; *Eck et. al.,* 2005], which are Dunhuang (40°N, 94°E) for the N. Pacific Ocean, Solar Village (24°N, 46°E) for the Indian Ocean, and Cape Verde (16°N, 22°W) for the N. Atlantic Ocean. As shown in Table 2.1, dust in Arabian Sea is most absorbing among three regions, with SSA at 550nm to be 0.933, while dust in Yellow Sea is more scattering. For LW radiative forcing consideration, the field sampled refractive index data near the Taklamakan Desert [*Shi et al*., 2005], Afghanistan [*Sokolik et al.,* 1993], and Barbados [*Volz,* 1973] were employed to represent the dust aerosols over the N. Pacific Ocean, the Indian Ocean, and the N. Atlantic Ocean. These refractive index data, as shown in Figure 2.1, were applied to MIE code by using the size distribution for transported dust from OPAC dataset with mode radius of 0.5 μm and standard deviation of 2.0 [*Hess et al.*, 1998] to consider the spectral variation of SSA in the LW spectrum. It's clearly seen that at around 9 μm, Saharan dust shows the largest absorption (Figure 2.1a, the imaginary part of the refractive index) among the three regions, suggesting strong absorption of LW flux by Saharan dust [*Volz*, 1973].

Table 2.1: SSA, ASY, and ANG (550nm) for YS (Dunhuang), AS (Solar Village), and SC (Cape Verde) from AERONET dust-dominated sites.

Parameter	**YS**	**AS**	**SC**
SSA	0.964	0.933	0.948
ASY	0.745	0.680	0.690
ANG	0.299	0.410	0.360

The monthly mean temperature, specific humidity, surface wind, and geopotential height derived from the ECMWF ERA-40 [*Uppala et al.,* 2005]

reanalysis data (1981-2001) are used to describe the state of the atmosphere. The NOAA OI-2 SST data (1971-2000) [*Reynolds et al.*, 2002] are employed to estimate IR emissions from the ocean surface. For the cloud fraction and optical depth, 15 types of ISCCP (International Satellite Cloud Climatology Project)-D2 monthly mean cloud products (1984-2000) are combined into 4 cloud types: low, mid, high, and deep convective clouds [*Rossow and Schiffer*, 1999; *Rossow et al.*, 1996; *Chung et. al.*, 2005].

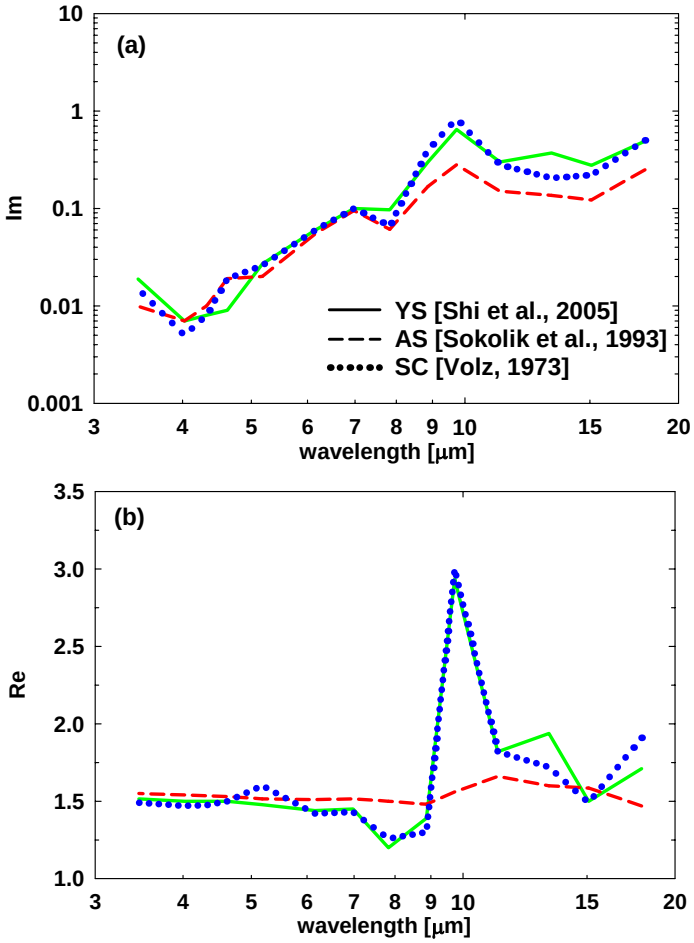

Figure 2.1: Spectral variation of (a) imaginary part, and (b) real part of dust refractive index for Yellow Sea (YS, from Shi et al., 2005), Arabian Sea (AS, from Sokolik et al, 1993), and Saharan Coast (SC, from Volz, 1973).

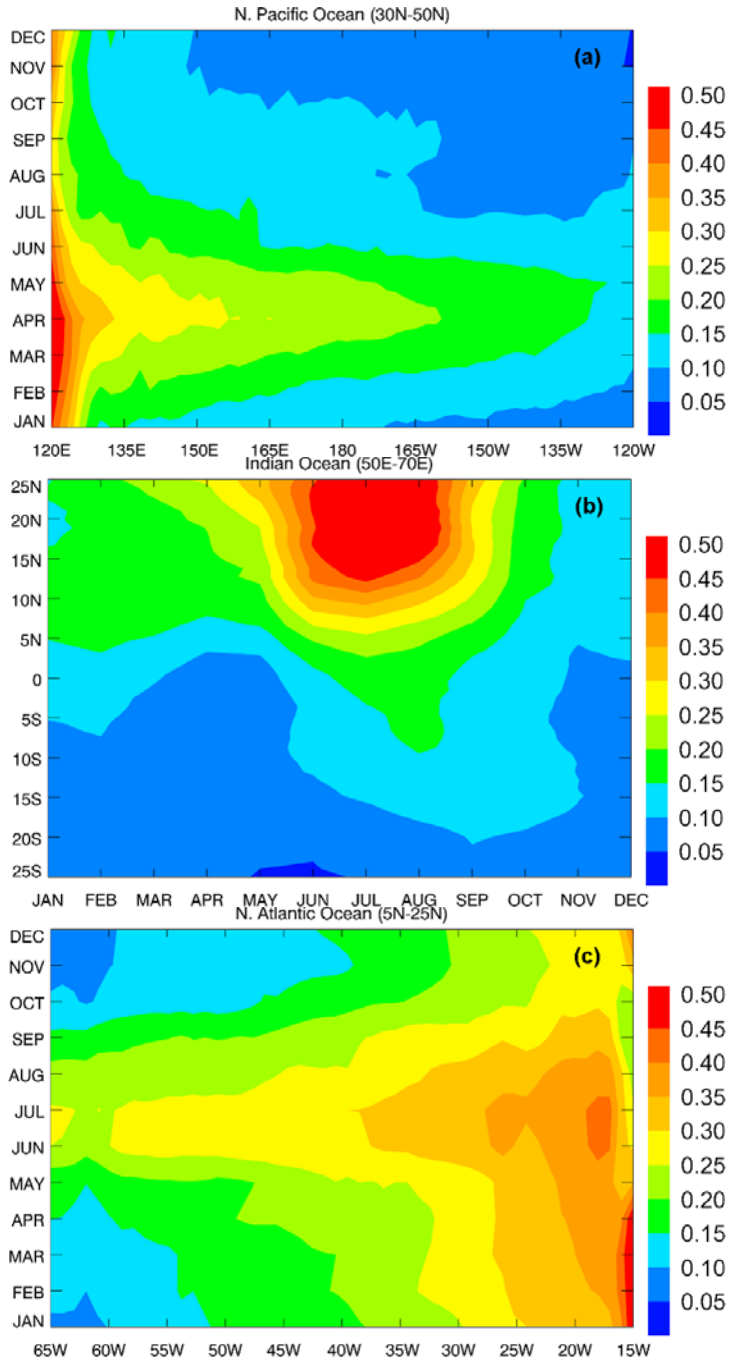

Figure 2.2: The spatial and temporal distributions of 20-year averaged (1981-2001) AVHRR AOD (630nm) (a) as a function of longitude over the N. Pacific Ocean (latitude range: 30°N~50°N), (b) as a function of latitude over the Indian Ocean (longitude range 50°W~70°E), and (c) as a function of longitude over the N. Atlantic Ocean (latitude range 5°N~25°N).

2.3 Climatological Results

Climatological results derived from the aforementioned satellite data are presented in this section. The seasonal variation, spatial distribution, the dust fraction relative to total AOD, and dust vertical profile are described for the dust plumes over the Pacific, Indian, and Atlantic oceans.

2.3.1 Seasonal Variation

The spatial and temporal distributions of 20-year averaged (1981-2001) AVHRR AOD (630nm) are showed as a function of longitude over the N. Pacific Ocean (latitude range: 30°N~50°N) (Figure 2.2a), as a function of latitude over the Indian Ocean (longitude range 50°W~70°E) (Figure 2.2b), and as a function of longitude over the N. Atlantic Ocean (latitude range 5°N~25°N) (Figure 2.2c). The high aerosol loading and maximum transport across the oceans can be seen clearly in March-April-May (MAM) over the N. Pacific and in June-July-August (JJA) over both the Indian and the N. Atlantic oceans. During other seasons, although high AOD exists near the coast, the transport of aerosols is limited and AOD is usually less than 0.15 in the remote oceans.

The annual cycle of the aerosol plumes derived from long term AVHRR AOD data is consistent with the acknowledged dust seasons in previous studies. Based on 49 years (1949-2002) daily observed data from 681 national meteorological stations in northern China, *Zhou and Zhang* [2003] demonstrated that the frequency of severe dust storms in spring accounts for more than 80% in the whole year. The study by *Chun and Lim* [2004] also confirms that spring is the season with the most frequent

East Asian dust storms over Korea. Based on the surface observations, *Ackerman and Cox* [1989] showed the annual peak of dust outbreaks over Arabian regions from late spring to early fall. *Li and Ramanathan* [2002] reported similar findings by utilizing satellite data with wind field from surface to 500mb. The study by *Prospero and Carlson* [1981] as well as *Mbourou et al.* [1997] pointed out that the greatest dust concentrations occur in the summer months at Barbados, and trade winds can transport Saharan dusts to the Caribbean cross the Atlantic when the ITCZ (Intertropical Convergence Zone) moves northward in summer. In our study, dust seasons are defined to be boreal spring (MAM) for the Pacific and JJA for the Indian and Atlantic Oceans.

2.3.2 Regional Distribution

In Figure 2.3, seasonal mean spatial distributions of 20-year averaged AVHRR AOD (630nm) are shown for the dust season only over the Pacific Ocean (MAM), Indian Ocean (JJA), and Atlantic Ocean (JJA). The geographic distribution of dust plumes has been demonstrated clearly, with high AOD close to the continental coast line and gradually declining with distance away from the source. Large amounts of dust particles are removed from the atmosphere during long-range transport crossing the ocean sectors, resulting in large AOD gradients from the source to the remote ocean.

By means of the long term NCEP/NCAR (National Centers for Environmental Prediction / National Center for Atmospheric Research) wind fields, *Li and Ramanathan* [2002] found that the long range transport patterns of the dust plumes are

mainly determined by the prevailing winds over each ocean sector. With the assistance of the strong mid-latitude westerlies, the Pacific dust plume (Figure 2.3a) is transported northeastward across the Pacific Ocean and can reach as far as the west coast of North America, where AOD is still as high as ~0.15. The southward spread of the dust plume from Arabian and Indian continent can reach to as south as 5°N with AOD larger than 0.2 (Figure 2.3b), although the prevailing wind is southwestly during the well-known Indian summer monsoon season. This southwest winds not only blow the clean maritime air towards the continent, might also carry dust particles from Somalia to the Arabian Sea. The extremely high AOD (>0.6) over the Arabian Sea is also caused by dust aerosols originating from the Arabian Peninsula, transported by the strong northwesterly offshore wind [*Pease et al.,* 1998], which is one branch of the cyclonic flow with low pressure center over the Asian mainland owing to strong surface heating in the summer time [*Sirocko,* 1991]. The westward transport of dust plume over the N. Atlantic Ocean (Figure 2.3c) is assisted by the equatorial trade winds when the ITCZ moves northward in the summer, however, this transport is mainly confined in the narrow band between 10°N and 20°N due to both the geographic distribution of dust sources and the prevailing wind belt. To quantitatively compare the dust plumes, three target areas (marked by the black box in Figure 2.3) with same areas (20° by 20°) are selected as the Yellow Sea (YS, 30°N-50°N, 120°E-140°E) in the N. Pacific Ocean, the Arabian Sea (AS, 5°N-25°N, 50°E-70°E) in the Indian Ocean, and the Saharan Coast (SC, 5°N-25°N, 15°W-35°W) in the Eastern Atlantic Ocean. The results hereafter were retrieved for the target areas only.

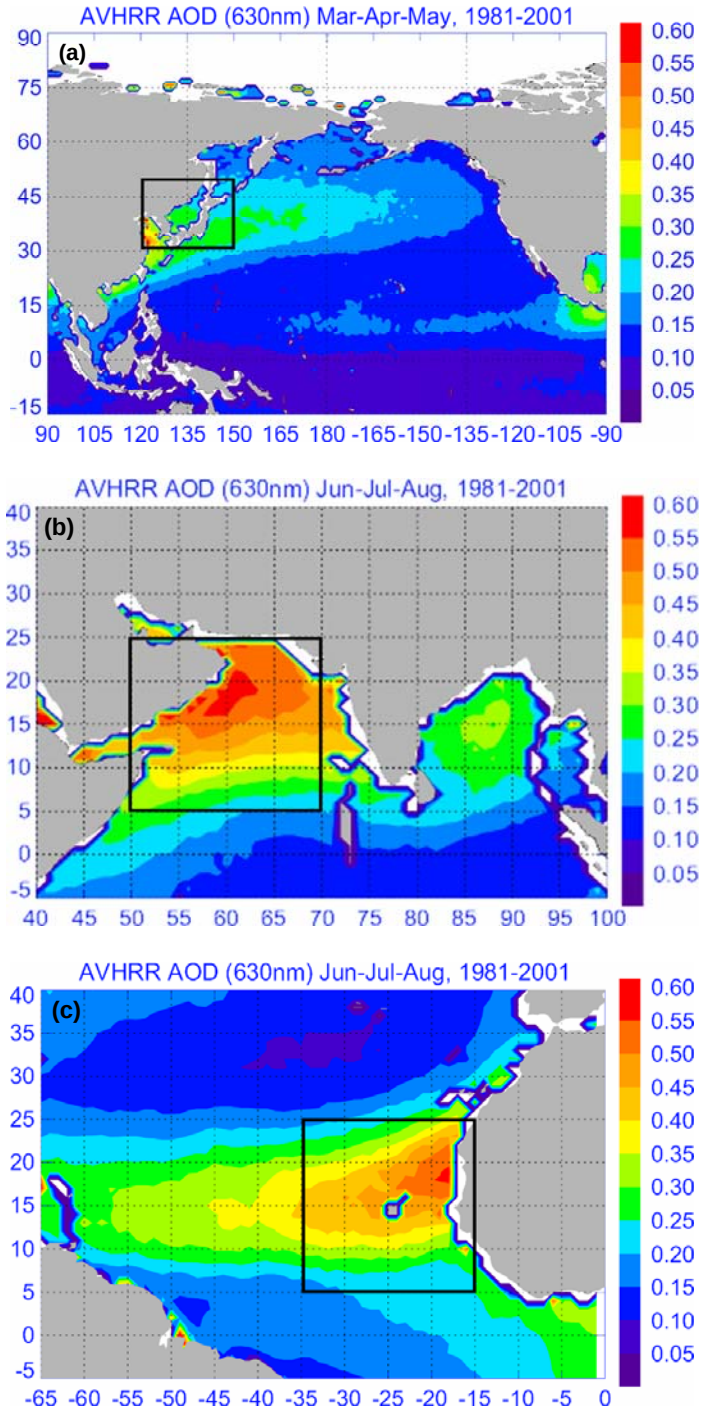

Figure 2.3: Seasonal mean AVHRR AOD (630nm) (averaged from 1981 to 2001) over the (a) Pacific Ocean (MAM), (b) Indian Ocean (JJA), and (c) Atlantic Ocean (JJA). Target area (20° by 20°) is marked by the black box.

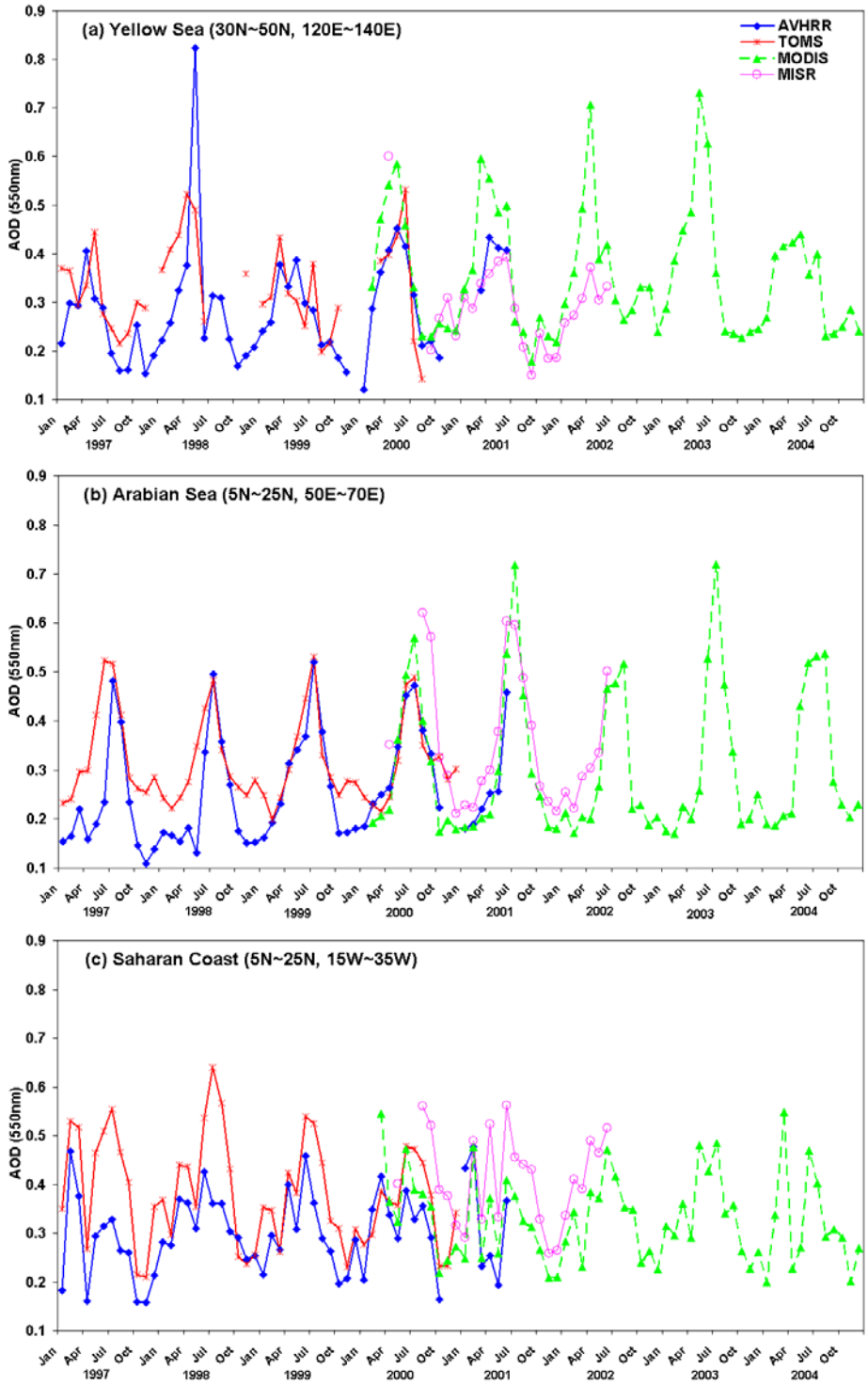

Figure 2.4: Consistencies of AOD (550nm) from AVHRR, TOMS, MISR, and MODIS dataset over (a) YS, (b) AS, and (c) SC.

2.3.3 AOD Consistency among Different Spacecraft Observations

The assessment of the accuracy of AOD products from different satellite datasets is a prerequisite to an analysis of dust radiative impacts. MODIS AOD has been validated with the ground-based AERONET observations with mixed results [*Remer et al.,* 2002; *Chu et al.,* 2002; *Ichoku et al.,* 2002; *Chung et al.,* 2005]. While instantaneous MODIS values compare well with AERONET, monthly mean values have biases of about 0.05 in certain regions [*Remer et al.,* 2002]. In this study, I examine the consistency of different AOD datasets derived by AVHRR, TOMS, MISR, and MODIS. Since each AOD dataset has been retrieved at its specific wavelength, i.e., 630 nm for AVHRR, 380 nm for TOMS, 558 nm for MISR, and 550 nm for MODIS, MODIS Ångström exponent data were employed to interpolate AOD from different wavelength to an identical wavelength 550 nm for the comparison. Figure 2.4 shows the comparison of AOD at 550 nm among four satellite datasets from January 1997 to December 2004. All of the data sets reveal similar seasonal cycle and clearly show AOD peak during the boreal summer (JJA) over AS and SC, and in the spring time (MAM) over YS.

Quantitative comparisons using MODIS AOD as the reference are shown in Table 2.2 over the three regions. It shows that AVHRR AOD is smaller than MODIS AOD over all three regions, with the bias ranging from a negligible -0.003 over AS to -0.087 over YS, which might comes from the idealized assumption of non-absorbing aerosols in the retrieval algorithm of AVHRR. For TOMS and MISR, the results are dependent on regions, since both produce smaller AOD over YS, while larger AOD

over AS and SC. The fairly small RMS (root mean square) error confirms the consistency among different satellite data sets and supports our approach of employing AVHRR AOD data for the study of dust plume climatology.

Table 2.2: Mean AOD difference between MODIS and AVHRR, TOMS, and MISR over Yellow Sea (YS), Arabian Sea (AS), and Saharan Coast (SC). The values in parenthesis represent RMS error.

Datasets \ Region	YS	AS	SC
AVHRR-MODIS	-0.087 (0.068)	-0.003 (0.045)	-0.038 (0.071)
TOMS-MODIS	-0.084 (0.074)	+0.022 (0.070)	+0.012 (0.065)
MISR-MODIS	-0.071 (0.094)	+0.074 (0.070)	+0.095 (0.048)

2.3.4 Dust Fraction

One major advantage of the MODIS aerosol dataset is the detailed information of particle-size-related aerosol optical properties, i.e., small mode AOD and large mode AOD [*Tanre et al*., 1997]. The ratio of large or small mode AOD to total AOD highlights the importance of particle size and can help distinguish the dominance between natural aerosol (mainly coarse mode aerosol) and man-made aerosol (primarily small mode) [*Remer et al*., 2002]. The recent research by *Bellouin et al.* [2005] employed MODIS small mode AOD to estimate the global annual mean direct radiative forcing by anthropogenic aerosols. In our study, MODIS large mode AOD data are used to estimate the fraction of dust particles relative to total aerosols, which is further compared with GOCART model results to test its ability for the estimation of dust fraction. Figure 2.5 shows monthly variation of MODIS large mode AOD ratio over YS, AS, and SC averaged from 2000 to 2004. The error bar, representing the five-year averaged standard deviation of the ratio in each month is defined as:

$$err = \frac{\sum_{j=2000}^{2004} E_j}{5}, \qquad \text{where } E_j = \sqrt{\frac{\sum_{i=1}^{N}(x_i - \bar{x})^2}{N-1}}, \tag{1}$$

x_i is the ratio at *i* grid in *j* year, $\bar{x}$ is the regional mean ratio in the investigating region, N is the total number of grids with available data.

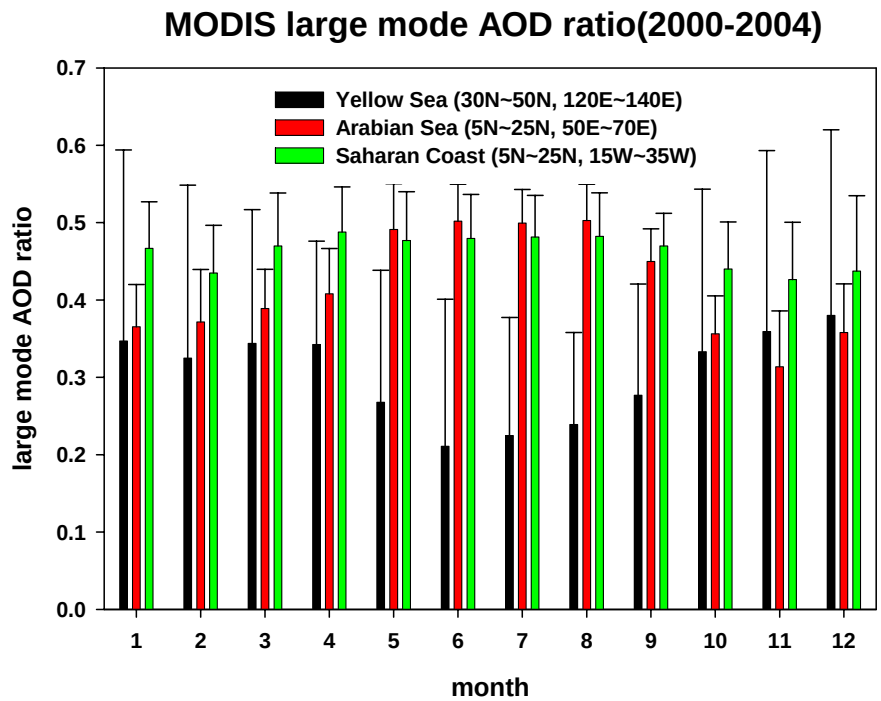

Figure 2.5: MODIS large mode AOD ratio over YS, AS, and SC.

It's clearly seen in Figure 2.5 that large mode AOD ratios seldom exceed 50% over all the three regions throughout most of the months, implying relatively large contributions of fine mode aerosols, which are mainly composed of anthropogenic aerosols. Clear seasonal cycles of the large mode AOD ratio can be seen over YS and AS, with minimum large mode ratio over YS during summer while maximum over AS the same period. Over SC, however, the large mode ratio shows very small annual variations, implying relatively persistent and stable sources for coarse mode aerosols.

The lowest large mode ratio (<40%) and the greatest error bar (~±30%) are found over YS, which suggests the complex nature of aerosol components and varying emission of coarse aerosol particles at that region.

Although MODIS large mode AOD ratio can be used to estimate the fraction of coarse particles, it has large uncertainty to represent the whole contribution of mineral dust because sea salt aerosols are unavoidably included in the large mode aerosols over the oceanic region, while some dust particles with small size might be excluded from the large mode AOD ratio. To validate MODIS large mode ratio, GOCART model results are used to derive the dust AOD fraction during dust season and compared with MODIS large mode ratio. Owing to the limited availability of GOCART model results, dust fractions from GOCART are only shown for the year 2001 (Figure 2.6). It's clearly seen that MODIS large mode ratio is much smaller than GOCART dust fraction over SC (Figure 2.6c), and the maximum dust fraction estimated by GOCART is over 80% in June, while MODIS large mode ratio is less than 50%. Even though MODIS large mode ratios are close to GOCART dust fractions over YS and AS (Figure 2.6a, 2.6b), if the contribution of sea salt aerosols are subtracted from MODIS large mode AOD ratio the dust contribution estimated by MODIS large mode ratio will become smaller than GOCART values. The seasonal mean MODIS large mode AOD ratios are 32%, 50%, and 48% for YS, AS, and SC, respectively, while 29%, 54%, and 77% from GOCART dust fractions for each corresponding region.

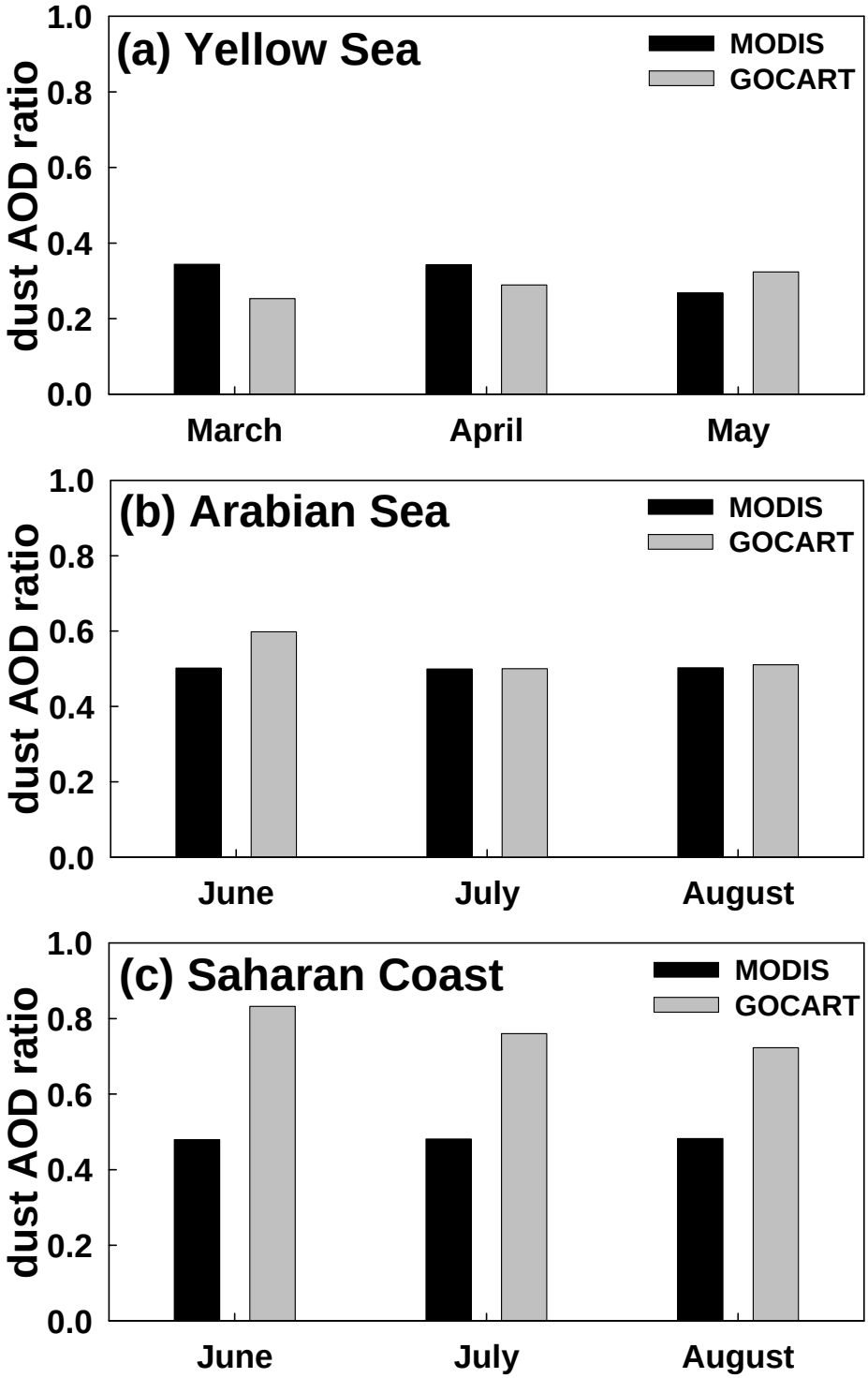

Figure 2.6: Comparison between MODIS large mode AOD ratio (2000-2004) and GOCART (2001) dust fraction during the dust season over (a) YS, (b) AS, and (c) SC.

Another possible uncertainty of dust fraction estimated by the MODIS large mode ratio is the exclusion of fine mode dust particles. Fine mode dust particles were found to account for large amount of total dust optical depths [*d'Almeida and Schütz*, 1983; *Duce*, 1995]. To demonstrate the possible contribution of fine mode dust particles to total AOD, AERONET fine mode AOD fraction measured near the desert source regions are investigated. The fine mode AOD fraction during dust season (MAM) accounts for about 25% of total AOD at Dunhuang site, which is close to the major dust source region (~550km east of the Taklamakan Desert basin). Similar results can be found over other AERONET dust-dominated sites. For example, during summer time, the fine mode AOD fractions at Solar Village and Cape Verde are 37% and 27%, respectively. The large value of fine mode AOD fraction over the AERONET dust-dominated sites during the dust season implies that fine mode dust particles might also have large contribution to total dust optical depth.

In view of the obvious deficiency to distinguish sea salt from large dust particles, and to extract the small size dust particles from fine mode aerosols, MODIS large mode AOD ratio will cause large uncertainty to estimate dust AOD fraction. Without more sophisticated observations, dust fraction from the model is probably the only way to estimate the optical depth by dust aerosols only. However, the reliability of GOCART one year model result might lead to some errors to the radiative forcing calculations, which will be discussed with details in Section 5. In this study, the seasonal averaged GOCART dust AOD fractions are used to estimate the contribution of dust particles.

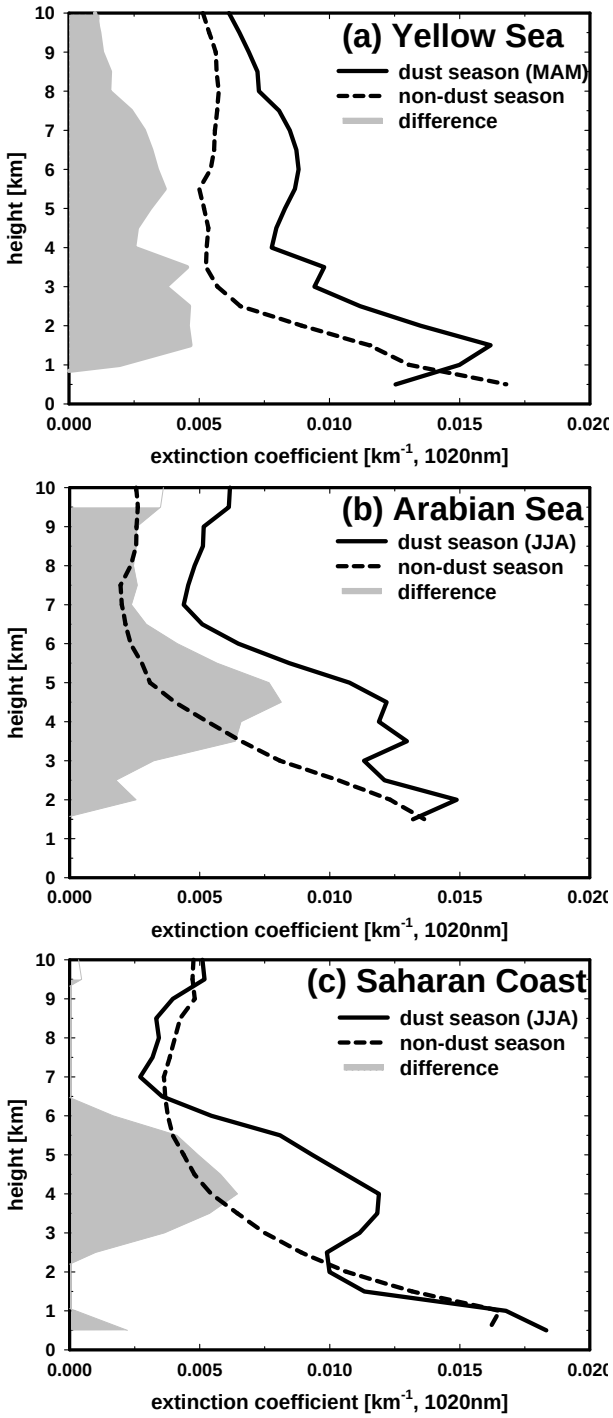

Figure 2.7: Vertical distribution of aerosol extinction coefficients [km^{-1}] at 1020nm measured from SAGE II (1981~2001 excluding volcanic years) for dust season (solid line), non-dust season (dashed line), and the differences (grey shadow) over (a) YS, (b) AS, and (c) SC.

2.3.5 Vertical Profile

2.3.5.1 Method and Results

The vertical distribution of dust plume is one of the critical parameters in the assessment of dust radiative forcing [*Claquin et al.,* 1998]. The model study by *Carlson and Benjamin* [1980] showed that the atmospheric heating rate can be changed dramatically by the elevated Saharan dust layer. *Liao and Seinfeild* [1998] claimed that clear sky LW forcing and cloudy sky TOA SW forcing are very sensitive to the altitude of the dust layer. *Meloni et al.* [2005] pointed out that SW aerosol radiative forcing at TOA had a strong dependence on aerosol vertical profiles. SAGE II aerosol extinction coefficient data [km^{-1}] provide a potential way to estimate the vertical structure of dust plumes. During the observation period of SAGE II from 1984 to 2001, there were several major volcanic eruptions, such as El Chichon in 1982 and Pinatubo in 1991, which may contaminate the real signal of tropospheric aerosols. To avoid the influences of volcanic aerosols, the aerosol profile during volcanic years were excluded.

The averaged aerosol profiles during the dust season (MAM for YS, JJA for AS and SC) are shown by the solid lines in Figure 2.7. For the comparison, the aerosol profiles during the non-dust season, which is the remaining nine months of the year, are marked by the dashed lines. One of the most impressive features is that all three non-dust season profiles show similar patterns, with maximum extinction coefficient close to the surface and nearly exponentially decreased with height. This type of aerosol profile is commonly seen for the boundary layer aerosols [*Ramanathan et al.,*

2001]. On the contrary, the aerosol profiles in dust season are more complex, presenting multiple peaks above the planetary boundary layers. By subtracting the non-dust season aerosol profiles from the dust season profile, the contribution of background aerosols can be eliminated. The residual signal highlighted by the gray shadow in Figure 2.7 is due to the excess occurrence of mineral dust during the dust season, which is regarded to be the real distribution of dust plumes. It is clearly seen that during the periods of investigation (dust season), dust plumes are elevated into the free troposphere with the single peak around 4 km over AS and SC. In contrast, the dust plume over YS presents more multi-layered complex structure rather than the single-layered distribution, with relatively small magnitude of extinction coefficient around 4 km.

The elevated dust plume over SC in the summer was described in detail by *Prospero and Carlson* [1981]. The bare desert surface is heated strongly during summer time and results in an extremely unstable and highly developed thermal mixing layer. During vertical mixing, dust particles are lifted into the free troposphere [*Carlson and Prospero*, 1972; *Tindale and Pease*, 1999]. When the hot, dry, and stable dusty air moves offshore blown by the easterly winds, it is undercut by the cool, moist maritime air and confined between two inversion layers around 850 hPa and 500 hPa, respectively [*Prospero and Carlson*, 1981]. Similar mechanism can be applied to AS for the elevated single layer dust plume. The multi-layer structure of the dust plume over YS was claimed to be associated with different contributions from two major dust sources over East Asia, i.e., the Gobi desert and the Taklamakan Desert

[*Sun et al.,* 2001]. Using long term climatological records of dust storms and meteorological data in China, *Sun et al.* concluded that mineral dust originating from the Gobi Desert can not be lifted to altitudes higher than 3km, while dust particles raised from the Taklamakan Desert are able to be entrained to the upper troposphere and can be transported over long distance. The combination of these two dust sources might result in a multiple layered structure for the East Asian dust plume.

2.3.5.2 Comparison with Published Dust Profiles

The elevated layer-structure of dust plumes has been observed directly by many field experiments [*Dulac and Chazette*, 1998]. The Saharan dust plume was characterized by the aircraft measurements during BOMEX (Barbados Oceanographic and Meteorological Experiment) [*Prospero and Carlson*, 1972] and SHADE [*Highwood et al.,* 2003]. Dust profiles were also documented by the lidar observations in PRIDE [*Colarco et al.,* 2003b], ACE-2 [*Welton et al.,* 2000], and SOFIA/ASTEX (Surface of the Ocean, Fluxes and Interactions with the Atmosphere/Atlantic Stratocumulus Transition Experiment) [*Chazette et al*., 1997]. Over the Mediterranean, field measurements reported that the stable Saharan layer was situated above the trade wind marine boundary layer [*Hamonou et al.,* 1997; *Hamonou and Chazette*, 1998; *Pe´rez et al.,* 2006; *Mattis et al.,* 2002; *Müller et al.,* 2003; *di Sarra et al*., 2001].

Over the N. Indian Ocean, the top of the dust layer over the southwest monsoon region was found to reach a height range from 400 hPa during summer to 600 hPa during late spring and early fall [*Ackerman and Cox*, 1989]. Lidar

observations accompanied with the backward trajectory analysis in the study of *Müller et al.* [2001] during INDOEX [*Ramanathan et al.,* 2001] demonstrated that aerosols below 2500 m were solely from the pristine Indian Ocean with sea salt and sulfate aerosols as the major components, while the elevated aerosol layer with large backscatter and extinction coefficient at ~3800 m altitude was mineral dust originating from the Arabian Peninsula and Somali region.

Numerous observations over East Asia [*Sasano,* 1996; *Liu et al.*, 2002; *Zhou et al.,* 2002; *Murayama et al.,* 2004; *Murayama et al.,* 2001; *Shimizu et al.,* 2004] have shown the elevated dust plumes in the free troposphere during spring time. *Kwon et al.* [1997] revealed that air masses between 2 km and 4 km height mainly come from the Gobi Desert, while air parcels between 4 km and 7 km were originated from the region near the Taklamakan Desert. Based on aircraft observation, ground-based lidar measurements, and backward trajectory analysis, *Matsuki et al.* [2003] claimed that Taklamakan Desert is an important source for the background dust in the upper troposphere above 4 km. The airborne measurements during ACE-Asia also detected multiple aerosol layers near Tokyo [*Murayama et al.,* 2003], which are the planetary boundary layer with fine aerosols from surface to 1.2~1.5 km, an upper layer above ~3.5 km dominated by dust particles, and an intermediate layer in between with the mixture of dust and fine aerosols. By means of Raman lidar observations at Nagoya (35.1°N, 137.0°E), *Sakai et al.* [2000] found that the vertically integrated aerosol backscattering coefficients showed two peaks in spring, one is within the height range from 2 km to 4 km, another is between 4 km to 8 km. *Murayama et al.* [2001]

coordinated a ground-based lidar network to observe the East Asian dust and highlighted the existence of a thin dust layer in the higher troposphere. Because dust particles can act as ice nuclei for cirrus clouds, the presence of uplifted dust particles in the upper troposphere may imply a potential indirect effect [*DeMott et al.,* 2003; *Sassen et al.,* 2003].

To validate the dust profile derived from this study, I compared the SAGE II dust profiles with previous published observations. All the altitude dependent parameters were normalized with respect to their maximum values to get the dimensionless signal based on the following equation:

$$F(h) = \frac{Ext(h)}{Ext_{\max}}, \qquad (2)$$

where $F(h)$ is the normalized signal ranging from zero to one as a function of height, $Ext(h)$ is the measured profile with individual unit, $Ext_{\max}$ is the maximum value of the measured profile. The normalization method can not only maintain the original pattern of the aerosol profile, but also make the comparison more feasible. The comparisons of the normalized dust profiles are showed in Figure 2.8. For YS (Figure 2.8a), most observations presented multiple dust layers except the lidar backscatter signal derived from the study of *Liu et al.* [2002], which exhibits a single dust layer with a peak at ~ 4 km. The varying profiles from different field observations indicate that the vertical structure of the dust plume over East Asia is very complex. Owing to the scarcity of observations in the summer time over AS, only one lidar profile [*Müller et al.,* 2001] is available for the comparison (Figure 2.8b). Although the peak level of

the lidar observation is slightly lower than what I found from SAGE II data, they both detected the elevated dust layer in the mid troposphere. The second peak at ~1 km height observed by lidar was tracked to be the maritime aerosols by the trajectory analysis [*Müller et al.,* 2001]. Over SC (Figure 2.8c), all published profiles presented the elevated aerosol vertical structure with the peak level between 2 km and 4 km. The upper boundary of dust plume derived from SAGE II is slightly higher than the previous observations, which might come from the average method used in our study. However, the varieties of dust vertical profiles from individual lidar and aircraft observation do imply there's great diversity of dust vertical structure. It's worth noting that lidar and aircraft measurements could have more local effects owing to the limitation of observation period and covering area, while SAGE II represents the climatological vertical distribution of the dust plumes over large region with a decadal time-scale. In spite of the uncertainty of SAGE II aerosol extinction coefficient data, the consistency between SAGE II profiles and previous findings in the literature confirms the reliability of SAGE II data to detect the elevated dust plumes. In the following sections, the elevated dust profiles derived from SAGE II are used to retrieve the radiative forcing caused by mineral dust.

2.4. Radiative Impacts

The direct radiative forcing of dust is defined as the difference of net radiative flux (downward minus upward flux) [Wm^{-2}] with dust and without dust. The TOA radiative forcing represents the warming/cooling effect on the whole atmosphere-Earth system induced by mineral dust, while the surface forcing is limited to the Earth

surface only. The difference between the TOA forcing and the surface forcing represents the flux change within the atmosphere. The atmospheric flux changes are used to calculate the heating rate changes [K/day] by dust. Seasonal averaged MODIS AOD data (2000~2004) and GOCART dust fraction (2001) are combined to derive the optical depth of dust aerosols. Both SW and LW radiative forcing are calculated for the three target regions (YS, AS, and SC) under the clear and all sky conditions.

2.4.1 Clear Sky Dust Forcing

Figure 2.9 illustrated the geographic distributions of seasonal mean SW and LW dust forcing [Wm^{-2}] at the ocean surface over three target regions. The patterns of both SW (Figure 2.9a, c, e) and LW (Figure 2.9b, d, f) dust forcing follow the regional distribution of dust AOD, with highest forcing near the coastline and gradually decreasing toward the remote ocean. It's clearly seen that the SW dust effect at the ocean surface is cooling everywhere, while the LW forcing adds energy to the ocean surface. That is because dust particles both scatter and absorb the incoming solar radiation, both of these processes lead to the reduction of the SW flux reaching the dark ocean surface, which is also called the surface dimming. Dust particles also absorb the outgoing terrestrial flux emitted from the ocean surface and underlying atmosphere, and re-emit the IR flux in all directions. The downward part of the emitted LW flux adds energy to the ocean surface. However, the magnitude of LW forcing is fairly small compared to the strong SW cooling. The largest LW warming is ~15 Wm^{-2} over SC, while the strongest SW cooling to the ocean surface is larger than -55 Wm^{-2} over AS.

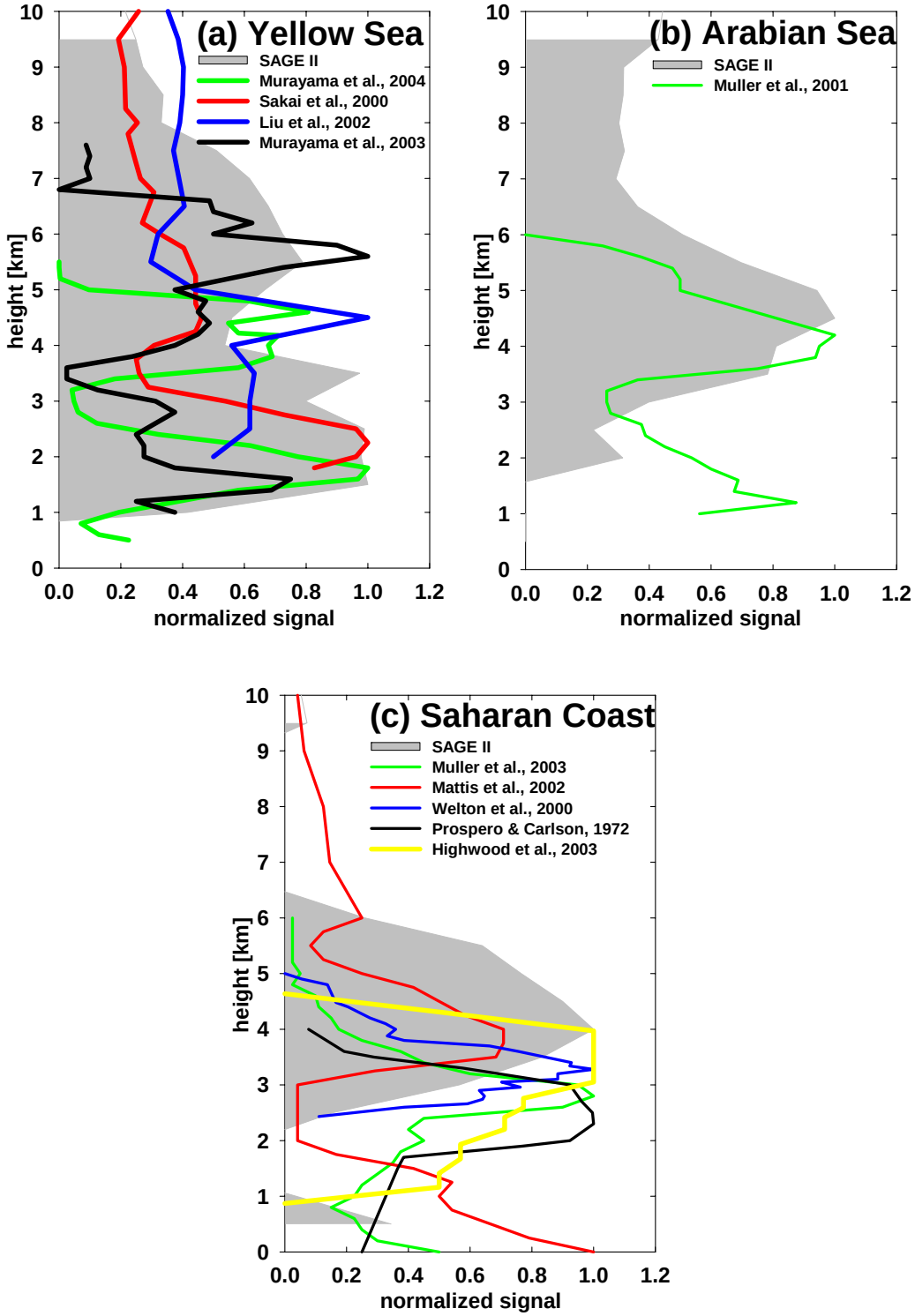

Figure 2.8: Comparison of dust vertical distribution between SAGE II (grey shadow) and previous observations (lines) over (a) YS, (b) AS, and (c) SC.

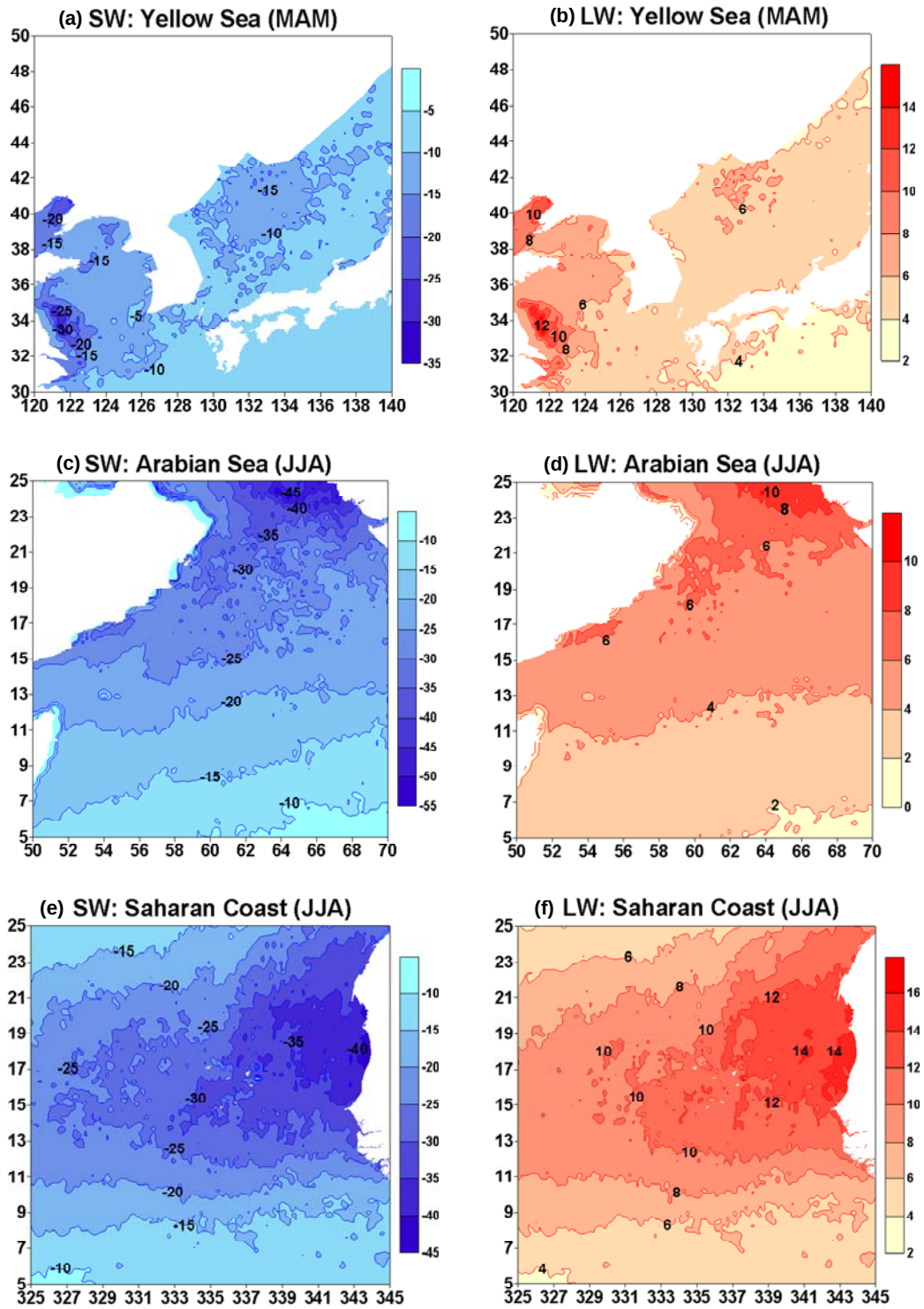

Figure 2.9: Clear sky seasonal mean SW (a, c, e) and LW (b, d, f) dust forcing [Wm^{-2}] at the surface over YS (a, b), AS (c, d), and SC (e, f).

Dust forcing efficiency [$Wm^{-2}\tau^{-1}$], defined as the rate of change of radiative forcing per unit increase in dust AOD [*Ramanathan et al.,* 2001], is derived from the slope of the dust radiative forcing with respect to dust AOD, which is an effective method for comparison of aerosol forcing among different studies. The SW dust forcing efficiency [$Wm^{-2}\tau^{-1}$] at the TOA (surface) is -43.7 (-63.7), -42.1 (-78.3), -41.1 (-69.5) for YS, AS, and SC, respectively. However, the LW dust forcing efficiency at TOA (surface) is relatively smaller, only +25.5 (+31.8), +18.1 (+15.4), and +22.8 (+24.7) $Wm^{-2}\tau^{-1}$ over YS, AS, and SC, respectively. The prior study by *Li et al.* [2004] estimated the TOA and surface forcing efficiencies for the Saharan dust to be -35±3 and -65 $Wm^{-2}\tau^{-1}$, respectively. It is important to note that *Li et al.'*s TOA forcing was obtained from satellite radiation budget studies. The retrieved model values in this study are consistent with *Li et al.'*s [2004] values.

Processes involved in the radiative interactions with dust particles are illustrated in Figure 2.10 for the clear-sky conditions. Owing to the non-uniform distributions of dust plumes in both spatial and time scales, the regional and seasonal averaged dust optical depths are relatively small, which are 0.15 for YS, 0.28 for AS, and 0.31 for SC at 550 nm. The SW radiative forcing by dust is negative both at TOA and at the surface. The magnitude of surface forcing is much larger than the TOA forcing because of the large absorption of solar radiation by the atmosphere, noting that the atmospheric flux change equals TOA forcing minus surface forcing. The strongest SW forcing occurs over AS, although the regional and seasonal mean dust AOD over AS is smaller than that over SC. The fairly strong absorption (SSA ~0.93 at

550nm) of Arabian dust is the main reason for the strong SW forcing. On the contrary, the magnitude of LW TOA forcing is comparable to that of LW surface forcing, which leads to very small effect of LW forcing in the atmosphere. Although the positive LW forcing can compensate about half of the negative SW forcing at the TOA, the total dust forcing (SW+LW) is still dominated by the SW forcing, i.e., dust plume has a negative forcing on the earth-atmosphere system. As shown in Figure 2.10, the total dust radiative forcing over AS is the largest among the three regions and the total forcing over YS is the minimum, the atmospheric absorption over YS only accounts for ~20% of the atmospheric absorption over AS.

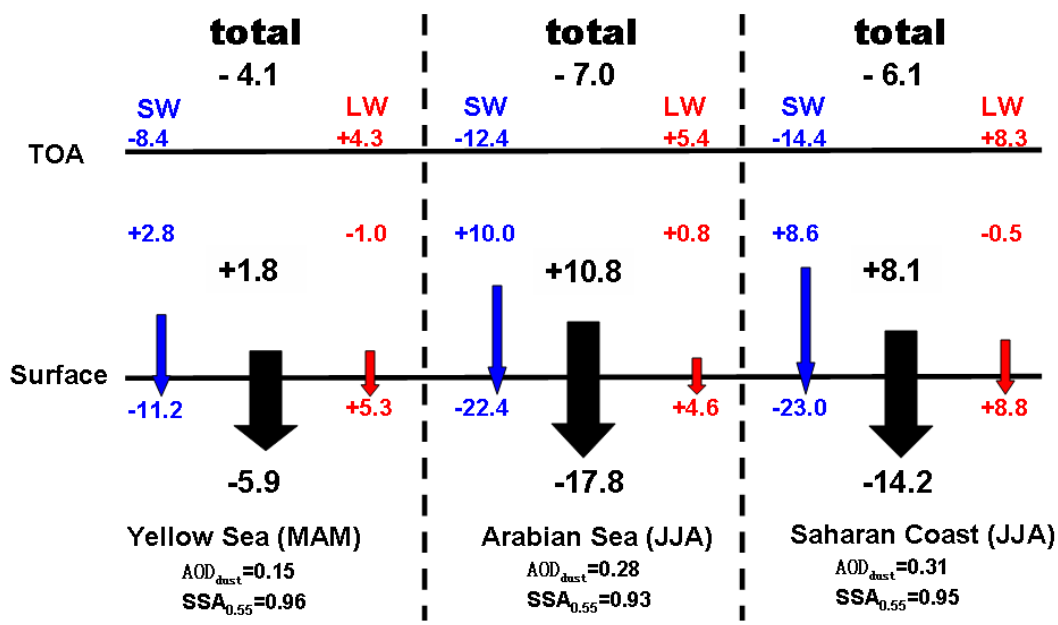

Figure 2.10: Clear sky regional and seasonal mean SW, LW, and total (SW+LW) radiative forcing [Wm^{-2}] by dust plumes.

Although large differences of the selected region and observation period between this study and others make a direct comparison difficult, the results presented here are comparable to the values reported in prior studies. The ACE-Asia reported -

5.5 and -9.3 Wm^{-2} forcing at TOA and surface, respectively, for the mineral dust (SSA ~0.98) over the East Asia (20°N-50°N, 100°E-150°E) during 5-15 April 2001 [*Seinfeld et al.,* 2004]. The PRIDE campaign [*Christopher et al.*, 2003] assessed the diurnal mean SW dust forcing at TOA and surface to be -12.3±9.6 and -18.1±15.8 Wm^{-2} in the Puerto Rico region during summer months. LW forcing values explored in our study are in the range of the IR dust forcing reported by *Sokolik et al.* [1998], which are 2~7 Wm^{-2} at TOA and 7~14 Wm^{-2} at surface for background conditions over arid or semiarid regions.

The SW, LW and net (SW+LW) dust heating rate under clear sky conditions are shown by the dashed lines in Figure 2.11. Mineral dust absorbs the incoming solar radiation and enhances heating of the layer where dust plumes exist. The absorption along with the scattering cuts down the incoming solar flux thus decreasing the heating rates of the air below the dust layer (Figure 2.11a). The maximum SW dust heating is located in the mid troposphere over AS with the value about 0.5 K/day. The heating rate over YS is very small (less than 0.15 K/day for the peak) owing to strong scattering, which is in the range of 0.08~0.4 K/day estimated by *Nakajima et al.* [1989] for the East Asian yellow sand. On the contrary, the LW effect (Figure 2.11b) of the dust plumes enhances the LW cooling of the free troposphere because the upward and downward emissions of the LW flux by the dust is larger than the absorbed LW radiation. The net effect is energy loss inside the dust layer. One of the important features in Figure 2.11b is the strong LW warming below the base of the dust layer.

That is because the elevated dust plumes increase downwelling LW flux and enhance the atmospheric absorption in the lower atmosphere.

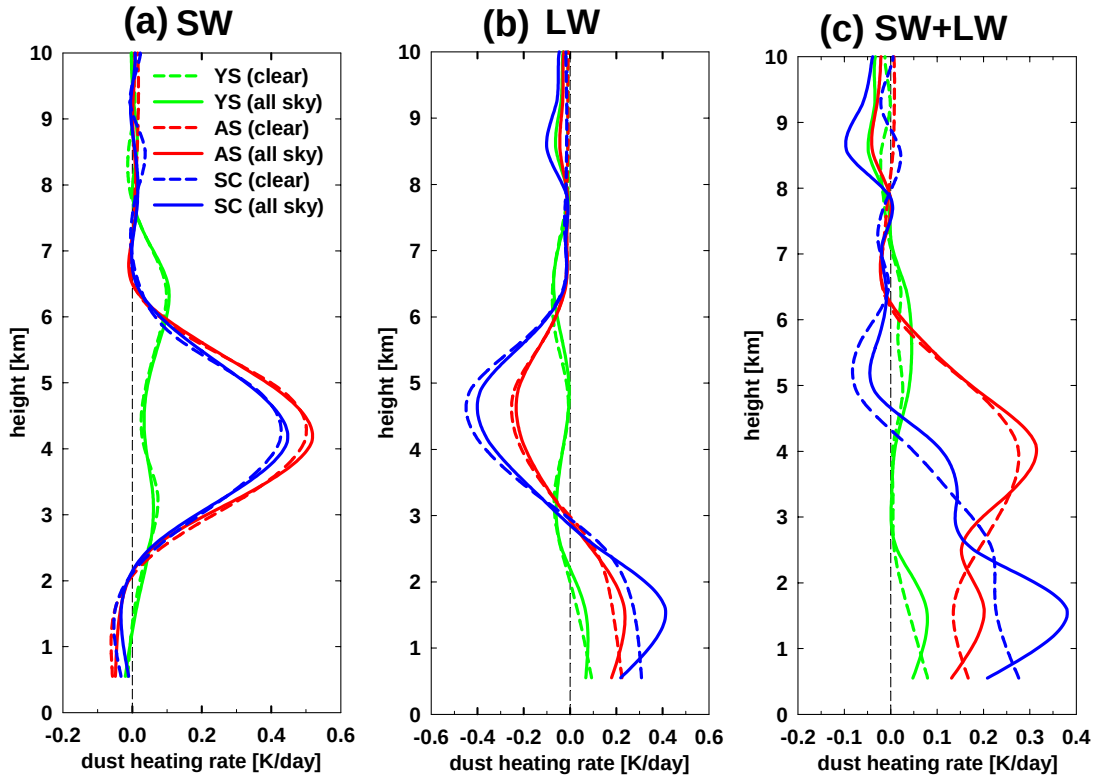

Figure 2.11: Regional and seasonal mean dust heating rate [K/day] under clear sky (dashed line) and all sky (solid line) for (a) SW, (b) LW (c) total (SW+LW).

It's seen that SW (Figure 2.11a) and LW (Figure 2.11b) dust heating rates are determined by the vertical structure of the dust plumes, while total dust heating rate (Figure 2.11c) is more complex due to the counteracting effects between SW and LW. Over YS, total dust heating rate is the smallest among three regions, the maximum warming is less than 0.1 K/day as a result of the small dust optical depth, strong scattering properties, and multiple layered vertical structure. As to the dust plume over AS, the SW warming inside the dust layer is approximately twice the LW cooling, so

the total heating rate change over AS is positive from the surface to ~6 km, with maximum warming inside the dust layer centered at ~4 km. Although the vertical profile over SC is similar to that over AS, the total heating rate change of Saharan dust has a different pattern, with maximum warming near the surface, gradually decreasing with altitude, and turning to negative heating rate above ~4 km.

2.4.2 All Sky Dust Forcing

I re-ran the MACR model with seasonally averaged cloud fraction and cloud optical depth derived from ISCCP data. The dust radiative forcing under all sky conditions is compared with that under clear sky as listed in Table 2.3. The occurrence of clouds reduces dust radiative forcing both in SW and in LW. The reduction of SW TOA forcing is nearly equivalent to the reduction of surface forcing with a value of about 5~7 Wm^{-2}, which implies a negligible change in the atmospheric absorption (<0.3 Wm^{-2}) owing to the competing effects by different clouds. For instance, the existence of low clouds over the dark ocean increases the surface albedo thus enhancing the SW absorption by the elevated dust layer, while high clouds block the incoming solar flux and result in less absorption by dust aerosols. Thus the net effect of clouds on the atmospheric absorption induced by dust plumes is quite small. The weakening of the LW dust forcing by clouds is fairly mild, and the maximum difference between all sky and clear sky is less than 2 Wm^{-2}.

Even though the occurrence of clouds results in a small change to the atmospheric absorption, dust heating rate can be affected greatly by clouds, especially for the LW heating rate (Figure 2.11b). The warming below the dust layer under all

sky conditions (solid lines in Figure 2.11) is greatly enhanced mainly because low clouds absorb more LW flux emitted from the upper dust layer than clear sky, which results in the excess warming in the cloud layer. The change of the SW dust heating rate by clouds is fairly small compared with its influence on the LW effect. As shown by the solid lines in Figure 2.11a, the SW dust heating rates under all sky are similar to the clear-sky conditions, except that the warming inside the dust layer increases slightly and the cooling below the dust layer weakens by within 0.1 K/day. The total dust heating rates under all sky are mainly affected by the LW effect of clouds. Overall, the low level clouds have been found to have a strong effect on dust heating rate change, especially causing additional warming below the dust layer. As discussed by *Prospero and Carlson* [1981], stratiform clouds are always found in the marine boundary layer under the elevated dust layer, which implies more complex interactions of dust plumes with clouds.

Table 2.3: Comparison of dust radiative forcing [Wm^{-2}] between clear sky and all sky conditions over Yellow Sea (YS), Arabian Sea (AS), and Saharan Coast (SC).

region	Sky cond.	TOA			Surface			Atmos. Absp		
		SW	LW	total	SW	LW	Total	SW	LW	total
YS	All	-3.24	+3.18	-0.06	-6.01	+4.11	-1.9	+2.76	-0.93	+1.83
	Clear	-8.36	+4.31	-4.05	-11.17	+5.3	-5.87	+2.81	-0.99	+1.82
AS	All	-6.37	+4.63	-1.74	-16.31	+3.84	-12.47	+9.94	+0.79	+10.73
	Clear	-12.41	+5.41	-7.0	-22.36	+4.56	-17.8	+9.96	+0.85	+10.81
SC	All	-6.91	+7.21	+0.3	-15.87	+7.01	-8.86	+8.96	+0.2	+9.16
	Clear	-14.37	+8.3	-6.07	-23.03	+8.8	-14.23	+8.66	-0.5	+8.16

2.5 Consideration of Other Factors

Although the results for dust direct radiative forcing are valid for oceanic regions in clear-sky and all-sky conditions, conclusions would differ over land regions,

especially for the SW TOA radiative forcing. This is because the surface reflectance is much higher over land than over the ocean. The occurrence of dust layer over the dark ocean surface increases the planetary albedo and enhances the outgoing SW flux at TOA, thus causes large negative SW TOA forcing. However, over the land region, the magnitude of negative TOA forcing can be reduced and even the sign can be changed from negative to positive because the elevated dust layer can trap part of the outgoing SW flux reflected by the bright surface, thus the energy loss at TOA is reduced. The detailed discussion of uncertainties of SW radiative forcing with respect to surface albedo can be found from the studies by *Claquin et al.* [1998] and *Liao and Seinfeld* [1998]. The LW radiative forcing by mineral dust is a strong function of the surface temperature which presents far greater diurnal variation over land compared with oceans. For example, *Haywood et al.* [2005] showed that the TOA LW forcing of mineral dust could reach +50 Wm^{-2} at local noon over hot desert surfaces. However, this issue is beyond the scope of this paper.

Although this study attempt to minimize errors by relying on much observational parameters for model input to estimate dust radiative forcing, the results have some unavoidable uncertainties coming from the input parameters, such as MODIS AOD, dust AOD fraction and SSA. As discussed by *Remer et al.* [2002], the uncertainty of MODIS AOD over the ocean is about ±0.05. The sensitivity test in this study showed that this MODIS AOD uncertainty can lead to about 12% to 33% uncertainty to total dust radiative forcing. The application of GOCART dust AOD fraction is another possible source of error. If MODIS large mode AOD ratio were

used, dust AOD will increase 10% over YS, and decrease about 7% and 38% over AS and SC, respectively. The change of dust AOD by using MODIS large mode AOD ratio will further bring about 2% to 37% uncertainty to the calculated dust forcing. The other major uncertainty of the estimated dust forcing arises from SSA. A ±0.03 uncertainty of AERONET SSA [*Dubovik et al.,* 2000] can lead to about 12% uncertainty in the SW TOA forcing. The largest error caused by SSA uncertainty lies in the atmospheric absorption with maximum uncertainty of about 90% over YS. Although the aforementioned three parameters have large effects to the calculated dust radiative forcing, the pattern of dust heating rate is not affected, only the magnitude of dust heating rate changes with the range from 0.04 to 0.2 K/day, where SSA was found to have the largest effect in regulating the magnitude of dust heating rate.

Dust vertical profile can also bring uncertainties to the estimated forcing. Owing to the sparsity of SAGE II data at the level close to the Earth surface, the boundary layer aerosol signals might be filtered by SAGE II retrieval technique. To test the uncertainty of boundary dust aerosols on dust radiative forcing, exponentially decreased profiles extending from ocean surface to the base of the elevated dust layer was added to the SAGE II dust profile. The sensitivity tests showed that the inclusion of boundary dust aerosols causes 1% to 17% uncertainty of TOA forcing, 3% to 17% uncertainty of surface forcing, and 15% to 50% uncertainty of atmospheric absorption. The occurrence of boundary layer dust aerosol has large effect on both the pattern and the magnitude of dust heating rate. Large change of heating rate pattern was found near the boundary layer, where SW heating rate switched from slight cooling to slight

warming and the magnitude of LW warming decreased owing to the energy loss from these boundary layer dust aerosols. Inside the elevated dust layers, the magnitudes of both SW warming and LW cooling were diminished. The overall change in the magnitude of the total dust heating rate change is within 0.1 K/day. Although applications of the SAGE II data for description of dust vertical profiles reveal encouraging results, it is recommended that a comprehensive data-comparison analysis should be conducted by using tropospheric measurements from different instruments. Observations by ICESat (Ice, Cloud, Land Elevation Satellite) with the space-based lidar started since January 2003 [*Anon*, 2003] can provide a valuable dataset to perform cross-check with SAGE II for the dust vertical profiles on a climatological basis.

The satellite data exhibits considerable variability on decadal time scales. As displayed in Figure 2.12, the volcanic eruptions bring large amounts of aerosol particles and cause the greatest positive anomalies even only the dust season was considered. The maximum AOD anomaly was 0.18 for the Saharan Coast and 0.17 for the Arabian Sea, occurring in 1982 when the El Chichon erupted; the maximum AOD anomaly for Yellow Sea was 0.14, appearing in 1992, a year after the Pinatubo eruption; and the maximum global mean anomaly was found in the second year of Pinatubo with a value of 0.11. Despite being shadowed by the volcanic eruption, an increasing trend of AOD anomaly can be defined clearly from mid 1990's to early this century. The transition from negative anomalies to positive anomalies during dust season deserves some concerns since it may imply the increasing trend of dust

emission in recent decades. The historical study over China by *Zhou and Zhang* [2003] also showed an increasing trend of severe dust events in China from late 1990's. More observations and model studies are required to better understand the trend of dust plumes.

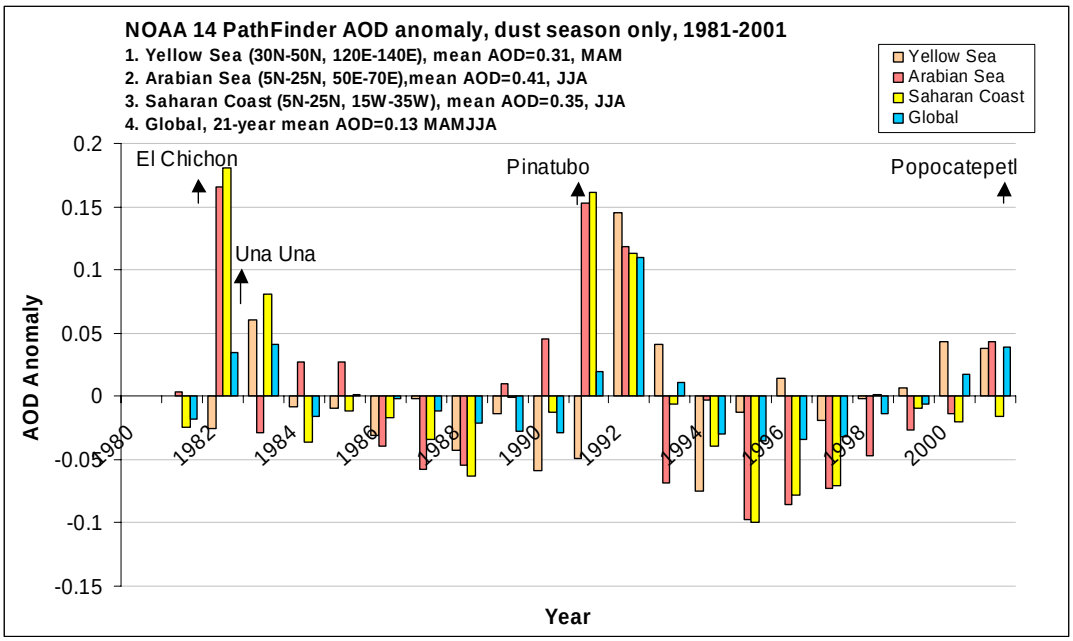

Figure 2.12: AOD anomalies from 1981 to 2001 in the dust seasons over YS, AS and SC. Global mean AOD anomaly is also shown for comparison.

In this study, mineral dust was simplified to be externally mixed with other aerosol species, that is, dust particles are suspended in the air individually and have no interaction with other aerosol particles. Field observations and laboratory experiments suggest that dust particles can be mixed with sulfate, organic carbon, and sea salt aerosols [*Iwasaka et al.,* 2003; *Andreae et al.*, 1986; *Zhang et al.,* 2003a; *Song et al.,* 2005; *Clarke et al.,* 2004; *Zhang et al.,* 2003b]. For example, the SSA during dust season is about 0.91 at AERONET Beijing site, which is the downstream of

anthropogenic pollutions. In contrast, in the upstream desert site Dunhuang, larger SSA (~0.96) was observed in the same period. However, it is presently difficult to define the fraction of the "polluted" dust particles and the "unpolluted" dust particles. According to *Jacobson* [2001], absorption of solar radiation is greatly enhanced if the aerosol particle is accompanied by black carbon. Thus, the radiative forcing estimated in this study may underestimate the SW effect of dust plumes. In the future study, more observations will be combined to investigate the radiative impacts of the dust-soot plumes. Another issue requiring further research is the assessment of the radiative impact by the anthropogenic dust particles, such as those due to agricultural activity and land-surface changes etc. On the basis of the model estimation by *Tegen et al.* [1996], about 30~50% mineral dust particles are associated with the anthropogenic sources. Although great efforts have been made to evaluate the radiative impacts of anthropogenic dust, large uncertainties still exist in estimating the fraction of man-made dust particles.

2.6 Summary and Conclusions

Through the analysis of long-term AVHRR AOD datasets, the climatological distributions of three major dust plumes spreading over the Pacific, the Indian, and the Atlantic Oceans during last two decades were examined. Distinct dust seasons have been identified to be March-April-May for the dust plume over the Pacific Ocean, and June-July-August for those over the Indian Ocean and the Atlantic Ocean. The transport patterns as well as the geographic distribution of dust plumes gradually declining from the source continent to the remote oceans were clearly illustrated. By

subtracting the non-dust season profile from the dust season SAGE II aerosol profile, I were able to determine the layer-like structures of the dust plumes showing high concentrations in the free troposphere. An elevated single dust layer was found above marine boundary layer with peak around 4 km over AS and SC, and multi-layered structure of dust plumes were found over YS. The agreement of the dust profiles between SAGE II and lidar and aircraft observations implied that our findings are consistent with previous studies. Large mode MODIS AOD data are analyzed to show the annual cycle of the coarse mode particles. The comparison with GOCART dust fraction demonstrated that MODIS large mode AOD ratio might have uncertainty to accurately estimate the contribution of dust particles relatively to total AOD.

Direct radiative forcing of dust plumes was estimated by Monte-Carlo radiative transfer model. Although LW warming compensated part of SW cooling, SW forcing dominates the total effect of dust plumes with negative TOA forcing everywhere over the ocean. The dust plume over AS causes the largest forcing among the three dust plumes, with the clear sky regional and seasonal mean net forcing to be about -7.0 Wm^{-2} and -17.8 Wm^{-2} at the TOA and ocean surface, respectively. The large flux divergence between the TOA forcing and surface forcing results in the largest atmospheric heating over AS, with the clear sky atmospheric heating to be +10.8 Wm^{-2}. The atmospheric absorption induced by dust plume over YS was the smallest (<2 Wm^{-2}) due to the small dust AOD (fraction) and strong SW scattering.

The atmospheric heating rate changes by dust depend on the vertical distribution of the dust plumes under the clear sky. Large SW heating was found

inside the dust layer due to strong absorption of the incoming solar radiation, with the maximum heating to be around +0.5 K/day over AS and centered at ~4 km where dust concentration peaks. The LW effect results in a strong cooling throughout the dust layer with the maximum cooling located just above the dust peak level and moderate heating below the dust layer. Dust plumes over SC exert the maximum LW effect on heating rates, with up to -0.5 K/day LW cooling in the free troposphere and about +0.3 K/day warming in the boundary layer. The net heating rate by the dust plumes is the sum of the SW and the LW heating rates. Over SC, large LW cooling inside the dust layer offsets up to 80% SW heating and results in about -0.1 K/day net heating rate change at the height ~5 km over SC. Over AS, the net heating rate change is dominated by SW heating because the maximum LW cooling is less than 60% of the SW heating, which leads to +0.3 K/day net heating inside the dust layer and moderate heating below the dust base. The net heating rate change over YS is the smallest among the three regions, with magnitude within 0.1 K/day. The occurrence of clouds masked the effect of dust plumes by reducing the forcing both at TOA and at the surface; however, the heating rate change in all sky showed little difference from clear sky except that the LW warming below the dust layer was enhanced by low level clouds. The strong radiative forcing by dust plumes over the oceans implies further impacts on the hydrological cycle, atmospheric stability, and global cloud coverage.

This study is motivated by the urgent need to fully understand the climate impacts of dust plumes over the world-wide oceans. By investigating the climatological distribution and direct radiative forcing of three major dust plumes over

the Pacific, the Indian, and the Atlantic Oceans, I would like to stimulate more profound studies to reveal the impacts of dust particles on cloud formation, general circulation, and water budget.

Acknowledgments

The MODIS AOD data come from NASA GSFC distributed Active Archive Center, and the SAGE II data from NASA Langley Research Center. The authors thank Dr. Shane Mattoo for her help in the MODIS AOD format. I am thankful to the anonymous reviewers for their helpful comments and constructive suggestions that have resulted in improvements of this manuscript. This study was partially funded by the National Science Foundation (NSF) through grant ATM 9612887, and by the NASA NAS1-98141.

Publication Acknowledgement

The text of Chapter 2, in full, is a reprint of a published paper, Zhu A, Ramanathan V, Li F, and Kim D, "Dust plumes over the Pacific, Indian, and Atlantic oceans: Climatology and radiative impact", Journal of Geophysical Research-Atm 112: Art, No. D16208 August 31 2007. I was the primary researcher and author.

References

Ackerman, S. A., and S. K. Cox (1989), Surface weather observations of atmospheric dust over the southwest summer monsoon region, *Meteorol. Atmos. Phys.,* 41, 19-34.

Andreae, M. O., R. J. Charlson, F. Bruynseels, H. Storms, R. Van Grieken, and W. Maenhaut (1986), Internal mixtures of sea salt, silicates and excess sulfate in marine aerosols, *Science*, 232, 1620– 1623.

Antuña, J. C., A. Robock, G. L. Stenchikov, L. W. Thomason, and J. E. Barnes (2002), Lidar validation of SAGE II aerosol measurements after the 1991 Mount Pinatubo eruption, *J. Geophys. Res.,* 107(D14), 4194, doi:10.1029/2001JD001441.

Bellouin, B., O. Boucher, J. Haywood, and S. Reddy (2005), Global estimates of aerosol direct radiative forcing from satellite measurements, Nature, 438, 1138-1141.

Carlson, T. N., and J. M. Prospero (1972), The large scale movement of Saharan air outbreaks over the northern equatorial Atlantic, *J. Appl. Meteorol*., 11, 283–297.

Carlson, T. N., and S. G. Benjamin (1980), Radiative heating rates for Saharan dust, *J. Atmos. Sci.*, 37, 193–213.

Chazette P., J. Pelon, C. Moulin, V. Trouillet, I. Carrasco, F. Dulac, W. Guelle, P. Bousquet, and P. H. Flamant (1997), Synergy between lidar and Meteosat measurements for a Saharan dust event during SOFIA/ASTEX, *J. Aerosol Sci.,* 28, S659-S660.

Chin, M., et al. (2002), Tropospheric aerosol optical thickness from the GOCART model and comparisons with satellite and Sun photometer measurements, *J. Atmos. Sci.*, 59, 461–483.

Christopher, S. A., J. Wang, Q. Ji, and S. Tsay (2003), Estimation of diurnal shortwave dust aerosol radiative forcing during PRIDE, *J. Geophys. Res*., 108(D19), 8596, doi:10.1029/2002JD002787.

Chu, D. A., Y. J. Kaufman, C. Ichoku, L. A. Remer, D. Tanré, and B. N. Holben (2002), Validation of MODIS aerosol optical depth retrieval over land, *Geophys. Res. Lett*., 29(12), 8007, doi:10.1029/2001GL013205.

Chun, Y., Lim, J.Y. (2004), The recent characteristics of Asian Dust and haze events in Seoul, Korea, *Meteorology and Atmospheric Physics* 87, 143–152.

Chung, C. E., V. Ramanathan, D. Kim, and I. A. Podgorny (2005), Global anthropogenic aerosol direct forcing derived from satellite and ground-based observations, *J. Geophys. Res*., 110, D24207, doi:10.1029/2005JD006356.

Clarke, A. D., et al. (2004), Size distributions and mixtures of dust and black carbon aerosol in Asian outflow: Physiochemistry and optical properties, *J. Geophys. Res*., 109, D15S09, doi:10.1029/2003JD004378.

Claquin, T., M. Schulz, Y. J. Balkanski, and O. Boucher (1998), Uncertainties in assessing radiative forcing by mineral dust, *Tellus*, Ser. B, 50, 491–505.

Clough, S. A., F. X. Kneizys, and R. W. Davies (1989), Line shape and the water vapor continuum, *Atmos. Res*., 23, 229– 241.

Colarco, P. R., et al. (2003a), Saharan dust transport to the Caribbean during PRIDE: 2. Transport, vertical profiles, and deposition in simulations of in situ and remote sensing observations, *J. Geophys. Res*., 108(D19), 8590, doi:10.1029/2002JD002659.

Colarco, P. R., O. B. Toon, and B. N. Holben (2003b), Saharan dust transport to the Caribbean during PRIDE: 1. Influence of dust sources and removal mechanisms on the timing and magnitude of downwind aerosol optical depth events from simulations of in situ and remote sensing observations, *J. Geophys. Res*., 108(D19), 8589, doi:10.1029/2002JD002658.

d'Almeida G.A. and L. Schütz (1983), Number, mass and volume distributions of mineral aerosols and soils of Sahara, *J. Clim. Appl. Meteorol*., 22, 233-243, 1983.

DeMott, P. J., K. Sassen, M. R. Poellot, D. Baumgardner, D. C. Rogers, S. D. Brooks, A. J. Prenni, and S. M. Kreidenweis (2003), African dust aerosols as atmospheric ice nuclei, *Geophys. Res. Lett.*, 30(14), 1732, doi:10.1029/2003GL017410.

di Sarra, A., T. Di Iorio, M. Cacciani, G. Fiocco, and D. Fuà (2001), Saharan dust profiles measured by lidar at Lampedusa, *J. Geophys. Res*., 106(D10), 10,335–10,348.

Diner, D.J., W.A. Abdou, C.J. Bruegge, J.E., Conel, K.A. Crean, B.J. Gaitley, M.C. Helmlinger, R.A. Kahn, J.V. Martonchik, S.H. Pilorz (2001), MISR aerosol optical depth retrievals over southern Africa during the SAFARI-2000 dry season campaign, *Geophys. Res. Lett*. 28 (16), 3127-3130.

Dubovik, O., A. Smirnov, B. N. Holben, M. D. King, Y. J. Kaufman, and I. Slutsker (2000), Accuracy assessments of aerosol optical properties retrieved from AERONET Sun and sky radiance measurements, *J. Geophys. Res*., 105, 9791-9806.

Dubovik, O., B.N.Holben, T.F.Eck, A.Smirnov, Y.J.Kaufman, M.D.King, D.Tanre, and I.Slutsker (2002), Variability of absorption and optical properties of key aerosol types observed in worldwide locations, *J. Atm. Sci*., 59, 590-608.

Duce, R. A (1995), Sources, distributions, and fluxes of mineral aerosols and their relationship to climate, in Aerosol Forcing of Climate (eds Charlson, R. J. & Heintzenberg, J.), 43−72 (Wiley, New York).

Dulac, F., and P. Chazette (1998), Balloonborne profiling of African dust over the tropical Atlantic, *J. Aerosol Sci*., 29, S1265– S1266.

Eck, T. F., et al. (2005), Columnar aerosol optical properties at AERONET sites in central eastern Asia and aerosol transport to the tropical mid-Pacific, *J. Geophys. Res*., 110, D06202, doi:10.1029/2004JD005274.

Fu, Q., and K. N. Liou (1992), On the correlated k-distribution method for radiative transfer in nonhomogenous atmospheres. *J. Atmos. Sci*., 49, 2139-2156.

Ginoux, P., M. Chin, I. Tegen, J. Prospero, B. Holben, O. Dubovik, and S. J. Lin (2001), Sources and distributions of dust aerosols simulated with the GOCART model, *J. Geophys. Res*., 106, 20,255– 20,273.

Gong, S. L., X. Zhang, T. Zhao, I. G. Mckendry, D. A. Jaffe, and N. Lu (2003), Characterization of soil dust aerosol in China and its transport and distribution during 2001 ACE-Asia: 2. Model simulation and validation, *J. Geophys. Res*., 108(D9), 4262, doi:10.1029/2002JD002633.

Goody, R. M., R. West, L. Chen, and D. Crisp (1989), The correlated k-distribution method for radiation calculations in nonhomogenous atmospheres, *J. Quant. Spectrosc. Radiat. Transfer*, 42, 539-550.

Hamonou, E., P. Chazette (1998), Evidence of Saharan mineral aerosols transport to the Mediterranean inside well-defined layers, *J. Aerosol Sci*., 29, S1263-S1264.

Hamonou, E., P. Chazette, A. Papayannis, D. Balis, F. Marenco, V. Santacesaria, G. Ancellet (1997), Ground-based measurements of Saharan dust optical properties in the frame of the European MEDUSE Project, *J. Aerosol Sci*., 28, S695-S696.

Harrison, S. P., K. E. Kohfeld, C. Roelandt, and T. Claquin (2001), The role of dust in climate changes today, at the Last Glacial Maximum and in the future, *Earth Sci. Rev*., 54, 43–80.

Haywood, J. M., R. P. Allan, I. Culverwell, T. Slingo, S. Milton, J. Edwards, and N. Clerbaux (2005), Can desert dust explain the outgoing longwave radiation anomaly over the Sahara during July 2003?, *J. Geophys. Res*., 110, D05105, doi:10.1029/2004JD005232.

Haywood, J., P. Francis, S. Osborne, M. Glew, N. Loeb, E. Highwood, D. Tanré, G. Myhre, P. Formenti, and E. Hirst (2003), Radiative properties and direct radiative effect of Saharan dust measured by the C-130 aircraft during SHADE: 1. Solar spectrum, *J. Geophys. Res*., 108(D18), 8577, doi:10.1029/2002JD002687.

Hess, M., P. Koepke, and I. Schult (1998), Optical properties of aerosols and clouds: the software package OPAC. *Bull. Am. Meteorol. Soc*., 79, 831–844.

Highwood, E. J., J. M. Haywood, M. D. Silverstone, S. M. Newman, and J. P. Taylor (2003), Radiative properties and direct effect of Saharan dust measured by the C-130 aircraft during Saharan Dust Experiment (SHADE): 2. Terrestrial spectrum, *J. Geophys. Res*., 108(D18), 8578, doi:10.1029/2002JD002552.

Holben B.N., T.F.Eck, I.Slutsker, D.Tanre, J.P.Buis, A.Setzer, E.Vermote, J.A.Reagan, Y.Kaufman, T.Nakajima, F.Lavenu, I.Jankowiak, and A.Smirnov, 1998: AERONET - A federated instrument network and data archive for aerosol characterization, *Rem. Sens. Environ*., 66, 1-16.

Huang, J., B. Lin, P. Minnis, T. Wang, X. Wang, Y. Hu, Y. Yi, and J. K. Ayers (2006), Satellite-based assessment of possible dust aerosols semi-direct effect on cloud water path over East Asia, *Geophys. Res. Lett*., 33, L19802, doi:10.1029/2006GL026561.

Husar, R. B., et al. (2001), Asian dust events of April 1998, *J. Geophys. Res*., 106(D16), 18,317–18,330.

Ichoku, C., D. A. Chu, S. Mattoo, Y. J. Kaufman, L. A. Remer, D. Tanré, I. Slutsker, and B. N. Holben (2002), A spatio-temporal approach for global validation and analysis of MODIS aerosol products, *Geophys. Res. Lett*., 29(12), 8006, doi:10.1029/2001GL013206.

Intergovenmental Panel on Climate Change (IPCC) (2001), Climate Change 2001, Contribution of Working Group I to the Third Assessement Report of the Intergovernmental Panel on Climate Change, Cambridge Univ. Press, New York.

Iwasaka, Y., et al. (2003), Importance of dust particles in the free troposphere over the Taklamakan Desert: Electron microscopic experiments of particles collected with a balloonborne particle impactor at Dunhuang, China, *J. Geophys. Res*., 108(D23), 8644, doi:10.1029/2002JD003270.

Jacobson, M. Z. (2001), Strong radiative heating due to the mixing state of black carbon in atmospheric aerosols, *Nature*, 409, 695-697.

Kato, S, T. P. Ackerman, J. H. Mather, and E. E. Clothiaux (1999), The k-distribution method and correlated-k approximation for a shortwave radiative transfer model, *J. Quant. Spectrosc. Radiat. Transfer*, 62, 109-121.

Kaufman, Y.J., D. Tanré (1998), Algorithm for remote sensing of tropospheric aerosol from MODIS, http://modis.gsfc.nasa.gov/data/atbd/atbd_mod02.pdf.

Kaufman, Y.J., D. Tanré, O. Dubovik, A. Karnieli, L.A. Remer (2001), Absorption of sunlight by dust as inferred from satellite and ground-based remote sensing, *Geophysical Research Letters*, 28 (8), 1479-1482.

Kaufman, Y. J., I. Koren, L. A. Remer, D. Tanré, P. Ginoux, and S. Fan (2005), Dust transport and deposition observed from the Terra-Moderate Resolution Imaging Spectroradiometer (MODIS) spacecraft over the Atlantic Ocean, *J. Geophys. Res*., 110, D10S12, doi:10.1029/2003JD004436.

Kent G.S., C.R.Trepte, P.H. Wang, P.L. Lucker (2003), Problems in separating aerosol and cloud in the Stratospheric Aerosol and Gas Experiment (SAGE) II data set under conditions of lofted dust: Application to the Asian deserts, *J. Geophys. Res.*, 108 (D14), 4410, doi:10.1029/2002JD002412.

Kent, G. S., C. R. Trepte, K. M. Skeens, and D. M. Winker (1998), LITE and SAGE II measurements of aerosols in the southern hemisphere upper troposphere, *J. Geophys. Res.*, 103(D15), 19,111–19,128.

Kwon, S. A., Y. Iwasaka, T. Shibata, and T. Sakai (1997), Vertical distribution of atmospheric particles and water vapor densities in the free troposphere: Lidar measurement in spring and summer in Nagoya, Japan, *Atmos. Environ*., 31, 1459-1465.

Lacis, A. A., and V. Oinas (1991), A description of the correlated k distribution method for modeling nongray gaseous absorption, thermal emission, and multiple scattering in vertically inhomogenous atmospheres, *J. Geophys. Res*., 96, 9027-9063.

Lau, K.M., M. K. Kim, and K. M. Kim (2006), Asian summer monsoon anomalies induced by aerosol direct forcing: the role of the Tibetan Plateau, *Climate Dynamics*, 26, 855-864.

Li, F., A. M. Vogelmann and V. Ramanathan (2004), Saharan dust aerosol radiative forcing measured from space, *J. Climate*, 17(13), 2558-2571.

Li, F., and V. Ramanathan (2002), Winter to summer monsoon variation of aerosol optical depth over the tropical Indian Ocean, *J. Geophys. Res*., 107(D16), 4284, doi:10.1029/2001JD000949.

Liao, H. and J.H. Seinfeild (1998), Radiative forcing by mineral dust aerosols: Sensitivity to key variables, *J. Geophys. Res*., 103(D24), 31,637-31,645.

Liu, Z., N. Sugimoto, and T. Murayama (2002), Extinction-to-backscatter ratio of Asian dust observed with high-spectral-resolution lidar and Raman lidar, *Appl. Opt*., 41, 2760– 2767.

Lunt, D.J., and P.J. Valdes (2002), The modern dust cycle: Comparison of model results with observations and study of sensitivities, *J. Geophys. Res*., 107(D23), 4669, doi:10.1029/2002JD002316.

Mahowald, N. M., D. R. Muhs, S. Levis, P. J. Rasch, M. Yoshioka, C. S. Zender, and C. Luo (2006), Change in atmospheric mineral aerosols in response to climate: Last glacial period, preindustrial, modern, and doubled carbon dioxide climates, *J. Geophys. Res*., 111, D10202, doi:10.1029/2005JD006653.

Marchuk, G., Mikhailov, G., Nazarahev, M., Darbinjan, R., Kargin, B., and Elepov, B. (1980), The Monte Carlo Methods in Atmospheric Optics, Springer-Verlag, New York.

Martins, J.V., D. Tanré, L. Remer, Y. Kaufman, S. Mattoo, R. Levy (2002), MODIS cloud screening for remote sensing of aerosol over oceans using spatial variability, *Geophys. Res. Lett*., 29, 10.1029/GL013252.

Matsuki, A., et al. (2003), Seasonal dependence of the long-range transport and vertical distribution of free tropospheric aerosols over east Asia: On the basis of aircraft and lidar measurements and isentropic trajectory analysis, *J. Geophys. Res.*, 108(D23), 8663, doi:10.1029/2002JD003266.

Mattis, I., A. Ansmann, D. Müller, U. Wandinger, and D. Althausen (2002), Dual-wavelength Raman lidar observations of the extinction-to-backscatter ratio of Saharan dust, *Geophys. Res. Lett*., 29(9), 1306, doi:10.1029/2002GL014721.

Mbourou, G. N., J. J. Bertrand, and S. E. Nicholson (1997), The diurnal and seasonal cycles of wind-born dust over Africa North of the Equator, *J. Applied Meteor*., 36, 868-882.

Meloni, D., A. D. Sarra, T. D. Iotio, and G. Fiocco (2005), Influence of the vertical profile of Saharan dust on the visible direct radiative forcing, *Journal of Quantitative Spectroscopy Radiative Transfer*, 93, 497-413.

Müller, D., I. Mattis, U. Wandinger, A. Ansmann, D. Althausen, O. Dubovik, S. Eckhardt, and A. Stohl (2003), Saharan dust over a central European EARLINET-AERONET site: Combined observations with Raman lidar and Sun photometer, *J. Geophys. Res*., 108(D12), 4345, doi:10.1029/2002JD002918.

Müller, D., K. Franke, F. Wagner, D. Althausen, A. Ansmann, J. Heintzenberg, and G. Verver (2001), Vertical profiling of optical and physical particle properties over the tropical Indian Ocean with six-wavelength lidar 2. Case studies, *J. Geophys. Res*., 106(D22), 28,577–28,596.

Murayama, T., D. Mu¨ller, K. Wada, A. Shimizu, M. Sekiguchi, and T. Tsukamoto (2004), Characterization of Asian dust and Siberian smoke with multi-wavelength Raman lidar over Tokyo, Japan in spring 2003, *Geophys. Res. Lett*., 31, L23103, doi:10.1029/2004GL021105.

Murayama, T., et al. (2001), Ground-based network observation of Asian dust events of April 1998 in east Asia, *J. Geophys. Res*., 106(D16), 18,345–18,360.

Murayama, T., et al. (2003), An intercomparison of lidar-derived aerosol optical properties with airborne measurements near Tokyo during ACE-Asia, *J. Geophys. Res*., 108(D23), 8651, doi:10.1029/2002JD003259.

Myhre, G., A. Grini, J. M. Haywood, F. Stordal, B. Chatenet, D. Tanré, J. K. Sundet, and I. S. A. Isaksen (2003), Modeling the radiative impact of mineral dust during the Saharan Dust Experiment (SHADE) campaign, *J. Geophys. Res*., 108(D18), 8579, doi:10.1029/2002JD002566.

Nakajima, T., M. Tanaka, M. Yamano, M. Shiobara, K. Arao, and Y. Nakanishi (1989), Aerosol optical characteristics in the yellow sand events observed in May, 1982 in Nagasaki, part II: *Model, J. Meteorol. Soc. Jpn*., 67, 279– 291.

Pease, P. P., V. P. Tchakerian, and N. W. Tindale (1998), Aerosols over the Arabian Sea: geochemistry and source areas for aeolian desert dust, *J. Arid Environ*., 39, 477–496.

Penner, J. E., et al. (2001), Aerosols, their direct and indirect effects, in Climate Change 2001: The Scientific Basis. Contribution of Working Group I to the Third Assessment Report of the Intergovernmental Panel on Climate Change, edited by J. Houghton et al., pp. 289– 348, Cambridge Univ. Press, New York.

Pérez, C., S. Nickovic, J. M. Baldasano, M. Sicard, F. Rocadenbosch, and V. E. Cachorro (2006), A long Saharan dust event over the western Mediterranean: Lidar, Sun photometer observations, and regional dust modeling, *J. Geophys. Res*., 111, D15214, doi:10.1029/2005JD006579.

Perlwitz, J., I. Tegen, and R. L. Miller (2001), Interactive soil dust aerosol model in the GISS GCM: 1. Sensitivity of the soil dust cycle to radiative properties of soil dust aerosols, *J. Geophys. Res*., 106(D16), 18,167–18,192.

Podgorny, I. A., A. M. Vogelmann, and V. Ramanathan (1998), Effects of cloud shape and water vapor distribution on solar absorption in the near infrared, *Geophys. Res. Lett.*, 25(11), 1899–1902.

Podgorny, I. A., and V. Ramanathan (2001), A modeling study of the direct effect of aerosols over the tropical Indian Ocean, *J. Geophys. Re*s., 106(D20), 24,097–24,106.

Prospero J. M. and T. N. Carlson (1981), Saharan air outbreaks over the tropical North Atlantic, *Pure Appl. Geophys*.119, 677–691.

Prospero, J. M., and T. N. Carlson (1972), Vertical and areal distribution of Saharan dust over the western equatorial North Atlantic ocean, *J. Geophys. Res*., 77, 5255–5265.

Prospero, J. M., P. Ginoux, O. Torres, S. E. Nicholson, and T. E. Gill (2002), Environmental characterization of global sources of atmospheric soil dust identified with the NIMBUS 7 Total Ozone Mapping Spectrometer (TOMS) absorbing aerosol product, *Rev. Geophys*., 40(1), 1002, doi:10.1029/2000RG000095.

Raes, F., T. Bates, F. Mcgovern, and M. Van-Liedekerke (2000), The 2nd aerosol characterization experiments (ACE-2) general overview and main results, *Tellus*, 52B, 111-125.

Ramanathan, V., et. al (2001), Indian ocean experiment: An integrated analysis of the climate forcing and effects of the great Indo-Asian haze, *J. Geophys. Res*, 106 (D22): 28371-28398.

Remer, L. A., et al. (2002), Validation of MODIS aerosol retrieval over ocean, *Geophys. Res. Lett*., 29(12), 8008, doi:10.1029/2001GL013204.

Reynolds, R.W., N.A. Rayner, T.M. Smith, D.C. Stokes, and W. Wang (2002), An improved in situ and satellite SST analysis for climate, *J. Climate*, 15, 1609-1625.

Rossow, W.B., A.W. Walker, D.E. Beuschel, and M.D. Roiter (1996), International Satellite Cloud Climatology Project (ISCCP) Documentation of New Cloud Datasets. WMO/TD-No. 737, World Meteorological Organization, 115 pp.

Rossow, W.B., and R. A. Schiffer (1999), Advances in Understanding Clouds from ISCCP, *Bull. Amer. Meteor. Soc*., 80, 2261-2288.

Rothman, L. S., et al. (2003), The HITRAN molecular spectroscopic database: edition of 2000 including updates through 2001, *J. Quant. Spectros. Radiat. Transfer*, 82, 5–44.

Sakai, T., T. Shibata, S. A. Kwon, Y. S. Kim, K. Tamura, and Y. Iwasaka (2000), Free tropospheric aerosol backscatter, depolarization ratio, and relative humidity measured with the Raman lidar at Nagoya in 1994-1997: Contributions of aerosols from the Asian Continent and the Pacific Ocean, *Atmos. Environ*. 34, 431–442.

Sasano, Y. (1996), Tropospheric aerosol extinction coefficient profiles derived from scanning lidar measurements over Tsukuba, Japan from 1990 to 1993, *Appl. Opt*., 35(24), 4941–4952.

Sassen, K., P. J. DeMott, J. M. Prospero, and M. R. Poellot (2003), Saharan dust storms and indirect aerosol effects on clouds: CRYSTAL-FACE results, *Geophys. Res. Lett*., 30(12), 1633, doi:10.1029/2003GL017371.

Satheesh, S. K., V. Ramanathan, Xu Li-Jones, J. M. Lobert, I. A. Podgorny, J. M. Prospero, B. N. Holben, and N. G. Loeb (1999), A model for the natural and antropogenic aerosols over the tropical Indian Ocean derived from Indian Ocean Experiment data, *J. Geophys. Res*., 104(D22), 27,421– 27,440.

Seinfeld, J. H., et al. (2004), Regional climatic and atmospheric chemical effects of Asian dust and pollution, *Bull. Am. Meteorol. Soc*., 85(3), 367–380.

Shao, Y. P., et al. (2003), Northeast Asian dust storms: Real-time numerical prediction and validation, *J. Geophys. Res*., 108(D22), 4691, doi:10.1029/2003JD003667.

Shi, G., H. Wang, B. Wang, S. Gong, T. Zhao, W. Li and T. Aoki (2005), Sensitivity experiments on the effects of optical properties of dust aerosols on their radiative forcing under sky condition, *J. Met. Soc. Japan*, 83A, 333-346.

Shimizu, A., N. Sugimoto, I. Matsui, K. Arao, I. Uno, T. Murayama, N. Kagawa, K. Aoki, A. Uchiyama, and A. Yamazaki (2004), Continuous observations of Asian dust and other aerosols by polarization lidars in China and Japan during ACE-Asia, *J. Geophys. Res*., 109, D19S17, doi:10.1029/2002JD003253.

Sirocko, F. (1991), Deep-sea sediments of the Arabian Sea: A paleoclimatic record of the southwest-Asian summer monsoon, *Geologische Rundschau*, 80, 557–66.

Sokolik, I. N. and O. B. Toon (1999), Incorporation of mineralogical composition into models of the radiative properties of mineral aerosol from UV to IR wavelengths, *J. Geophys. Res*., 104, 9423-9444.

Sokolik, I. N., A. Andronova, and T. C. Johnson (1993), Complex refractive index of atmospheric dust aerosols, *Atmos. Environ*., 27, 2495– 2502.

Sokolik, I. N., D. M. Winker, G. Bergametti, D. A. Gillette, G. Carmichael, Y. J. Kaufman, L. Gomes, L. Schuetz, and J. E. Penner (2001), Introduction to special section: Outstanding problems in quantifying the radiative impacts of mineral dust, *J. Geophys. Res.*, 106(D16), 18,015–18,028.

Sokolik, I. N., O. B. Toon, and R. W. Bergstrom (1998), Modeling the radiative characteristics of airborne mineral aerosols at infrared wavelengths, *J. Geophys. Res.*, 103(D8), 8813–8826.

Song, C. H., and G. R. Carmichael (2001), A three-dimensional modeling investigation of the evolution processes of dust and sea-salt particles in East Asia, *J. Geophys. Res*., 106, 18,131–18,154.

Song, C.H., K. Meier, R.J. Weber, V. Kapustin, and A. Clarke, Dust composition and mixing state inferred from airborne composition measurements during ACE-Asia C130 Flight#6 (2005), *Atmos. Environ*., 39, 359-369.

Stowe LL, H. Jacobowitz, G. Ohring, K.P. Knapp, N.R. Nalli (2002), The Advanced Very High Resolution Radiometer (AVHRR) Pathfinder Atmosphere (PATMOS) climate dataset: Initial analyses and evaluations, *J. Climate*, 15 (11): 1243-1260.

Stowe, L. L., A. A. Ignatove, and R. R. Singh (1997), Development, validation and potential enhancements to the second generation operational aerosol product at NOAA/NESDIS, *J. Geophys. Res*, 102 (D14): 16923-16934.

Sun, J., M, Zhang, and T. Liu (2001), Spatial and temporal characteristics of dust storm in China and its surrounding regions, 1960-1999: Relations to source area and climate, *J. Geophys. Res*., 106, (D10), 10325-10333.

Tanré, D., J. Haywood, J. Pelon, J. F. Léon, B. Chatenet, P. Formenti, P. Francis, P. Goloub, E. J. Highwood, and G. Myhre (2003), Measurement and modeling of the Saharan dust radiative impact: Overview of the Saharan Dust Experiment (SHADE), *J. Geophys. Res.*, 108(D18), 8574, doi:10.1029/2002JD003273.

Tanré, D., Y.J. Kaufman, B.N. Holben, B. Chatenet, A. Karnieli, F. Lavenu, L. Blarel, O. Dubovik, L.A. Remer, and A. Smirnov (2001), Climatology of dust aerosol size distribution and optical properties derived from remotely sensed data in the solar spectrum, *J. Geophys. Res*, 106 (D16), 18205-18217.

Tanré, D., Y.J. Kaufman, M. Herman, and S. Mattoo (1997), Remote sensing of aerosol properties over oceans using the MODIS/EOS spectral radiances, *J. Geophys. Res*, 102 (D14), 16971-16988.

Tegen, I., A. A. Lacis, and I. Fung (1996), The influence on climate forcing of mineral aerosols from disturbed soils, *Nature*, 380, 419–422.

Thomason, L.W., and G. Taha (2003), SAGE III aerosol extinction measurements: Initial results, *Geophys. Res. Lett*., 30 (12), 1613, doi:10.1029/2003GL017317.

Thomason, L.W., L.R. Poole, and T.R. Deshler (1997), A Global Climatology Of Stratospheric Aerosol Surface Area Density As Deduced From SAGE II: 1984-1994, *J. Geophys. Res.*, 102, 8967-8976.

Tindale, N.W., P. P. Pease (1999), Aerosols over the Arabian Sea: Atmospheric transport pathways and concentrations of dust and sea salt, *Deep–Sea Research* II 46, 1577–1595.

Torres O., P.K. Bhartia, J.R. Herman, A. Sinyuk, P. Giuoux, and B. Holben (2002), A long-term record of aerosol optical depth from TOMS observations and comparison to AERONET measurements, *J. Atmos. Sci*., 59, 398-413.

Torres O., P.K. Bhartia, J.R. Herman, Z. Ahmda, and J. Gleason (1998), Derivation of aerosol properties from satellite measurements of backscattered ultraviolet radiation: Theoretical basis, *J. Geophys. Res*., 103, 17,099-17,110.

Twomey, S. A. (1977), The influence of pollution on the shortwave albedo of clouds, *J. Atmos. Sci*., 34, 1149–1152.

Uppala, S. M., et al. (2005), The ERA-40 reanalysis. *Quart. J. Roy.Meteor. Soc*., 131, 2961-3012.

Vogelmann, A.M., V. Ramanathan and I. A. Podgorny (2001), Scale dependence of solar heating rates in convective cloud systems with implications to general circulation models, *J. Climate*, 14(N8), 1738-1752.

Volz, F. E (1973), Infrared optical constants of ammonium sulphate, Sahara dust, volcanic pumice and fly ash, *Appl. Opt*., 12, 564– 567.

Wang P.H., G.S. Kent, R.E. Veiga, G.K. Yue , L.R. Poole (1999), Fishman J, McCormick MP, A model for identifying the aerosol-only mode of SAGE II 1.02-μm extinction coefficient data at altitudes below 6.5 km, *J. Geophys. Res*, 104 (D8): 9609-9615.

Welton, E. J., et al. (2000), Ground-based lidar measurements of aerosols during ACE-2: Instrument description, results, and comparisons with other ground-based and airborne measurements, *Tellus*, 52B, 636– 651.

Woodward, S. (2001), Modeling the atmospheric life cycle and radiative impact of mineral dust in the Hadley Centre climate model, *J. Geophys. Res*., 106(D16), 18,155–18,166.

Zender, C. S., H. Bian, and D. Newman, Mineral Dust Entrainment and Deposition (DEAD) model: Description and 1990s dust climatology, *J. Geophys. Res*., 108(D14), 4416, doi:10.1029/2002JD002775, 2003.

Zhang, D., J. Zang, G. Shi, Y. Iwasaka, A. Matsuki, and D. Trochkine (2003a), Mixture state of individual Asian dust particles at a coastal site of Qingdao, China, *Atmos. Environ*., 37, 3895–3901.

Zhang, D., Y. Iwasaka, G. Shi, J. Zang, A. Matsuki, and D. Trochkine (2003b), Mixture state and size of Asian dust particles collected at southwestern Japan in spring 2000, *J. Geophys. Res*., 108(D24), 4760, doi:10.1029/2003JD003869.

Zhou Z., and G. Zhang (2003), Typical severe dust storms in northern China during 1954-2002, *Chinese Science Bulletin*, 48(21), 2366-2370, 2003.

Zhou, J., G. Yu, C. Jin, F. Qi, D. Liu, H. Hu, Z. Gong, G. Shi, T. Nakajima, and T. Takamura (2002), Lidar observations of Asian dust over Hefei, China, in spring 2000, *J. Geophys. Res*., 107(D15), 4252, doi:10.1029/2001JD000802.

Chapter 3

Mixing State and Radiative Impacts of Atmospheric Brown Clouds over the North Indian Ocean

3.1 Introduction

The importance of airborne aerosol particles for the atmospheric environment and the global climate has been studied for decades. Through reflection and absorption, atmospheric aerosols interact with solar radiation, cut down the incoming solar flux, and lead to surface dimming, which greatly influences the temperature, precipitation, agriculture, and life. The direct effect of aerosols depends on the distribution and loading of aerosols in the atmosphere and their optical properties. Some colored aerosols, such as black carbon (BC) commonly referred to as soot; a certain organic carbon known as brown carbon [*Andreae and Gelenser*, 2006]; and mineral dust, have considerable abilities to trap energy in the air and warm the atmosphere.

Though the overall effect of atmospheric aerosols is negative at the top-of-the-atmosphere (TOA), some carbonaceous aerosols, such as black carbon, have a positive radiative forcing on the earth-atmosphere system and contribute to climate warming. As the byproduct of incomplete combustion of fossil fuels and biomass, black carbon (BC) aerosols strongly absorb sunlight. It has been shown that aerosols mixed with BC reduce diurnally and seasonally averaged solar fluxes at the surface by as much as 20 Wm^{-2} over the entire N. Indian Ocean and increase atmospheric solar heating by as much as 50% [*Ramanathan et al.*, 2001a]. *Jacobson* [2001] investigated the warming

potential of BC and suggested that the positive forcing caused by BC itself may nearly balance the net cooling of other anthropogenic aerosols and BC might exceed methane to become the second most important warming agent after carbon dioxide. *Flanner et al.* [2007] conducted the first global climate study with coupled BC/snow forcing and snow aging and estimated the global annual mean BC/snow forcing was in the range of +0.054 to +0.049 Wm^{-2} for strong (1998) and weak (2001) boreal fire years, respectively. The seasonal variation of BC/snow forcing indicates that the strongest forcing happens mostly in local springtime when large amounts of snow are exposed to intense sunlight and peak snowmelt occurs. Surface darkening by BC aerosols exceeds aerosol dimming over the Arctic and explains 30-50% of Arctic warming. A recent review by *Ramanathan and Carmichael* [2008] reported the warming effect of BC in the atmosphere is about three to four times greater than the prevailing estimates and the solar heating by BC may be just as culpable as CO_2 in the rapid retreat of the Himalayan-Tibetan glaciers.

With the aid of more sophisticated, state-of-the-art numerical models, the influence of aerosols on atmospheric circulation and the hydrological circle can be investigated. The model study by *Menon et al.* [2002] showed that absorbing aerosols like BC may be responsible for the decrease in precipitation over the northern part of India and the north-south shift of the rainfall pattern in East China (south flood, north drought). *Lau et al.* [2006] postulated the so-called “elevated heat pump” mechanism to explain the combined effect of BC and dust on summer monsoons in India. They stated that large amounts of BC and dust has built up over the Tibetan Plateau during

late spring and early summer and aerosol induced heating in the upper troposphere amplified the meridional temperature gradient to trigger the onset of Indian monsoon rainfall in its early stages. However, their model used the prescribed sea surface temperature (SST), and so any changes to the ocean resulting from the surface dimming effect of aerosols was not included. Using a global coupled climate model with interactive ocean and prescribed greenhouse and aerosol forcing, *Ramanathan et al.* [2005] conducted a numerical study and found that an increase in atmospheric brown clouds (ABC) was the primary factor leading to decrease in monsoon rainfall over S. Asia. This is because when the ocean temperature is coupled with the rest of the climate system, the dimming of surface radiation decreases on the north-south SST gradient and decelerates the monsoon rainfall. This statement has received support from other independent studies [*Lau and Kim*, 2007; *Meehl et al.*, 2008]. *Meehl et al.* [2008] showed that the effect of BC in regulating Indian monsoon rainfall relies in part on changes in the SSTs of the Arabian Sea and Bay of Bengal (BOB). During the premonsoon season (Mar-Apr-May) the loading of BC over South Asia reduces the incoming solar radiation reaching the surface and heats the lower troposphere, which enhances the tropospheric temperature contrast between the Tibetan Plateau and areas to the south and increases precipitation over North India, with some decreased rainfall over Southwest India, BOB, and Southeast Asia. With the development of a monsoon over India, a reduced surface temperature extended to the Arabian Sea and BOB and the elevated heat source became weaker owing to the decrease of BC concentration by wet removal. The combination of these two factors weakened the meridional

temperature gradient and thus BC tends to reduce the precipitation over much of India during the monsoon season of Jun-Jul-Aug (JJA).

The mixing assumption of BC is a critical factor in the creation of a forcing estimate and it affects forcing by factors of 1.6 to 2.9 [*Bond et al.,* 2006]. Three different mixing states were assumed in the previous studies, which are: 1) external mixing, in which there is no physical interaction among particles; 2) perfect internal mixing (or volume mixing), in which all aerosol species are perfectly mixed with each other at the molecular level, meaning that all particles have the same composition; 3) core-shell internal mixing (or coated mixing), in which solid particles such as BC and mineral dust serve as the core and are encapsulated by well-mixed non-absorbing materials. The theoretical study showed that absorption is always increased when light-absorbing particles (LAP) are internally mixed with other materials. *Bond et al.* [2006] suggests that the absorption of aged soot particles mixed with other aerosols is about 1.5 times greater than that of fresh aerosols. *Shiraiwa et al.* [2008] found that coating reduces the single scattering albedo (SSA) of PM1 aerosols from the Asian flow by 0.01 to 0.02. *Chandra et al.* [2004] shows that SSA can decrease from 0.9 (external mixture) to 0.78 when soot is covered in a shell, which explains the 15 to 34 Wm^{-2} excess of atmospheric absorption. On the global scale, model study [*Jacobson*, 2000 and 2001] reported that the direct radiative forcing of soot aerosols is 0.27 Wm^{-2} for external mixing and 0.58 Wm^{-2} for core-shell mixing, but is enhanced to 0.78 Wm^{-2} for internal mixing, which clearly indicates that the magnitude of direct aerosol radiative forcing is largely dependent on the mixing state of BC with other aerosols.

The external mixing assumption usually underestimated absorption and positive forcing by LAP, and ignored aerosol aging during its atmospheric transport. Freshly emitted particles may coagulate with other preexisting aerosols, be coated by gaseous species, and become oxidized during their lifetime. *Moffet and Prather* [2009] found that the majority of soot particles measured in Mexico City and Riverside were associated with sulfate, organics, nitrate, and water. The study by *Okada et al.* [2001] showed that organic material from biomass burning was internally mixed with inorganic salts such as sulfate, nitrate and soot. The single particle chemistry analysis from INDOEX [*Guazzotti et al.,* 2001] found no single particles containing pure sulfuric acid, sodium sulfate or ammonium sulfate, and for all detected particles, sulfates were associated with other materials. About 75% of fine (0.2-1.0 μm) sulfate associated particles are associated with carbon-containing particles with potassium, 12% with OC/EC particles, 10% with dust particles, and 3% with sea-salt. *Naoe and Okada* [2001] examined the aerosol samples collected in the urban air of Japan and found a dominant number (75%) of internally mixed soot-particles in a "polluted" case in the radius range of 0.01-0.2 μm.

Perfect internal mixing often overestimates absorption, which is remarkably unrealistic and not physically reasonable. Take refractory soot particles for example. Light-absorbing elemental carbon particles do not dissolve and the contiguous sp2-bonded carbon structure which governs the absorption of soot will be disrupted if other material is evenly distributed throughout the particles [*Bond et al.,* 2006]. Diesel soot particles coated with secondary organic compounds from the experiment were

observed at the large aerosol chamber facility AIDA in Germany [*Schnaiter et al.*, 2005]. A laboratory study by *Zhang et al.* [2008] clearly demonstrated the formation of sulfuric acid coating on soot particles when subsaturated sulfuric acid was exposed to soot agglomerates. *Zhang et al.* [2008] found that soot particles acquired a large mass fraction of sulfuric acid and underwent a marked change in morphology and optical properties. Sulfuric acid molecules readily condense on particles and coat them efficiently, mainly due to their sticky nature and high water affinity. The condensed H_2SO_4 is subsequently stabilized from interaction with water vapor. Thus, H_2SO_4 exposure will greatly enhance hydrophilicity of soot aerosols. The formation of the hygroscopic shell and the compaction of the soot core considerably enhance the absorption and scattering of aged soot particles. *Zhang et al.* [2008] also conducted the comparison experiment using polystyrene latex (PSL) particles as counterparts, and found that the condensation of sulfuric acid is proportional to the surface area of the particle and independent of its chemical composition and microphysical structure. Thus, the H_2SO_4 coating process may also apply to other solid particles.

Field observations also suggest that core-shell mixing is probably the most realistic mixing state. During the MILAGRO (Megacity Initiative: Local and Global Research Observations) campaign in and near Mexico City, *Adachi and Buseck* [2008] employed aircraft to collect over 8000 particles with aerodynamic diameters from 0.05 to 0.3μm. Using a transmission electron microscope (TEM) technique combined with chemical analysis, they found that most of the sampled particles over Mexico City and adjacent areas were coated with sulfates and organic matter. *Hasegawa and Ohta*

[2002] showed that soot-encapsulated particles were present in very high numbers (42-49%) at the urban site of Japan. Large percentage of soot-containing particles that had both K and S were detected in the free troposphere over Australia [*Okada et al.*, 2005]. The samples taken by aircraft showed that about 50% of these mixed particles with radii larger than 0.2um were covered with semi-transparent material, probably organic material. Even in the clean air over the remote Southern Ocean, about 10-45% of sulfate particles were found to contain soot aggregates within them [*Posfai et al.*, 1999]. *Shiraiwa et al.* [2007] stated that the main coating materials on BC are sulfate and organics, and the contribution of sulfate, organics, and nitrate explains almost the entire coating variance. During the daytime, sulfate and organics accounted for about 90% of the coating on BC, and during the nighttime, under high-RH conditions, nitrate contributed substantially to coating.

The field observation and laboratory experiments suggest that freshly emitted particles might be externally mixed, whereas aged particles are mostly mixed with sulfate and/or organic matter and water and over a remote marine atmosphere almost all aged particles are covered in an aqueous shell. The objective of this study is to explore the likely mixing state of aerosols over the N. Indian Ocean and understand the role of coating on aerosols in regulating radiative forcing and atmospheric heating. This study applies field measured aerosol microphysical and optical properties into the core-shell mixing model and investigates the likely mixing state and radiative forcing of atmospheric aerosols over the North Indian Ocean. It investigates the effects of hygroscopic coating on optical properties and the radiative impacts of light absorbing

particles. The role of mixed brown carbon in radiative forcing and heating rate is estimated quantitatively. The observation data and the design of aerosol mixing model are described in sections 2 and 3, respectively. The resulting aerosol mixing state, optical properties, and radiative forcing are discussed in section 4, followed by model results validation. Finally, the effects of the coating process on aerosol optical properties and radiative forcing is explored in section 6.

3.2 MAC Observation

The Maldives Autonomous Unmanned Aerial Vehicle (UAV) Campaign (MAC) employed lightweight UAVs that flew in the atmospheric layer between 0.5 and 3 km over the Indian Ocean off the coast of Hanimaadhoo (6.76°N, 73.18°E) in March of 2006 [*Ramanathan et al.,* 2007]. A total of 18 different scientific flight missions were operated during the MAC campaign. The synchronized measurements of aerosols, clouds, temperature, humidity, and upward and downward solar fluxes provided profound insight into the role of atmospheric aerosols in regulating solar heating. For the stacked flight mission, three UAVs flew vertically stacked with one above the cloud, one in cloud, one below cloud. This formation not only provided unique insights into the vertical distribution of aerosols, clouds and atmosphere, it also enabled the in-situ measurement of atmospheric absorption by aerosols and clouds. Instruments installed onboard the UAVs were miniaturized in order to reduce the payload. Aerosol and radiation instruments were onboard the aircrafts that flew below and above clouds, including the condensation particle counter (CPC), optical particle counter (OPC), aerosol absorption photometer, aerosol inlet, pyranometer, and Photo-

synthetically Active Radiation (PAR sensor). A cloud droplet porbe (CDP), liquid water content probe (LWC), gust probe, and video camera were installed in the in-cloud aircraft to gather data about the clouds. All UAVs had meteorological parameter sensors, data acquisition systems, and batteries. Ground-based observations were taken simultaneously at the Maldives Climate Observatory in Hanimaadhoo (MCOH). MCOH used a CIMEL sunphotometer operated by AErosol RObotic NETwork (AERONET), Pyranometers, and other aerosols instruments performing physical, optical, and chemical measurements. Detailed information about UAVs and other instrumentation used in MAC are discussed in *Ramana et al.* [2007] and *Corrigan et al.* [2008].

This study uses data from March 29, mainly because atmospheric conditions were cloud-free and the effect of aerosols on atmospheric absorption and heating rate can be easily differentiated from the contributions of gases. Table 3.1 lists observation items that are used in this study. The CPC measures the total particle concentration for the particles larger than 10nm, the OPC samples aerosol number concentrations in 8 size bins (diameter larger than 0.3, 0.42, 0.58, 0.8, 1.12, 1.55, 2.16, 3.0 μm, respectively), the Aethalometer provides aerosol absorption coefficients at three wavelengths (370, 520, and 880 nm), the Kipp & Zonen CM21 Pyranometer measures the incoming and reflected solar radiation in the broadband (0.3-2.8 μm), the CIMEL sunphotometer gives the columnar integrated aerosol optical depths (AOD) at 550 nm, and the meteorological sensor samples the relative humidity of the ambient air.

Table 3.1: Observation items from MAC campaign used in this study.

Instrument	Observation
CPC (D_p>0.10 μm)	Total particle concentration [#/cm3]
OPC (D_p: 0.3-5.0 μm)	Aerosol size distribution [#/cm3]
Aethalometer	Absorption coefficient at 370, 520, 880nm [Mm-1]
Pyranometer (0.3-2.8 μm)	Broadband fluxes [Wm^{-2}]
Meteorological	Relative humidity
sunphotometer (MCOH)	AOD at 550nm

Total particle concentration and AOD are combined to derive the vertical profile of the aerosol extinction coefficient (550nm) based on the assumption that aerosol extinction is proportional to the total particle number concentration. The total particles concentration profile measured by the CPC was normalized with regard to its maximum value. This normalized profile was then applied to the extinction coefficient profile using AOD as the constraint, i.e. the integration of the extinction coefficient through the atmospheric column should approximate the AOD measured by AERONET. Figure 3.1 shows the CPC measurement and derived aerosol extinction coefficient. The elevated peak at around 2.0 km was clearly demonstrated where aerosol number concentration was as high as ~2500 cm^{-3} about 2 times larger than that observed near the surface. The estimated extinction coefficient followed the vertical pattern of aerosol concentration and showed a maximum value of ~140 Mm^{-1} at the peak level.

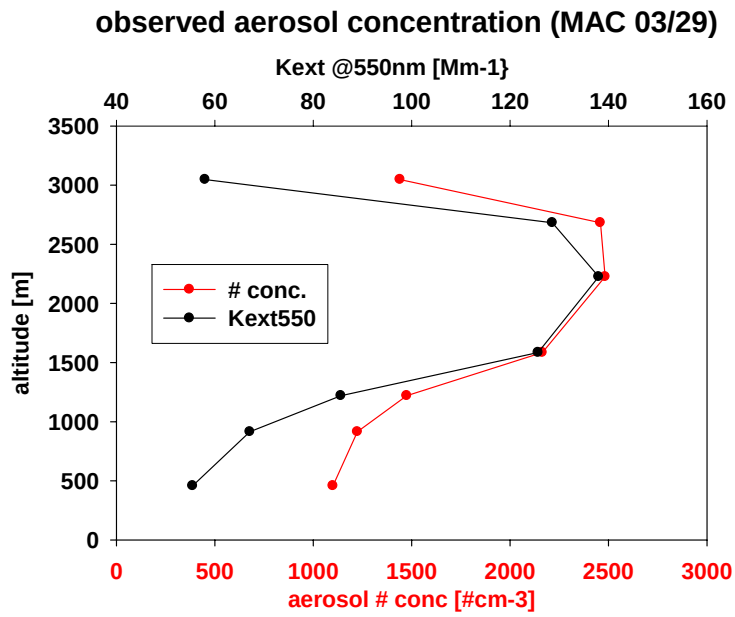

Figure 3.1: Vertical profile of aerosol total number concentration [#/cm^{-3}] and extinction coefficient at 550 nm.

The aerosol size distribution measured by OPC is shown in Figure 3.2. Below the marine boundary layer (MBL), the size distribution was broader and coarse particles made greater contributions to the particle numbers. Concentrations of fine particles (D_p < 0.5 μm) greatly increased with height and also presented an elevated peak at around 2.0 km. This elevated aerosol peak layer was also captured by the Aethalometer. Aerosol absorption coefficients observed at near ultraviolet, mid of visible, and near infrared regions (figure 3.3) all had the highest value at the 1.5 to 2.0 km layer. The distinct characteristics of these elevated aerosols suggest that they probably have different sources from the marine boundary layer aerosols. The NOAA-HYSPLIT (Hybrid Single-Particle Lagrangian Integrated Trajectory) [*Draxler and Hess*, 1998] 5-day back-trajectory analysis (Figure 3.4) indicates that the air mass of

these strong absorbing fine particles above the MBL originated from the Indian Subcontinent, while the air masses at 500 m came from the Arabian Peninsula.

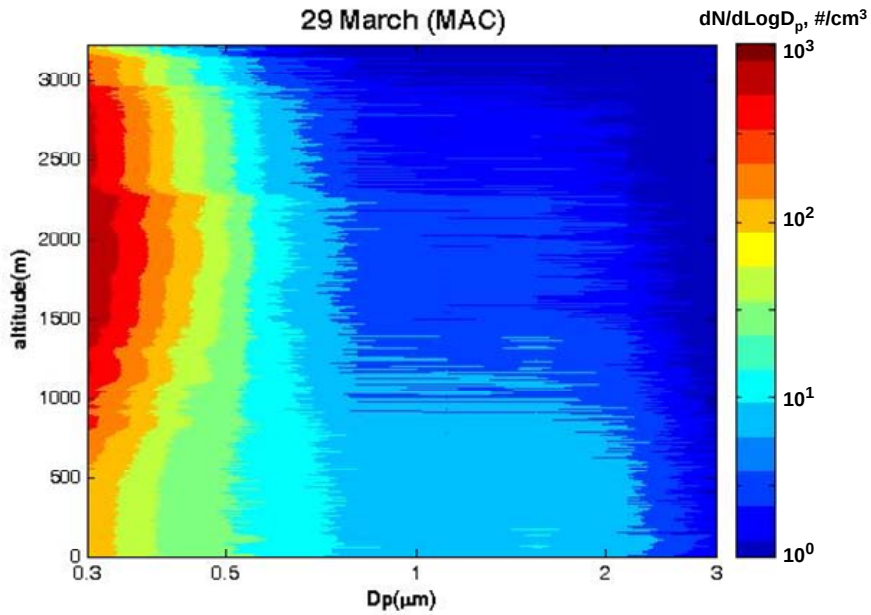

Figure 3.2: OPC measured aerosol number size distribution.

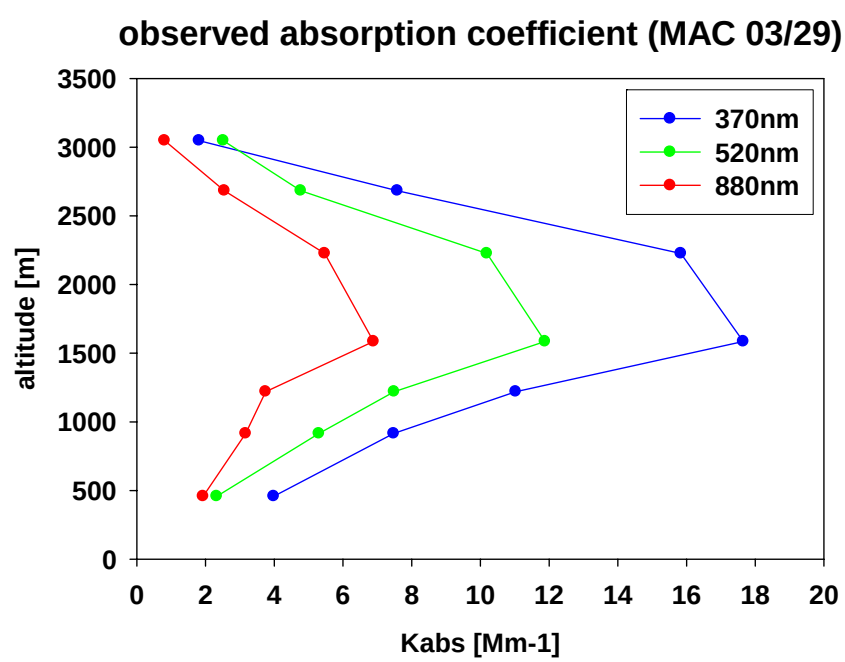

Figure 3.3: Vertical profile of aerosol absorption coefficient at 370, 520, and 880 nm.

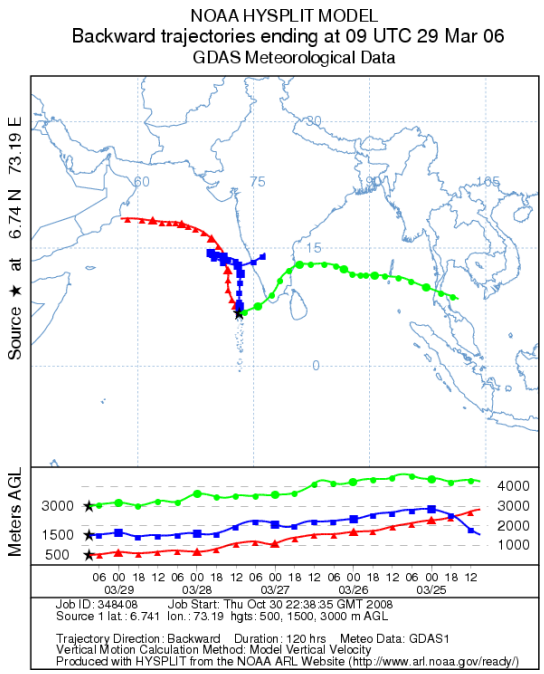

Figure 3.4: Five-day HYSPLIT back-trajectories at 500 m (red), 1500 m (blue), and 3000 m (green) levels at MCOH on 29 Mar, 2006.

Though in the infrared band some of the aerosols show complex wavelength dependence on absorption, the absorption pattern in shorter wavelengths, from near UV through visible to near infrared, is relatively simple. It decreases monotonically with increasing wavelength and approximately follows the power law. The Absorption Angström Exponent (AAE) is termed as the negative of the slope of the absorption on a log-log plot and approximately represents the wavelength dependence of aerosol absorption. As discussed by *Kirchstetter et al.* [2004] and *Bergstrom et al.* [2007], the absorption of black carbon is generally considered to vary weakly with wavelength, and the AAE of BC is typically around 1.0. Meanwhile brown carbon and mineral dust have strong absorption in the ultraviolet and blue spectral regions and largely reduced absorption toward longer wavelengths in the solar band, so they tend to have a larger

AAE (2 to 6). Thus, larger AAE indicates strong absorption in the UV band and the presence of brown carbon or mineral dust. Figure 3.5 shows the AAE estimated from absorption coefficients measured at three wavelengths (370, 520, and 880nm). AAE values are in the range of 0.8 to over 1.2 and larger AAE values are found in the elevated aerosol layer.

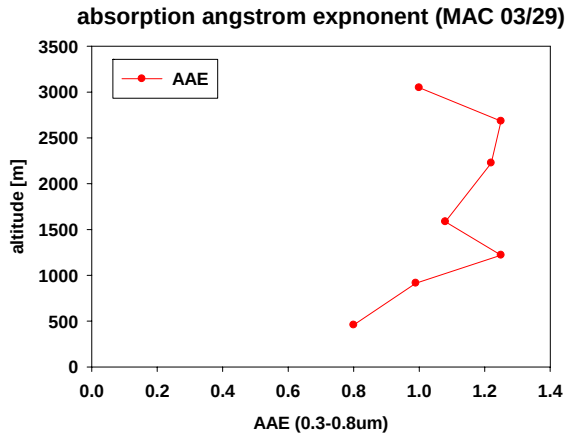

Figure 3.5: Vertical profile of absorption *Angström* Exponent (AAE).

3.3 Description of Mixing Model

The probable mixing state of atmospheric aerosols can be investigated by developing a simplified mixing model. As demonstrated in the schematic in Figure 3.6, the aerosol mixtures are composed of four types of particles, including three types of light-absorbing aerosols: black carbon (BC), brown carbon (BB), and mineral dust (DU). These particles can absorb nonnegligible amounts of solar flux and make great contributions to the atmospheric heating rate. Non-absorbing aerosol is also a significant component in the mixing model, which is made up of sulfate (SU), non-absorbing organics (OC), nitrate (NO_3), sea salt (SS), and water vapor (H_2O). Surface coating of non-absorbing materials is considered to be the main aging process for solid

BC, BB, and DU particles transported to the observatory. The condensation of sulfuric acid and organic gases forms the aqueous shell on the absorbing core, and not only modifies the optical and hygroscopic properties of these particles, but also alters their impacts on radiation and clouds. The collision of different solid particles is not considered in this mixing model though they are observed during the aging of atmospheric aerosols.

A series of look-up-tables (LUT) containing aerosol optical properties were developed to be used with the mixing model. Each LUT consists of the pre-calculated extinction, scattering, and absorption efficiency for each type of particle at individual size. All particles are assumed to be spherical. The optical properties of non-absorbing particles are estimated using Mie code. The relative contribution of each species (sulfate, nitrate, organic, sea salt) is allowed to vary from zero to unity and the average optical properties are recorded in the LUT. Sea salt aerosols are assumed to distribute from the surface to the top of MBL (~1.0 km) owing to the limitation of boundary layer mixing. Ambient RH is considered to account for the variations in the aerosol refractive index at different water vapor levels. Core-shell model [*Bohren and Huffman*, 1983] is applied to calculate the optical properties of coated BC, BB, and DU with a concentric shell of negligible absorption. The volume ratio of core/shell was allowed to vary from 0.1 (small core, thick shell) to 1.0 (bare core with no coating). The solid core is assumed to be located at the center of the shell. The effects of RH on the optical properties of coating material are taken into account as previously described.

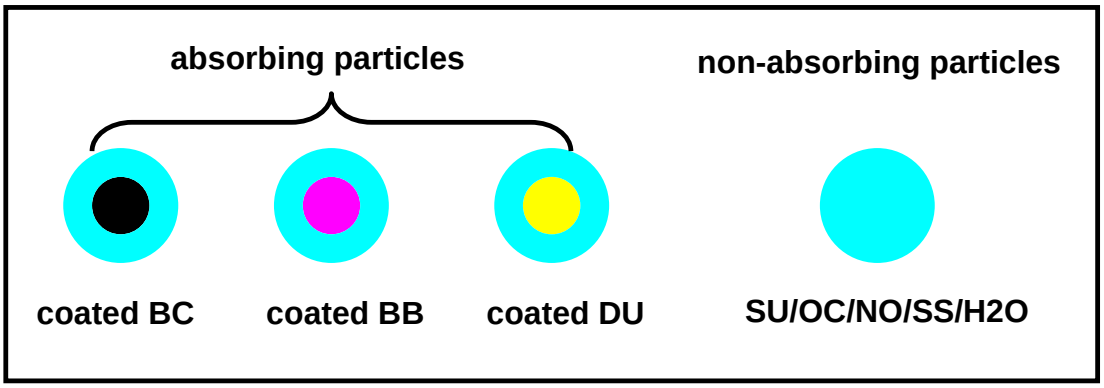

Figure 3.6: Schematic of mixing model, where BC is black carbon, BB is brown carbon, DU is dust, SU is sulfate, OC is non-absorbing organic carbon, NO is nitrate, SS is sea salt, H2O is water vapor.

OPC measurements provide an aerosol size distribution that can be used to calculate aerosol optical properties; however, it only covers particles with diameters greater than 0.3 μm. Information about the size of large amounts of particles smaller than 0.3 μm is missing. The so-called "effective size" (similar to the effective radius, but for the diameter) is used to represent the mean size of the aerosols in the range of 0.01-0.3 μm. The effective size is defined as $D_e = 2r_e$, where $r_e = \frac{\int r^3 n(r)dr}{\int r^2 n(r)dr}$ is the volume by surface area weighted mean radius of the aerosol particles for a given size distribution. The size distributions collected during INDOEX [*Bates et al.*, 2002] are employed to represent the size distribution for particles smaller than 0.3 μm. In consideration of different back-trajectories for marine boundary layer aerosols and aerosols lying above the MBL, the Arabian aerosols and Indian Subcontinent aerosols were chosen to calculate the effective size at 55% relative humidity for aerosols below and above MBL, respectively. Hygroscopic growth was also taken into account in

calculating the effective size for aerosols in the range of 0.01-0.3 μm at ambient relative humidity. Based on the study of *Maßling et al.* [2003], Growth factor (gf), termed as the ratio of ambient particle size to dry particle size, $gf(RH) = \frac{D_p(RH)}{D_p(dry, RH \le 5\%)}$, can be estimated using the empirical equation $gf(RH) = A(1-RH)^{\gamma}$, where A and γ are the fit parameters derived for the averaged growth factors of the more-hygroscopic particles fractions at 90%, 75%, 55%, and 30%, and RH is the relative humidity in the range of 0.0-1.0. *Maßling et al.* [2003] found that for the Northern hemisphere marine type particles, A is about 0.9756 and γ is -0.2831 for particles with an initial dry size of ~150nm. As shown in Figure 3.7, the effective size of fine mode aerosols follows the vertical pattern of ambient relative humidity. The long range transported aerosols above PBL were clearly distinguished and showed larger effective size than boundary layer aerosols.

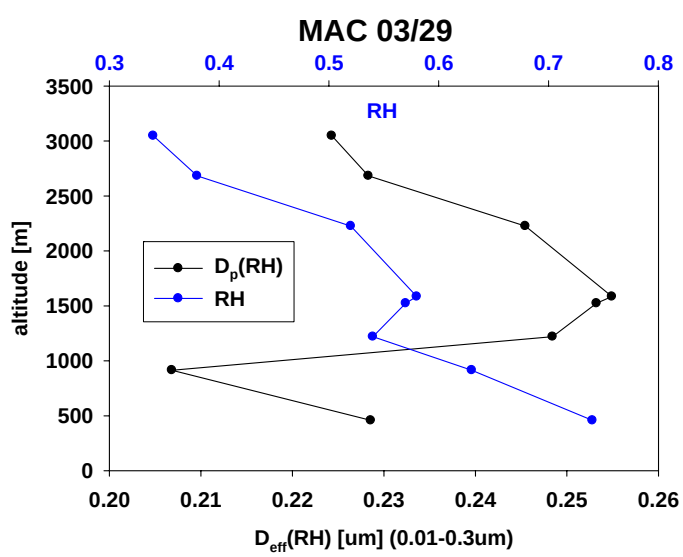

Figure 3.7: Vertical profile of ambient RH (blue line) and effective size (black line) for fine mode aerosols.

The optical efficiency of the pre-calculated LUT is employed by the mixing model to derive the scattering and absorption coefficients at different altitudes. For each type of particle the number fraction is allowed to vary from zero to one throughout the whole size distribution (0.01 to ~5.0 μm) using CPC measured total number concentration and OPC measured size distribution as constraints. The observed optical properties, such as the extinction coefficient at 550 nm, absorption coefficient at 880 nm, and AAE, are used as criteria. All simulated results with optical properties close to observations (±25% uncertainty) are regarded to be the probable mixing combinations. The absorption coefficient at 880 nm is chosen because the absorption at this band is dominated by BC, and the contribution by BB and DU is negligible. First, the number fraction and core/shell volume ratio for coated BC particles can be determined. Then, the coated BB and coated DU particles are considered in order to simulate the spectral dependence of absorption coefficients using AAE as validation. Finally, the non-absorbing particles are included to match the observed number concentration and extinction coefficient at 550 nm.

3.4 Results

3.4.1 Aerosol Number

The limited constraints of the mixing model result in numerous mixing combinations, and each has similar optical properties but a different particle number concentration and/or different core/shell volume ratio. Figure 3.8 is the probable vertical distribution of particle number fractions estimated by the mixing model. There are a wide range of mixing possibilities for each type of particles especially for DU

and non-absorbing particles. Carbonaceous aerosols presented relatively narrow possibilities. The number fraction of BC particles ranges from 2% up to a maximum of 36% and the range is quite narrow at altitudes above 2.5 km where absorption is relatively low. For BB particles, the range of number fraction is smaller within the MBL and larger within the layer from 1.5 to 2.5 km where high aerosol number concentrations and absorption coefficients were observed. Both BC and non-absorbing particles were indispensable throughout the observation layer from surface to about 3.0 km. For DU particles, the number fraction can range from zero to over 90%. DU particles were found be the required component in the aerosol mixtures at layers above 2.5 km. Although not shown in the figure, it should be noted that the volume ratio of core/shell for BC, BB, and DU varies for different mixing combinations with large number fractions usually corresponding to relatively small cores.

In order to narrow down the possibilities and find the likely mixing state, ground-based aerosol chemical measurements from MCOH are applied to the model results. The Aerosol Time-of-Flight Mass Spectrometer (ATOFMS) [*Prather et al*., 1994; *Gard et al.,* 1997; *Guazzotti et al.,* 2001] was operated at MCOH observatory during the ABC Post Monsoonal Experiment (APMEX). Although operated during a different season (from October 15 to November 5, 2004), APMEX captured the characteristics of aerosols with diameter from 0.5-2.5 μm in the Indian monsson transition period and provided further insights into aerosol chemical composition and mixing state [*Spencer et al.,* 2008]. Eight major particle types were observed during APMEX, which are fresh sea salt, aged sea salt, elemental carbon with sea salt (EC-

SS), elemental carbon with sulfate (EC-SU), fly ash, potassium-biomass, organic carbon, and calcium-dust.

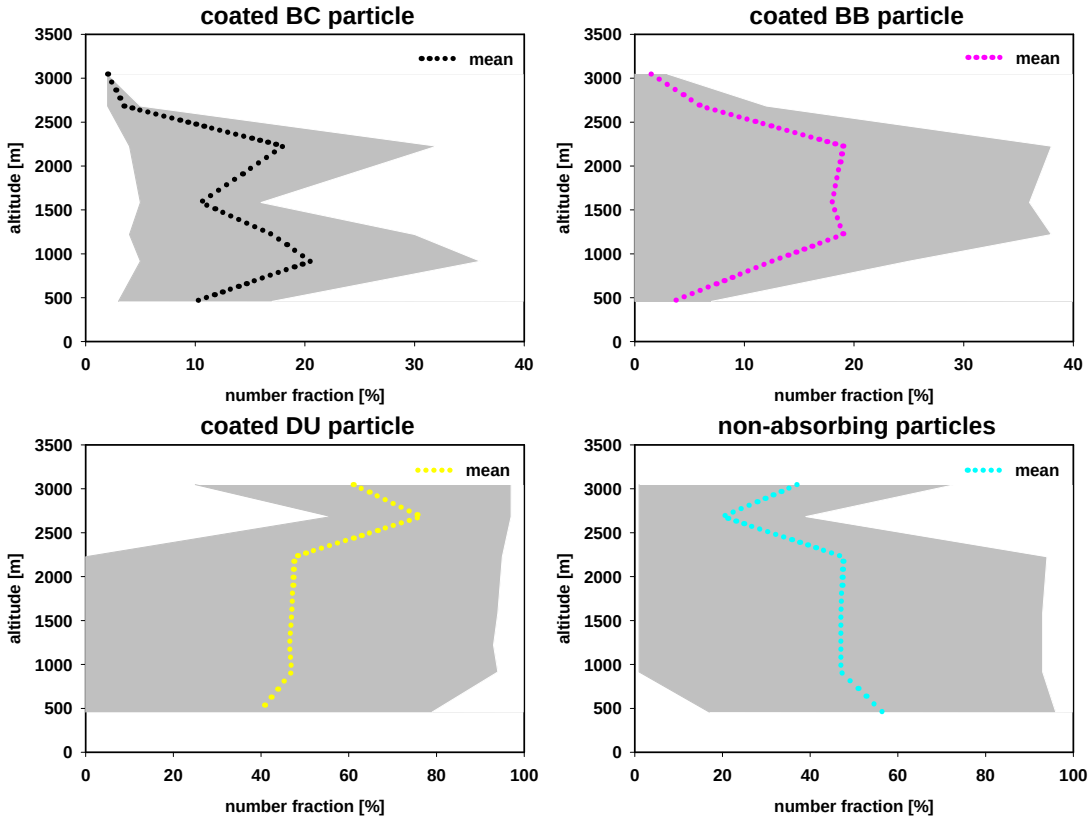

Figure 3.8: Number fraction (in percentage) of coated BC, coated BB, coated DU and non-absorbing particles estimated by mixing model. The range of likely values is indicated by gray shadow, and the mean value is highlighted by the dotted line.

To match the aerosol categories to the mixing model, particle types from APMEX are regrouped in the following way: elemental carbon associated particles (EC-SS and EC-SU) are classified as BC particles, potassium-biomass particles is referred to as BB, calcium-dust and fly ash are accounted as DU, and the sum of the rest of the particles (fresh sea salt, aged sea salt, OC) are used to represent the non-absorbing particles. Based on the back-trajectory analysis, APMEX aerosols are categorized into three groups: air mass from the Arabian Sea, air mass from India/the

Bay of Bengal (BOB), and air mass from the Indian Ocean. The average number fraction of APMEX aerosols with different sources is shown in Figure 3.9. Dust accounted for a large portion of aerosols originating from the Arabian Sea, while for aerosols from Indian/BOB the samples were dominated by carbonaceous particles. As for aerosols from the Indian Ocean, they were mainly composed of non-absorbing particles such as sea-salt.

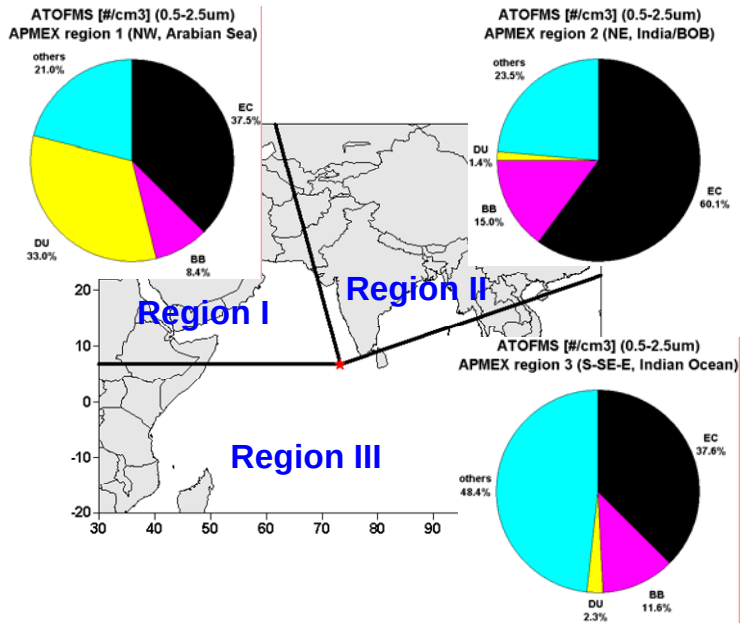

Figure 3.9: Average number fractions of aerosols as observed from ATOFMS during 15 Oct- 5 Nov, 2004 (data from Spencer et al., [2008]).

As discussed in the previous section, on March 29, during the MAC experiment, the air mass at 500 m over MCOH was from the Arabian Peninsula. Because of this, the average composition of Arabian Sea aerosols from APMEX can be applied to model simulations to find the likely mixing state of aerosols below MBL. For the air above MBL, back-trajectory analysis suggests that aerosols might originate from the Indian Subcontinent and BOB. The ATOFMS measurements during APMEX

show that Indian/BOB aerosols are primarily of carbonaceous particles, thus BC and BB are chosen as the main filter criteria for aerosols above MBL. Figure 3.10 shows the vertical distribution of aerosol number concentration and fractions for the likely mixing state. From the boundary layer to the elevated layer at around 1.0 to 2.5 km, the contribution of light-absorbing particles increases by a factor of more than two. The highest BC concentration is found at the level of maximum total particle number concentration. BB particles peaked at ~1.5 km where a high absorption coefficient was observed. Non-absorbing particles prevail over most of the vertical layers except at around 2.6 km where dust particles dominate and account for about 60% of the total particle number concentration. The different vertical pattern of BC, DU, and non-absorbing particles confirms that air masses at different levels have different sources.

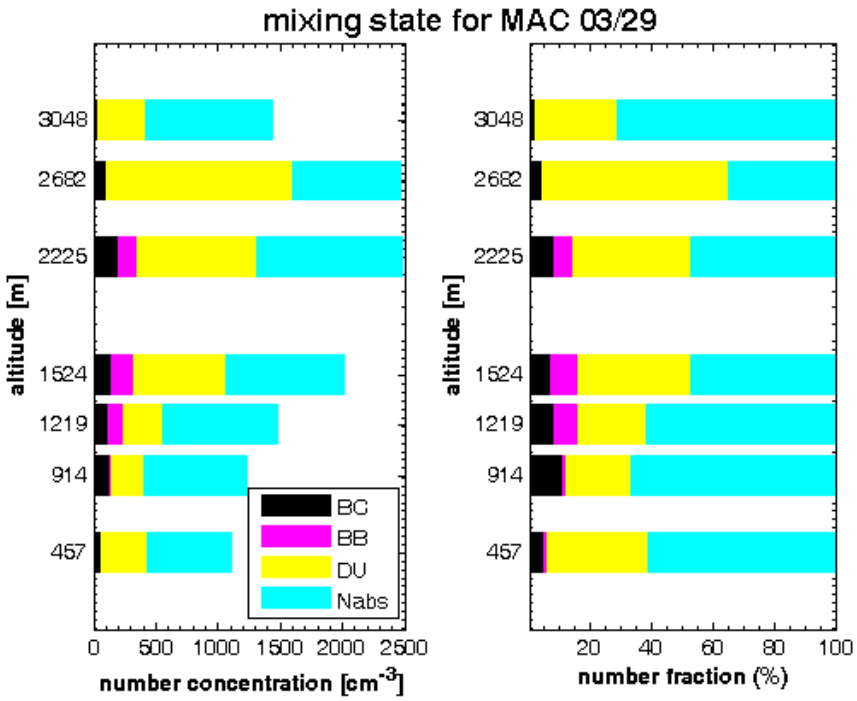

Figure 3.10: Vertical distribution of aerosol number concentration [cm^{-3}] and fractions [%] for likely mixing state of model results.

3.4.2 Aerosol Mass

Given the size distribution and number concentration of each type of particles and the volume ratio of core/shell for coated particles the mass of each aerosol species can be estimated with assumed mass density. The mass density of BC was reported in the range from ~1.0 to 2.0 gcm^{-3} depending on the combustion condition. In this study, median value 1.50 gcm^{-3} is used for BC. As for the BB, DU, and non-absorbing material, the mass densities used are 1.0, 2.5, and 1.8 gcm-3, respectively. The mass of coatings on the core of BC, BB, and DU are counted as part of the mass for non-absorbing materials. Figure 3.11 shows the vertical distribution of aerosol mass concentrations and fractions for fine particles (D_p<1.0 μm). The mass concentrations of fine aerosols peaks at ~2.0 km with a maximum mass concentration of about 45 μgcm^{-3}. Non-absorbing materials dominate the mass of fine aerosol and account for over 90% of the mass of aerosols below MBL. The contribution of mineral dust to the mass of aerosols increases with altitude and peaks at ~2.6 km. The total contribution of carbonaceous aerosols (BC+BB) to fine aerosol mass is less than 6% throughout the layer and the highest mass concentration of carbonaceous aerosols is about 2.0 μgcm^{-3} at the elevated layer around 1.5 km.

The column averaged mass contribution of each type of aerosol species to the total mass of fine aerosols (D_p<1.0 μm) is presented in Figure 3.12a. Overall, non-absorbing materials dominate and account for over 67% of total fine aerosol mass. The mass fraction of mineral dust ranks second highest at about 29%. Carbonaceous aerosols contribute about 4% of fine aerosol mass, with 2.6% by BC and 1.2% by BB.

To improve our understanding of the redistribution of non-absorbing materials and answer the question "How much non-absorbing materials condenses on the surface of light-absorbing particles?", the mass of non-absorbing materials contributed by the coating on BC, BB, DU particles, and even non-absorbing particles themselves is estimated in Figure 3.12b. In the column averaged conditions, about 20% of non-absorbing materials condense on the surface of mineral dust. The coatings on BC and BB account for about 4% and 3% of total non-absorbing mass, respectively. Overall, approximately 30% of non-absorbing materials condense on the surface of absorbing particles. This part of non-absorbing material actually enhances the absorption and plays a role as a heating agent.

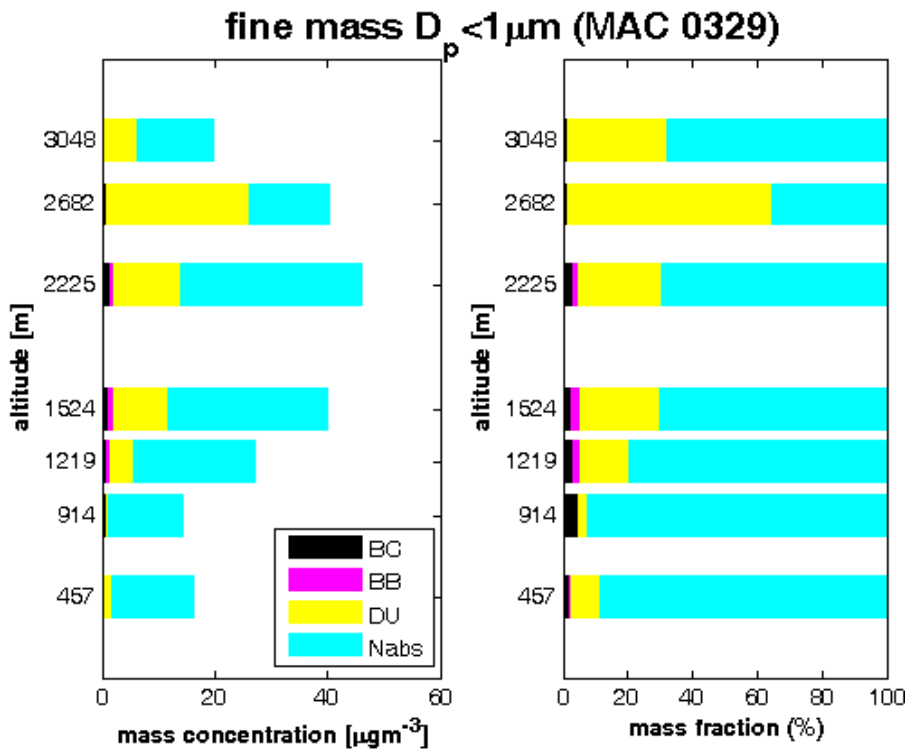

Figure 3.11: Vertical distribution of mass concentration [μgcm^{-3}] and fractions [%] for fine aerosol particles (Dp<1.0 μm).

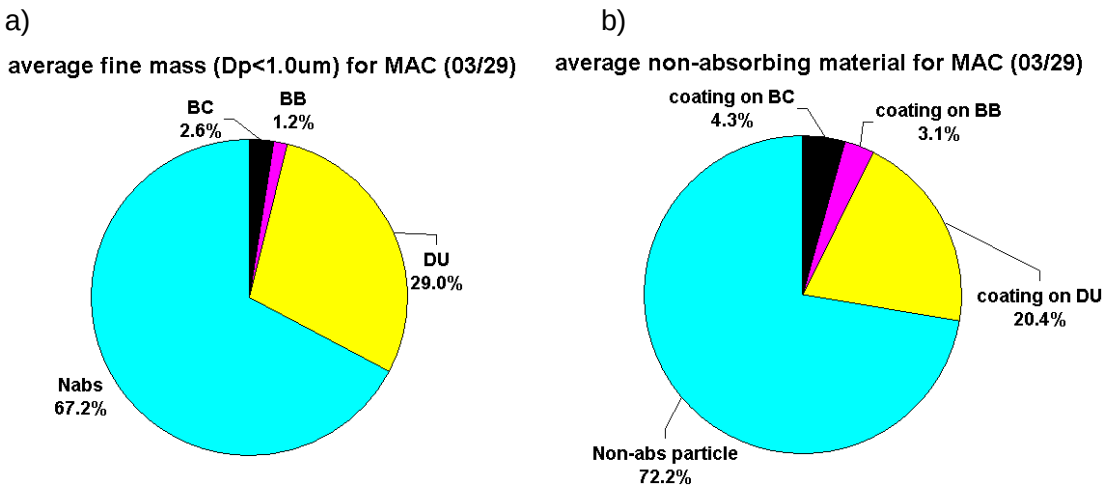

Figure 3.12: Column averaged a) contribution to total mass, and b) contribution to non-absorbing materials for fine particles (Dp<1.0 μm).

3.4.3 Optical Properties

Detailed information about aerosol optical properties is one of the key parameters for accurately estimating aerosol forcing. Figure 3.13 shows the spectrally-resolved vertical distribution of absorption coefficients for each type of particles. Though they make small contributions to mass, BC particles exert strong absorption when coated by non-absorbing materials. The absorption of coated BC particles extends from near the surface to about 3.0 km and the maximum absorption is at about 2.0 km. Coated BB particles show strong absorption in the layer above MBL, while the absorption of DU particles peaks at even higher altitudes, around 2.5 km. The absorption of BC presents relatively weak wavelength dependence in the broad spectrum from near ultraviolet to near IR. The absorption of BB and DU is confined in a narrow band from UV to about 550 nm and indicates a strong spectral variation.

Not demonstrated in figures, but also important for radiative transfer calculation, are the scattering and extinction coefficients. As opposed to absorption

dominated by BC particles, scattering and extinction were dominated by DU and non-absorbing particles. The ratio between scattering and extinction gives the value of aerosol single scattering albedo (SSA), which is often used as a parameter to describe how "dark" and absorbing the atmospheric aerosols are. Figure 3.14 indicates the spectral distribution of SSA as a function of height. Larger SSA is found below MBL, indicating the strong scattering properties of marine aerosols. From the top of MBL to about 2.5 km, SSA is smaller and presents great spectral variance.

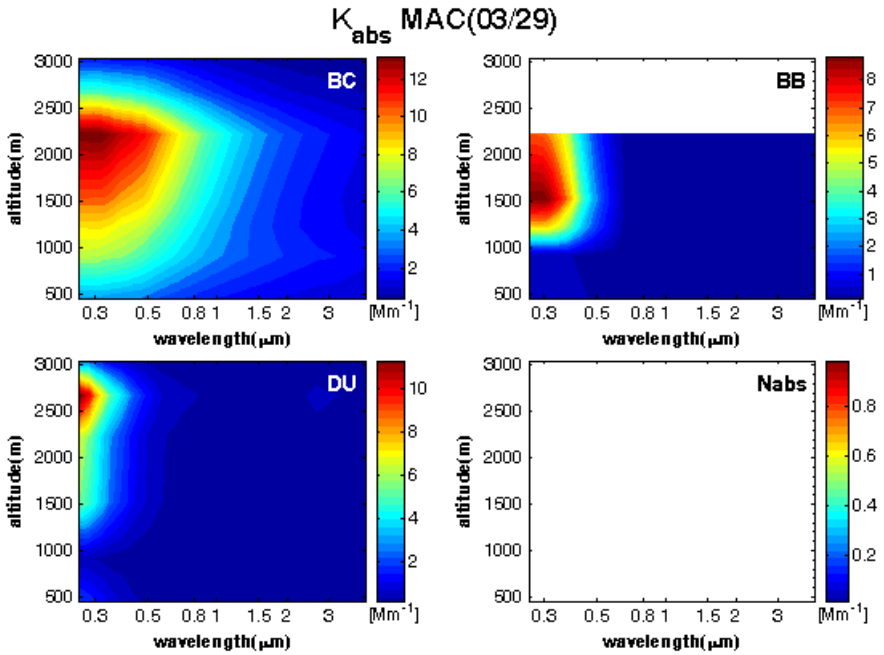

Figure 3.13: Vertical distribution of spectrally-resolved absorption coefficients for coated BC, BB, DU and non-absorbing particles.

Aerosol optical depth (AOD) can be estimated by integrating the extinction coefficient with height throughout the column. Model simulated AOD at 550 nm is 0.29, about 15% smaller than ground-based AERONET measurements, which gave 0.32 for the daily average column AOD. The contribution to AOD by each type of aerosol is estimated and shown in Figure 3.15. Non-absorbing particles account for

about 45% of the total AOD, followed by coated DU particles with 38% AOD fraction. The contribution of coated carbonaceous aerosols to AOD contrasts greatly with their low fraction in mass. Coated BC and BB particles account for 17% total AOD, about 12.5% for BC and 4.5% for BB particles. The coating of non-absorbing materials on the surface of BC and BB particles is the main reason for the amplification of optical depth of carbonaceous aerosols.

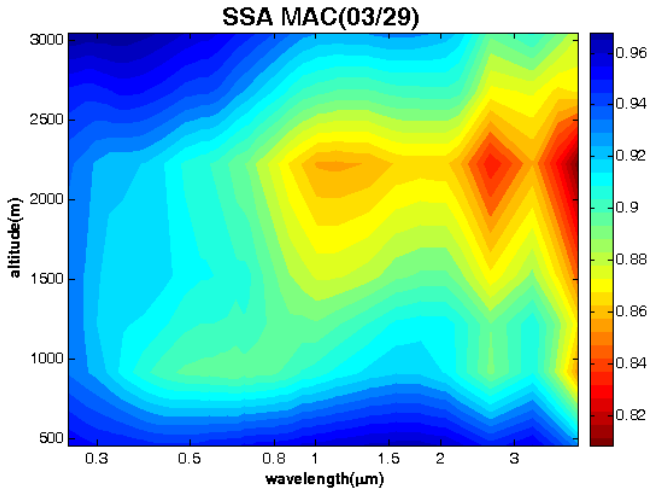

Figure 3.14: Vertical distribution of spectrally-resolved aerosol single scattering albedo (SSA) for total particles.

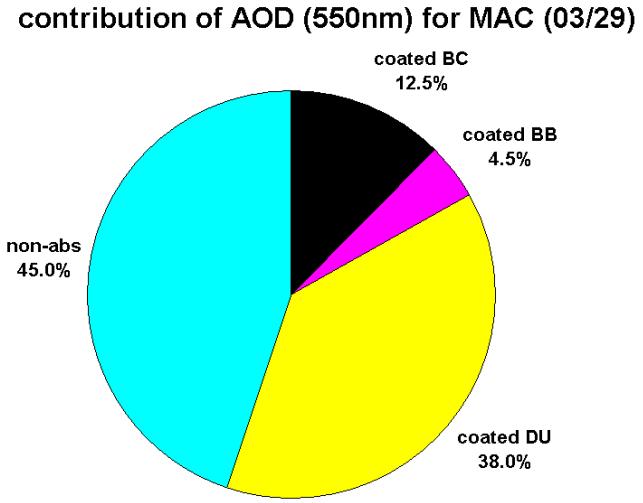

Figure 3.15: Contribution of aerosol optical depth at 550nm for MAC (03/29).

3.4.4 Radiative Forcing

Model simulated optical properties are applied to the Monte Carlo Aerosol-Cloud-Radiation (MACR) model to estimate the radiative impacts of atmospheric aerosols. MACR [*Podgorny and Ramanathan,* 2001; *Podgorny et al.*, 1998; *Satheesh et al.*, 1999; *Vogelmann et al.*, 2001] was developed by Center for Clouds, Chemistry and Climate (C^4), Scripps Institution of Oceanography during INDOEX [*Ramanathan et al.,* 2001a] and it computes the photon transport in any given media to estimate the radiative flux at each interface using the Maximum Cross-Section Method [*Marchuk et al.*, 1980]. In the current version, a total of 32 SW bands (from 0.25 to 5.0 μm) and 16 LW bands (from 3.0 to 1000.0 μm) are used for the solar and terrestrial radiation calculations, respectively. MACR can estmiate the scattering, absorbing, and emission of gases, clouds, and aerosols. To account for the gaseous absorption, the updated gas absorption data set HITRAN2000 [*Rothman et al.,* 2003] and CKD2.4 for the water vapor continuum [*Clough et al.,* 1989] are incorporated with the correlated-*k* distribution method [*Kato et al.,* 1999], which includes up to 20 correlated-*k* coefficients at each band. The absorption of radiation by water vapor, ozone, carbon dioxide, and oxygen are considered in both SW and LW portions [*Zhu et al.,* 2007]. Trace gases, such as CH_4, N_2O, and CO are also contained in the LW absorption calculation.

The term of aerosol forcing used in this study is referred to as the change of SW radiative fluxes caused by total aerosols or individual aerosol type, not the forcing by anthropogenic aerosols defined in the IPCC report. Radiative flux is calculated for

cases “with aerosol” and “without aerosol”, and the difference between them results in the aerosol forcing. Figure 3.16 shows the change of net (downward minus upward) solar flux caused by aerosol mixtures. Between 2.0 km and the surface, net solar flux is greatly decreased, especially in the visible spectrum, and the largest effect is found in the blue band. The weakening of net flux is mainly caused by reduction of downward flux, which is greatly diminished by absorbing particles. For the layer above 2.0 km, net solar flux increases with higher altitude. The absorption of the reflected solar radiation by carbonaceous aerosols decreases the upward flux and results in the convergence of net solar flux at ~3.0 km.

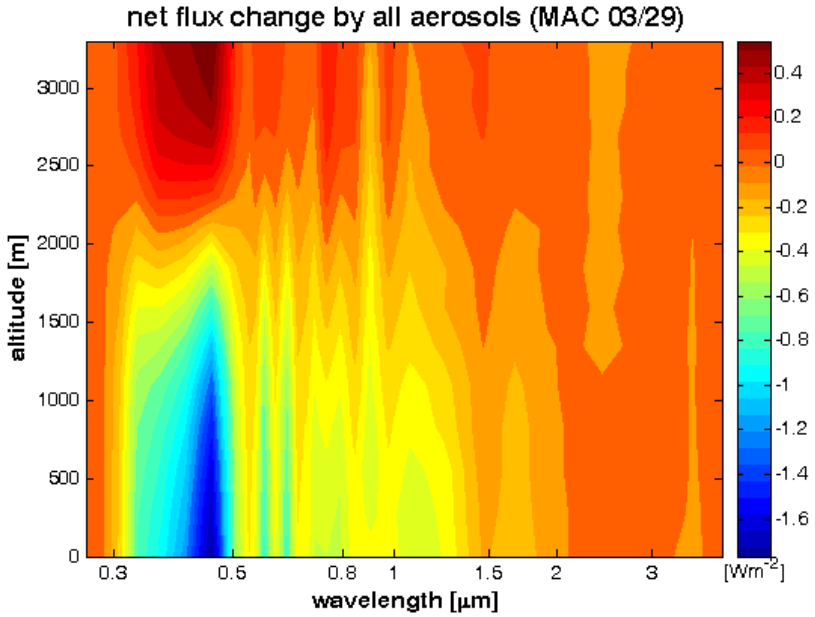

Figure 3.16: Vertical distribution of diurnal mean net flux change by aerosols.

Figure 3.17 demonstrates the diurnal mean radiative forcing by each type of particle and the total of all aerosols. At the top-of-the-atmosphere (TOA), carbonaceous aerosols exert positive forcing, thus increasing the solar flux received by

the earth-atmosphere system. In contrast, mineral dust and non-absorbing aerosols showed negative forcing and work to cool the planet. Although the negative forcing by dust and non-absorbing particles may offset the positive forcing induced by carbonaceous aerosols to some extent, the overall effect at TOA was positive and dominated by BC aerosols, which could cause as much as 7 Wm^{-2} excess flux to the entire earth-atmosphere system. The forcing at the Earth's surface showed more consistency and similarity. Through absorption and/or reflection, all types of aerosols reduced the downward solar flux reaching the surface and resulted in surface dimming. BC and dust both have strong effects on surface radiation budget and each of them cause about 5 Wm^{-2} deficit of solar flux at the surface. The total aerosol forcing at the surface is around -12 Wm^{-2}, which is about 3 times stronger than the forcing at TOA. The difference between TOA forcing and surface forcing leads to the flux change in the atmosphere. A positive value implies a flux convergence in the air, that is, the atmosphere gains excess energy and warms.

Each absorbing agent's contribution to atmospheric heating rate (0.5-3.0 km) is demonstrated in Figure 3.18. Much heating is caused by gases such as ozone, water vapor and oxygen; however aerosol heating is nonnegligible accounting for about one third of total heating. In the 0.5 to 3.0 km layer, BC presents over 26% of atmospheric heating, followed by BB and DU, which contribute 3.9% and 2.5%, respectively. The large contribution of carbonaceous aerosols to atmospheric heating rate can greatly enhance the warming trend caused by greenhouse gases and exert severe impacts on regional climate.

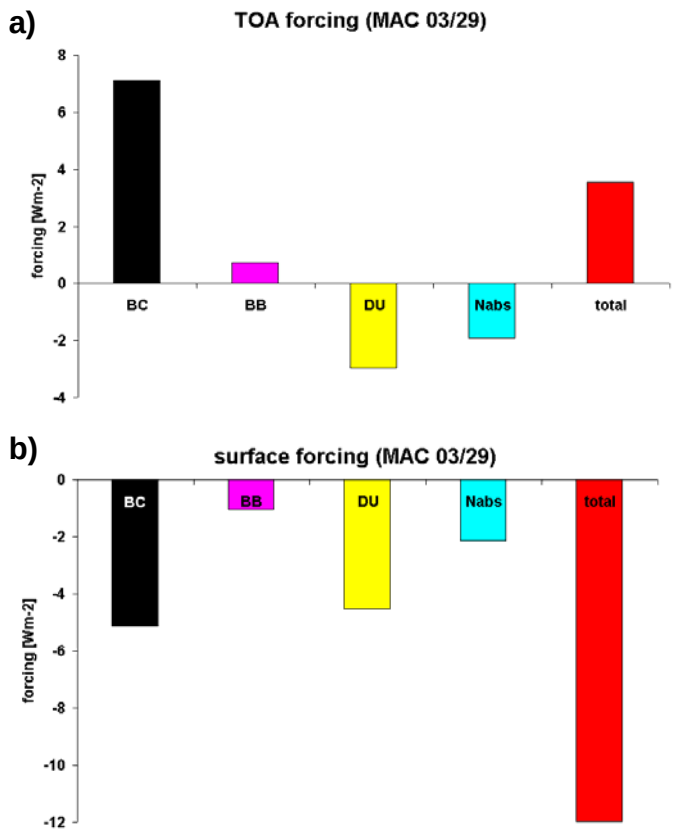

Figure 3.17: Diurnal mean radiative forcing at a) TOA, and b) surface.

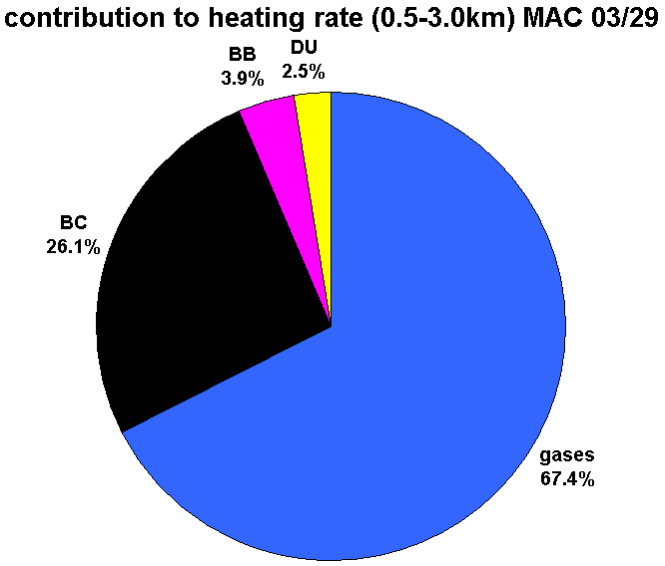

Figure 3.18: Contribution of diurnal mean atmospheric heating rate in the layer between 0.5 and 3.0km.

Figure 3.19 demonstrates the vertical distribution of diurnal mean atmospheric heating rate change caused by atmospheric aerosols. As high as 0.8 $Kday^{-1}$ of excess heating is built up in the air where light-absorbing aerosols are located (Figure 3.19a). Aerosol induced heating rate change is dominated by BC, which alone could increase heating rate by 0.6 $Kday^{-1}$ at ~2.0 km. The spectrally-resolved heating rate change (Figure 3.19b) indicates that aerosol heating is strongly dependent on wavelength. Aerosol induced heating rate is mainly confined to the visible band with the largest heating occurring the blue band.

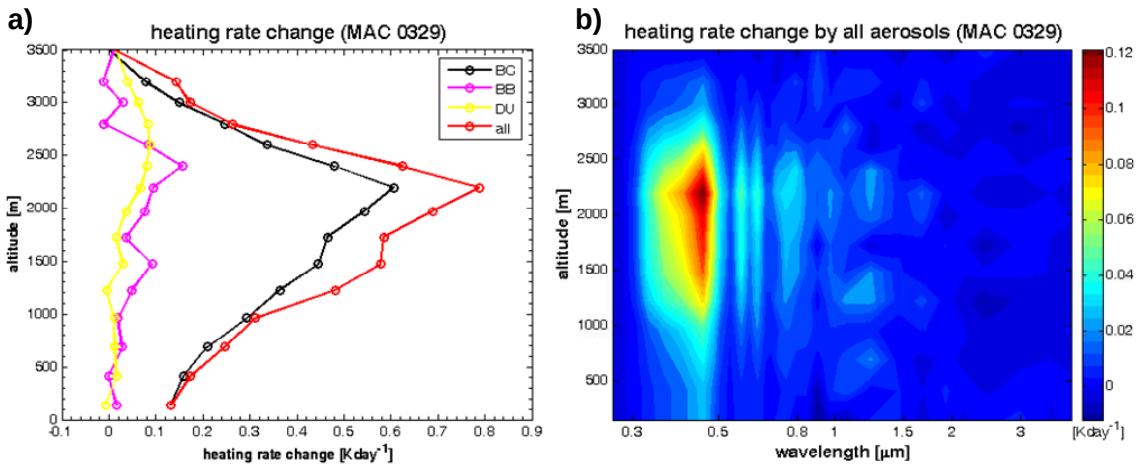

Figure 3.19: Vertical distribution of diurnal mean atmospheric heating rate by atmospheric aerosols for a) broadband (0.25-5.0 μm), and b) spectrally-resolved.

3.5 Validation of Mixing Model

Field observations from MAC and previous studies such as APMEX and INDOEX are employed to validate the mixing model. The total aerosol number concentration measured by CPC and the size-resolved number concentration observed by OPC are used in the model and the comparisons with model results are shown in

Figure 3.20 and 3.21, respectively. Modeled aerosol number concentration and size distribution lie in the center of observed data and closely agree with measurements. The potential mixing state can be modeled using the aerosol absorption coefficient measured by the Aethalometer. A comparison of absorption coefficients at 370, 520, and 880 nm is shown in Figure 3.22 (a-c). Model simulations accurately capture the vertical pattern of absorption coefficients at all three wavelengths and the difference between modeled results and observations is less than 25%. The Absorption Angström Exponent indicates the spectral variation of aerosol absorption. Modeled AAE value is within 25% uncertainty of the value derived from measured absorption coefficients (Figure 3.22d).

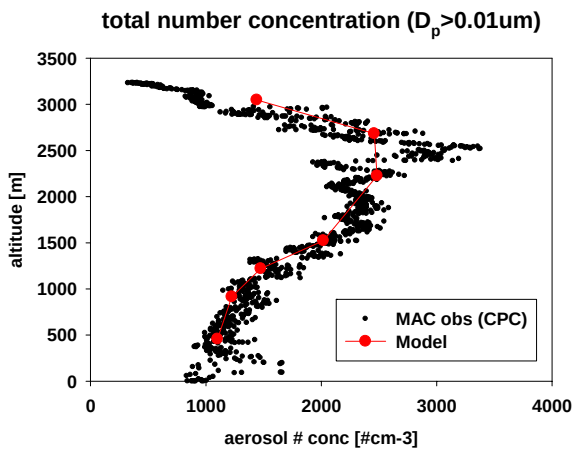

Figure 3.20: Comparison of total aerosol number concentration (Dp>10 nm).

Good agreement between model simulations and observation-based data is also found in extinction coefficients at 550 nm. The observed profile of extinction coefficients is indirectly derived from the vertical distribution of aerosol number concentration and AOD. It can be seen in Figure 3.23 that model simulations slightly underestimate extinction coefficients for the layer at 1.5 km. Overall, the uncertainty

of modeled extinction coefficients was within 25% throughout the layers from ~0.5 to 3.0 km.

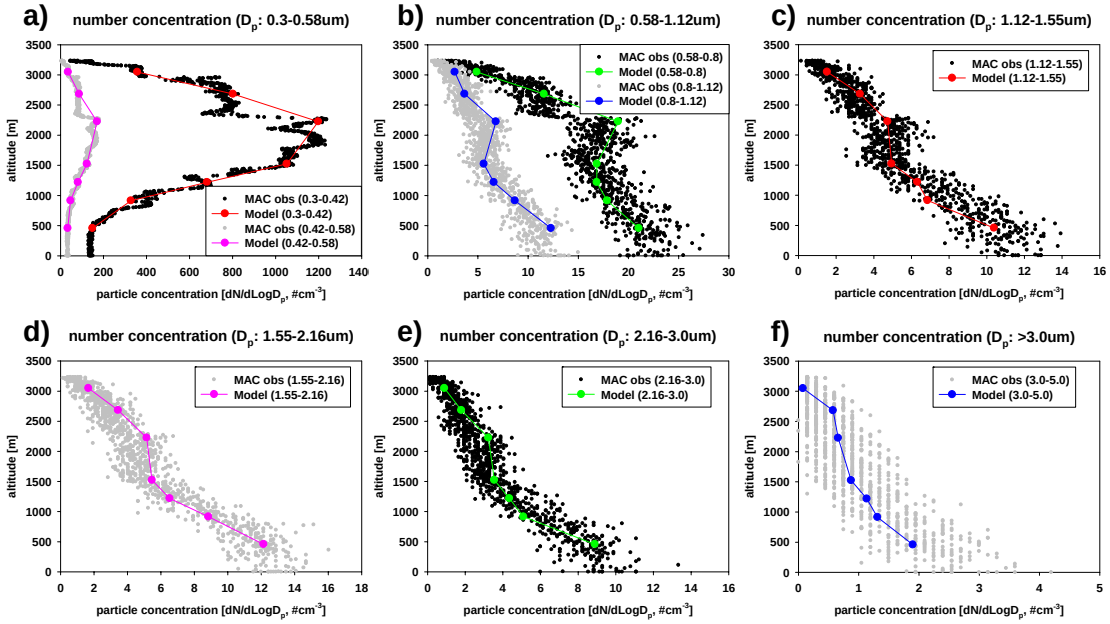

Figure 3.21: Comparison of aerosol number concentration at a)0.3-0.58 µm, b)0.58-1.12 µm, c)1.12-1.55 µm, d)1.55-2.16 µm, e)2.16-3.0 µm, and f)>3.0 µm.

Aerosol single scattering albedo is also used to validate model results. The vertical profile of SSA at 550nm is derived from MAC observed absorption and extinction coefficients. K_{abs} at 550 nm is obtained from K_{abs} measured at 370, 520, and 880 nm, assuming the power-law relationship between absorption and wavelength applies. Ground-based AERONET measurement also provides SSA value for column averaged conditions. AERONET estimated SSA is about 0.89 at 550nm on March 29. Figure 3.24 demonstrates that modeled SSA is smaller than the indirectly derived SSA from MAC observation, but larger than the column mean value suggested by

AERONET. Aerosols in the elevated layer from the top of MBL to about 2.5 km have smaller SSAs than the boundary layer aerosols and overlying particles.

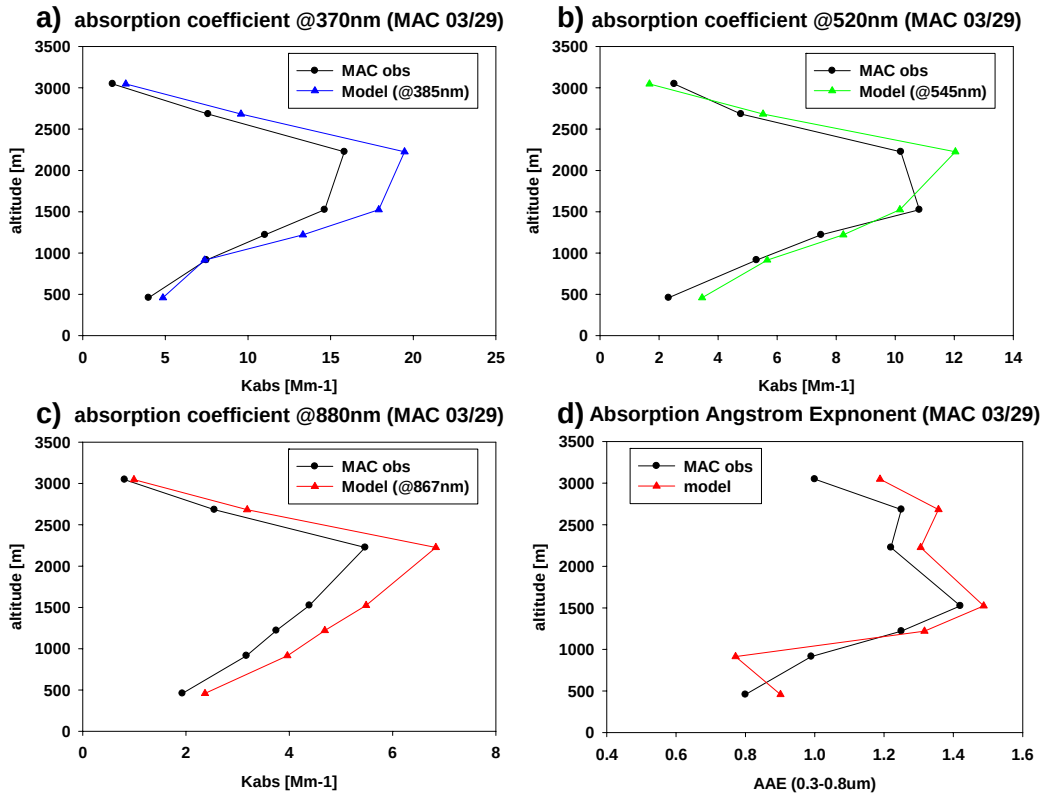

Figure 3.22: Comparison of absorption coefficient at a)370 nm, b)520 nm, c)880 nm, and d) absorption Angström exponent.

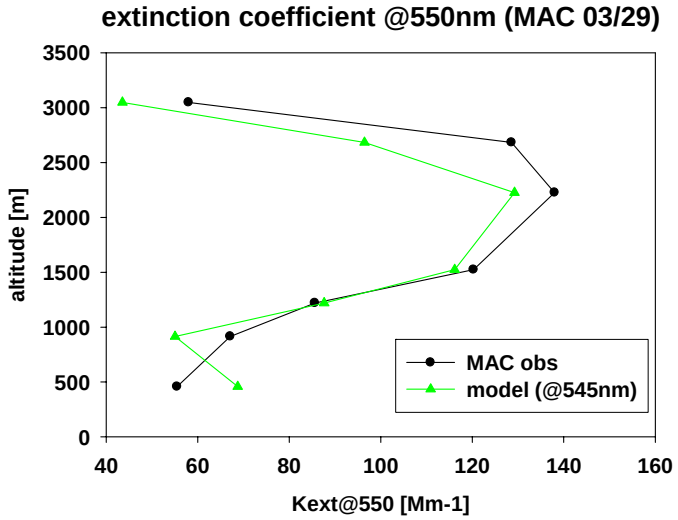

Figure 3.23: Comparison of extinction coefficient at 550 nm.

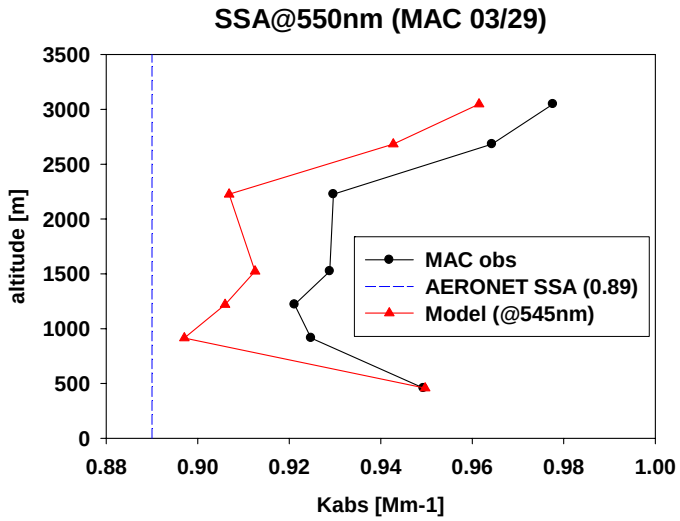

Figure 3.24: Comparison of single scattering albedo at 550 nm.

Another optical parameter used for model validation is each type of aerosol particle's AOD (550 nm) contribution. *Ramanathan et al.* [2001] presented the relative contributions of various chemical species to AOD over the tropical Indian Ocean during INDOEX. Some assumptions have been made for INDOEX results to make them consistent with model categories of this study. K^+ from INDOEX is regarded as BB in the mixing model because potassium is usually the indicator of biomass burning aerosols. Fly ash is ascribed to dust particles. The rest of the components such as OC, NH^{4+}, SO_4^{2-}, sea-salt, NO^{3-}, and MISS (minor inorganic species) are attributed to the non-absorbing particles category. Table 3.2 lists the difference between the MAC model results and the INDOEX findings for contributions to AOD by BC, BB, DU, and non-absorbing aerosols. The contribution by BC to column AOD is about 11% and 12.5% for INDOEX and MAC, respectively. The contributions of BB and DU to AOD during MAC are twice as larger as INDOEX, while the percentage of non-absorbing particles from MAC is much smaller than that in INDOEX.

Table 3.2: Comparison of contribution to AOD (550 nm). For INDOEX, BB refers to K^+, DU is the sum of dust and fly ash, and Nabs is the sum of OC, $NH4^+$, SO_4^{2-}, sea-salt, NO_3^-, and MISS (minor inorganic species).

AOD contribution (%)	BC	BB	DU	Nabs
MAC	12.5	4.5	38.0	45.0
INDOEX	11.0	2.0	19.0	68.0

Model simulated aerosol chemical composition can be compared with field observations. Average chemical composition was obtained from ATOFMS measurements during APMEX and is shown in Figure 3.9 for three different air masses. ATOFMS detected high contributions of BC and BB particles, with the number fraction ranging from 37 to 60% for BC and from around 8 to 15% for BB. DU and non-absorbing particles from APMEX are about 1-33% and 21-48% for DU and Nabs, respectively. In contrast to that, model results from MAC indicate relatively low occurrences of BC (5%) and BB (1%) and high occurrences of non-absorbing particles (61%) near the surface. At around 450m, the modeled DU percentage is constrained by APMEX measured Arabian Sea aerosols and it is within the upper limit of the dust percentage from APMEX (33%).

The chemical composition in terms of aerosol mass from ground-based filter samples at the MCOH and INDOEX studies is also used for model validation. Atmospheric particulate matter was sampled on quartz fiber filters and Teflon filters at MCOH for over two years between 2004 and 2007 [*Stone et al.,* 2007]. Fine aerosol particles were collected daily using a medium-volume PM2.5 sampler. Inorganic and water-soluble ions (chloride, nitrate, sulfate, sodium, potassium, calcium, and ammonium) were identified by ion chromatography techniques, while elemental

carbon and organic carbon were analyzed using a thermal optical method. The chemical composition of fine aerosols during Feb-Mar-Apr over MCOH is characterized here in order to validate MAC model results. The sum of Cl^-, NO^{3-}, SO_4^{2-}, Na^+, NH_4^+, Ca^{2+}, and OM (approximately double the mass of OC) is used as the surrogate for non-absorbing aerosols. Potassium is used to trace brown carbon. The remaining mass after subtracting the EC, K^+, and the non-absorbing materials from total PM2.5 is ascribed to dust. Aerosol mass concentration for particles with diameter smaller than 1.0 μm from INDOEX [*Ramanathan et al.,* 2001] is also employed to validate model results.

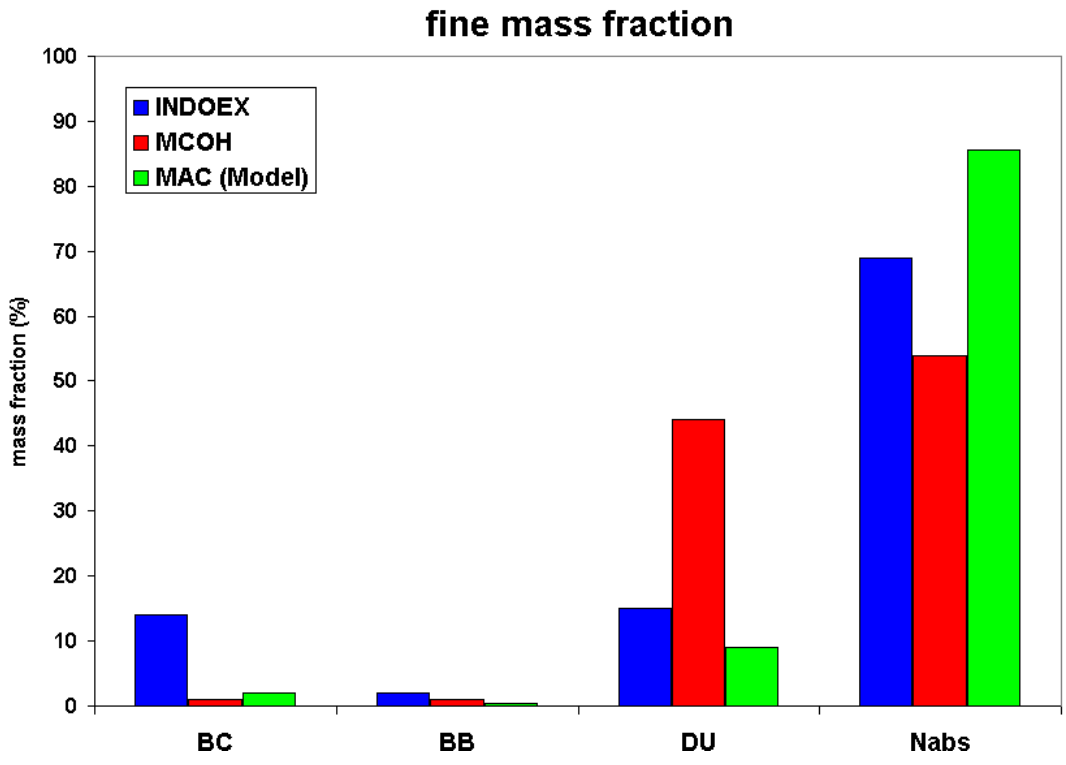

Figure 3.25: Comparison of mass contribution for fine aerosols (Dp<1.0 μm). For INDOEX, BB refers to K^+, DU is the sum of dust and fly ash, and Nabs is the sum of OC, NH_4^+, SO_4^{2-}, sea-salt, NO_3^-, and MISS (minor inorganic species). Data for MCOH is the average of Feb-Mar-Apr for 2005 and 2006, and BC refers to EC, BB refers to K^+, Nabs is the sum of Cl^-, NO_3^-, SO_4^{2-}, Na^+, NH_4^+, Ca^{2+}, and organic matter (2*OC).

Figure 3.25 shows that INDOEX, MCOH, and the MAC model estimate all suggest the dominance of non-absorbing materials in the mass of fine aerosols near the surface over the North Indian Ocean. Model results from MAC predicted non-absorbing particles to be about 85% of fine aerosol mass and ranked the highest among three, while the minimum percentage is about 55%, estimated from filter measurements of PM2.5 particles at the MCOH observatory. There is a large discrepancy of BC and mineral dust. INDOEX estimates a BC mass fraction of over 10% and MCOH and the MAC model suggest that BC mass is within 2% of total fine aerosol mass over the South Indian Ocean. MOCH filter measurements detected the largest fraction of dust and suggest that over 40% of fine aerosol mass might come from particles consisting of elements such as H, O, Al, Mg, Fe, Li, Si, Ti, Pb, Mn etc. Both INDOEX and the MAC model predict similar dust fractions, 15% and ~10% respectively, in the mixing model for boundary layer aerosols. The contribution of BB to fine aerosol mass is less than 2% for both observations and the MAC model.

Table 3.3: Comparison of measured and model calculated atmospheric absorption between different altitude levels on 29 March.

Altitude km]	3.05-1.52	2.59-1.20	2.13-0.94	1.52-0.46	0.5-3.0
SZA[degree]	28-17	15-8	5-3	7-16	Daily mean
Observation	84.22±5.11	77.34±5.84	64.36±2.83	44.73±3.30	41.5±3.3
Model	75.02	74.50	65.05	56.54	42.2

Finally, broadband radiative flux measured by a Pyranometer onboard the UAVs is used to compare model simulations. Observed atmospheric absorption is obtained from the difference in net fluxes (incoming flux minus outgoing flux)

measured at two different levels. Table 3.3 shows the comparison of observed and modeled atmospheric absorption at different layers. The observed fluxes are normalized to the cosine of mean solar zenith angle. The difference between model results and measured atmospheric absorption show some dependence on solar zenith angle and the vertical location. For the elevated layer (1.5-3.0 km), the model underestimates absorption by about 10%. By contrast, in the lower atmosphere (from 0.5 to 1.5 km), the model overestimates absorption by as much as 25%. The model agrees well with measurements there is a small solar zenith angle, i.e., the sun is overhead. The model shows good agreement on the diurnal mean absorption for the layer between 0.5 and 3.0 km. The observed and model simulated absorption are ~41.5 and 42.4 Wm^{-2}, respectively, and the difference between model and measurement was less than 2%. Overall, the mixing model did a good performance in finding the likely mixing state of aerosols over the North Indian Ocean. Model results are consistent with field observations in terms of aerosol chemical composition, optical properties and radiative effect. The comparison confirms the ability of the aerosol mixing model and its potential application for aerosols in other regions.

3.6 Discussion

To understand the effect of coating on aerosol optical properties and radiative forcing, a “no-coating external mixing” scenario can be performed. In this scenario, particles are externally mixed with each other and there is no interaction between non-absorbing and absorbing particles, that is, BC, BB, and DU are present as the bare particles with no coating of sulfuric acid or organic gases on their surfaces. The

"internal core-shell mixing" scenario says that the mass of non-absorbing materials condensed on the surface of BC, BB, and DU particles is evenly spread over the existing non-absorbing particles so that the mass and number concentrations of each type of particle is conserved and the size distribution is fixed. The optical properties for the "no coating" aerosols are calculated and compared to those aerosols with coating. Compared to the "with coating" scenario, the contribution of absorbing particles to AOD decreased from 12.5% to 9.1% for BC, from 4.5% to 2.3% for BB, from 38% to 21% for DU if they were not coated by non-absorbing materials. Conversely, the contribution of non-absorbing particles to AOD increased from 45% for the "with coating" case to ~68% for the "no coating" case.

Aerosol induced radiative forcing in the "no coating" scenario is compared to the "with coating" case in Figure 3.26. When absorbing particles become more intensely coated with non-absorbing materials the radiative forcing of BC, BB and DU at both the TOA and the surface amplifies the effect of absorbing particles on atmospheric absorption. Diurnal mean surface forcing is enhanced from about -9.5 Wm^{-2} for the "no coating" case to -12.0 Wm^{-2} for the "coated" case. Aerosol forcing at TOA for coated mixing is over 20% greater than no coating conditions. The largest enhancement of radiative forcing is from dust aerosols, and their TOA and surface forcing is amplified by factors of over 7 and 3, respectively, compared to the "no coating" conditions. The overall effects of coating on aerosol forcing are dominated by absorbing particles. They increase total forcing by about 20% at the TOA and 25% at the surface. Coating leads to an increase in TOA forcing and a decrease in surface

forcing, which results in net energy gain and excess heating in the atmosphere. The diurnal mean column absorption by atmospheric aerosols increased over 24% when BC, BB, and DU particles are coated by non-absorbing materials. Compared to "bare aerosols" without coating, coated aerosols trap about 2.4 Wm^{-2} extra solar fluxes in the 0.5 to 3.0 km layer. This corresponds to about 0.08 $Kday^{-1}$ of additional heating to the air. The vertical distribution of this additional heating is caused by the coating process and is highlighted in Figure 3.27. The aerosol induced heating rate is greatly increased form near surface to ~ 3.0 km when light-absorbing particles are covered by non-absorbing materials. The maximum heating rate increase is as large as 0.17 $Kday^{-1}$ and located at ~2.0 km where carbonaceous aerosols are present in high concentrations.

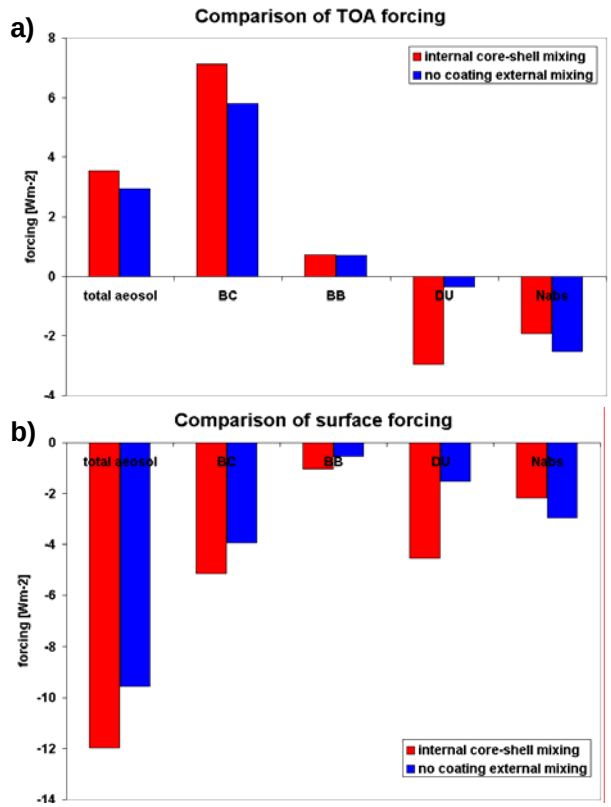

Figure 3.26: Comparison of diurnal mean radiative forcing at a) TOA, and b) surface for "with coating" and "no coating" scenarios.

The comparison of the mixing model with the "no coating" scenario suggests that a coating of non-absorbing materials on absorbing particles has a large effect on aerosol forcing and heating rates. Extensive observations and further studies are needed to advance our understanding of aerosol particles' impacts on the climate.

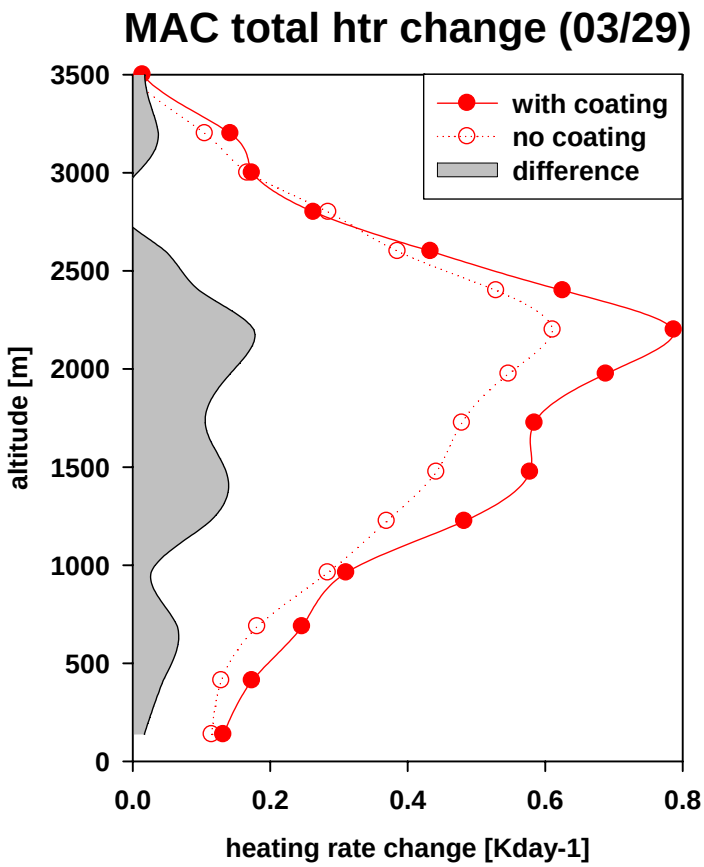

Figure 3.27: Comparison of diurnal mean aerosol heating rate for "with coating" (solid line) and "no coating" (dotted line) scenarios. The gray shadow indicates the excess heating caused by coating.

Some uncertainties of model results related to aerosol size distribution should be noted. OPC only provides aerosol size distribution for particles with diameter larger than 0.3 μm, thus detailed information about the size distribution for aerosols smaller than 0.3 μm is unknown. In this study, the effective size is used to represent the mean

size of fine aerosols for particle size from 0.01 μm to 0.3 μm. The overall size distribution that is used to calculate aerosol optical properties is shown in Figure 3.28. Using one effective size to represent all fine particles smaller than 0.3 μm will unavoidably bring errors to the model simulations.

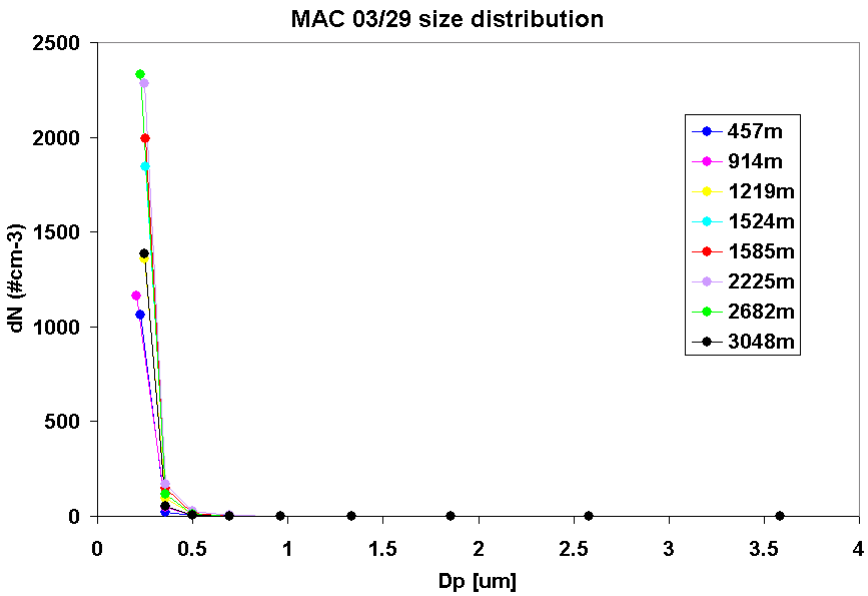

Figure 3.28: Aerosol size distribution used in model simulation.

In addition to the uncertainty caused by the effective size, using one size distribution based on OPC measurement to all aerosol species will lead to further uncertainty because BC is normally in the submicron size and dust usually dominates the coarse particles. However, MAC experiment did not have measurements that can provide the size distribution for individual aerosol component. Although previous studies showed the typical size distribution of BC, dust and biomass burning aerosols, to merge them into one size distribution that can match OPC measurements and fit MAC experiment needs further constraints. In order to emphasize the major concern of this study, that is to evaluate the effect of aerosol mixing state, especially the

influence of coating on coating on absorbing particles, certain simplification and assumption have been made and more sensitivity studies are need to estimate the uncertainty related to aerosol size in the future.

3.7 Conclusion

A core-shell mixing model was designed to understand the mixing state and radiative impacts of aerosols in the atmospheric brown clouds over the North Indian Ocean during the transition period associated with South Asian monsoons. The condensation and the adsorption of sulfuric acid and organic gases on the surface of light-absorbing particles such as black carbon, brown carbon, and mineral dust are assumed to be the main aging process during their atmospheric transport. The optical properties of these particles experience large modification after they become coated with sulfates, organics, nitrate, salt, and water. Both scattering and absorption coefficients of light-absorbing aerosols were greatly enhanced when they were coated by non-absorbing materials. Compared to the external mixing case, the contribution to AOD by coated aerosols went from 9.1% to 12.5% for BC, from 2.3% to 4.5% for brown carbon, and from 21% to 38% for dust. Coatings of non-absorbing materials on light-absorbing particles also lead to stronger radiative forcing and greater atmospheric heating. The diurnal mean aerosol forcing was enhanced over 25% at the surface, over 20% at TOA, and over 20% in the atmosphere when the core-shell mixing assumption was made. For the layer from 0.5 to 3.0 km where most aerosols are distributed, coatings of non-absorbing materials on BC, BB, and dust lead to an

additional 2.4 Wm^{-2} solar fluxes trapped in the air, which corresponded to 0.08 $Kday^{-1}$ of extra heating in the lower atmosphere.

The mixing state of light-absorbing aerosols plays an important role in observed surface dimming and atmospheric solar heating. Both laboratory studies and filed observations indicate that external mixing might only be applicable for the freshly emitted particles close to their sources. Particles with a lifetime of over 3 days are mostly aged and already mixed with other aerosols. SO_2 and/or organic gases readily condense and adsorb on the surface of a solid particle and further oxidize in the ambient atmosphere, changing to SO_4^{2-} and/or organic compounds. The acquisition of an aqueous coating can considerably alter the optical properties and hygroscopicity of light-absorbing particles. Furthermore, the aged particles provide favorable sites for SO_2 oxidation in aerosol water or in cloud droplets and can become CCN or be scavenged from the atmosphere. Hence, the conventional external mixing assumption used in most climate models might cause some uncertainties in estimating both direct and indirect forcing by aerosols.

Acknowledgments

The ATOFMS data come from Prof. Prather's research group. The authors thank Dr. Matthew Spencer for his help in ATOFMS data.

References

Adachi, K. and P. R. Buseck (2008), Internally mixed soot, sulfates, and organic matter in aerosol particles from Mexico City, *Atmos Chem Phys*, 8, 6469-6481.

Andreae, M. O., and A. Gelencser (2006), Black carbon or brown carbon? The nature of light-absorbing carbonaceous aerosols, *Atmos Chem Phys*, 6, 3131-3148.

Bates, T. S., D. J. Coffman, D. S. Covert, and P. K. Quinn (2002), Regional marine boundary layer aerosol size distributions in the Indian, Atlantic, and Pacific Oceans: A comparison of INDOEX measurements with ACE-1, ACE-2, and Aerosols99, *J. Geophys. Res.*, 107(D19), 8026, doi:10.1029/2001JD001174.

Bergstrom, R. W., P. Pilewskie, P. B. Russell, J. Redemann, T. C. Bond, P. K. Quinn, and B. Sierau (2007), Spectral absorption properties of atmospheric aerosols, *Atmos Chem Phys*, 7, 5937-5943.

Bohren, C. F., and D. R. Huffman (1983), Absorption and Scattering of Light by Small Particles, John Wiley, Hoboken, N. J.

Bond, T. C., G. Habib, and R. W. Bergstrom (2006), Limitations in the enhancement of visible light absorption due to mixing state, *J. Geophys. Res.*, 111, D20211, doi:10.1029/2006JD007315.

Chandra, S., S. K. Satheesh, and J. Srinivasan (2004), Can the state of mixing of black carbon aerosols explain the mystery of 'excess' atmospheric absorption?, *Geophys. Res. Lett.*, *31*, L19109, doi:10.1029/2004GL020662.

Clough, S. A., F. X. Kneizys, and R. W. Davies (1989), Line shape and the water vapor continuum, *Atmos. Res., 23,* 229– 241.

Corrigan, C. E., G. C. Roberts, M. V. Ramana, D. Kim, and V. Ramanathan (2008), Capturing vertical profiles of aerosols and black carbon over the Indian Ocean using autonomous unmanned aerial vehicles, *Atmos Chem Phys*, 8, 737-747.

Draxler, R. R., and G. D. Hess (1998), An overview of the HYSPLIT-4 modeling system for trajectories, dispersion, and deposition, *Aust. Meteorol. Mag.,* 47, 295– 308.

Flanner, M. G., C. S. Zender, J. T. Randerson, and P. J. Rasch (2007), Present-day climate forcing and response from black carbon in snow, *J. Geophys. Res.*, 112, D11202, doi:10.1029/2006JD008003.

Gard, E., J.E. Mayer, B.D. Morrical, T. Dienes, D.P. Fergenson, and K.A. Prather (1997), Real-time analysis of individual atmospheric aerosol particles: Design and performance of a portable ATOFMS, *Analytical Chemistry, 69* (20), 4083-4091.

Guazzotti, S.A., K.R. Coffee, and K.A. Prather (2001), Continuous measurements of size-resolved particle chemistry during INDOEX-Intensive Field Phase 99, *J. Geophys. Res., 106* (D22), 28607-28627.

Hansen, J., and L. Nazarenko (2004), Soot climate forcing via snow and ice albedos, *Proc. Natl. Acad. Sci.*, *101*(2), 423–428.

Hansen, J., M. Sato, and R. Ruedy (1997), Radiative forcing and climate response, *J. Geophys. Res.*, 102(D6), 6831–6864.

Hasegawa, S. and S. Ohta (2002), Some measurements of the mixing state of soot-containing particles at urban and non-urban sites, *Atmos Environ* 36, 3899–3908.

Intergovernmental Panel on Climate Change (IPCC) (2007), Climate change 2007: the scientific basis. In: Solomon, S. (Ed.), Contribution of Working Group I to the Fourth Assessment Report of the Intergovernmental Panel on Climate Change. Cambridge Univ. Press, New York.

Jacobson, M. Z. (2000), A physically-based treatment of elemental carbon optics: Implications for global direct forcing of aerosols, *Geophys. Res. Lett.*, *27*(2), 217–220.

Jacobson, M. Z. (2001), Strong radiative heating due to the mixing state of black carbon in atmospheric aerosols, *N*ature, 409, 695-697.

Kato, S, T. P. Ackerman, J. H. Mather, and E. E. Clothiaux (1999), The k-distribution method and correlated-k approximation for a shortwave radiative transfer model, *J. Quant. Spectrosc. Radiat. Transfer, 62*, 109-121.

Kirchstetter, T. W., T. Novakov, and P. V. Hobbs (2004), Evidence that the spectral dependence of light absorption by aerosols is affected by organic carbon, *J. Geophys. Res.*, 109, D21208, doi:10.1029/2004JD004999.

Lau, K. M., and K. M. Kim (2007), Does aerosol weaken or strengthen the Asian monsoon? *Mountains, Witnesses of Global Change,* R. Baudo et al., Eds., Elsevier, 370 pp.

Lau, K. M., M. K. Kim, and K. M. Kim (2006), Asian summer monsoon anomalies induced by aerosol direct forcing: The role of the Tibetan Plateau, *Climate Dyn.,* 26, 855–864.

Maßling, A., A. Wiedensohler, B. Busch, C. Neusüß, P. Quinn, T. Bates, and D. Covert (2003), Hygroscopic properties of different aerosol types over the Atlantic and Indian Oceans, *Atmos Chem Phys*, 3, 1377-1397.

Marchuk, G., G. Mikhailov, M. Nazarahev, R. Darbinjan, B. Kargin, and B. Elepov (1980), The Monte Carlo Methods in Atmospheric Optics, Springer-Verlag, New York.

Meehl, G. A., J. M. Arblaster, and W.D. Collins (2008), Effects of Black Carbon Aerosols on the Indian Monsoon, *Journal of Climate*, 21, 2869-2882.

Menon, S., J. Hansen, L. Nazarenko, and Y. Luo (2002), Climate effect of black carbon aerosols in China and India, *Science*, 297, 2250– 2252.

Moffet, R. C. and K. A. Prather (2009), In-situ measurements of the mixing state and optical properties of soot with implications for radiative forcing estimates, *Proceedings of the National Academy of Sciences*, 106(29),11872-11877.

Naoe, H., and K. Okada (2001), Mixing properties of submicrometer aerosol particles in the urban atmosphere - with regard to soot particles, *Atmospheric Environment*, 35, 5765-5772.

Okada, K., M. Ikegami, Y. Zaizen, Y. Makino, J. B. Jensen, J. L. Gras (2001), The mixture state of individual aerosol particles in the 1997 Indonesian haze episode, *Journal of Aerosol Science*, 32, 1269–1279.

Okada, K., Ikegami, M., Zaizen, Y., Tsutsumi, Y., Makino, Y., Jensen, J. B., and Gras, J. L. (2005), Soot particles in the free troposphere over Australia, Atmos. Environ., 39, 5079–5089.

Podgorny, I. A., A. M. Vogelmann, and V. Ramanathan (1998), Effects of cloud shape and water vapor distribution on solar absorption in the near infrared, *Geophys. Res. Lett.*, *25*(11), 1899–1902.

Podgorny, I. A., and V. Ramanathan (2001), A modeling study of the direct effect of aerosols over the tropical Indian Ocean, *J. Geophys. Res.*, *106*(D20), 24,097–24,106.

Pósfai, M., J. R. Anderson, P. R. Buseck, and H. Sievering (1999), Soot and sulfate aerosol particles in the remote marine troposphere, *J. Geophys. Res.*, 104(D17), 21,685–21,693.

Prather, K.A., T. Nordmeyer, and K. Salt (1994), Real-time characterization of individual aerosol-particles using Time-of-Flight Mass Spectrometry, *Analytical Chemistry, 66* (9), 1403-1407.

Ramana, M. V., V. Ramanathan, D. Kim, G. C. Roberts, and C. E. Corrigan (2007), Albedo, atmospheric solar absorption and heating rate measurements with stacked UAVs, *Q. J. Roy. Meteorol. Soc.,* 133, 1913–1931.

Ramanathan, V., C. Chung, D. Kim, T. Bettge, L. Buja, J. T. Kiehl, W. M. Washington, Q. Fu, D. R. Sikka, and M. Wild (2005), Atmospheric Brown Clouds: Impacts on South Asian Climate and Hydrological Cycle, *PNAS*, Vol. 102, No. 15, 5326-5333.

Ramanathan V. and G. Carmichael (2008), Global and regional climate changes due to black carbon, *Nat Geosci* 1, 221–227.

Ramanathan, V. et. al (2001a), Indian Ocean EXperiment: An integrated analysis of the climate forcing and effects of the great Indo-Asian haze, *J. Geophys. Res, 106* (D22): 28371-28398.

Ramanathan, V., P. J. Crutzen, J. T. Kiehl and D. Rosenfeld (2001b), Aerosols, Climate, and the Hydrological Cycle, *Science*, 294, 2119-2124.

Ramanathan, V., M. V. Ramana, G. C. Roberts, D. Kim, D., C. E. Corrigan, C. Chung, and D. Winker (2007), Warming trends in Asia amplified by brown cloud solar absorption, *Nature*, 448, 575–578, doi:10.1038/nature06019.

Rothman, L. S., et al. (2003), The HITRAN molecular spectroscopic database: edition of 2000 including updates through 2001, *J. Quant. Spectros. Radiat. Transfer, 82,* 5–44.

Satheesh, S. K., V. Ramanathan, Xu Li-Jones, J. M. Lobert, I. A. Podgorny, J. M. Prospero, B. N. Holben, and N. G. Loeb (1999), A model for the natural and antropogenic aerosols over the tropical Indian Ocean derived from Indian Ocean Experiment data, *J. Geophys. Res., 104(D22)*, 27,421– 27,440.

Schnaiter, M., C. Linke, O. Möhler, K.-H. Naumann, H. Saathoff, R. Wagner, U. Schurath, and B. Wehner (2005), Absorption amplification of black carbon internally mixed with secondary organic aerosol, *J. Geophys. Res.*, 110, D19204, doi:10.1029/2005JD006046.

Shiraiwa, M., Y. Kondo, N. Moteki, N. Takegawa, Y. Miyazaki, and D. R. Blake (2007), Evolution of mixing state of black carbon in polluted air from Tokyo, Geophys. Res. Lett., 34, L16803, doi:10.1029/2007GL029819.

Shiraiwa, M., Y. Kondo, N. Moteki, N. Takegawa, L. K. Sahu, A. Takami, S. Hatakeyama, S. Yonemura, and D. R. Blake (2008), Radiative impact of mixing state of black carbon aerosol in Asian outflow, *J. Geophys. Res.*, 113, D24210, doi:10.1029/2008JD010546.

Spencer, M. T., J. C. Holecek, C. E. Corrigan, V. Ramanathan, and K. A. Prather (2008), Size-resolved chemical composition of aerosol particles during a monsoonal

transition period over the Indian Ocean, *J. Geophys. Res.*, 113, D16305, doi:10.1029/2007JD008657.

Stone, E. A., G. C. Lough, J. J. Schauer, P. S. Praveen, C. E. Corrigan, and V. Ramanathan (2007), Understanding the origin of black carbon in the atmospheric brown cloud over the Indian Ocean, *J. Geophys. Res.,* 112, D22S23, doi:10.1029/2006JD008118.

Twomey, S. A. (1977), The influence of pollution on the shortwave albedo of clouds, J. Atmos. Sci., 34, 1149– 1152.

Vogelmann, A.M., V. Ramanathan and I. A. Podgorny (2001), Scale Dependence of Solar Heating Rates in Convective Cloud Systems with Implications to General Circulation Models, *J. Climate, 14(N8)*, 1738-1752.

Zhang, R., Khalizov, A., Pagels, J., Zhang, D., Xue, H., and McMurry, P. H. (2008), Variability in morphology, hygroscopicity, and optical properties of soot aerosols during atmospheric processing, *Proc. National Acad. Sci.* 105(30), 10291-10296.

Zhu, A., V. Ramanathan, F. Li, and D. Kim (2007), Dust plumes over the Pacific, Indian, and Atlantic oceans: Climatology and radiative impact, *J. Geophys. Res.*, 112, D16208, doi:10.1029/2007JD008427.

Chapter 4

Spectral Signature of Aerosol Radiative Forcing over the Tropical Indian Ocean

4.1 Introduction

The aerosol forcing estimated by most previous studies is the broadband value, which is the integrated forcing over the full solar spectral range. Very few of them investigated the wavelength variances of aerosol forcing with high spectral resolution. *Meywerk and Ramanathan* [1999] filled this gap by providing the observation-based spectral fluxes over the surface of the tropical Indian Ocean using a photodiode array spectroradiometer. They found a shift in the wavelength of the maximum intensity of the observed direct irradiance from ~470 nm for the pristine day to ~580 nm for the polluted day and suggested a stronger influence of the aerosol extinction in the shorter wavelength. To fully understand the effect of aerosols on the spectral variation of solar radiation, it is necessary to employ the spectrally-resolved radiative transfer model with moderate to high resolutions.

The motivation of this study is to thoroughly investigate the spectral signature of aerosol forcing and link the spectral flux change to aerosol optical properties and size distribution. The main question addressed in this chapter is the ability of models to simulate the spectral dependence of aerosol radiative forcing. The ABC Post-Monsoon Experiment (APMEX) over the tropical Indian Ocean provides intensive field observations that can be used to study the spectral variation of aerosol forcing. The study presented in this chapter uses the measurements of aerosol's scattering and absorption, size distribution, vertical profile, and chemical composition under the

clear-sky conditions during APMEX as bases for input parameters of the spectrally-resolved radiative transfer model. Simulations from this model can then be compared and validated with the observed spectral irradiance. The spectral signature of aerosol radiative forcing can be investigated by removing the contributions of radiation associated with an aerosol-free atmosphere; this radiation is the result of Rayleigh scattering and atmospheric gases absorption.

4.2 Spectrally-resolved Radiative Transfer Model: MODTRAN

MODerate spectral resolution atmospheric TRANSsmittance (MODTRAN) computer code is a spectrally-resolved atmospheric radiative transfer model (RTM), which provides very accurate calculations by means of a rigorous mathematical formulation and a very fine spectral resolution [*Berk et al.,* 2003]. The latest version of MODTRAN 4.3 provides two schemes to compute multiple scattering: an approximate 2-stream algorithm and a DISORT N-stream option. MODTRAN4 can now complement a multiple scattering routine while maintaining the basic 1 cm^{-1} spectral resolution by introducing a Correlated-k (CK) capability that is expressly compatible with Beer's law formulations based on tuned spectral selection for full DISORT calculations [*Stamnes et al.,* 1988]. It also produces a complete spectral suite for the faster MODTRAN-default multiple scattering option. This process is most accurate in atmospheric windows where the multiple scattering effects have the greatest significance. The current approach for molecular absorption accommodates line overlap and partial correlations between both molecular species and solar irradiance, while maintaining internal band model spectral resolution at either 1 cm^{-1}, 5 cm^{-1} or 15

cm^{-1} binning. MODTRAN either specifies the ground surface as Lambertian or includes the effects of various Bidirectional Reflectance Distribution Functions (BRDFs). MODTRAN supports adjacency effects, allows users to specify input data as pre-defined quantities or give data explicitly and considers spherical refraction and earth curvature (ray bending) in the calculation of atmospheric slant path and attenuation amounts along the path. The standard output of MODTRAN consists of spectrally resolved atmospheric transmittances, optical depths, radiances, single-scattered solar and lunar radiance, direct solar and lunar irradiance and multiple-scattered solar and thermal radiance.

MODTRAN includes a molecular band model to account for molecular absorption on the bases of the updated spectral database HITRAN 2001 [*Rothman et al.,* 2003]. The effects of O_2 collision bands, the CKD2.4 H_2O continuum-type absorption [*Clough et al.,* 1989], molecular scattering, aerosol and hydrometeor absorption and scattering are also included. The code provides representative atmospheric aerosol, cloud and rain models with options to replace them with user-modeled or measured values. Six reference atmospheres, each defined by temperature, pressure, density, and mixing ratios for H_2O, CO_2, O_3, N_2O, CO, CH_4, and O_2 all as a function of altitude allow a wide range of climatological choices. The code also contains atmospheric molecular constituent profiles with separate molecular profiles (0-120 km) for 21 minor and trace gases (NO, SO_2, NO_2, NH_3, HNO_3, OH, HF, HCl, HBr, HI, ClO, OCS, H_2CO, HOCl, N_2, HCN, CH_3Cl, H_2O_2, C_2H_2, C_2H_6, PH_3) are available. A total of 6 atmospheric models are available from MODTRAN default

atmospheres as listed in Table 4.1. The user can enter a variable for the CO_2 mixing ratio and for this study, it is taken to be 365 ppmv (parts per million by volume) to represent current CO_2 content. The concentration and vertical profile of temperature and water vapor are based on measurements and the following sections will discuss them in details.

Table 4.1: Built-in geographical-seasonal model atmospheres provide by MODTRAN.

Model Atmosphere	**Location**	**Time of the Year**
Tropical	15N	Annual average
Mid-latitude summer	45N	July
Mid-latitude winter	45N	January
High-latitude summer	60N	July
High-latitude winter	60N	January
US standard	US	1976

With the employment of Correlated-k Beer's Law algorithm [*Lacis and Oinas*, 1991] to describe local layer, species-specific transmittance as input for the radiance calculations, MODTRAN4 is capable of efficiently and correctly (usually within 3-5%) calculating the scattering and absorption signatures of realistic molecular, aerosol and cloudy environments in the lower and middle atmosphere for both the visible and IR. It does so by allowing the explicit definition of water and ice cloud vertical profiles and spectral data, either by scaling and combining default model clouds or by redefining entirely new model clouds with micro-layering options. It permits rapid identification of atmospheric contaminants/signatures in window regions as well as accurate spectral calculations of heating/cooling budgets in the presence of clouds for both thermal and solar spectral regimes. In regions of molecular opacity, where weighting functions peak in the atmosphere, MODTRAN4 is expected to play a role in

very quick ‘primitive’ retrievals, avoiding the large number of line-by-line (LBL) calculations. The addition of a Correlated-k capability to MODTRAN provides an accurate and fast means for evaluation of the effects of clouds and heave aerosol loading on retrievals (both surface properties and species concentration profiles) and on atmospheric radiative heating/cooling calculations.

Aerosol models can then be combined with these reference atmospheres as required. The aerosol models in MODTRAN are defined by regions that contain typical aerosol sources. The sources are representative of rural, urban, desert and maritime environments. For higher altitudes, the aerosols are assumed to be the same whether over land or sea. For the purpose of assigning aerosol models, the atmosphere is divded into vertical 4 regions: the boundary layer (0 - 2 km), the free troposphere or background troposphere (2 - 10 km), the lower stratosphere (10 - 30 km) and the upper atmosphere (30 - 100 km). This is only provided as a guide. The modelling of aerosols in MODTRAN has two key functions: to accurately represent the chemical and physical properties of aerosol particles and from that account for their optical properties (.g. refractive index); and to accurately represent of the vertical distribution of the aerosol number concentration in the atmosphere. In MODTRAN the calculation of the normalized attenuation coefficients is done independently of the calculation of the vertical profile of the aerosol concentration. The user is now able to move the aerosol models to arbitrary regions and scales, and to compress and stretch the vertical profiles as required.

Preliminary verification, validation and assessment of MODTRAN4 has shown that it is capable of improved syntheses and analyses of total (direct plus scattered) solar and thermal energy components for cloud and aerosol decks, plumes and other realistic, non-clear sky conditions within the stratosphere and troposphere. However, the focus of the majority of previous studies using MODTRAN was on IR atmospheric transmission. No major attempt has been made to characterize the spectral signature of radiative forcing by atmospheric aerosols using MODTRAN. The main focus of this study is to fill in this gap and explore aerosol radiative forcing in detail by means of both MODTRAN model simulation and field observation.

4.3 APMEX Study

As follow-up to the successful Indian Ocean Experiment (INDOEX) campaign [*Ramanathan et al.,* 2001a], the Atmospheric Brown Cloud (ABC) project [*Ramanathan et al.,* 2007a] was designed to collect continuous measurements of atmospheric aerosols and solar radiation to broaden the capabilities of numerical models and help people to better understand the climate impacts of accumulated greenhouse gases and rising air pollution over the Asian-Pacific region. A series of aerosol-radiation-climate observatories was constructed for long-term observation of the chemical composition, physical characterization, and optical properties of atmospheric aerosol particles, radiative variation, and cloud properties. As one significant part of the ABC-Asia project, ABC Post-Monsoon Experiment (APMEX) was conducted at the Maldives Climate Observatory on Hanimaadhoo Island (MCOH) with airborne and ground-based observations from October 1, 2004 to November 15,

2004. The main goal of APMEX was to collect intensive measurements on aerosol and radiation during the Indian monsoon transition period, when air masses changes from marine to polluted and to gain insight into the impact on regional radiation budget and climate change from human-made air pollution. To avoid cloud contamination in the radiative measurements and clearly identify the spectral characteristics of aerosol forcing, only cloudless sky cases during the observation period are under investigation by the author of this study. Based on the meteorological and radiation measurements, October 16, 17, 18, and 19 will be considered in this study.

MCOH is located on the northern point of the island of Hanimaadhoo (6.776°N, 73.183°E) in the Republic of Maldives and undergoes the tropical monsoon climate, including distinct seasonal precipitations and the reversal of prevailing wind directions between wet and dry seasons. During the summer monsoon, or wet season (June-September), southwestly wind carries warm marine air mass from the Southern Hemisphere northward and brings moisture and precipitation over India and surrounding areas. Atmospheric aerosols are blown away and removed by the precipitation. October is the monsoon transition month when dominant winds shift from southwesterly to northeasterly to begin winter, or dry season (December-February). The northeasterly wind dominates in winter monsoon season and carries large amounts of pollutants from across the continent of Asia to the relatively clean ocean. The change in prevailing winds over this region during transition period recorded by APMEX provides a unique opportunity to investigate the physical/chemical/optical properties and variations of atmospheric aerosols during

different periods of the Indian monsoon season as well as their radiative effects. *Corrigan et al.* [2006] investigated the impact of monsoon transitions on the physical and optical properties of aerosols at MCOH and found an increase of nearly an order of magnitude in scattering and absorbing aerosols during the transition between the clean and polluted seasons in 2004.

In order to better understand the source of the aerosol particles arriving at MCOH observatory, the NOAA-HYSPLIT (Hybrid Single-Particle Lagrangian Integrated Trajectory) [*Draxler and Hess*, 1998] model can be used for air mass trajectory analysis. The 5-day and 10-day backward trajectories during four selected cases from APMEX are shown in Figure 4.1. These cases show tracks of air parcels starting at 500, 1500, and 3000 m levels above MCOH. Air parcels in the levels below 1500 m are coming from the Arabian Sea, illustrating the relatively pristine marine-time origin of aerosols detected at MCOH. Long-term trajectories at 500 m suggest that desert-type particles from Arabian peninsula and/or Somalia region might also be transported to MCOH by the westerly wind in the lower level. At higher altitudes, air parcels passed through the southern part of the Indian subcontinent and brought more continentally influenced particles to the MCOH.

During APMEX, aerosol and radiation instruments were installed at MCOH to make continuous measurements. The properties observed included broadband and narrow band radiative flux, spectral irradiance, aerosol optical properties and chemical composition, aerosol vertical profiles, and meteorological variables. The complete list of instruments installed at MCOH is presented in Table 4.2. Detailed information

about instrument specification and installation at MCOH observatory are discussed by *Ramana and Ramanathan* [2006] and *Corrigan et al.* [2006]. The observational results and applications of in-situ measurements from this study are given below.

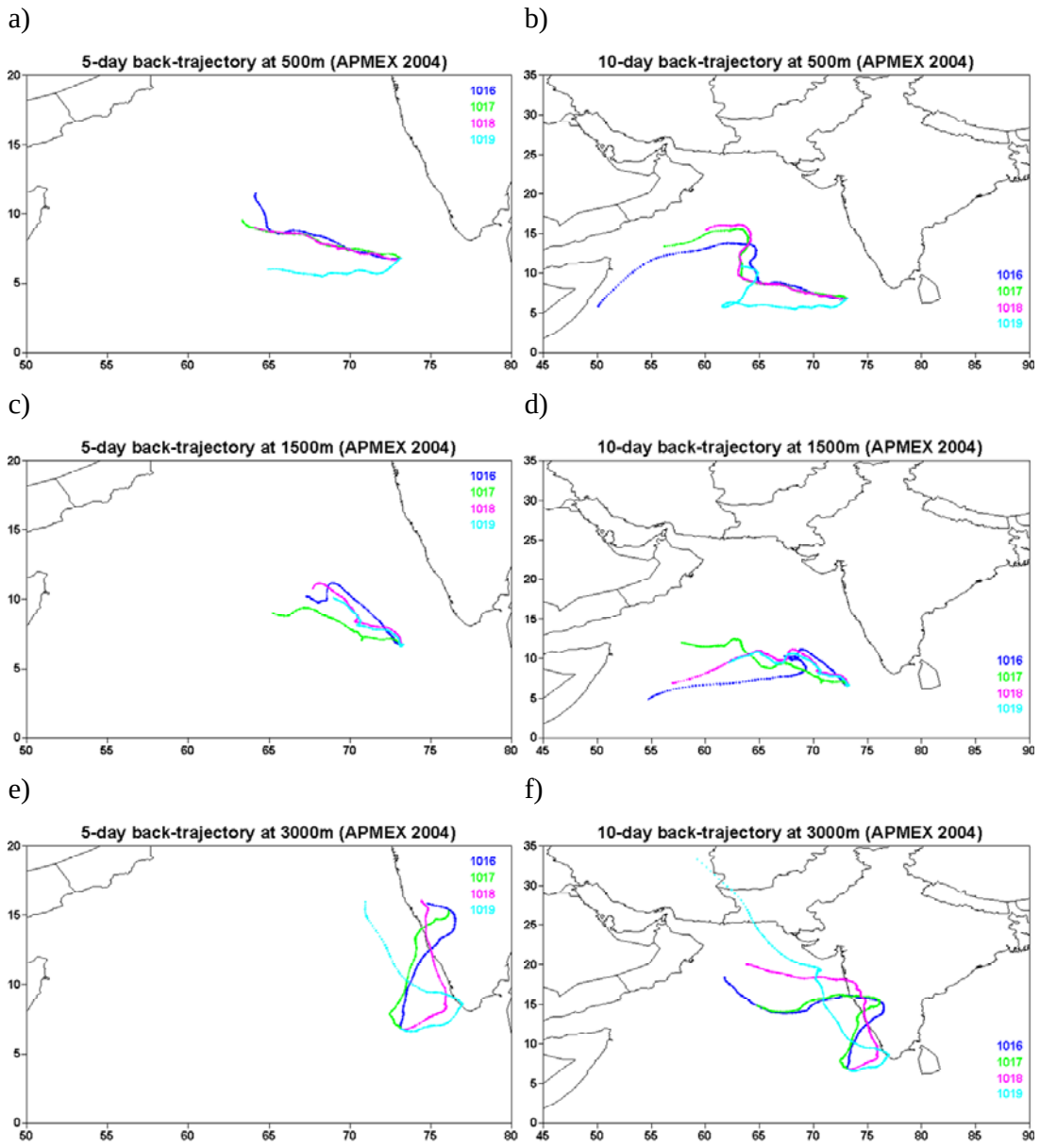

Figure 4.1: 5-day (a, c, e) and 10-day (b, d, f) backward trajectories starting at 500 m (a, b), 1500 m (c, d), and 3000 m (e, f) levels.

4.3.1 Spectral Radiation Measurements

The spectroradiometer is the optical instrument employed in many applications requiring spectrally-resolved quantitative measurements of radiance, irradiance, and reflectance or transmission of light energy. The instrument used during the APMEX campaign to measure global downward irradiance at the surface was made by Analytical Spectral Devices (ASD) Inc. The Ultraviolet/Visible-Near Infrared (UV/VNIR) spectrum, the 325 - 1075 nm wavelength domain, is measured with a 512 channel silicon photodiode array overlaid with an order separation filter. The spectral sampling interval of 1 nm presents detailed features of incoming solar spectrum at the surface. A thorough technical description of the basic concepts, operation, and calibration methods of this instrument can be found in the instrument's user guide [*Curtiss and Goetz*, 1997]. The employment of ASD in INDOEX was discussed by *Meywerk and Ramanathan* [1999] with detailed analysis of the instrument's reliability, corrections, and application to studying aerosol radiative forcing.

The ASD measured spectral irradiances during four selected clear sky cases are shown in Figure 4.2. The integration of irradiance at each sampling interval represents the total flux throughout the detection wavelength range from 325 to 1075 nm. The variation of total flux over time shows the diurnal change of incoming solar flux and varies smoothly with solar zenith angle (shown by the black line with the axis on the right) for the clear sky condition. The fluctuation of total flux is mainly due to the presence of clouds, which greatly affects the downwelling flux reaching the ground by reflecting the sunlight back to space when the sky is overcast. Partial cloud cover also

greatly enhances the intensity of diffuse skylight illumination, which causes a sharp increase in the observed downwelling solar flux. Thus, it is clearly that it was cloud-free on the mornings of October 16, 18, and 19, and in the afternoon of October 17. The time-spectrum plot presents not only the temporal variation but also the spectral signature of the downward irradiance. The solar energy in the visible band is significant when the sun is overhead. Water vapor absorption is distinctively demonstrated by the sharp diminishment of irradiance in the near-IR region.

Table 4.2: Observation parameters and instruments deployed at ABC MCOH during the APMEX.

Parameter	**Instrument**
Aerosol absorption coefficient	Aethalometer (370, 430, 470, 520, 590, 700 880 nm)
Aerosol scattering coefficient	Nephelometer (450, 550, 700 nm)
Total particle concentration	CPC (0.01-5.0 um)
Broadband solar radiation	Pyranometer (0.3-2.8 um)
up/down visible radiation	Photosynthetically Active Radiation (PAR, 0.4-0.7 um)
Temperature, pressure, relative humidity	meteorological instruments
Aerosol vertical profiles	Micro pulse Lidar (523nm)
Spectral irradiance	Spectroradiometer (Analytical Spectral Devices, Inc. ASD FieldSpec UV/VNIR, 325-1075nm)
Column ozone	Microtops ozonemeter
Aerosol optical depth	Microtops Sun photometer (380, 440, 500, 675, 870, 1020nm); CIMEL Sun photometer (340, 380, 440, 500, 670, 870, 1020 nm)
column precipitable water	Microtops Sun photometer (940nm)
single particle chemical composition	Aerosol time-of-flight mass spectrometer (ATOFMS)

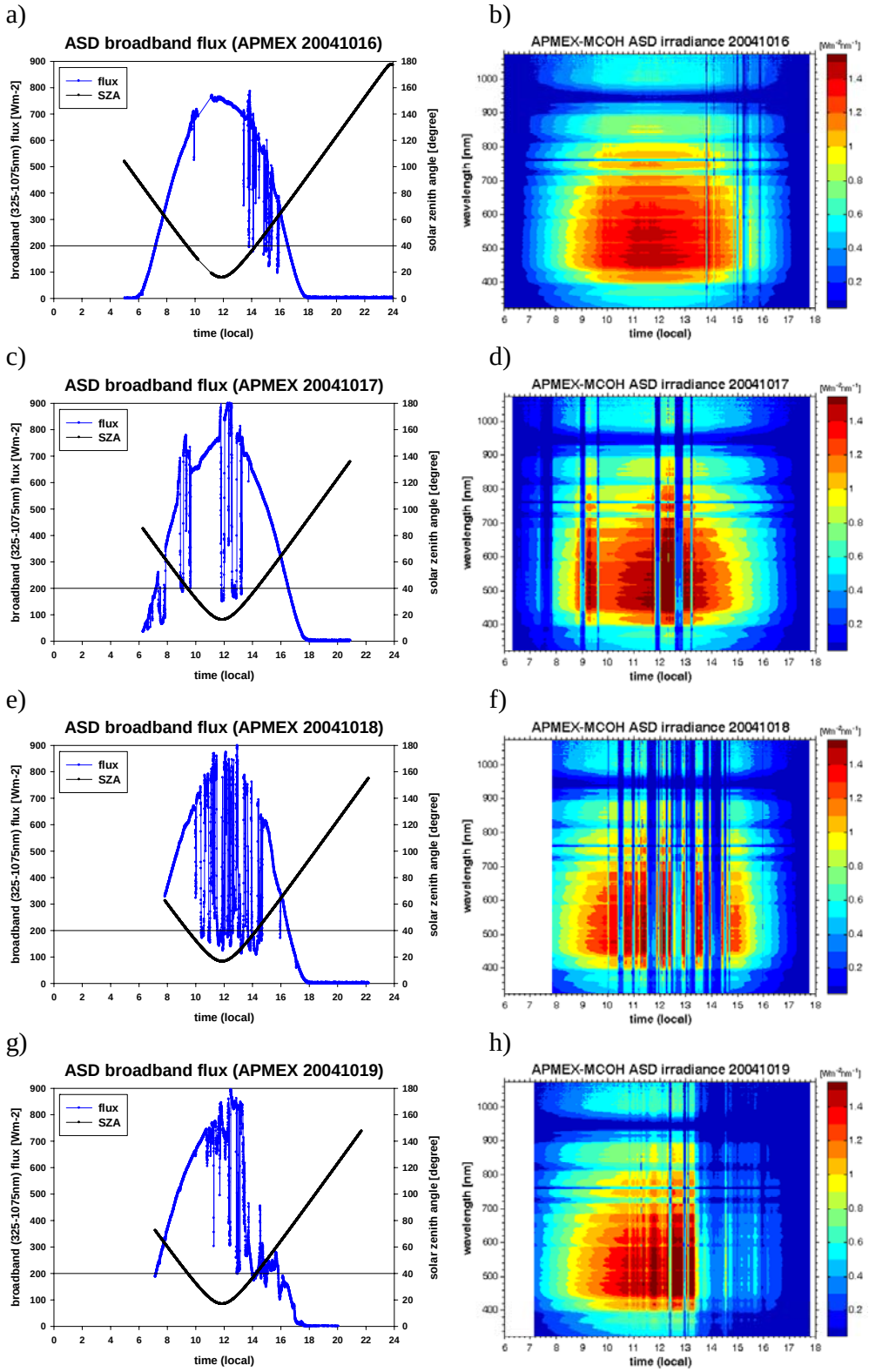

Figure 4.2: ASD broadband (325-1075nm) flux (a, c, e, g) and spectral irradiance (b, d, f, h) at MCOH for October 16 (a, b), 17 (c, d), 18(e, f), and 19 (g, h) 2004.

To exclude cloud ‘contamination’ and make the comparison reasonable, we selected the data with same solar zenith angle (SZA) around 40 degrees (±0.2 degrees) under cloud free conditions as the representative spectral irradiance. The average spectral irradiances for four clear sky cases are shown in Figure 4.3. The distinct solar absorption features of molecules in the visible and near infrared can be clearly identified from the observed irradiance at the surface, such as the water absorption in the visible and near-IR regions, oxygen absorption bands A (760 nm) and B (690 nm), absorption by NO_2 in the visible region and absorption by ozone in the UV and visible regions. By far, water vapor exerts the strongest modification of the incoming solar spectrum and absorbs a significant amount of solar flux in the lower atmosphere. In the near-IR region, water vapor has a large number of overtone and combination bands, which arise from ground state transitions. In the wavelength range of ASD spectroradiometer, three distinct water vapor absorption bands can be clearly identified, centered at 0.72, 0.82, and 0.94 μm and present non-negligible contribution to the solar heating of the atmosphere. In the visible band, although water vapor also has a number of absorption lines associated with overtone and combination transitions, the contribution to the absorption and atmospheric heating is quite small.

4.3.2 Aerosol Optical Measurements

The optical properties of atmospheric aerosols near the surface were measured using a ground-based nephelometer and aethalometer. The TSI 3563 mode nephelometer is used to measure aerosol scattering coefficients (K_{sca}) at three visible wavelengths (450, 550, and 700 nm). The absorption coefficients (K_{abs}) are

determined by a filter-based Magee Scientific AE-31 aethalometer at 7 wavelengths (370, 430, 470, 520, 590, 700, and 880 nm). More sampling results collected from the nephelometer and the aethalometer during APMEX are discussed by *Corrigan et al.*, [2006]. The 2-hour average value of scattering and absorption coefficients when SZA is around 40 degrees is shown in Figure 4.4. The scattering coefficients from four different cases show similar spectral patterns and are nearly parallel to each other. October 18 has the highest scattering and the K_{sca} at 550 nm is about 50 Mm^{-1}. The lowest scattering occurred on October 16 with K_{sca} less than 20 Mm^{-1}. The absorption coefficients measured at various wavelengths show quite different spectral dependences. Although K_{abs} measured at 880 nm has similar value, 0.4 Mm^{-1} in several different cases, the absorption in the shorter wavelength, especially in the near UV region, varies from 0.6 to 1.8. The slope of absorption in the log-log coordinates quantitatively provides the wavelength dependence of absorption, and it varies from 0.78 on October 16 to 1.76 on October 17, indicating strong absorption in near UV bands on October 17.

During APMEX, aerosol optical depth (AOD) was measured at multiple wavelengths using a Microtops Sun photometer. This study will analyze and use the measured AOD at 550 nm for further application. The cloud-screened AOD data collected by Microtops is compared with the measurements by CIMEL, which is operated by AERONET. The comparison showed that the AOD difference between these two instruments is consistent with previous findings and within the instrument uncertainties [*Ramana and Ramanathan*, 2006]. For the four selected clear sky cases

with 40 degree SZA, the AOD at 550 nm is 0.12, 0.12, 0.16, and 0.14 for October 16, 17, 18, and 19, respectively.

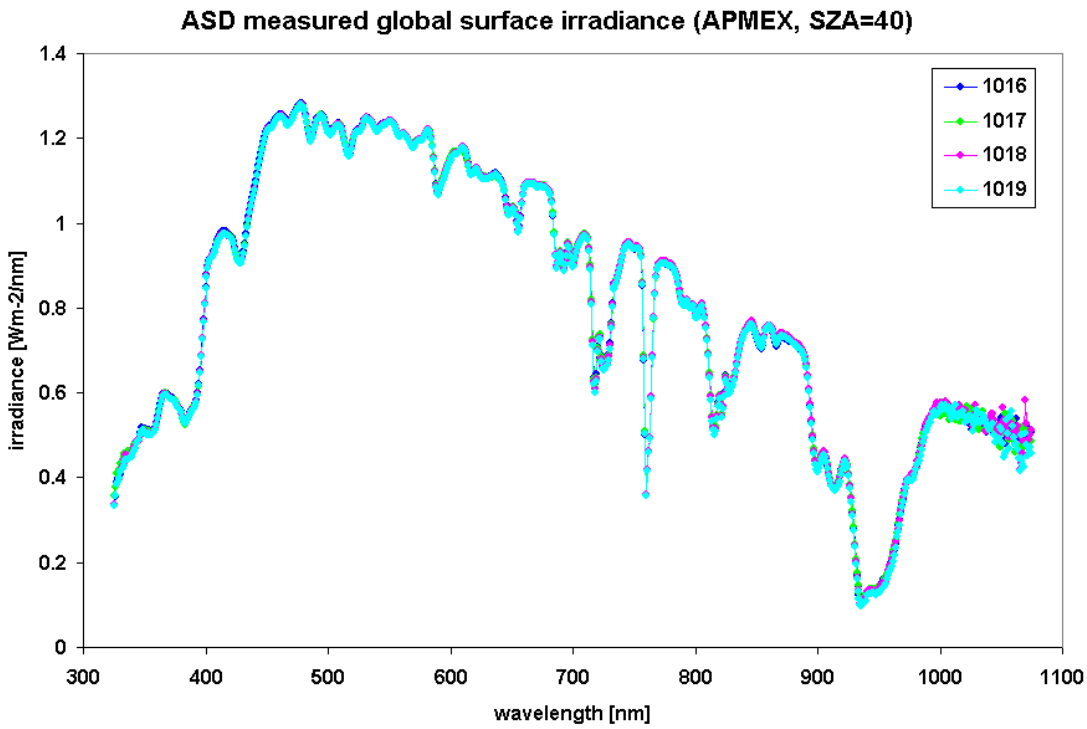

Figure 4.3: Spectral irradiances at 40 degree solar zenith angle under clear sky condition for Oct 16, 17, 18, and 19, 2004.

4.3.3 Chemical Composition Measurement: ATOFMS

The Aerosol Time-of-Flight Mass Spectrometer (ATOFMS) [*Prather et al.*, 1994; *Gard et al.*, 1997; *Guazzotti et al.*, 2001] was operated at MCOH observatory during APMEX from October 15 to November 5, 2004. ATOFMS captured the characteristics of aerosols with aerodynamic size from 0.3-2.5 µm in the period when Indian monsoon switches from a southwestly flow to northeasterly wind, the monsoon transition time. The size-resolved chemical composition of aerosol particles during APMEX was measured by means of ATOFMS and other aerosol characterization

instruments [*Spencer et al.*, 2008]. More detailed description of the technical features of the ATOFMS can be found in *Prather et al.*, [1994] and *Gard et al.*, [1997]. A number of articles have been published that discuss the scientific application of ATOFMS in various field experiments including INDOEX [*Guazzotti et al.*, 2001] and Ice in Clouds Experiment-Layer Clouds (ICE-L) [*Pratt et al.*, 2009], among others. The study by *Moffet and Prather* [2009] demonstrated that the real-time observation of size-resolved aerosol mass spectrum from ATOFMS provided further insight into aerosol chemical composition and mixing states.

a)

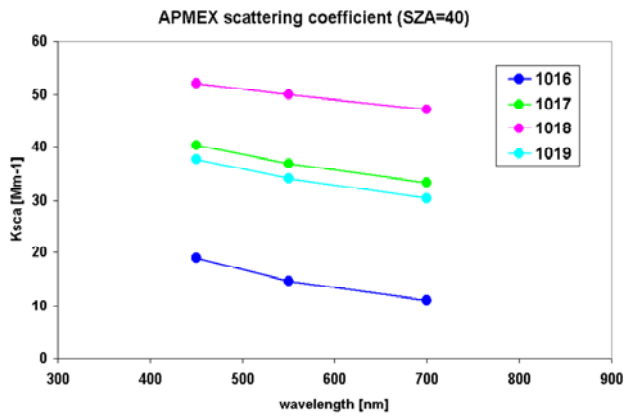

b)

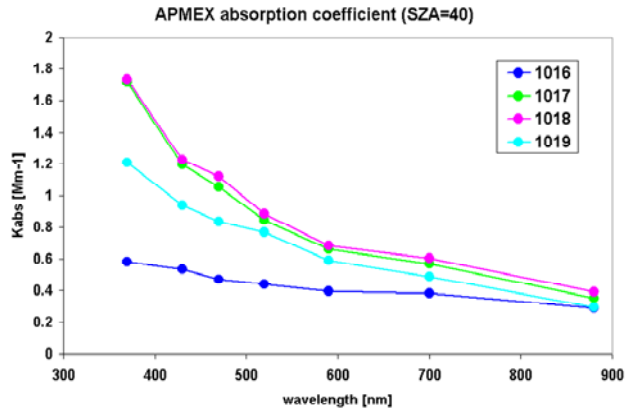

Figure 4.4: 2-hour average scattering (a) and absorption (b) coefficients measured at various wavelengths for October 16, 17, 18, and 19, 2004.

Eight major particle types were observed during APMEX: fresh sea salt, aged sea salt, elemental carbon with sea salt (EC-SS), elemental carbon with sulfate (EC-SU), fly ash, potassium-biomass (biomass/biofuel burning), organic carbon (OC), and calcium-dust. So called “missing” particles, such as ammonium sulfate and wet sea salt were sized by the ATOFMS but do not produce mass spectra because they scatter strongly and absorb very little laser light. The observed particle concentration for particles less than 2.5 μm in size is scaled by an Aerodynamic particle sizer (APS) and corrected for the over counting of fly ash and the undercounting of fresh sea salt. The results shown below are kindly provided by Prather’s group and more detailed analyses of the instrumentation, method, and results have been published elsewhere [*Spencer et al.*, 2008].

The temporal variation of particle number concentrations of different chemical classes is demonstrated in Figure 4.5. Particle number concentrations showed strong diurnal variation on the four selected days. Fly ash particles greatly increased in the afternoon on October 16 and 17. EC-sulfate aerosols showed relatively constant concentration throughout October 19. Overall, October 19 shows the highest total particle number concentration and is consistent with the AOD measurement, which also indicates the largest aerosol loading in October 19. Figure 4.6 presents the diurnal average particle number fractions of different chemical classes. It’s clearly seen that EC-sulfate and fly ash account for most of the particle number concentration, where EC-sulfate particles contribute about 30% and the fraction of fly ash ranges from around 25% to as high as nearly 50%. The contribution of fresh sea-salt particles ranks

the third among all types of aerosols, followed by biomass/biofuel burning aerosols, which showed nearly constant contribution with number fractions around 7%. The concentration of OC is surprisingly low while in the other areas of the world, OC is commonly detected by ATOFMS. *Spencer et al.* [2008] has explained the possible reasons for the virtually absence of OC during APMEX as being low ozone concentration, cloud and rain scavenging, and the overshadowing of OC signal by intense inorganic ions such as K and Na.

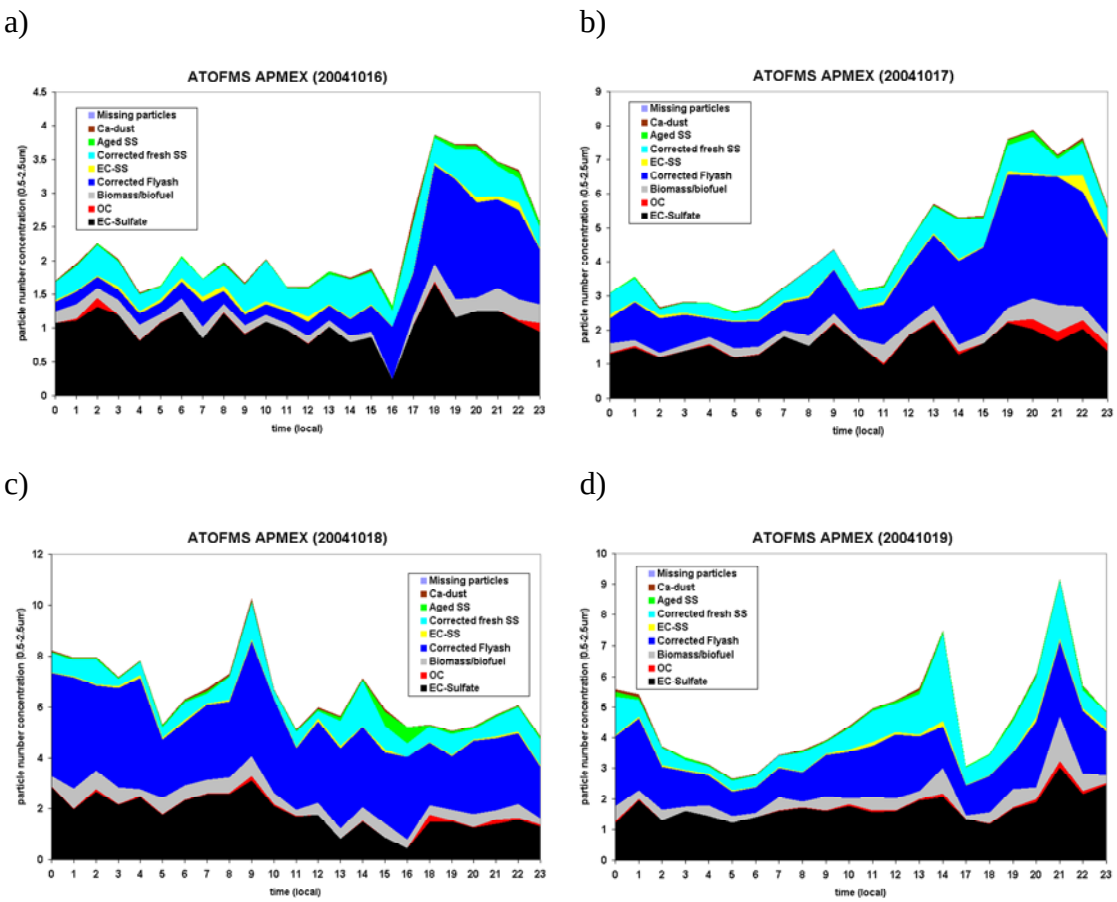

Figure 4.5: Time series for the particle number concentrations of different chemical classes measured during October 16 (a), 17 (b), 18 (c), and 19 (d) after scaling and correction.

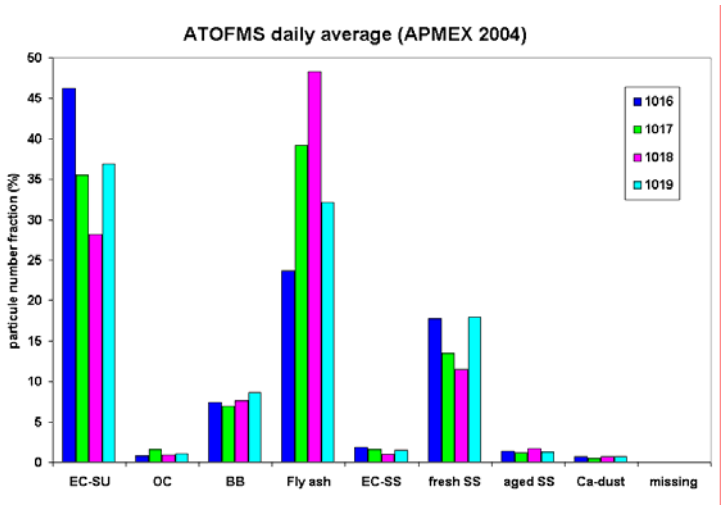

Figure 4.6: Diurnal average particle number fraction [%] of different chemical classes measured during October 16 (a), 17 (b), 18 (c), and 19 (d) after scaling and correction.

4.3.4 Aerosol Vertical Profile Measurement: Lidar

A Micro-Pulse Lidar (MPL) was installed at MCOH and operated continuously during APMEX to measure the vertical distribution of tropospheric aerosols. The MPL system transmits green colored laser pulses of short duration (10 nm) and high pulse repetition frequency (2500 Hz). The returned MPL signals have very high resolution (30 m vertical interval and 1 minute time interval) and good signal-to-noise ratio. The intensity of backscattered light is determined by the atmospheric loading of constituents such as molecules, aerosols, and clouds. Although the MPL signal can reach an altitude of 60 km, the data below 8 km is analyzed to retrieve aerosol vertical profiles while considering the possible distribution and vertical mixing of aerosols in free troposphere. Assuming an altitude-independent ratio of backscatter to extinction ratio, aerosol extinction profile can be determined with the assistance of Microtops measured AOD at 550 nm. The extinction coefficients around 40 degrees SZA during the four selected cases are determined using a 30-minute average. The results are

normalized with respect to the maximum value of individual profile and presented in Figure 4.7. It is clearly seen that aerosol particles are mainly distributed in the lower atmosphere. Contrary to the commonly seen boundary layer aerosol profile (maximum value near the surface and exponential decrease with height in the boundary layer), the selected cases from APMEX show different vertical distribution with peak above the surface mixed layer (around 0.5 km). The elevated aerosol layer peaked around 0.5 to 2.0 km and decreased until reaching an altitude of about 3.0 km. The extinction of aerosol particles above 3.0 km is fairly weak compared to the layer below.

4.3.5 Others

Aircraft measurements provide the vertical profiles of ambient temperature, pressure, and relative humidity, and can be combined with the default Tropical annual average atmosphere described by *McClatchey et al.* [1972] to derive a user-defined atmospheric profile. Ground-based measurements provide the column amount of water vapor and ozone. The global nitrogen dioxide (NO_2) measured by the Ozone Monitoring Instrument (OMI) on board the EOS-AURA satellite [*Boersma, et al.*, 2007] can be used to accurately account for the absorption of NO_2 in the UV and visible regions. The default NO_2 profile provided by MODTRAN can be used to prescribe the vertical distribution of NO_2. The column amount of NO_2 around MCOH is about 0.10, 0.08 and 0.09 DU for October 16, 18, and 19. The AURA sampling data from October 17 is missing so the average value of October 16 and 18 is used. The column total NO_2 amount is applied to scale with the default NO_2 profile. The column ozone amount was 283, 280, 277, 280 DU and the precipitable water was 3.9, 4.0, 4.0,

and 4.1 cm for October 16, 17, 18, and 19, both of them were measured by ground-based instruments.

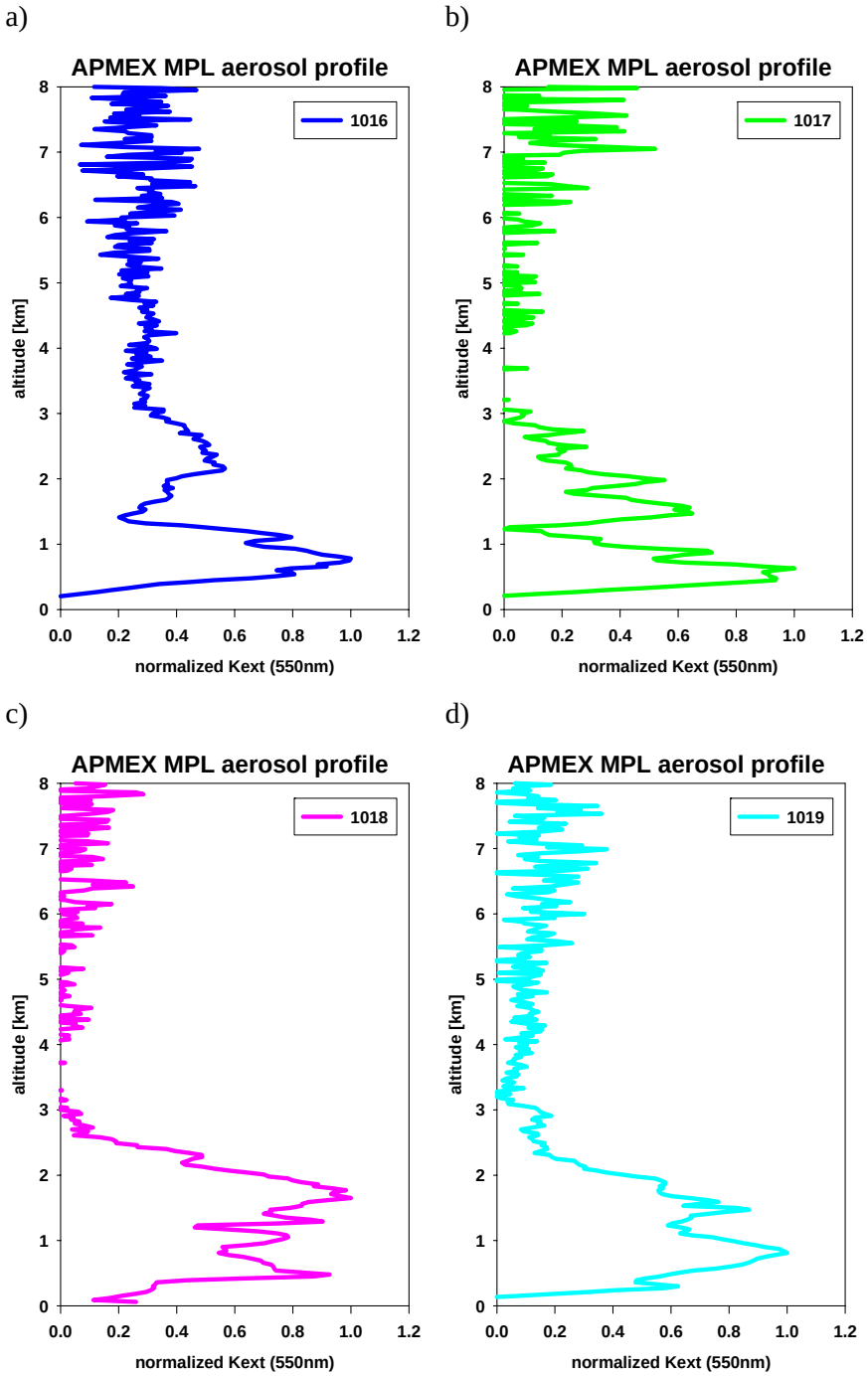

Figure 4.7: Normalized aerosol vertical profile derived from MPL lidar for October 16 (a), 17 (b), 18 (c), and 19 (d) in 2004.

4.4 Aerosol Model

To accurately investigate the spectral signature of aerosol radiative forcing, it is necessary to obtain the spectral variation of aerosol optical properties. Spectrally-resolved aerosol extinction coefficients and absorption coefficients are the major input variables required by the MODTRAN model to simulate spectral irradiance changes by aerosols. Two distinct approaches are employed in this study: the first method directly applies the aerosol scattering and absorbing coefficients measured by Nephelometer and Aethalometer to the MODTRAN model and is termed as the physically constrained aerosol model. The second aerosol model is the chemically constrained model, which uses the aerosol chemical composition observed by ATOFMS as the constraint to model the spectral variation of aerosol optical properties.

For the chemically constrained aerosol model, the aerosol mixtures are assumed to be composed of four types of particles, including three types of light-absorbing aerosols: black carbon (BC), brown carbon (BB), and mineral dust (DU). These particles can absorb nonnegligible amounts of solar flux and make great contributions to the atmospheric heating rate. The non-absorbing aerosol which is the mixture of sulfate (SU), non-absorbing organics (OC), sea salt (SS), and water vapor (H_2O), is also a significant component. Non-absorbing materials coating the surfaces of absorbing particles is considered to be the main aging process for solid BC, BB, and DU particles transported to the observatory. A core-shell model, which is a mixture of multiple materials with a solid core surrounded by a spherical coating, can be used to represent the coated aerosol particles. Collision and coagulation between different

solid particles are not considered in the mixing model though they are also observed during the aging of atmospheric aerosols.

For non-absorbing particles, the spectrally-resolved extinction coefficient, single scattering albedo (SSA), and asymmetry factor can be estimated using Mie code and the refractive indices of sulfate, OC, and sea-salt are adopted from OPAC datasets [*Hess et al.*, 1998]. For coated absorbing aerosols, optical properties can be calculated using the core-shell model provided by *Bohren and Huffman* [1983]. The core-shell model provides great flexibility in modeling a range of aerosol mixtures. The refractive index of BC is based on OPAC and the findings from *Kirchstetter et al.* [2004] are used for brown carbon. The refractive index of mineral dust and fly ash employs the values for South Asia and the Indian Ocean discussed by *Zhu et al.* [2007]. The number fraction of each aerosol component can be derived from ATOFMS measurements, which provides the relative contribution of each aerosol component. The original eight chemical classes defined by ATOFMS are regrouped to simplify the aerosol types in order to apply them to the mixing model. BC particles coated with non-absorbing materials represent elemental carbon associated particles (EC-SS and EC-SU). Fly ash is one of the residues generated in the combustion of coal. The components of fly ash vary considerably depending on the source and makeup of the coal being burned, but all fly ash includes substantial amounts of silicon dioxide (SiO_2) and calcium oxide (CaO). Fly ash particles are generally spherical in shape and range in size from 0.5 μm to 100 μm. In this study, optical properties of fly ash are assumed to follow mineral aerosols, thus it accounts for fly

ash and calcium-dust as mineral dust (DU) for simplification. The category of potassium-biomass particles defined in ATOFMS refers to the mixture of EC and OC with potassium signal. The optical properties of brown carbon estimated by *Kirchstetter et al.* [2004] are used to represent the type of carbonaceous particle with evident biomass/biofuel burning source and are simply referred to as BB in the mixing model. The rest of the particles such as fresh sea salt, aged sea salt, and OC, all have negligible absorption and are categorized as non-absorbing particles (Nabs) in the aerosol mixing model. The changes in the particle refractive index as a function of relative humidity are considered so that the aerosol optical properties used in MODTRAN give an accurate representation of the atmospheric aerosol under ambient conditions. This study uses the unpolluted aerosol size distribution before the monsoon transition period discussed in *Corrigan et al.* [2006]. The spectrally-resolved extinction coefficient, SSA, and asymmetry factor can then be normalized with respect to the value at 550 nm for input into MODTRAN.

Both optical and chemical measurements obtained from MCOH are at surface and there is no observation of aerosol absorbing properties above the ground. Above the boundary layer (BL), aerosol characteristics become less sensitive to weather and geography, thus if the backward trajectories show similar patterns to those in the BL, we can simply assume that the air masses in the free troposphere are from sources similar to those of aerosols in the BL and aerosol optical and chemical properties measured at surface can be used for aerosols above BL. As indicated in Figure 4.7 and Figure 4.1, the majority of aerosols distributed in the air below 3 km and air masses

below 3 km are from the west and northwest. The optical and chemical properties measured at MCOH are applied to the whole column in this study due to the lack of detailed measurements in the upper air. The vertical profile of the aerosol extinction coefficient is derived from ground-based AOD measurements (550 nm) and lidar observations. Sun Photometer measured AOD constrains the column-integrated extinction and the lidar measurements provide the shape of the aerosol vertical distribution.

4.5 Results

The global irradiances simulated by both the physically constrained and chemically constrained models are compared with measurements collected from ASD for the selected four cases. As shown in Figure 4.8, both the physically constrained model and the chemically constrained model can simulate the spectral pattern of surface global irradiance well. Model simulations mirror observations at most parts of the shortwave bands except for the violet/blue channel from 400 nm to 500 nm where model results are slightly larger than observations. The integration of irradiance throughout the bands (325-1075 nm) gives the broadband global flux. As listed in Table 4.3, the physically constrained model overestimates the global flux for all cases and the largest difference is for October 16 with relative difference less than 4%. The chemically constrained model shows much better performance with differences within 1% for three of the four cases with exception for October 17 when the difference is as large as 2.68%.

The absolute and relative differences between model simulations and observation for October 16 are shown in Figure 4.9. The overestimation of the model simulation in the visible band is clearly demonstrated. In the band with wavelength less than 700 nm, models overestimate the global irradiance and the physically constrained model presents larger differences than the chemically constrained model. In the longer wavelength band, model results are slightly smaller than observation and the physically constrained model simulation is closer to observation. The difference relative to observation is mostly within 10% except for the bands where atmospheric gases have strong absorption, such as ozone bands in UV, oxygen bands centered at 690 nm and 760 nm, and water vapor bands centered at 720 nm, 820 nm, and 940 nm.

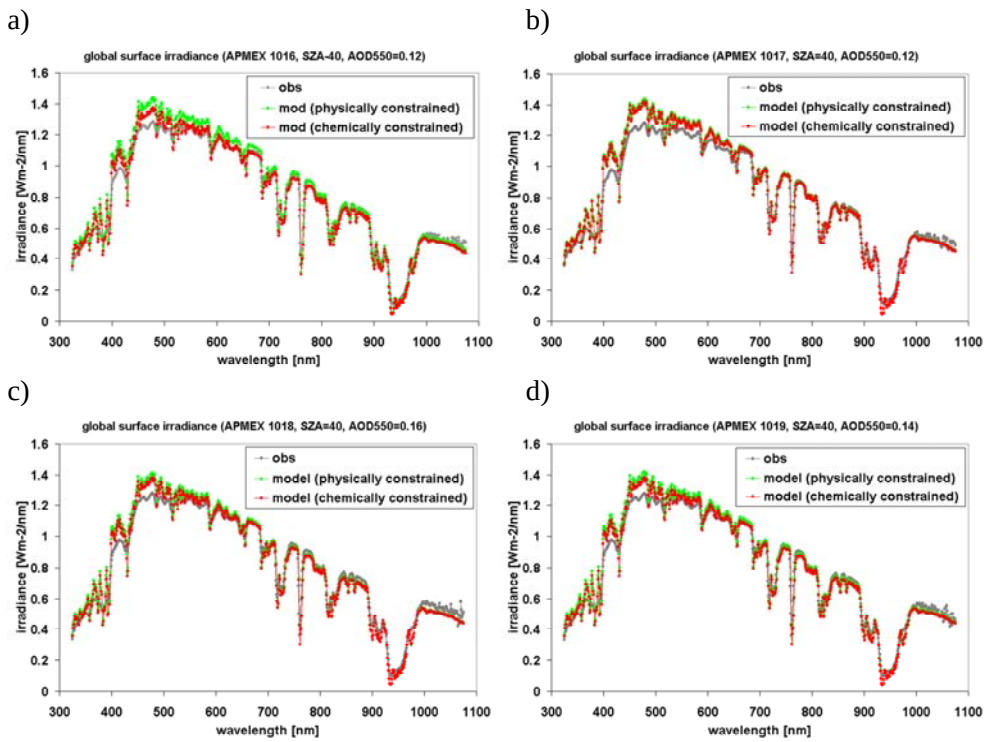

Figure 4.8: Comparison of surface global irradiance for October 16 (a), 17 (b), 18 (c), and 19 (d) in 2004. ASD observation is shown in gray line, green line indicates physically constrained model simulation, and red line is for chemically constrained model results.

Table 4.3: Comparison of integrated global surface flux (Wm^{-2}) between observation and model simulations. The absolute and percentage difference (relative to observation) between model results and observations are given inside the parenthesis.

date	**Observation (325-1075 nm)**	**Physically constrained model**	**Chemically constrained model**
Oct 16	604.1	627.4 (23.3; 3.86%)	602.1 (-2.0; -0.33%)
Oct 17	604.2	626.0 (21.8; 3.61%)	620.4 (16.2; 2.68%)
Oct 18	604.3	614.8 (10.5; 1.74%)	604.4 (0.1; 0.02%)
Oct 19	600.4	617.6 (17.2; 2.86%)	603.4 (3.0; 0.50%)

Figure 4.10 compares direct and diffuse irradiances between the physically constrained model and the chemically constrained model. The simulated direct irradiance is quite similar for both models and the largest difference between these two models comes from diffuse irradiance. The diffuse irradiance simulated by the physically constrained model is larger than the chemically constrained model throughout the spectrum, which indicates that the physically constrained model predicts more scattering than the chemically constrained the model. As shown in Figure 4.9, the chemically constrained model has better performance than the physically constrained model and the simulated irradiance in the chemically constrained model is closer to observations. The results of the comparison suggest that the chemically constrained aerosol model can better represent the optical properties of aerosol mixtures throughout the column, and overall, aerosol mixtures in the entirety of the atmospheric column are more absorbing than those observed at the surface.

a)

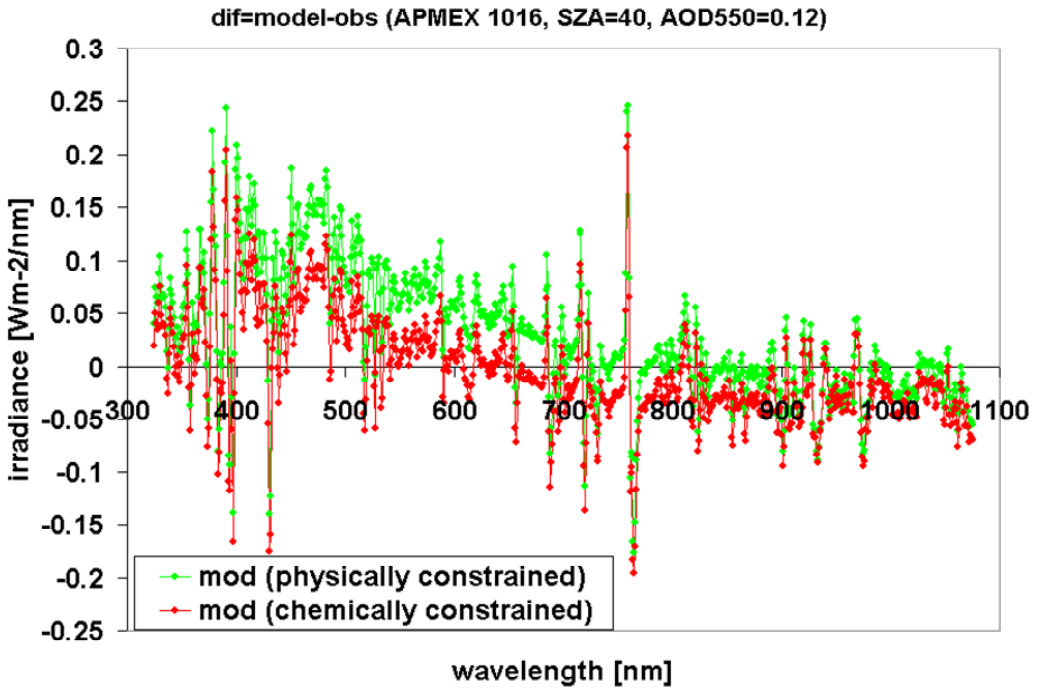

b)

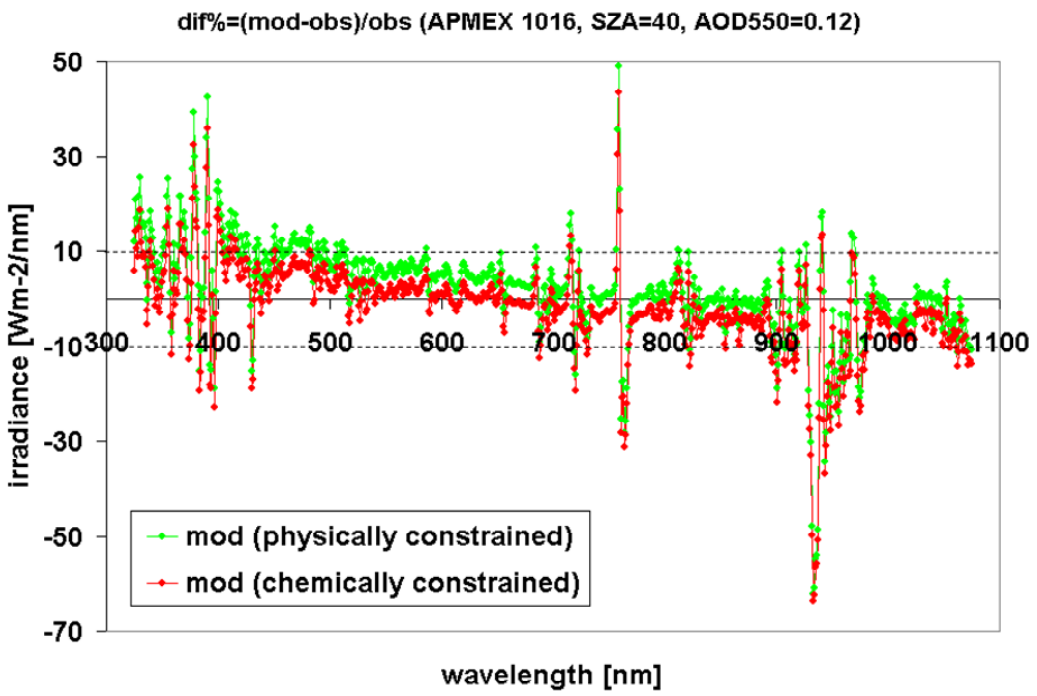

Figure 4.9: a) Absolute difference and b) percentage difference of surface global irradiance between model simulations and observation for October 16.

a)

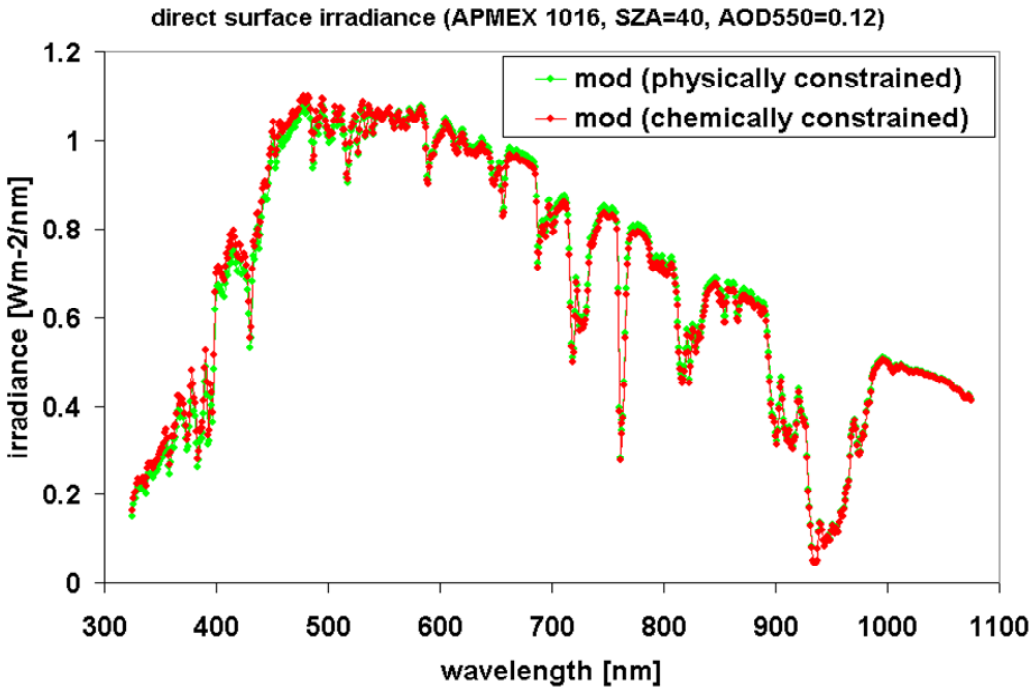

b)

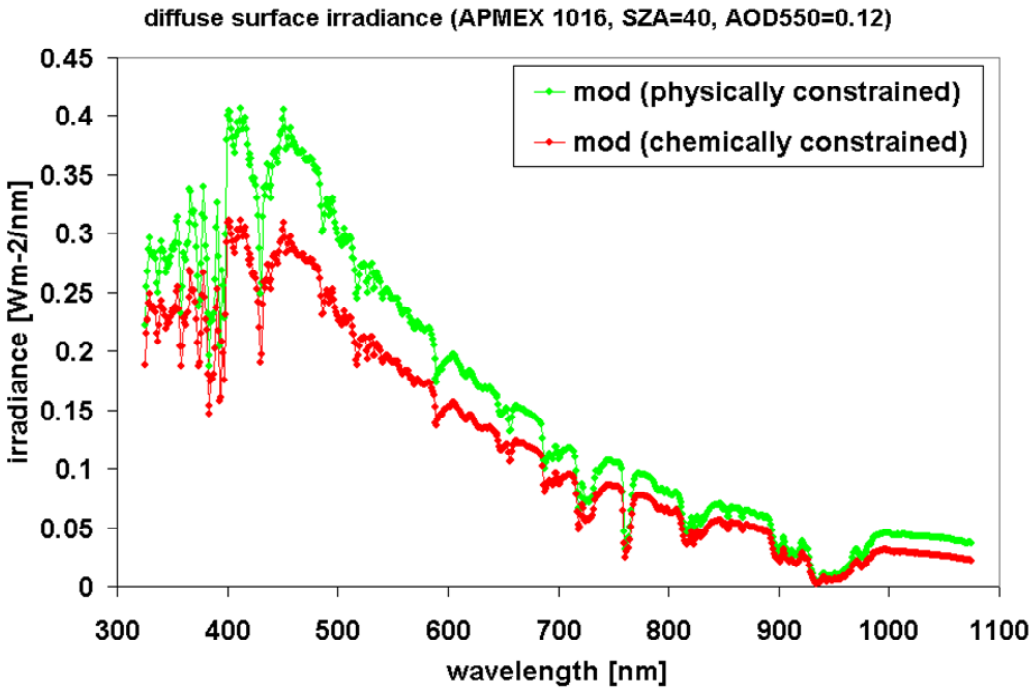

Figure 4.10: Model simulated a) direct and b) diffuse irradiance at the surface for October 16.

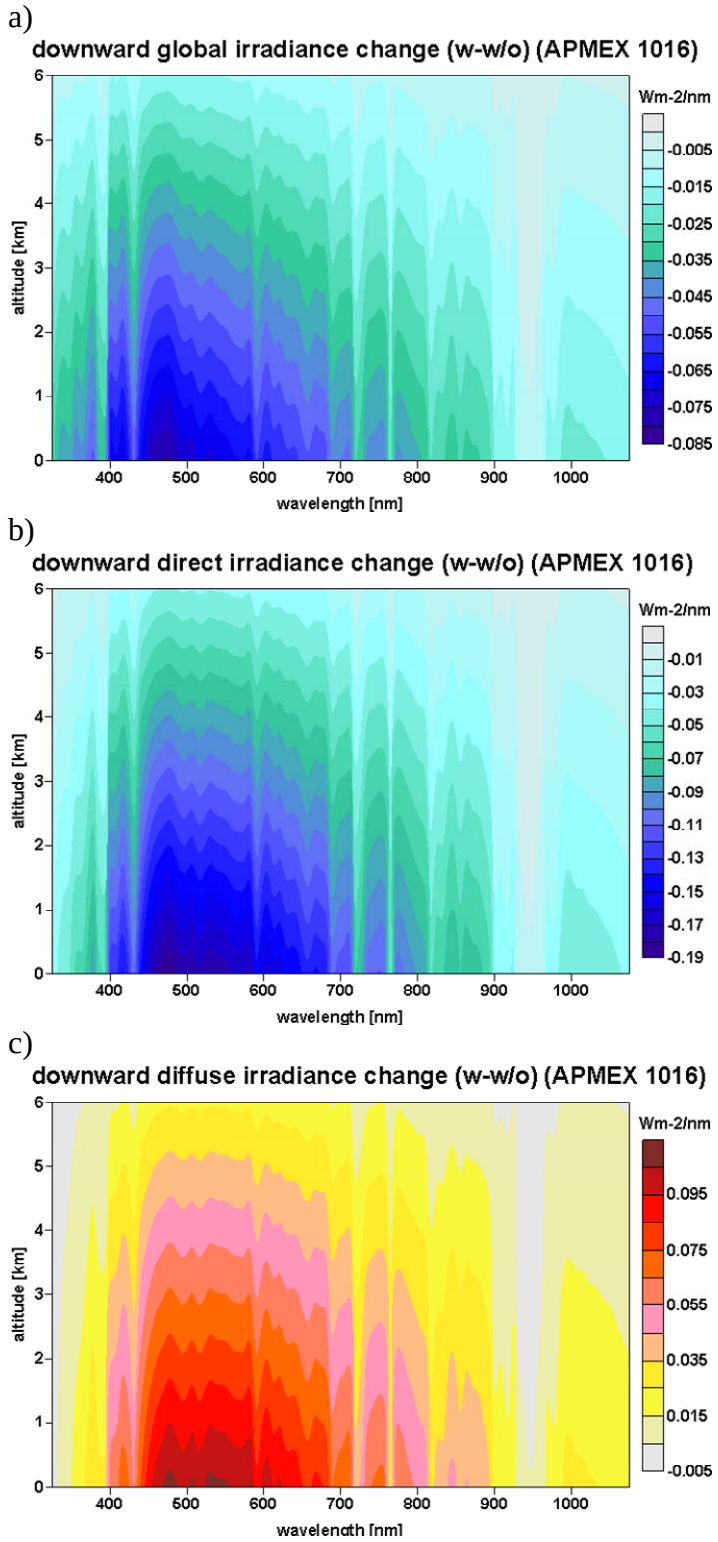

Figure 4.11: Simulation of aerosol induced a) global, b) direct, and c) diffuse irradiance change by the chemically constrained model for October 16.

To clearly demonstrate the role of aerosol mixtures in modifying incoming solar radiation and the spectral signature of aerosol forcing, which is defined as the difference of irradiance for the atmosphere with and without aerosols, Figure 4.11 presents the irradiance change induced by aerosols with moderate resolution. The downward global irradiance is decreased throughout the shortwave spectrum and large reduction occurs in the visible band with the strongest decrease in the green channel. The weakest reduction of downward irradiance lies in the water vapor absorption bands where absorption of solar radiation by water vapor is nearly saturated and the effect of aerosols is relatively small. The existence of aerosols acts to enhance the diffuse radiation, but the change in global radiation is dominated by direct radiation because its decrease is much larger than that of diffuse radiation. Thus the overall effect of aerosols is to decrease the downward radiation and lead to so-called “surface dimming”. The fact that aerosols can greatly reduce the incoming visible light that reaches the surface suggests that aerosols play a significant role in agriculture. This is because the photosynthetically active radiation ranging from 400 nm to 700 nm is of fundamental importance to plant physiology and biomass production.

Solar radiation absorbed by aerosols warms the atmosphere. As shown in Figure 4.12, the atmospheric heating rate is increased from the surface to about 6 km with large enhancement occurring in the visible band. Over the 940 nm water vapor absorption band, the net effect of aerosols is to reduce the atmospheric heating rate, mainly because water vapor absorption is nearly saturated in this band. The absorption and reflection of incoming solar radiation by aerosols, although it might be quite weak,

actually weakens the water vapor absorption. The excess heating of atmosphere by aerosols can further change the temperature and relative humidity profile and evaporate the clouds and lead to the semi-direct effect.

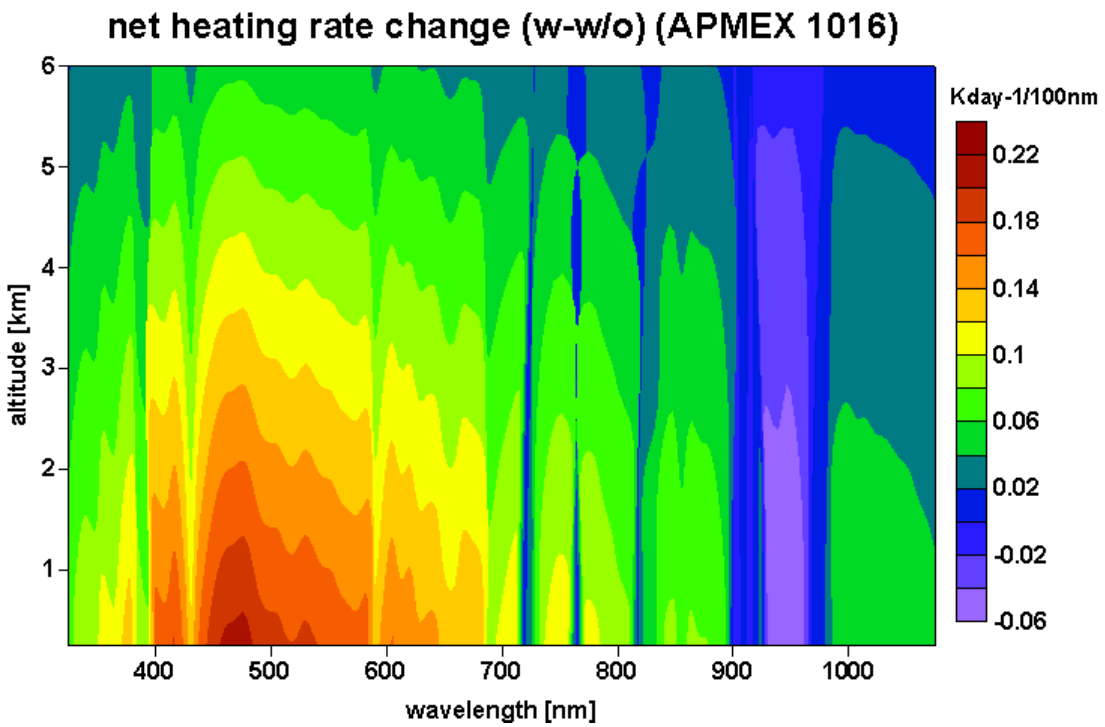

Figure 4.12: Simulation of aerosol induced atmospheric heating rate change by the chemically constrained model for October 16.

4.6 Summary and Discussion

The spectral signature of aerosol radiative forcing during APMEX can be investigated with the employment of a variety of ground-based measurements from APMEX, remote sensing data, spectrally-resolved radiative transfer model MODTRAN, and chemical analyses of single particles. The spectrally-resolved quantitative measurements of irradiance at MCOH in clear sky conditions during APMEX are used for this study. The spectral sampling interval of 1 nm for the ASD

spectroradiometer provides detailed features of the incoming solar spectrum at the surface and is used here for the comparison and validation of model simulation. This study designed two different aerosol models. One is the physically constrained model, which directly applies the observed aerosol scattering and absorbing coefficients measured at MCOH to the MODTRAN model. The other is the chemically constrained model, which uses the aerosol chemical composition observed in ATOFMS as the constraint to model the spectral variation of aerosol optical properties by assuming that the absorbing particles (such as BC, dust and brown carbon) coated with non-absorbing materials and mixed with each other externally.

The comparison between model simulation and ASD observation shows that both aerosol models simulate the spectral pattern of surface global irradiance well. Model simulations exactly follow the observation at most parts of the shortwave bands except the channel between 400 nm to 500 nm where model results are slightly larger than observations. The relative difference is within 10% for most of the spectrum, except for some gaseous absorption bands such as oxygen bands centered at 690 nm and 760 nm, and water vapor bands centered at 720 nm, 820 nm, and 940 nm. The difference in integrated irradiance throughout the bands (325-1075 nm) between the observation and model simulations is less than 4% and the chemically constrained model demonstrates much better performance than the physically constrained model. The separation of simulated direct and diffuse irradiance helps to explain the difference between these two aerosol models. The direct irradiance predicted by both models shows little difference, but there is a large difference between diffuse

irradiance in the two models. The diffuse irradiance simulated by the physically constrained model is larger than that predicted by the chemically constrained model, which suggests that aerosol mixtures simulated by the physically constrained model present much scattering properties and aerosol mixtures in the whole atmospheric column are more absorbing than those observed at the surface. The spectrally-resolved MODTRAN model assists in investigating the spectral signature of aerosol forcing. Results show that downward global irradiance is decreased throughout the shortwave spectrum and large reduction occurs in the visible band with strongest decrease at the green channel. The least reduction of downward irradiance lies in the gaseous absorption bands where absorption of solar radiation by gases is nearly saturated that so the effect of aerosols is relatively small. Aerosol absorption increases the atmospheric heating rate all the way from the surface to about 6 km with large enhancements occurring in the visible band. The extreme modification of photosynthetically active radiation by aerosols suggests that aerosols might play a fundamental role in agricultural processes.

Detailed information on the spectral variation of aerosol optical properties at different altitudes is necessary to determine the spectral signature of aerosol direct radiative forcing. Although using the observed aerosol scattering and absorption, as does the physically constrained model, is the most direct and convenient way to estimate aerosol forcing, the results in this study show that large discrepancies between the simulations of the physically constrained model and actual observations still exists especially in the visible band. The findings in this study suggest that the

measurement of aerosol scattering and absorption at the surface cannot represent the optical properties of aerosols throughout the column. Large uncertainties might be introduced into the estimation of aerosol forcing if aerosols above the boundary layer come from different sources and present distinct optical properties. A number of studies observed the elevated aerosol layers with different chemical compositions from those measured near the surface. *Zhu et al.* [2007] showed that major dust plumes over the Pacific, Indian and Atlantic Oceans are normally elevated and extinction peaks above the marine boundary layer. Using lightweight unmanned aerial vehicles, *Ramanathan et al.* [2007b] measured the vertical variation of aerosols and black carbon over the northern Indian Ocean. They found that although the boundary-layer aerosol number concentration and absorption coefficients were similar for both the clean period, when air-masses were of marine origin, and the polluted period, when air-masses from Asia were blown to the observatory over the northern Indian Ocean, the aerosol absorption coefficient above 1 km increased tenfold during polluted period and the number concentration increased from about 750 to about 2500 cm^{-3}.

Attempting to use the chemical measurements as constraints to estimate aerosol optical properties and solar irradiance changes brings other uncertainties. As described in the previous section, certain assumptions about aerosol size distribution and mixing state have been made in the chemically constrained aerosol model, which might lead to some errors in the simulated aerosol optical properties. Aerosol size distribution is commonly represented using lognormal distribution functions, which is

determined by three parameters: sigma, the standard deviation; R_{mod}, the mode radius; and N, the particle number density. Sensitivity tests with respect to these three parameters have been made for BC aerosol by varying one parameter while leaving the other two fixed. The results show that for the same aerosol species, although the magnitude of the scattering coefficient and the absorption coefficient will change for different particle number concentrations, SSA (the ratio between scattering and the sum of scattering and absorption) is independent of particle number N, given the fixed R_{mod} and sigma. As shown in Figure 4.13a, the magnitude of SSA increases by more than twice when R_{mod} increases from ~12 nm to 100 nm. Figure 4.13b shows the spectral variation of mass-normalized BC absorption cross-sections for different values of R_{mod}. It is clearly indicated that the absorption of smaller particles shows stronger wavelength dependence than that of larger particles and the Absorption Angström Exponent (AAE), termed as the negative of the slope of the absorption on a log-log plot, decreases from about 1 to 0.32. Not only does the size influence the model simulated aerosol absorption, but the shape of aerosol size distribution does as well. Figure 4.14 shows the dependence of SSA on sigma for a fixed R_{mod}. The sensitivity tests indicate that SSA depends on the sigma and increases with an increasing sigma. The influence of sigma on the spectral variation of absorption is relatively weak compared to that of R_{mod}. The mixing with other aerosol species will also change the results of aerosol absorption. As shown in Figure 4.15, the absorption strongly depends on the relative amount of BC in the mixture. The mixing of scattering aerosols such as sulfate during the aging of BC will greatly modulate the

absorbing properties of BC. More detailed information is needed to estimate aerosol optical properties using aerosol chemical composition taken from measurements.

a)

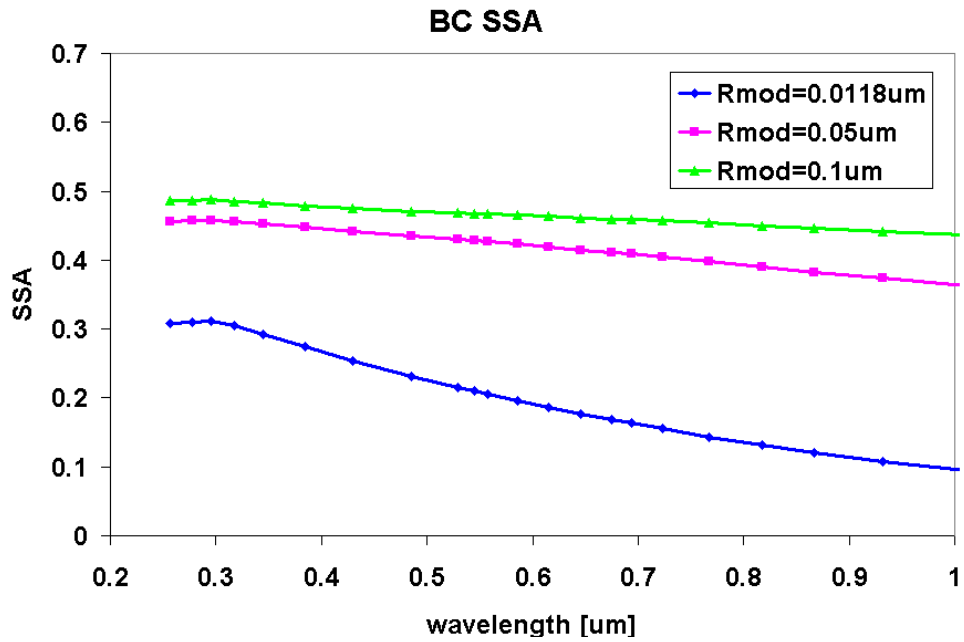

b)

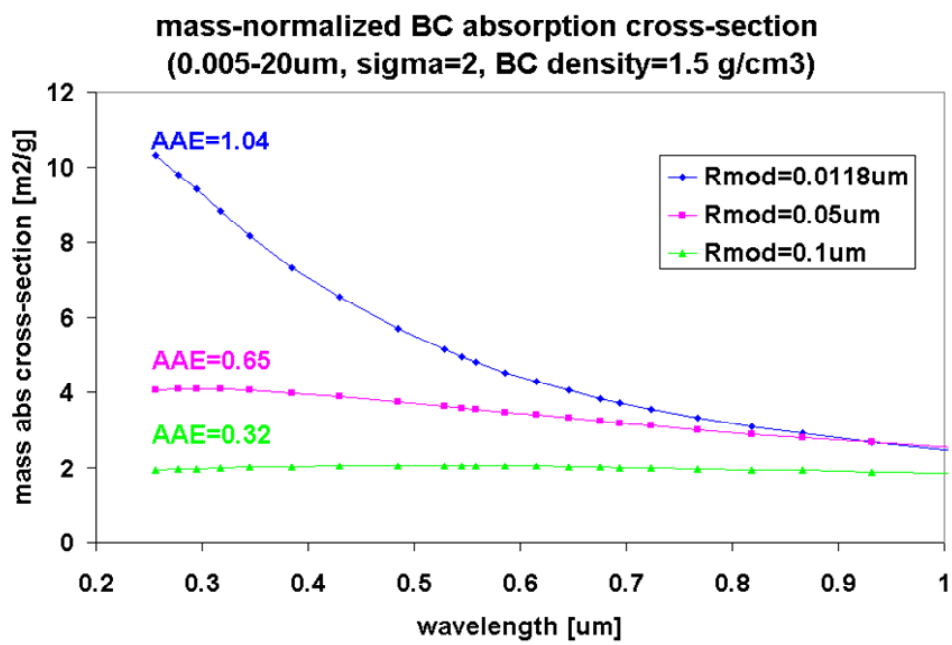

Figure 4.13: Spectral variation of a) SSA and b) mass-normalized absorption cross-section for BC with different R_{mod}.

a)

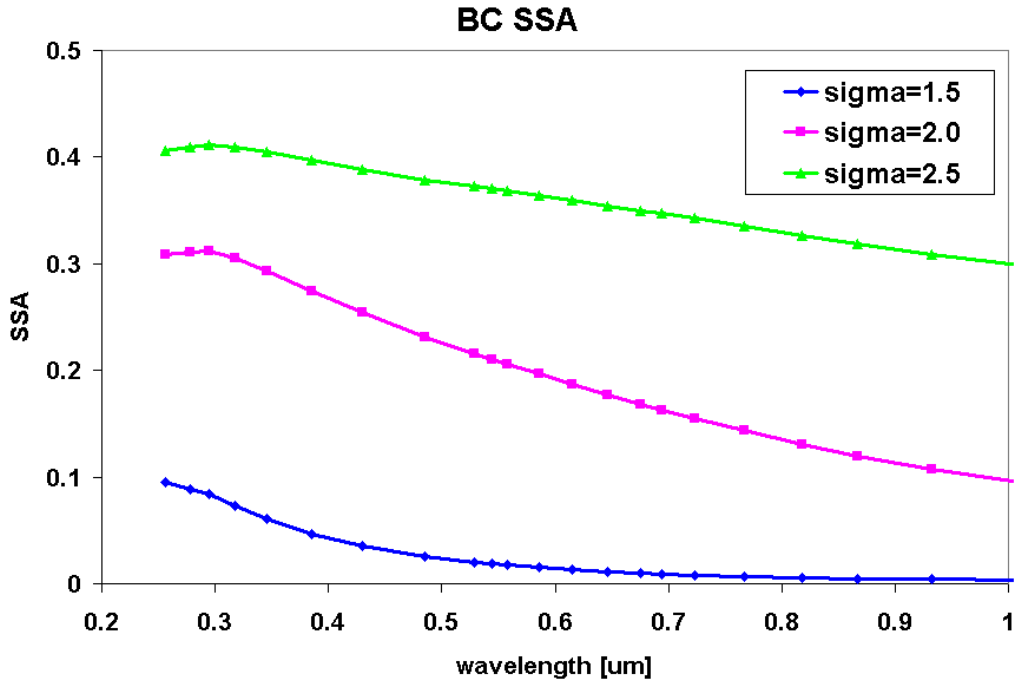

b)

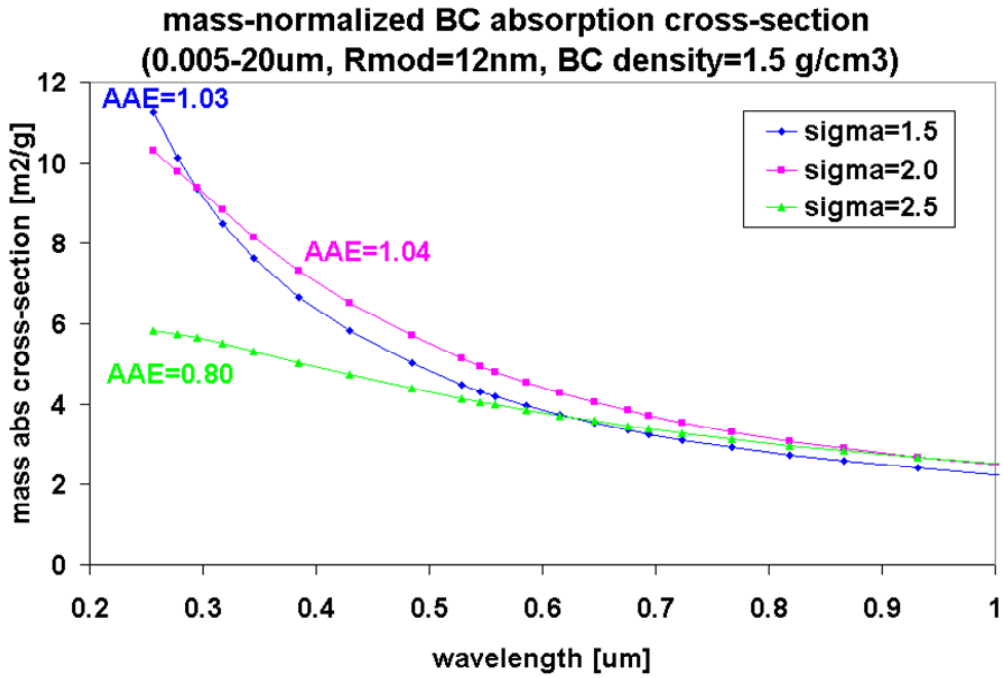

Figure 4.14: Spectral variation of a) SSA and b) mass-normalized absorption cross-section for BC with different sigma.

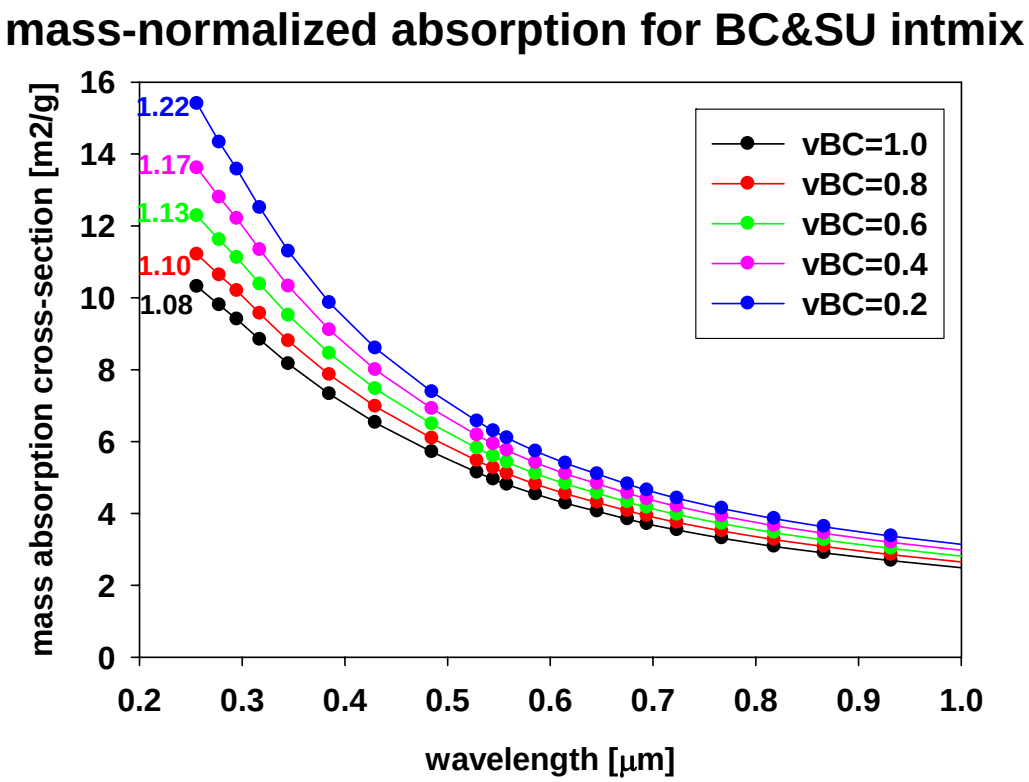

Figure 4.15: Mass-normalized absorption cross-section for aerosol mixture with BC internally mixed with sulfate, where vBC indicates the volume fraction of BC.

The combination of observation and numerical models will greatly improve our understanding of the spectral signature of aerosol radiative forcing. *Meywerk and Ramanathan* [2002] suggested that detailed studies of aerosol forcing based on spectral measurement and models are also necessary to settle the dispute on anomalous absorption, which stems from general model simulations typically underestimating solar absorption compared to observations. More intense spectral measurements around the world should be operated to provide comparisons and validation for modeled simulations. Current studies show that the spectrally-resolved radiative transfer model with moderate to fine resolution has been proved to produce a good simulation of the spectral variation of aerosol forcing. The results in this study

indicate that the accurate observations of aerosol's physical, chemical and optical properties are critical for modeled simulations. The development of techniques to monitor aerosol size, distribution, chemical composition, and mixing state will greatly improve models' performance. With increasing concern focused on issues related to the radiative and climate impacts of aerosols, much sophisticated studies of aerosol radiative forcing on nanometer spectral resolution are needed to thoroughly understand the effect of aerosols on radiation budget and climate change.

Acknowledgments

The ATOFMS data come from Prof. Prather's research group. The authors thank Dr. Matthew Spencer for his help in ATOFMS data.

Reference

Bohren, C. F., and D. R. Huffman (1983), Absorption and Scattering of Light by Small Particles, John Wiley, Hoboken, N. J.

Berk A., Anderson G. P., Acharya P. K., Hoke M. L., Chetwynd J. H., Bernstein L. S., Shettle E. P., Matthew M. W., Adler-Golden S. M. (2003), MODTRAN4 Version 3 Revision 1 User's Manual. Air Force Research Laboratory, Space Vehicles Directoriate, Air Force Materiel Command, Hanscom AFB, MA 01731-3010, Hanscom.

Boersma, K. F., H. J. Eskes, J. P. Veefkind, E. J. Brinksma, R. J. van der A, M. Sneep, G. H. J. van den Oord, P. F. Levelt, P. Stammes, J. F. Gleason, and E. J. Bucsela (2007), Near-real time retrieval of tropospheric NO2 from OMI, *Atmos. Chem. Phys.*, *7*, 2103-2118.

Chung, C. E., V. Ramanathan, D. Kim, and I. A. Podgorny (2005), Global anthropogenic aerosol direct forcing derived from satellite and ground-based observations, *J. Geophys. Res.*, 110, D24207, doi:10.1029/2005JD006356.

Clough, S. A., F. X. Kneizys, and R. W. Davies (1989), Line shape and the water vapor continuum, *Atmos. Res.*, 23, 229-241.

Corrigan, C. E., V. Ramanathan, and J. J. Schauer (2006), Impact of monsoon transitions on the physical and optical properties of aerosols, *J. Geophys. Res.*, 111, D18208, doi:10.1029/2005JD006370.

Curtiss, B., and A. F. H. Goetz (1997), Field spectrometry: Techniques and instrumentation, in *FieldSpec User's Guide*, pp. 45–58, appendix A, Analytical Spectral Devices, Inc., Boulder, CO, USA.

Draxler, R. R., and G. D. Hess (1998), An overview of the HYSPLIT_4 modeling system for trajectories, dispersion, and deposition, *Australian Meteorological Magazine*, *47*, 295-308.

Flanner, M. G., C. S. Zender, J. T. Randerson, and P. J. Rasch (2007), Present-day climate forcing and response from black carbon in snow, *J. Geophys. Res.*, 112, D11202, doi:10.1029/2006JD008003.

Gard, E., J.E. Mayer, B.D. Morrical, T. Dienes, D.P. Fergenson, and K.A. Prather (1997), Real-time analysis of individual atmospheric aerosol particles: Design and performance of a portable ATOFMS, *Analytical Chemistry*, *69* (20), 4083-4091.

Guazzotti, S.A., K.R. Coffee, and K.A. Prather (2001), Continuous measurements of size-resolved particle chemistry during INDOEX-Intensive Field Phase 99, *J. Geophys. Res.*, *106* (D22), 28607-28627.

Hansen, J., and L. Nazarenko (2004), Soot climate forcing via snow and ice albedos, *Proc. Natl. Acad. Sci.*, *101*(2), 423–428.

Hess, M., P. Koepke, and I. Schult (1998), Optical properties of aerosols and clouds: the software package OPAC. *Bull. Am. Meteorol. Soc*., 79, 831–844.

Intergovernmental Panel on Climate Change (IPCC) (2007), Climate change 2007: the scientific basis. In: Solomon, S. (Ed.), Contribution of Working Group I to the Fourth Assessment Report of the Intergovernmental Panel on Climate Change. Cambridge Univ. Press, New York.

Kim, D., and V. Ramanathan (2008), Solar radiation budget and radiative forcing due to aerosols and clouds, *J. Geophys. Res.*, 113, D02203, doi:10.1029/2007JD008434.

Kirchstetter, T. W., T. Novakov, and P. V. Hobbs (2004), Evidence that the spectral dependence of light absorption by aerosols is affected by organic carbon, *J. Geophys. Res.*, 109, D21208, doi:10.1029/2004JD004999.

Lacis, A. A., and V. Oinas (1991), A description of the correlated k distributed method for modeling nongray gaseous absorption, thermal emission, and multiple scattering in vertically inhomogeneous atmospheres. *J. Geophys. Res.*, 96, 9027-9063, doi:10.1029/90JD01945.

McClatchey et al. (1972), Optical properties of the atmosphere, Environ. Res. Pap., AFCRL-72-0497, Air Force Cambridge Res. Lab., Bedford, Mass.

Meywerk, J., and V. Ramanathan (1999), Observations of the spectral clear-sky aerosol forcing over the tropical Indian Ocean, *J. Geophys. Res.*, 104(D20), 24359-24370.

Meywerk, J., and V. Ramanathan (2002), Influence of anthropogenic aerosols on the total and spectral irradiance at the sea surface during the Indian Ocean Experiment (INDOEX) 1999, *J. Geophys. Res.*, *107*(D19), 8018, doi:10.1029/2000JD000022.

Moffet, R. C. and K. A. Prather (2009), In-situ measurements of the mixing state and optical properties of soot with implications for radiative forcing estimates, *Proc. Natl. Acad. Sci.*, 106**,** 11872-11877.

Prather, K.A., T. Nordmeyer, and K. Salt (1994), Real-time characterization of individual aerosol-particles using Time-of-Flight Mass Spectrometry, *Analytical Chemistry*, *66* (9), 1403-1407.

Pratt, K. A., P. J. DeMott, J. R. French, Z. Wang, D. L. Westphal, A. J. Heymsfield, C. H. Twohy, A. J. Prenni, and K. A. Prather (2009), In-situ detection of biological particles in cloud ice crystals. *Nature Geoscience*. 2:398-401.

Ramana, M. V., and V. Ramanathan (2006), Abrupt transition from natural to anthropogenic aerosol radiative forcing: Observations at the ABC-Maldives Climate Observatory, *J. Geophys. Res.*, 111, D20207, doi:10.1029/2006JD007063.

Ramanathan, V., et al. (2001a), Indian Ocean experiment: An integrated analysis of the climate forcing and effects of the great Indo-Asian haze, *J. Geophys. Res.*, 106, 28,371–28,398.

Ramanathan, V., P. J. Crutzen, J. T. Kiehl and D. Rosenfeld (2001b), Aerosols, Climate, and the Hydrological Cycle, *Science*, 294, 2119-2124.

Ramanathan, V., et al. (2007a), Atmospheric brown clouds: Hemispherical and regional variations in long-range transport, absorption, and radiative forcing, *J. Geophys. Res.*, 112, D22S21, doi:10.1029/2006JD008124.

Ramanathan, V., M. V. Ramana, G. C. Roberts, D. Kim, D., C. E. Corrigan, C. Chung, and D. Winker (2007b), Warming trends in Asia amplified by brown cloud solar absorption, *Nature*, 448, 575–578, doi:10.1038/nature06019.

Rothman, L. S., et al. (2003), The HITRAN molecular spectroscopic database: edition of 2000 including updates through 2001, *J. Quant. Spectros. Radiat. Transfer, 82,* 5–44.

Spencer, M. T., J. C. Holecek, C. E. Corrigan, V. Ramanathan, and K. A. Prather (2008), Size-resolved chemical composition of aerosol particles during a monsoonal transition period over the Indian Ocean, *J. Geophys. Res*., 113, D16305, doi:10.1029/2007JD008657.

Stamnes, K., S.-C. Tsay, W. Wiscombe, and K. Jayaweera (1988), Numerically Stable Algorithm for Discrete-Ordinate-Method Radiative Transfer in Multiple Scattering and Emitting Layered Media, *Applied Optics*, 27, 2502-2509.

Yu, H., et al. (2006), A review of measurement-based assessments of the aerosol direct radiative effect and forcing. *Atmos. Chem. Phys*., **6**, 613–666.

Zhu, A., V. Ramanathan, F. Li, and D. Kim (2007). Dust plumes over the Pacific, India, and Atlantic Oceans: Climatology and radiative impacts, *J. Geophys. Res*., 112, D16208, doi:10.1029/2007JD008427.

Chapter 5

Radiative Forcing and Climate Impacts of Aerosol Mixtures

5.1 Introduction

It has been recognized for many years that atmospheric aerosols strongly affect earth's climate and radiation balance. By means of reflection and absorption, aerosols directly reduce the solar radiation reaching the surface and lead to the so-called "surface dimming" effect. Absorbing aerosols, such as black carbon (BC), brown carbon, and mineral dust are found to have the ability to trap sunlight and warm the air. The excess heating caused by these absorbing aerosols can enhance the evaporation of clouds. This burning effect of absorbing aerosols is defined as aerosol semi-direct effect. Indirectly, aerosols can strongly modify cloud albedo and lifetime by acting as the cloud condensation nuclei (CCN) and ice nuclei. Furthermore, the deposition of BC on snow/ice greatly darkens the originally bright surface, alters the surface albedo and accelerates the melting of snow. *Hansen* et al. [1997] suggested that the climate sensitivity to absorbing aerosols was almost three times greater than the climate sensitivity to other forcings such as doubling CO_2. Modelling studies suggested that the re-distribution of solar energy by aerosols changes can further cause the modification of atmospheric circulation and hydrological cycle.

Intensified observations have been prompted to monitor the emission, physical and chemical characteristics, optical properties, and radiative forcing of aerosols in both regional and global scales. The developments of aerosol chemistry models

provide the approach to explore the emission, distribution, transportation, and evolution of aerosols during their lifetime in the atmosphere. Large effort has been put to assess the climate impacts caused by aerosols. However, the net effect of aerosols on the radiation budget and climate still constitutes one of the greatest uncertainties in attempts to predict and simulate climate change [IPCC, 2007]. For example, many studies suggested that absorbing aerosols have large impacts on monsoon rainfall over the Indian Subcontinent, but the results remain controversial and with heavy reliance on models. For example, the effects of aerosols on monsoon rainfall in a coupled model [*Ramanathan et al.,* 2005] were found to be different from that in uncoupled models with prescribed SSTs [*Lau et al.*, 2006] as a result of the response of the ocean to aerosol induced cooling at the surface. By superposing the observed SST changes on the climatological SSTs, *Chung and Ramanathan* [2006] conducted model simulations with CCM3, and linked the brown haze, the meridional SST gradient, and the regional monsoon rainfall in the India and the Sahel. They showed that the heterogeneous distribution of brown haze caused a strong latitudinal gradient of aerosol forcing at the surface, which led to the weakening of the meridional SST gradient in the northern Indian Ocean. The summertime weakening in the SST gradient weakens the monsoon circulation, resulting in less monsoon rainfall over India and excess rainfall in sub-Saharan Africa. Using a coupled ocean-atmosphere model with aerosols over South Asia prescribed according to observations, *Ramanathan et al.* [2005 and 2007] showed that anthropogenic aerosols increased atmospheric stability, weakened the latitudinal SST gradients in the Northern Indian

Ocean, and led to a weakening of the monsoon circulation and a reduction of monsoon rainfall over India during summer. To study the effect of BC on Indian summer monsoon, *Meehl et al.* [2008] employed CCSM3 and performed model experiments with varying BC aerosols. Their results showed that radiative effects of BC are significant during the premonsoon months (March-April-May) and the dimming effect decreases of surface temperature over most India, the Bay of Bengal, and the Arabian Sea, and BC induced shortwave heating warms the lower troposphere and the warmer air is advected northward and manifested by warming over the elevated heat source of the Tibetan Plateau, thus producing an anomalously strengthened meridional temperature gradient through most of the depth of the troposphere and enhanced rainfall over most of India. However, with the onset of the monsoon, BC concentration decreases and the elevated heat source and meridional temperature gradient decrease, which in combination with the anomalously cool SSTs in the Arabian Sea and Bay of Bengal, result in the reduced precipitation over much of India during the monsoon season of June-July-August. By means of an observation analysis, *Bollasina et al.* [2008] investigated the influence of aerosol variability on the South Asian summer monsoon and found that anomalously high aerosols in May led to the reduction of cloud amount and precipitation and increased surface shortwave radiation and land surface warming. As the monsoon progresses in June and July, the monsoon was intensified as the results of the increased thermal contrast. Their results suggested that although excessive aerosols are associated with the decline of precipitation over India in early spring, internal atmosphere-land surface feedback actually strengthens the

monsoon in subsequent summer months and land surface processes play important role in mediating monsoon evolution. Given the complexity of the radiative, cloud-microphysics, dynamic responses, and hydrometeorological processes involved with aerosols, thoroughly understand the influence of aerosols on monsoon rainfall is challenging.

In spite of the intense efforts to improve the understanding of the radiative and climate impacts of atmospheric aerosols, certain chronic and major problems remain in current studies. The first issue is the mixing state of different aerosols. Some studies emphasized on single aerosol species and neglected the fact that the chemical composition of aerosol particles might change during their aging process. Freshly emitted particles may coagulate with other preexisting aerosols, be coated by gaseous species, and get oxidized in their lifetime. Field observation showed that the majority of soot particles measured at Mexico City and Riverside were associated with sulfate, organics, nitrate, and water [*Moffet and Prather*, 2009]. The single particle chemistry analysis during INDOEX [*Guazzotti et al.,* 2001] indicated that sulfates were associated with other materials and that single particles containing pure sulfuric acid, sodium sulfate, or ammonium sulfate were rare. Some studies did consider the mixing of different aerosol species. Three different aerosol mixing states were employed in previous model studies. External mixing was widely used in most studies, which assumed that aerosol particles had no physical interaction with each other, thus the optical properties and radiative forcing of each aerosol component can be determined separately. Some assume that all aerosol species are perfectly mixed with each other at

the molecular level, thus all particles have the same composition and known as the perfect internal mixing (or volume mixing). Another mixing assumption is core-shell internal mixing (or coated mixing), in which solid particles such as BC and mineral dust serve as the core and are encapsulated by well-mixed non-absorbing materials. It has been shown from previous model studies and field measurements, accurate aerosol absorption properties are crucial for quantitative radiation budget estimates. Model studies showed that the direct radiative forcing of soot aerosols is 0.27, 0.58, and 0.78 Wm^{-2} for external mixing, core-shell mixing and internal mixing, respectively [*Jacobson,* 2000 and 2001]. The theoretical study showed that absorption is always increased when light-absorbing particles are internally mixed with other materials. *Bond et al.* [2006] suggested that absorption by aged soot particles mixed with other aerosols is about 1.5 times greater than that of fresh aerosols. The more realistic core-shell mixing state (or coated mixing) was not used in most studies.

Next, organic carbon was regarded by most if not all studies to have negligible absorption and simply treated as scattering aerosols in earlier studies. Recent studies suggested that certain organic carbon originated from biomass burning, termed as brown carbon [*Andreae and Gelenser*, 2006], has strong absorption in ultraviolet and blue spectral region and its absorption presents great wavelength dependence. The radiative and climate impacts of this absorbing brown carbon was missing in all previous model studies. Last, the vertical concentration of aerosols was found to be too close to surface for most studies and very few accounted the vertical distribution for elevated aerosol layers.

The aforementioned problems in earlier studies motivated this study. In conjunction with observations and numerical models, this study is in an attempt to investigate the radiative and climate impacts of aerosol mixtures. With the employment of radiative transfer model, the direct radiative forcing induced by aerosol mixtures was estimated for different mixing states. The NCAR climate model was adopted for the model simulations with fixed SSTs to investigate the potential impacts of aerosol mixtures on certain climate variables, such as cloud cover, temperature and relative humidity. The absorbing brown carbon was considered in the model to study its radiative forcing and climate impacts. In addition to the widely used external mixing assumption, the physically more realistic coated mixing was employed to estimate aerosol optical properties. The elevated aerosol profile was combined with commonly used boundary layer aerosol profiles to describe the vertical distribution of aerosols. The radiative transfer model and inputs for the calculation of aerosol direct radiative forcing are depicted in section 2. Aerosol direct radiative forcing for different mixing states is shown in section 3. The climate model and experimental results are described in section 4. Discussion and conclusions are discussed in section 6.

5.2 Radiative Transfer Model

The Monte-Carlo Aerosol Cloud Radiation (MACR) model was used on the T42 grid (approximately 2.8° × 2.8° resolution) to estimate shortwave (SW) aerosol direct radiative forcing. MACR model has been validated extensively with observations and employed widely to field experiments including Indian Ocean

Experiment (INDOEX) [*Ramanathan et al.*, 2001a; *Satheesh and Ramanathan*, 2000], ABC Post-Monsoon Experiment (APMEX) [*Ramana and Ramanathan*, 2006], and Maldives Autonomous unmanned aerial vehicle Campaign (MAC) [*Ramanathan et al.*, 2007; *Ramana et al.,* 2007]. It has also been used to estimate the direct effect of anthropogenic aerosols [*Chung et al.,* 2005] and the radiative impacts of dust plumes over the oceans [*Zhu et al.,* 2007]. Recently, *Kim et al.* [2008] incorporated multiple datasets with MACR and successfully produced the solar radiation budget on global scale.

5.2.1 Description of MACR

MACR was built upon the conception that the radiative transfer of incident light can be numerically simulated in terms of the fates of a large number of individual photons releasing from top-of-atmosphere and tracing them travelling through the medium. The subsequent fate of each photon, however, is determined by its chance to encounter with the scattering and/or absorbing particles in each layer. Although the fate of each photon is a random process, the probability of the journey of a particular photon is governed by Beer's Law which determines the fraction of the incident photons that can reach the lower boundary of the layer without being extinguished (scattered or absorbed). The scattering phase function (or asymmetry factor) may be regarded as a transformation probability function that redistributes the photons in different directions. The degree of single scattering albedo influences the fraction of extinguished photons that gets absorbed. To obtain statistically accurate results, one million photons were deployed in the simulations.

Totally 32 bands from 0.25 μm to 5.0 μm and 52 vertical layers are used in MACR to calculate of solar radiation. MACR has the ability to calculate the multiple scattering and absorption by gases, aerosols, clouds, and reflection from surface. HITRAN2000 and CKD2.4 databases were incorporated with the correlated k-distribution method to estimate gaseous absorption and water vapor continuum absorption. The model is capable of applying 3-D aerosol observations to explore the radiative impacts of aerosol mixtures [*Zhu et al.,* 2007].

5.2.2 Aerosol Input

The optical properties and aerosol distribution are two of the key parameters to estimate aerosol direct radiative forcing. Each of them is discussed in the following sections separately.

5.2.2.1 Aerosol Optical Properties

Three intrinsic optical properties: extinction coefficient, single scattering albedo (SSA), and asymmetry parameter are required to simulate the radiative forcing of aerosols. The aerosol optical depth (AOD), a quantitative measure of how much aerosols preventing the transmission of light, is widely used to represent the integrated columnar aerosol extinction and to evaluate aerosol direct radiative forcing. SSA, defined as the ratio of the scattering efficiency to total light extinction, characterizes the relative importance of scattering versus absorption for aerosol particles. Asymmetry parameter, which is the first moment of the phase function, denotes the relative strength of forward scattering for light encountering aerosol particles. The AOD data used in this study is the integration of MODIS (Moderate Resolution

Imaging Spectroradiometer) satellite observation, GOCART (The Goddard Chemistry Aerosol Radiation and Transport) model simulation, and ground-based AERONET (AErosol RObotic NETwork) measurements. Regions with high aerosol loading can be easily identified from the annual AOD map (Figure 5.1a), including eastern China, south Asia, north and central Africa. Detailed description about the integration method and the application of this assimilated AOD products have been discussed by *Chung et al.* [2005].

The way in which different aerosol species mix with each other plays a critical role in determining the optical properties of aerosol mixtures. Commonly used external mixing, which has BC, OC, sulfate, sea-salt, and dust externally mixed with no interaction with each other, was selected to provide the inter-comparison with other model studies listed in IPCC report, and named as the ipcc external mixing (ipcc). The second mixing state is similar to the aforementioned ipcc external mixing, but replaces 20% of OC with the absorbing brown carbon in order to test the effects of brown carbon (ext). Observations have shown that the aging process is unavoidable in the lifetime of aerosol particles because freshly emitted particles may coagulate with other preexisting aerosols, be coated by gaseous species, and get oxidized. Thus, the assumption that different aerosol components are externally mixed with no interaction might only be appropriate for freshly emitted particles close the source. To represent the aerosol mixtures that are more realistic and physically reasonable, the coated mixing (coat) was employed, which assumed that absorbing aerosols (BC, brown carbon, and dust) were coated with non-absorbing material (sulfuric acid) and

externally mixed with non-absorbing particles (non-absorbing OC and sea-salt mixed with sulfuric acid).

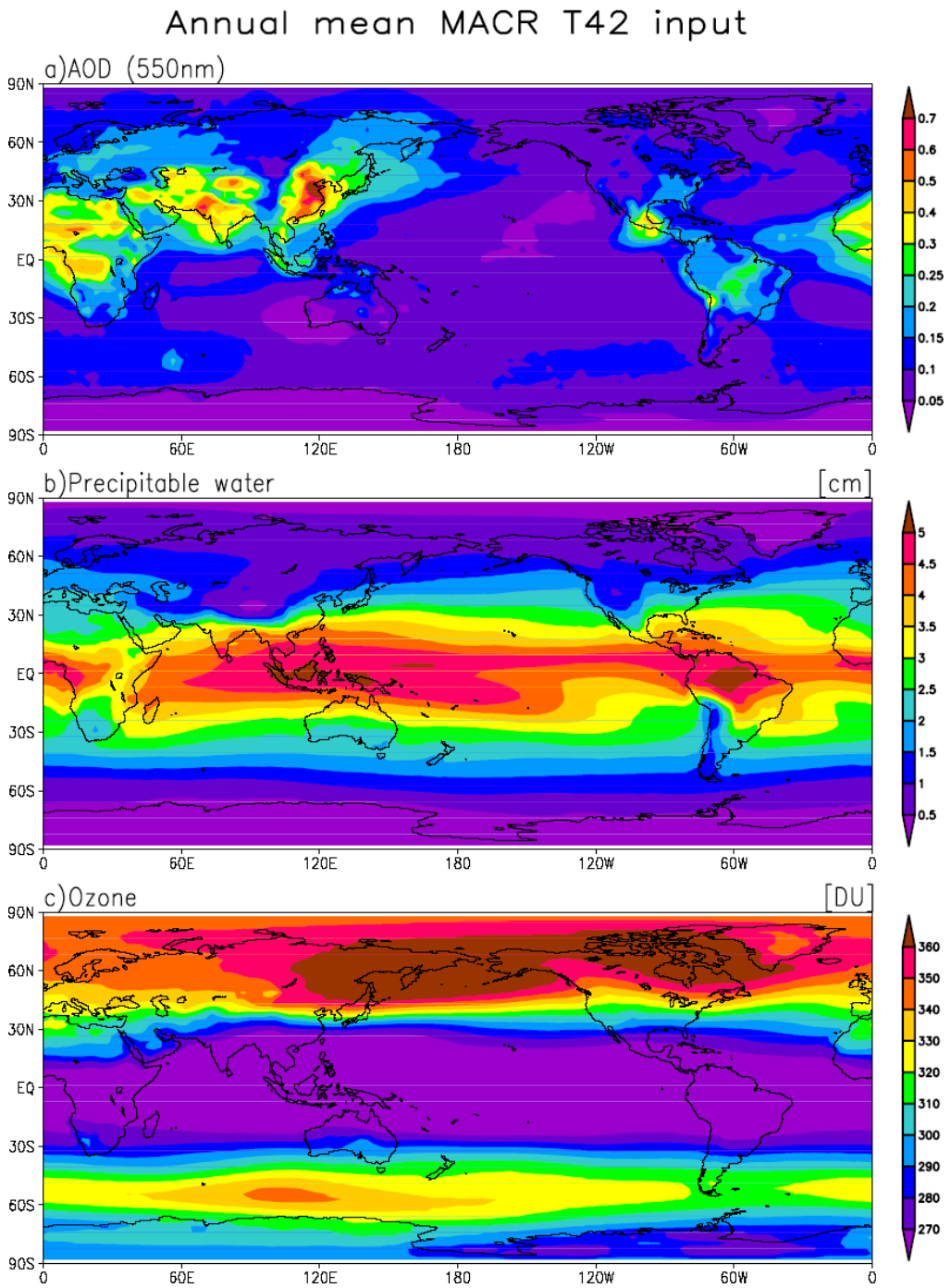

Figure 5.1: Annual mean a) assimilated AOD (550nm), b) precipitable water [cm], and c) columnar ozone amount [Du].

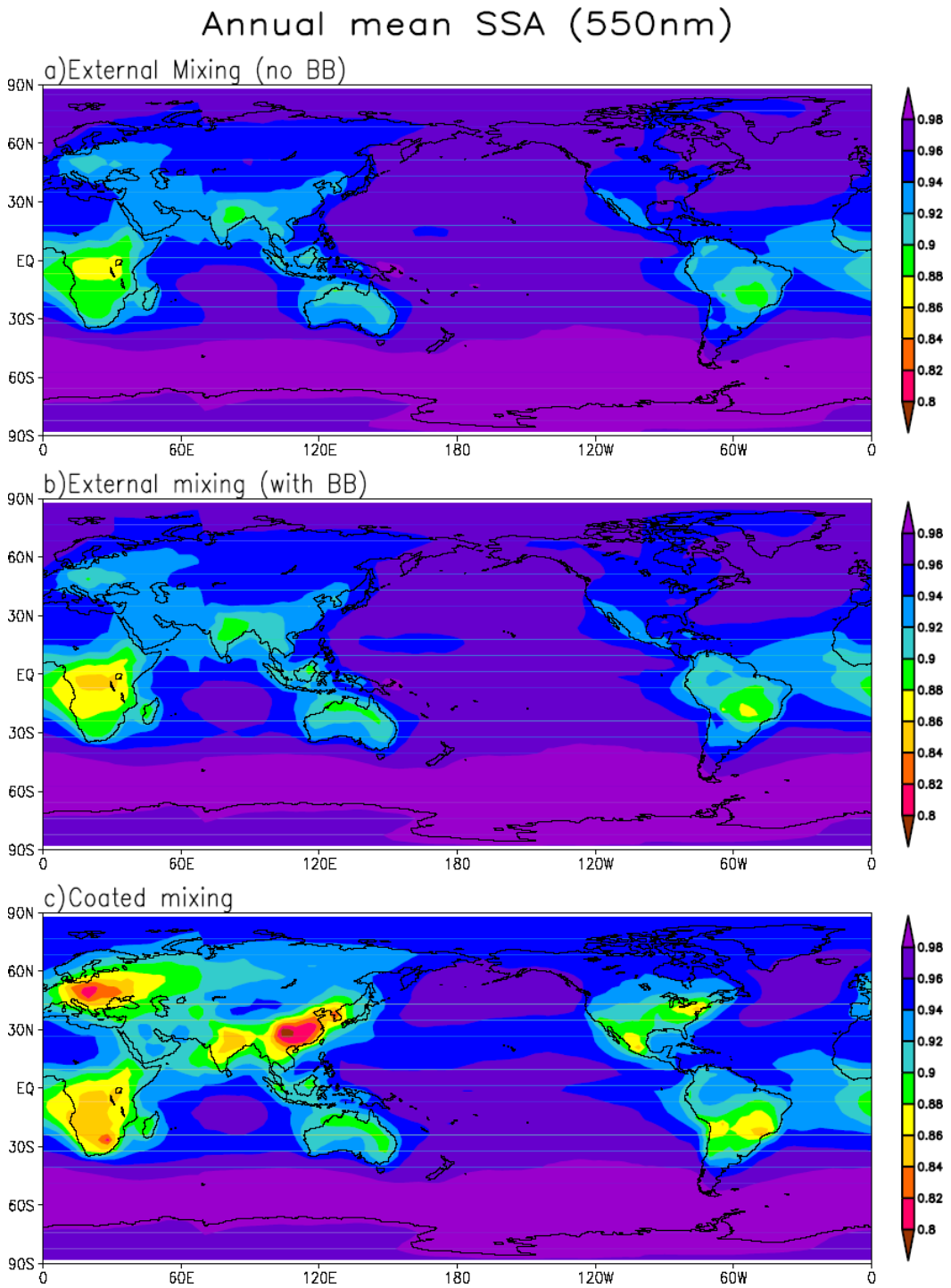

Figure 5.2: Annual mean aerosol single scattering albedo (at 550 nm) for a) ipcc external mixing (without brown carbon), b) external mixing (with brown carbon), and c) coated mixing.

For external mixing cases, extinction and absorption coefficients, and asymmetry factor for each aerosol component were calculated based on Mie theory. The coated spheres code provided by *Bohren and Huffman* [1983] was employed to calculate the optical properties for coated aerosols. The size distribution for individual aerosol component and refractive index of BC, sulfate, and sea-salt were adopted from OPAC datasets [*Hess et al.,* 1998]. For convenience in our parameterization, the refractive index of water soluble species from OPAC dataset was assigned to represent organic carbon which has weak absorption to solar radiation. The findings from *Kirchstetter et al.* [2004] were employed as the refractive index of brown carbon. Dust aerosols were categorized as three groups based on the study of *Zhu et al.*'[2007], including dust plumes over East Asia and the Pacific Ocean, over South Asia and the India Ocean, and over Africa and the Atlantic Ocean. The spectrally-resolved extinction coefficient was then normalized with respect to the value at 550 nm for the application of the assimilated AOD data. The fraction of each aerosol component was derived from GOCART model, which simulates major tropospheric aerosol components, including sulfate, dust, BC, OC, and sea-salt aerosols.

Model simulated aerosol single scattering albedo for aforementioned three mixing states are shown in Figure 5.2. It's clear that the consideration of brown carbon slightly increases aerosol absorption, especially over areas where OC has large contribution, such as equatorial Africa and South America. Aerosols become more absorbing when they are internally mixed. The coating of non-absorbing materials on the absorbing particles drastically increase the absorbing capability of aerosol particles.

Large enhancement of absorption for coated mixing state can be found over east and south china, India, Europe, southern Africa where BC and sulfate are known to be the major sources of emissions. The global annual mean SSA (550nm) for coated mixing state is 0.95, and for external mixing state SSA is about 0.96 (table 5.1).

Table 5.1: Global annual mean SSA (550nm) and all sky aerosol direct radiative forcing at the top-of-the-atmosphere (TOA), the atmosphere and the surface for different mixing states.

	ipcc	ext	coat
SSA@550nm	0.961	0.963	0.950
TOA	-1.48 (-0.78%)	-1.43 (-0.75%)	-1.28 (-0.67%)
Atmos	+2.53 (+4.30%)	+2.67 (+4.53%)	+3.32 (+5.64%)
SFC	-4.00 (-3.05%)	-4.10 (-3.13%)	-4.60 (-3.51%)

5.2.2.2 Aerosol Vertical Profile

It has been shown that aerosol induced radiative forcing is largely influenced by the relative location of aerosol layer and clouds [*Liao and Seinfeld*, 1998a and 1998b]. The vertical distribution of absorbing aerosols plays a key role in changing the pattern of atmospheric heating rate [*Carlson and Benjamin* 1980]. The vertical profile of atmospheric aerosols varies with time, location and different aerosol species. Boundary layer aerosol profile is conventionally used in model to represent the vertical distribution of aerosols with maximum concentration near the surface and decreasing rapidly with height. However, more observations also showed that aerosol particles can be advected to higher altitude as high as above the boundary layer and they peak at about 3 km [*Zhu et al.,* 2007]. We considered both boundary layer aerosol profile and elevated aerosol profile were concerned in this study. For tropical region

(30°S-30°N), we assume that aerosol profile is formed with two thirds of boundary layer aerosol and one third of elevated aerosols peaking at 3 km. For extratropics, the aerosol profile is assumed to be dominated by elevated aerosols, while boundary layer aerosols account for only one third of the total aerosols. Above 5 km, aerosol concentration is negligible.

5.2.3 Other Input

The ISCCP (International Satellite Cloud Climatology Project) D2 monthly mean cloud products were used to account for optical depth and coverage for four types of clouds, which are low-level, mid-level, high-level, and deep convective clouds. Approximately 10 years (Jan 1990 to Sep 2001) ISCCP D2 cloud data were averaged to generate the cloud climatology dataset. The ISCCP D2 products were also used to generate the mean surface albedo. The clear-sky visible surface reflectance data ranging from Jan 1990 to Dec 2000 is averaged to provide a climatological surface albedo. The vertically-integrated amount of precipitable water (Figure 5.1b) and ozone (Figure 5.1c) were derived from the Tiros Operational Vertical Sounder (TOVS). Six years of precipitable water data ranging from 1992 to 1997 were averaged for the model input. Ozone data covers two decades (Jan 1999 to Sep 2000) and its information has been included to ISCCP D2 products. A standard mid-latitude summer atmospheric profile was used in MACR model to describe the vertical distribution of ozone and water vapor. Both ISCCP data and TOVS data are a function of time and location and are interpolated onto the T42 grid for model input. More detailed information about these datasets was described by *Chung et al.* [2005].

5.3 Aerosol Direct Radiative Forcing

In this study, aerosol direct radiative forcing is defined as the difference of net solar radiation between the simulations with aerosols and without aerosols. The monthly mean aerosol radiative forcing (ARF) was calculated for different mixing states. Figure 5.3 shows the global distribution of annual mean aerosol direct radiative forcing for ipcc external mixing state. Clearly, aerosol forcing at the TOA is generally negative and the net effect of aerosols is to cool the Earth-Atmosphere system, with exceptions over areas covered by desert and ice/snow, where aerosols cause slight warming. Over these areas with high surface albedo, the presence of absorbing aerosols traps part of the sun light reflected from the underlying bright surface and reduces the overall co-albedo of the surface and air. Aerosols have large negative forcing at the surface by cutting off the incoming solar radiation through absorption and scattering, well known as “dimming” effect. The reduction of sun light reaching surface can be as large as over 30 Wm^{-2} over regions with high aerosol loading. Large amount of energy is trapped into the atmosphere by absorbing aerosols and this additional absorption may heat the air and causes extra warming.

Because of the heterogeneous distribution of emission sources over the continent, aerosol induced radiative forcing has large spatial gradient with larger radiative forcing over land than over the ocean. For ipcc external mixing, annual mean aerosol forcing over the ocean is about -1.32 and -3.09 Wm^{-2}, at the TOA and the surface, respectively, which leads to about 1.77 Wm^{-2} heating to the atmosphere over the oceans. While over the land, aerosol forcing enhanced by a factor of 1.26 at the

TOA (-1.66 Wm^{-2}) and 1.78 at the surface (-5.51 Wm^{-2}), so the atmospheric absorption over land is 3.85 Wm^{-2} and about twice as large as that over the oceans. The nonuniform spatial distribution of aerosol radiative forcing implies great change of temperature contrast between land and ocean.

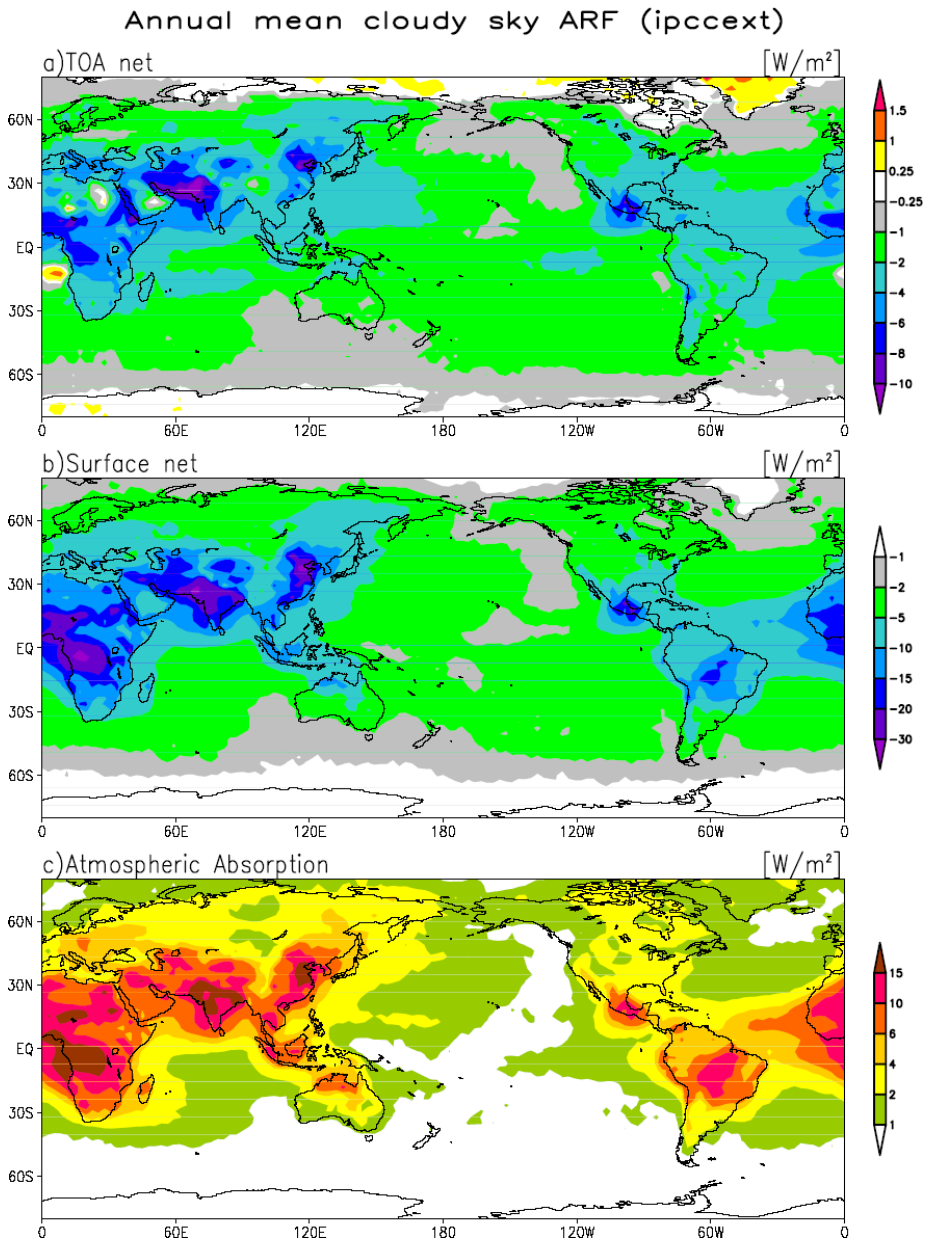

Figure 5.3: All sky annual mean aerosol radiative forcing at the a) TOA, the b) surface, and the c) atmosphere for ipcc external mixing state (without brown carbon).

It is clearly seen that aerosol radiative forcing is quite heterogeneous in space and presents large latitudinal variation and hemisphere asymmetry. As shown in Figure 5.4a, for ipcc external mixing, the largest aerosol forcing is found around 15°N due to high concentration of absorbing aerosols there. Aerosol forcing gradually decreases towards high latitude region and shows a minimum forcing over Polar Regions. Aerosol forcing at the TOA (surface) is -2.01 (-5.82) Wm^{-2} over Southern Hemisphere (SH) and -3.95 (-11.38) Wm^{-2} over Northern Hemisphere (NH), respectively. Aerosol forcing over NH is stronger than SH by a factor of ~2 simply because NH has more continents. More energy is trapped into atmosphere over NH than SH, which has great potential to modulate the atmospheric meridional circulation pattern.

Inclusion of brown carbon and the coating of non-absorbing materials on absorbing particles greatly increase aerosol absorption (Figure 5.4b). For externally mixed aerosols, replacing 20% OC with brown carbon slightly increased atmospheric absorption, As shown seen in Figure 5.5a, the replacement of 20% of OC with brown carbon leads to larger radiative forcing, mainly over tropical region, where OC contributes a large part of total aerosols. Compared to external mixing, the coating of non-absorbing materials on absorbing particles greatly amplifies atmospheric absorption over NH, especially in the mid-latitudes. The areas with great enhancement of atmospheric absorption by coated aerosols are mainly around industrial region, including East and South Asia, Europe, and East coast of US. As large as over 20

Wm^{-2} more heating is introduced to the atmosphere over East China where contributions of BC and sulfate are dominant.

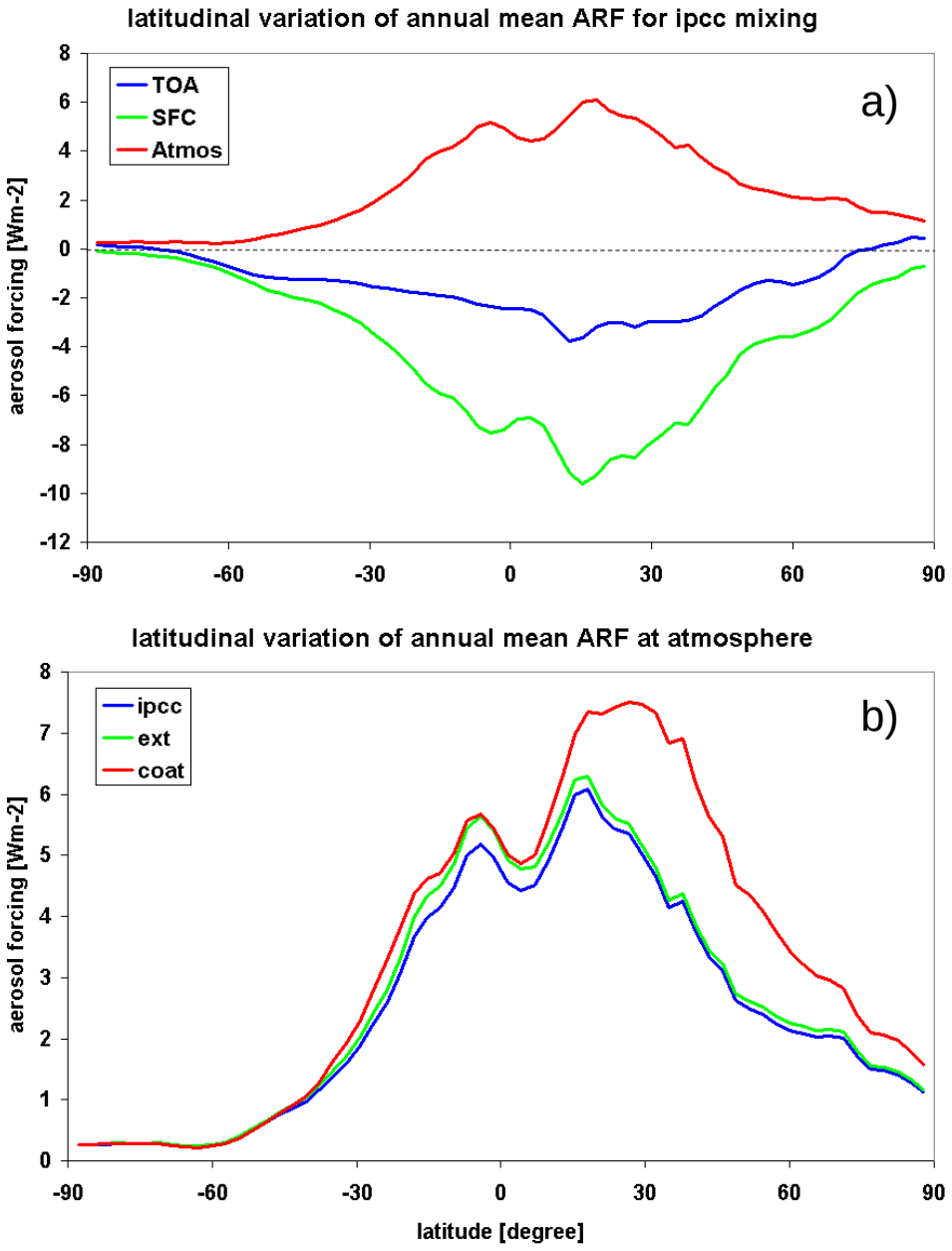

Figure 5.4: a) Latitudinal variation of all sky a) annual mean aerosol radiative forcing for ipcc external mixing, b) aerosol induced atmospheric absorption for different mixing states.

The global annual mean aerosol forcing for different mixing states are listed in table 5.1. Aerosol induced TOA forcing ranges from -1.48 Wm^{-2} for ipcc external mixing to -1.28 Wm^{-2} for coated mixing. The surface flux is reduced over 3% by the dimming effect of aerosols and as large as 5.6% more solar energy is trapped into the atmosphere due the absorption of aerosol particles. Inclusion of brown carbon slightly increases atmospheric absorption. Compared to external mixing, coated mixing has stronger radiative forcing at the surface but relatively weaker forcing at the TOA.

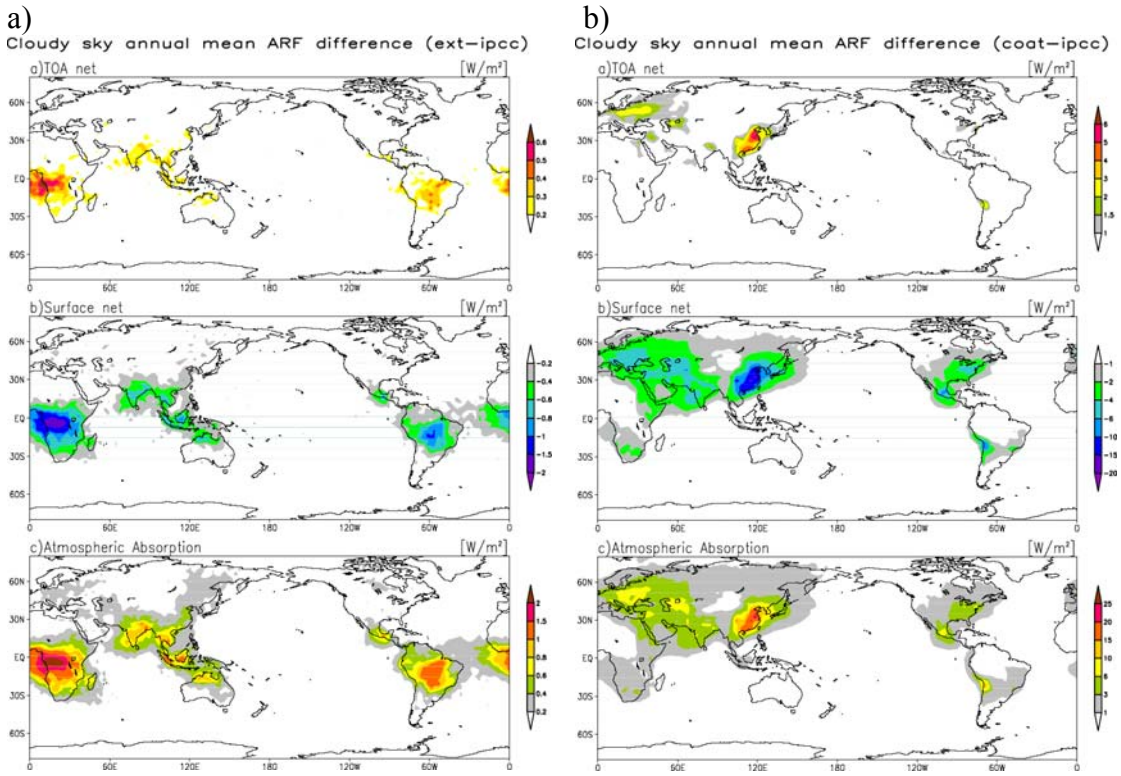

Figure 5.5: All sky annual mean ARF difference at the TOA, the surface, and the atmosphere for a) external mixing state (with brown carbon), and b) coated mixing state relative to ipcc external mixing state (without brown carbon).

The trapped solar energy warms up the air and consequently alters the atmospheric heating rate. Figure 5.6 represents heating rate change by aerosols for

different mixing states over tropics (30°S-30°N) and extratropics. The pattern of aerosol induced heating rate generally follows the prescribed aerosol vertical distribution. Aerosol induced heating peaks at 3 km for both tropics and extratropics. Over tropics, aerosols cause as large as over 0.12 Kday^{-1} more heating at ~3 km and about 0.09 Kday-1 heating near the surface, suggesting double peaks of heating. But over extratropics, a single peak of aerosol heating rate is detected at ~ 3 km (700 mb). Coated mixing leads to largest change of heating rate and showed strongest potential to warm the air in both tropics and extratropics.

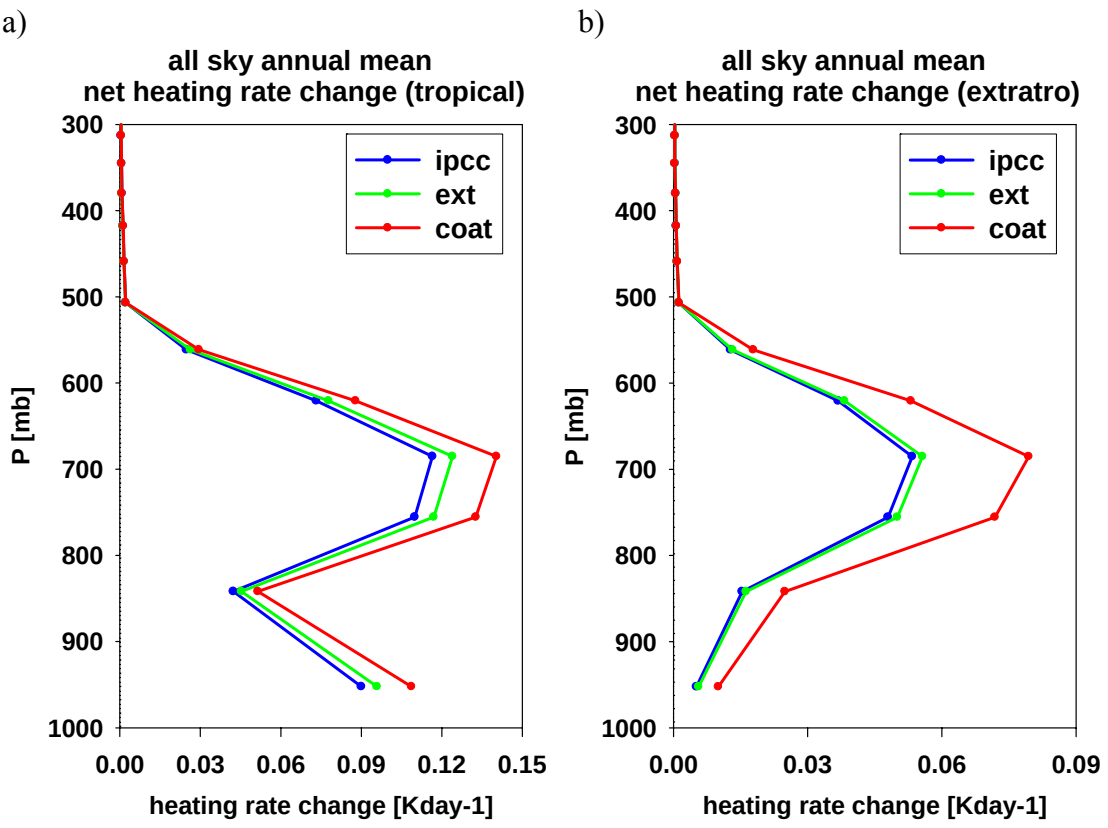

Figure 5.6: All sky annual mean heating rate change for a) tropical area (30S-30N) and b) extra-tropical area (90S-30S and 30N-90N).

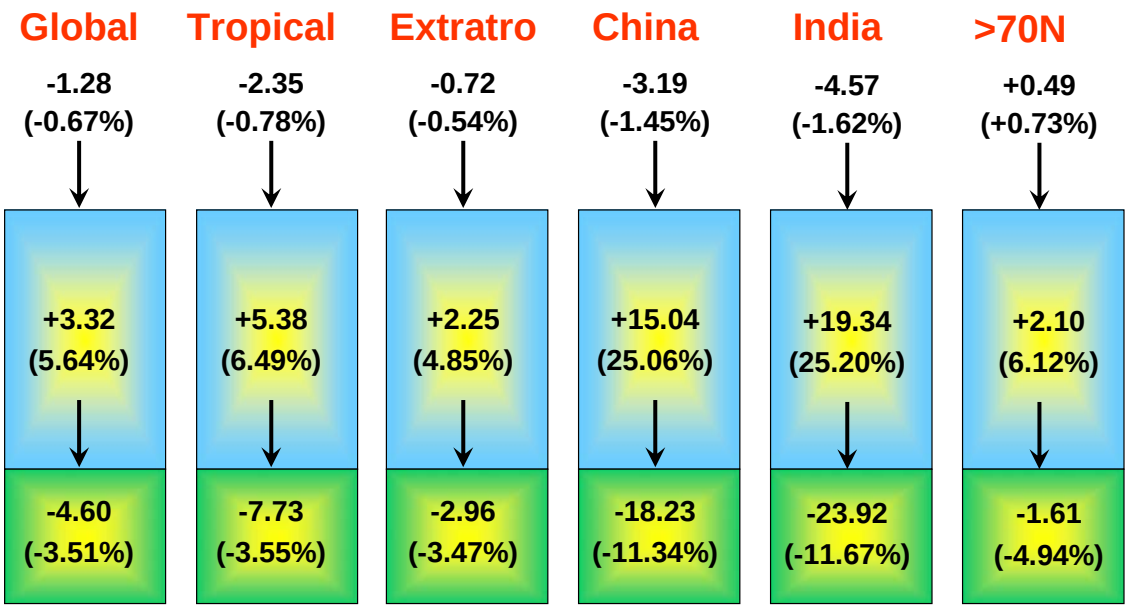

Figure 5.7: Comparison of all sky annual mean ARF (coated mixing state) for different region. Inside parenthesis are the percentage changes relative to without aerosol case.

Figure 5.7 presents the annual mean aerosol radiative forcing over global and different regions for coated mixing state. On global average, aerosols induce -1.28 Wm^{-2} radiative forcing at the TOA, indicating the net cooling effect of aerosols on the atmosphere-Earth system. At the Earth surface, there is a decrease of about 4.60 Wm^{-2} solar fluxes, which accounts for 3.51% reduction of solar flux reaching surface. Most of the reduced sunlight is trapped into the atmosphere (3.32 Wm^{-2}) and enhances atmospheric absorption by 5.64%. Aerosol induced radiative forcing is spatially nonuniform. Over tropical region (30°S-30°N), aerosol forcing is -2.35, +5.38, and -7.73 Wm^{-2} at the TOA, atmosphere, and surface, respectively, by a factor of 2 larger than the forcing over extratropics. Strongest aerosol forcing is found over China and India, where the TOA forcing is about 2 to 3 times larger, and surface forcing is about

4 to 5 times larger than global mean aerosol forcing, which leads to enormous heating to the atmosphere over these areas. Even over the Arctic region (>70°N), aerosol introduces about 2.10 Wm-2 additional warming to the atmosphere, which contributes to about 6.12% change of atmospheric absorption.

5.4 Numerical Experiments and Results

5.4.1 Description of CAM3

To understand the global climate impacts of aerosols, we employ NCAR Community Atmosphere Model version 3 (CAM3) was chosen to perform the numerical experiments in order to understand the climate impacts of aerosols. CAM3 is characterized by two computational phases: the dynamics, which advances the evolution equations for the atmospheric flow, and the physics, which approximates sub-grid phenomena such as convection, clouds, precipitation processes, shortwave and longwave radiation, turbulent mixing, boundary layer process, and surface exchange [*Collins et al.*, 2004]. The approximations in the physics are referred to as the physical parameterizations. CAM3 includes multiple options for the dynamics, referred to as dynamical cores. Three options of dynamical cores are supported for the CAM3: a spectral Eulerian, a spectral semi-Lagrangian, and a finite-volume. CAM3 includes an interactive land surface model [*Bonan* et al., 2002] which provides comprehensive treatment of land surface processes. This sophisticated model includes parameterization of land surface fluxes of energy, momentum, water, and CO2 exchange via bulk exchange formulas. CAM3 also provide an optional slab mixed-layer ocean/thermodynamic sea-ice models for coupling ocean components. Slab

ocean model allows for a fully-interactive treatment of surface exchange processes and ensures replication of realistic sea surface temperatures and ice distributions for the present climate.

The absorptivity/emissitivity formulation from *Ramanathan and Downey* [1986] is employed in CAM3 to represent longwave radiative transfer. The broadband approach based on the earlier work of *Ramanathan* [1976] is adopted to give the solution for a given gas. The two stream δ-Eddington approximation described in *Briegleb* [1992] is implemented for the reflectivity and transmissivity of shortwave radiation for each vertical layer under clear and overcast conditions. Gaseous absorption by O_3, CO_2, O_2, and H_2O, molecular scattering and scattering/absorption by cloud droplets and aerosols are included in CAM3. Updated parameterization obtained from the HITRAN2k and CKD2.4.1 data base increases the absorption of solar radiation by water. Total 19 discrete spectral and pseudo-spectral intervals are used to divide the solar spectrum. The surface albedo is specified in two wavelength bands (0.2-0.7 μm and 0.7-5.0 μm). Albedos for direct and diffuse incident radiation are distinguished, and albedos for ocean surfaces, geographically varying land surfaces, and sea ice surfaces are distinguished. CAM3 includes a mechanism for treating the slow variations in the solar constant over the 11-year cycle and during longer secular trends.

A more realistically prognostic treatment of cloud condensed water was employed in CAM3. Cloud amount and associated optical properties are evaluated through a diagnostic method introduced by *Slingo* [1987]. Cloud fraction depends on

relative humidity, atmospheric stability and convective mass fluxes. Three types of cloud are diagnosed by this scheme: low-level marine stratus, convective cloud, and layered cloud. Marine stratocumulus clouds are diagnosed using an empirical relationship between marine stratocumulus cloud fraction and the thermal stratification between the surface and 700mb derived by *Klein and Hartmann* [1993]. Convective cloud fraction in the model is related to updraft mass flux in the deep and shallow cumulus schemes according to a functional from suggested by *Xu and Krueger* [1991]. Layered clouds form when the relative humidity exceeds a threshold value with varies according to pressure. The total cloud within each volume is a maximum overlap of aforementioned three types of clouds within each grid box.

Prescribed aerosol data for computing shortwave aerosol radiative forcing is introduced in CAM3, which consist of five chemical species of aerosols, including sea salt, soil dust, black and organic carbon, and sulfate, and volcanic sulfuric acid. CAM3 includes the direct and semi-direct effects of tropospheric aerosols on shortwave fluxes and heating rates, but not first indirect effect.

5.4.2 Experimental Set-up

In order to investigate the impacts of aerosol mixtures on the climate, a series of numerical experiments were performed at a standard CAM3 configuration, i.e., T42 (2.8° × 2.8°) and L26 resolutions, using a spectral Eulerian dynamical core. The model was initialized in September, 2000. A climatological (averaged from 1981 to 2001) annual cycle of sea surface temperatures (SSTs) and sea ice distributions are prescribed as the ocean boundary conditions.

Four model experiments were performed to investigate the impacts of aerosol mixtures. The prescribed aerosols included in CAM3 were turned off for all four experiments. For the control run (cont), no aerosol effects were included thus the results represent the aerosol-free baseline condition. The pre-calculated aerosol radiative forcings for ipcc external mixing without brown carbon (ipcc), external mixing with brown carbon (ext), and coated mixing (coat) were directly inserted into CAM3 for the other three experimental runs with aerosol direct effects. All other variables and external forcings remain the same as the control run. The main reasons to directly insert pre-calculated aerosol radiative forcing into CAM3 instead of using CAM3 shortwave radiative transfer scheme to calculate aerosol forcing are: first, AOD distribution based on observation can be employed to calculate aerosol forcing and the dependence of aerosol loading on meteorological conditions (hygroscopic growth with relative humidity, transportation by wind, removal by precipitation etc.) can be removed; second, aerosol direct radiative forcing was pre-calculated from MACR thus the ratio of aerosol forcing at the TOA and at the surface is fixed and will not be affected by the variation of clouds in CAM3 because clouds have mask effects on aerosol direct radiative forcing. Thus, independent approach ensures that the estimated aerosol direct radiative forcing is largely based on observations.

CAM3 reaches equilibrium in less than one year when it is run uncoupled (i.e., without an ocean model) for prescribed boundary layer condition (SSTs, or aerosol radiative forcing). For each experimental simulation, the model was run for over 5 years to ensure the model reaching the equilibrium and the last four calendar year

simulations were averaged for the analysis to study the climate response of inserted aerosol direct radiative forcing.

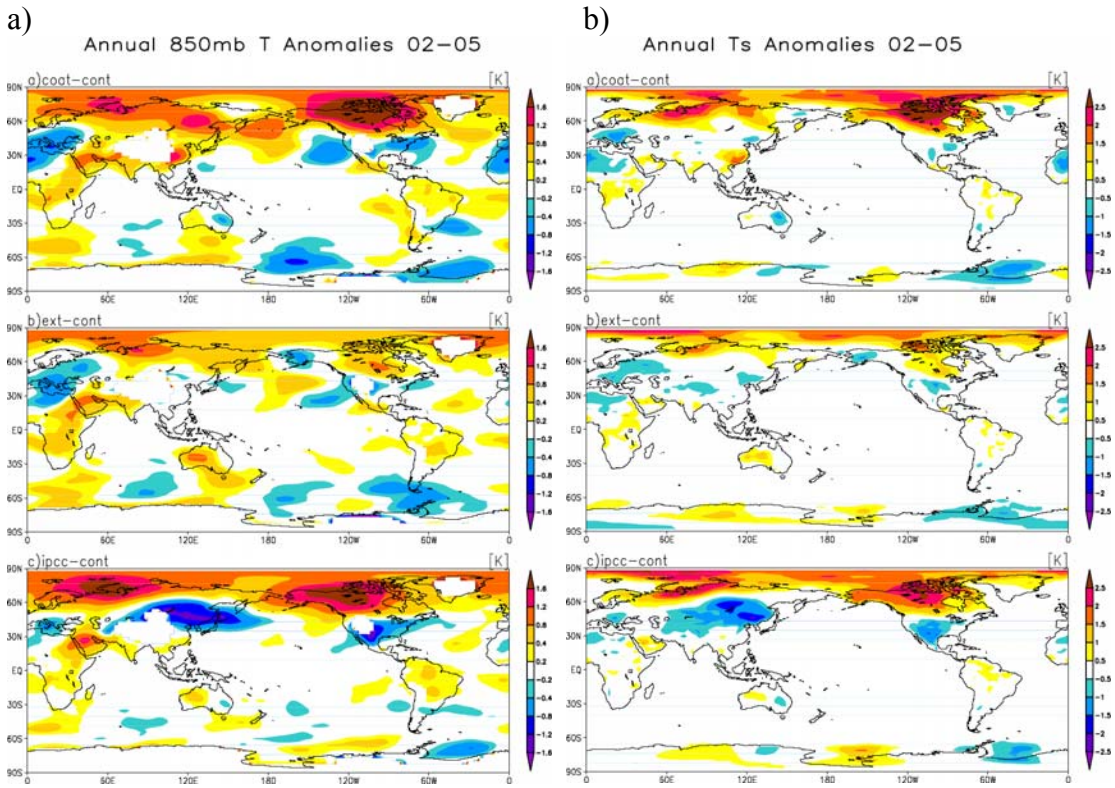

Figure 5.8: Annual mean temperature anomalies at a) 850 mb and b) surface.

5.4.3 Results

Figure 5.8 shows annual mean temperature differences between the three experimental simulations with aerosols and the aerosol-free control run at 850 mb and at the surface. The positive anomalies over high latitude (>60°N) in the NH are clearly seen in all three experiments with aerosols. The increases of temperatures are as large as about 2 K at 850 mb and over 2.5 K at the surface. Although the temperature anomalies demonstrates similar pattern for different mixing states, there is notable difference between coated mixing and ipcc external mixing over China, where

temperature anomalies switches from positive for the more absorbing coated mixing to negative for ipcc external mixing. The difference of temperature change over China suggests that aerosol mixing state might play a critical role in predicting regional climate change.

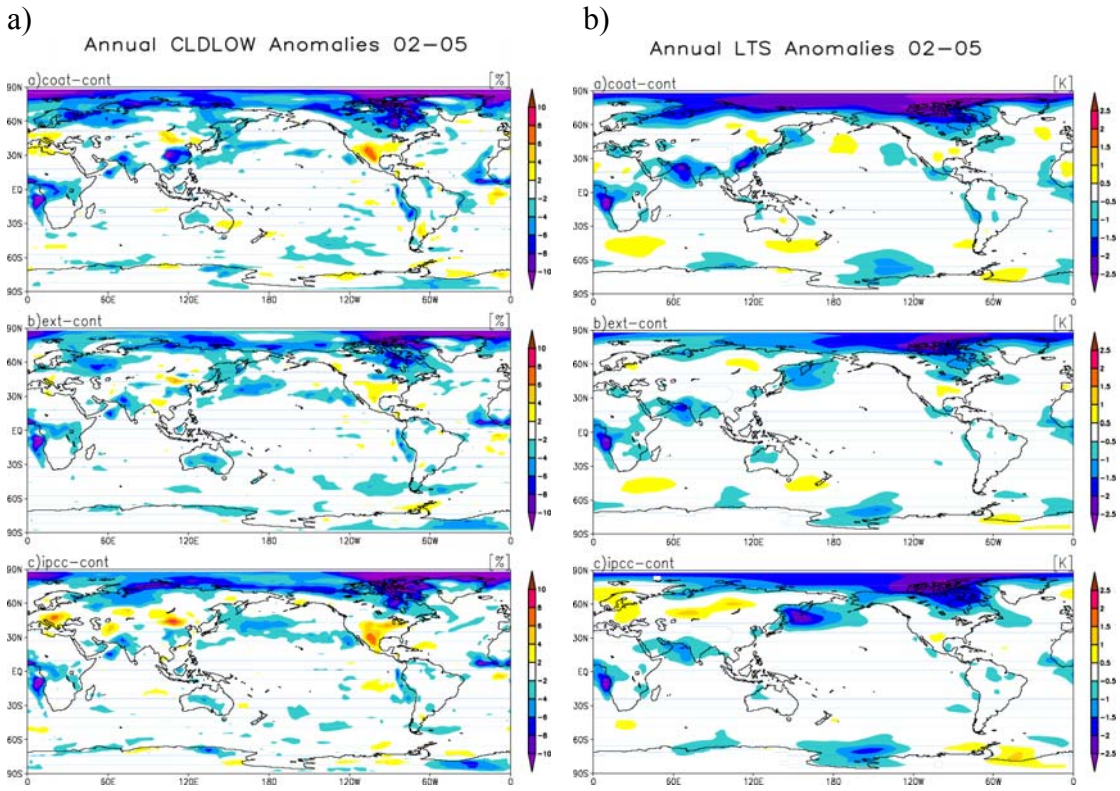

Figure 5.9: Annual mean a) low cloud fraction and b) LTS anomalies.

The positive anomaly of surface temperature derived from model simulations seems to be opposite to the well known "dimming" effect of aerosols, which tends to cool the surface by cutting off the downward solar flux. Further analysis of cloud cover change might be helpful to explain the surface warming. As shown in Figure 5.9a, aerosol mixtures lead to pronounced reduction of low cloud cover over land. The regions with great decrease of low clouds are: high latitude over NH (>60°N),

equatorial Africa, and South Asia. The decrease of low clouds is primarily caused by aerosol induced heating. The enhanced solar absorption by elevated aerosol layers greatly intensifies the evaporation of cloud droplets and accelerates cloud burning, also known as the aerosol semi-direct effects. The decrease of low clouds greatly reduces the planetary albedo and allows more solar radiation penetrate the lower troposphere and reach the surface. The change of surface temperature is partially the results of the competition between aerosol semi-direct effect and aerosol "dimming" effect, and is not solely determined by either of them. The rise in surface temperature in high latitude regions is likely related to the reduction of cloud amount.

As discussed by previous studies [*Klein and Hartmann*, 1993; *Wood and Bretherton*, 2006], stratiform low cloud cover is strongly correlated with lower-tropospheric stability (LTS) anomalies. Defined as the difference in potential temperature difference between the 700 mb level and the surface, the LTS can be used as a measure of the strength of the inversion that caps the planetary boundary layer (BL). Larger LTS value is associated with stronger, low-lying inversions, which leads to a lower entrainment rate because the air above the inversion has a higher potential temperature and greater energy is required to "pull" the dry air into the BL. Hence, a stronger inversion (large LTS) is more effective in trapping moisture within the BL and permitting greater cloud cover. Figure 5.9b clearly shows that the introduction of aerosol mixtures results in the decrease of LTS over regions with reduction of low clouds. Reduction of LTS implies the decrease of contrast in potential temperature across the inversion, which leads to a weakened inversions and a stronger cloud-top

entrainment rate. Entrainment brings dry free tropospheric air into BL and tends to dry the BL and burn the clouds. Therefore, aerosol mixtures cause excess heating to the air, weaken the boundary layer inversion, enhance the cloud-top entrainment, and result in the reduction of low clouds.

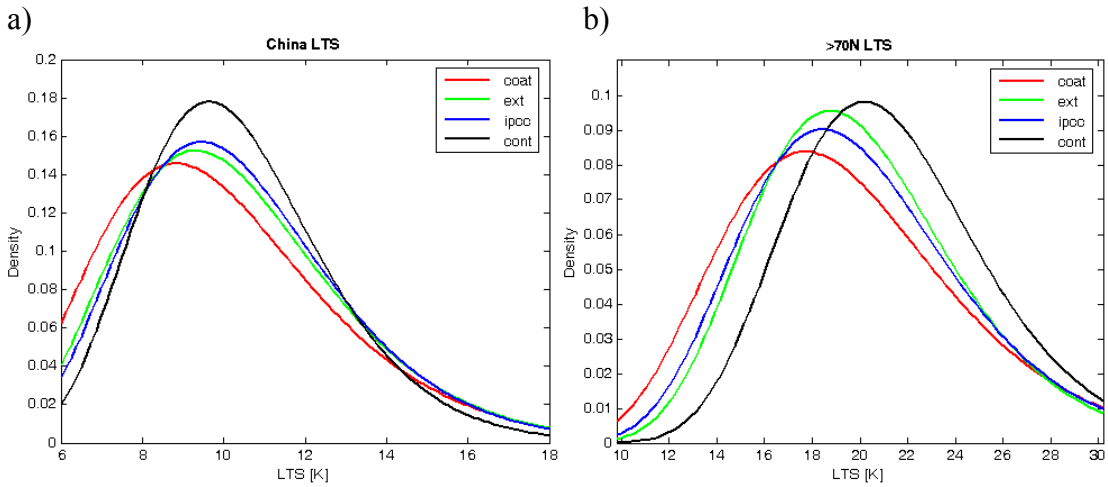

Figure 5.10: Probability density function of annual mean LTS over a) China and b) the Arctic region (>70N).

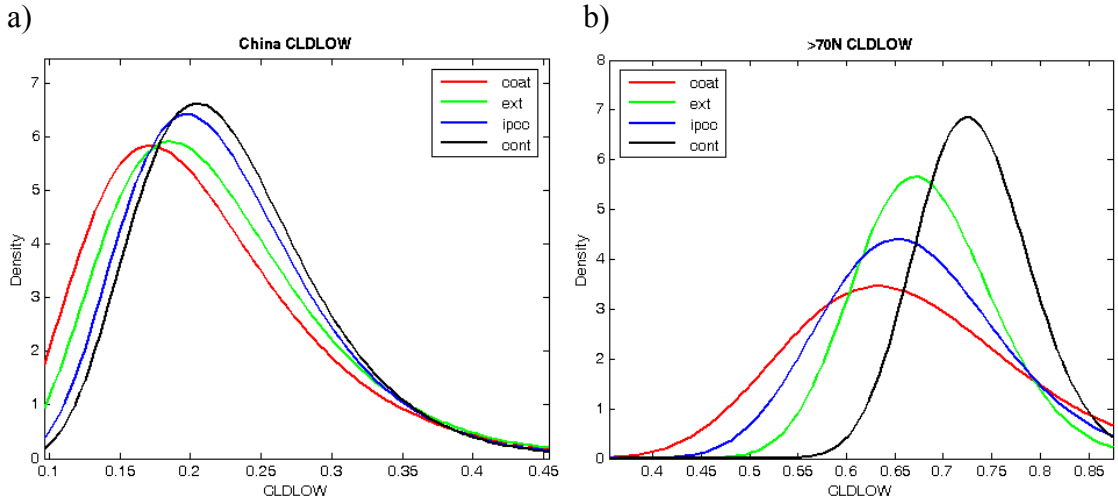

Figure 5.11: Probability density function of annual mean low cloud cover over a) China and b) the Arctic region (> 70N).

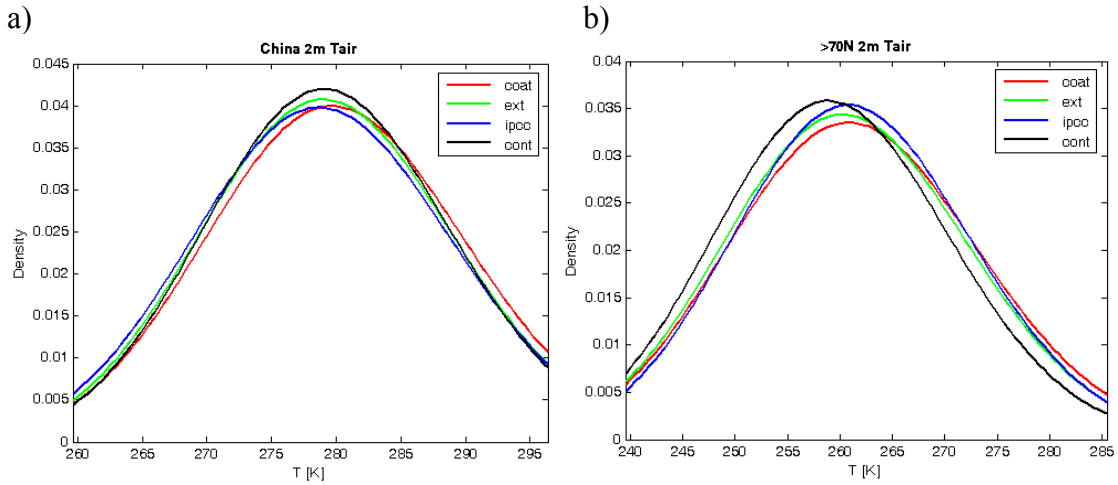

Figure 12: Probability density function of annual mean 2m surface air temperature over a) China and b) the Arctic region (> 70N).

To understand the role of aerosol mixing state in climate feedbacks, China and the Arctic region (>70°N) are selected for further analysis where substantial responses of temperature and low cloud were detected. The probability density function of LTS, low clouds, and 2m surface air temperature over China and the Arctic are shown in Figure 5.10, Figure 5.11, and Figure 5.12, respectively. The mean, median, and skewness of the curves shown in these figures are listed in Table 5.2. It is clearly seen that absorbing aerosols have large effects in decreasing the LTS and low clouds when they are internally coated mixed. Over China, the mean LTS reduces from 10.4 K for aerosol-free control run to 10.1 K and the reduction of LTS over the Arctic is as large as over 8% for internally coated mixing. Enhanced solar absorption by coated aerosols leads to great semi-direct effects and significant reduction of low clouds. Low cloud amount decreases by as large as 9% over both China and the Arctic in response to the excess heating to the lower troposphere by absorbing aerosols. In all three simulations with aerosols, the low cloud fraction decreases drastically. These results suggest that

cloud depletion effects of enhanced solar absorption are robust. The reduction of low clouds in turn further amplifies the warming of lower atmosphere and the surface. This warming effect of internally mixed absorbing aerosols is highly impressive over the high latitude regions and the 2m air surface temperate increases as large as 2 degree over the Arctic when absorbing aerosols are internally mixed. The results clearly indicate that the effect is relatively weak or negligible when absorbing aerosols are treated as the way most GCM studies have done, externally mixed.

Table 5.2: Mean, median, and skewness of the curves shown in Figure 5.10, 5.11, and 5.12 for the annual mean LTS, low cloud cover, and 2m surface air temperature over China and the Arctic region (>70N).

variable	region	item	cont	ipcc	ext	coat
LTS	China	mean	10.41	10.45	10.40	10.07
		median	9.60	9.62	8.89	9.41
		skewness	0.63	0.44	0.67	0.62
	>70 N	mean	21.38	20.01	20.12	19.57
		median	20.77	19.95	19.13	19.64
		skewness	0.05	0.12	0.19	0.10
CLDLOW	China	mean	0.23	0.23	0.22	0.21
		median	0.21	0.22	0.20	0.18
		skewness	0.43	0.44	0.86	0.68
	>70 N	mean	0.73	0.67	0.68	0.66
		median	0.72	0.68	0.69	0.68
		skewness	0.36	-0.92	-0.57	-1.40
2m T_{air}	China	mean	279.54	279.20	279.51	280.20
		median	279.92	280.00	280.05	280.50
		skewness	-0.06	-0.03	-0.08	-0.06
	>70 N	mean	259.61	261.50	261.00	261.65
		median	259.53	260.21	259.95	260.48
		skewness	0.06	0.17	0.15	0.08

The changes of temperature profiles over China and the Arctic are shown in Figure 5.13. Figure 5.13a suggests that different mixing states have different effects in temperature change over China. The commonly used ipcc external mixing leads to

cooling in the troposphere, while the more absorbing coated mixing results in the warming in the troposphere. Contrast to that, Figure 5.13b shows the changes of temperature profiles over the Arctic. The changes of temperature profiles show qualitatively similar responses to different mixing states. The presence of aerosol mixtures, no matter of their mixing states, leads to warming in the whole troposphere. As large as 2.3 K increase of temperature was detected near the surface for coated mixing experiment. As shown in Figure 5.14, the changes of relative humidity (RH) present very consistent pattern for different aerosol mixing states. Aerosol induced solar heating greatly decreases RH in the lower troposphere for both China and the Arctic. The largest reduction of RH, especially in the lower troposphere is caused by the coated mixing with the strongest absorbing ability. The decrease of RH is one of the major reasons for the depletion of low clouds over land, where water vapor supply from the surface is limited.

5.5 Summary and Discussion

Aerosol direct radiative forcing for different mixing states is estimated using MACR radiative transfer model. The results show that aerosol radiative forcing is quite heterogeneous in space and presents large latitudinal variation and hemisphere asymmetry. For external mixing, annual mean aerosol forcing at the TOA (surface) is -2.01 (-5.82) Wm^{-2} over Southern Hemisphere (SH) and -3.95 (-11.38) Wm^{-2} over Northern Hemisphere (NH), respectively. Aerosol forcing over NH is stronger than SH by a factor of ~2 simply because NH has more continents. More energy is trapped

into atmosphere over NH than SH and over the land than over the oceans, which implies great potential to modulate the atmospheric meridional circulation pattern.

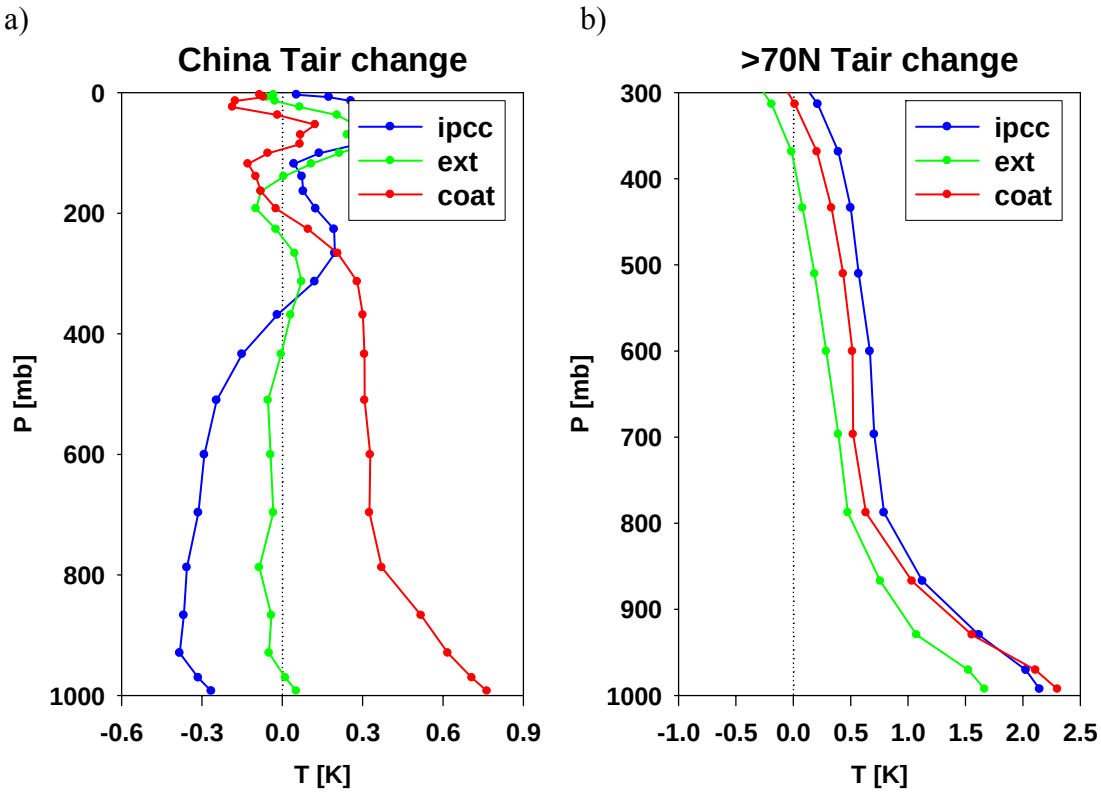

Figure 5.13: Regional annual mean temperature change over a) China and b) the Arctic region (> 70N).

Increasing concerns has been raised recently about the brown carbon, which is mainly originated from biomass burning and has strong absorption in the near-UV bands. To explore the radiative and climate effects of absorbing brown carbon, we conducted the simulations by replacing 20% OC with brown carbon and found that inclusion of brown carbon slight enhances atmospheric absorption and leads to larger radiative forcing, mainly over tropical region, where OC contributes a large part of total aerosols. It is highly uncertain about the fraction of brown carbon in OC, thus the findings about the radiative impacts of brown carbon in this study need further study.

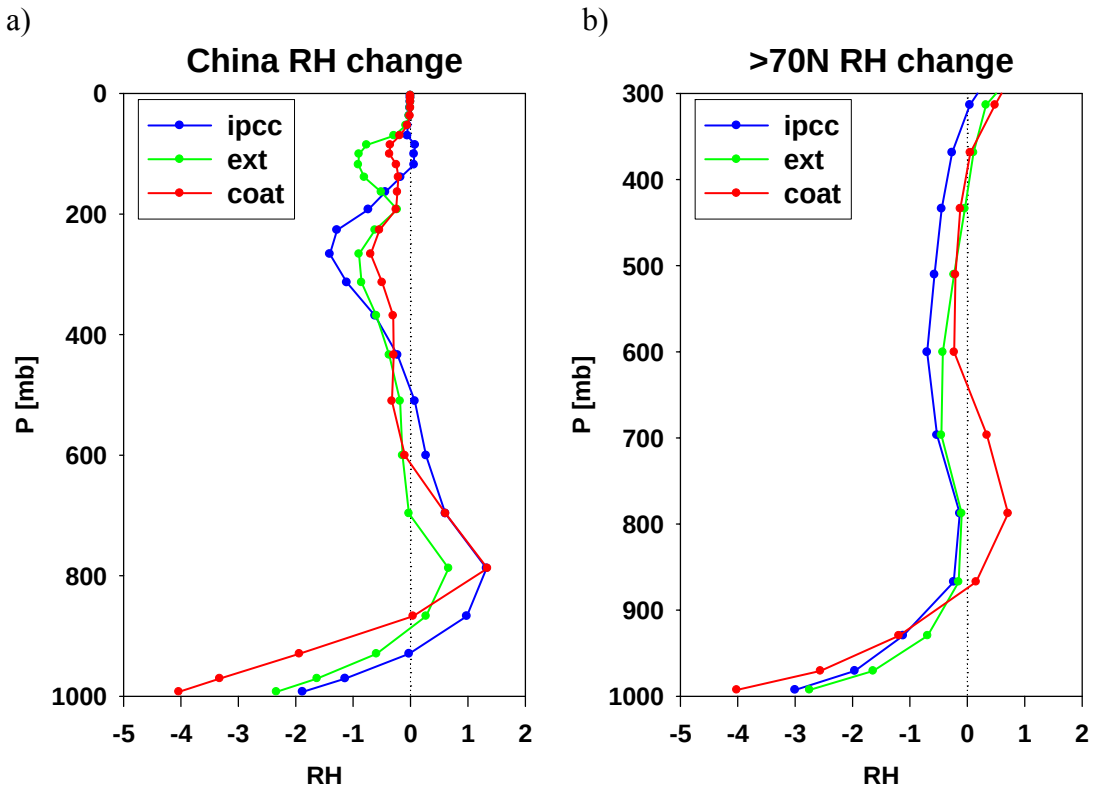

Figure 5.14: Regional annual mean relative humidity change over a) China and b) the Arctic region (> 70N).

The results in this study clearly indicate that the magnitude of direct aerosol radiative forcing is largely dependent on the mixing state of absorbing particles with other aerosols. The coating of non-absorbing materials on absorbing particles greatly amplifies atmospheric absorption compared with external mixing. The areas with great enhancement of atmospheric absorption by coated aerosols are mainly around industrial region, including East and South Asia, Europe, and East coast of US. As large as over 20 Wm^{-2} more heating is introduced to the atmosphere over East China where contributions of BC and sulfate are dominant. On global annual average, the externally mixed aerosols lead to about 2.5 Wm^{-2} atmospheric absorption, which corresponds to about 4.3% increase of atmospheric absorption relative to aerosol free

condition, while coated aerosols causes about 3.3 Wm-2 enhancement of atmospheric absorption.

By directly inserting aerosol radiative forcing into NCAR CAM3, we further explored the climate responses caused by aerosol mixtures. Large positive temperature anomalies are found over high latitudes (>60°N) in the NH. The warming of the surface may be attributed to the evaporation of low clouds from the absorption of solar flux by absorbing aerosols and subsequent heating of the air, well known as aerosol semi-direct effect. Great reduction of low clouds associated with decrease of LTS is found over China and the Arctic. The mean LTS reduce from 10.4 K for aerosol-free control run to 10.1 K over China and the reduction of LTS over the Arctic is as large as over 8% for coated mixing. Enhanced solar absorption by coated aerosols leads to great semi-direct effects and significant reduction of low clouds. Low cloud amount decreases by as large as 9% over both China and the Arctic in response to the excess heating to the lower troposphere by absorbing aerosols. The experiments in this study clearly demonstrate a large burning effect of low clouds by aerosol mixtures. Excessive heating by absorbing aerosols warms the air, reduces lower tropospheric stability and relative humidity over land, where water vapor supply is limited, and leads to more rapid detrainment of low clouds.

One of the significant findings of this study is that absorbing aerosols can lead to great reduction of low level clouds when they are internally mixed. The simulated cloudiness reduction is particularly strong over the Arctic and China. The reduction of cloud cover in turn amplifies the warming of lower atmosphere and the surface. The

effect is relatively weak or negligible when absorbing aerosols are treated as the way most GCM studies have done, externally mixed. The response of temperature change over China is inconsistent for different mixing assumptions. The results suggest that different assumptions in aerosol mixing state might result in different response of climate variables. Further thorough studies are needed to understand the impact of absorbing aerosols on long term climate change.

It is clearly demonstrated that the NCAR climate model with simple cloud parameterizations is able to capture the large semi-direct forcing induced by absorbing aerosol mixtures. Similar results about the burning effect of absorbing aerosols on low level marine clouds were found using cloud-resolving models. Enhanced absorption of solar heating by dark haze can desiccate the stratocumulus cloud layer [*Ackerman and Toon,* 1996] and intensify the dissipation of trade cumulus [*Ackerman et al.,* 2000]. *Johnson et al.* [2004] used a large-eddy model to investigate the semi-direct effect of absorbing aerosols on marine stratocumulus and found that absorbed solar radiation by absorbing aerosols may lead to a decrease of low cloud cover and liquid water path and cause a positive radiative forcing. The semi-direct effect is proportional to the aerosol absorbing ability (single scattering co-albedo, i.e. 1-SSA). Lower SSA or a higher aerosol optical depth could lead to the complete evaporation of the cloud layer. The sign, magnitude, and relative importance of direct and semi-direct aerosol effects depend essentially on how much absorbing aerosols is within or above the cloudy BL. Aerosol heating within cloud layers reduces cloud fractions, whereas aerosol heating above the cloud layer tends to increase cloud fractions. It seems that for marine

stratocumulus, even for moderately absorbing aerosols, the semi-direct forcing may far exceed the direct forcing. Hence, the semi-direct effect could be significantly affected by vertical distribution of absorbing aerosols, or mixing of aerosols, or by the removal of aerosols from BL by wet or dry deposition.

The model experiments in this study clearly demonstrate that absorbing aerosols play important roles in influencing meteorological variables such as temperature, relative humidity, and most importantly, the low cloud cover. Observations show that much of China has experienced significant decreases in cloud cover over the last half of the Twentieth century and the total emission of SO_2 and black carbon in China also had been continuously increasing until the mid-1990s. *Qian et al.* [2006] revealed that low cloud cover has decreased 0.33% per decade from 1954 to 2001 in China, and meanwhile, both surface solar radiation and pan evaporation have decreased based on newly available data from extended weather stations over China. *Mukai et al.* [2008] investigated the relationships among anthropogenic aerosol forcing, greenhouse gas (GHG) forcing, surface radiation budget, and cloud field based on model simulations with GCM coupled with an aerosol transport model and an ocean mixed-layer model. They showed that low-level clouds increase when anthropogenic aerosols increase and the increase of GHG causes the reduction of low-level cloud coverage and suggested that the observed decrease in the cloud cover in China might be influenced by both aerosol and GHG effects. However, only direct and indirect (both 1st and 2nd) aerosol effects were included in their study and the semi-direct effect of absorbing aerosols was missing, which have

significant influence on the change of low cloud cover. The observations of reduction of low clouds and surface solar radiation are consistent with findings of this study, which suggests that the semi-direct effect of internally mixed absorbing aerosols might also be one of the likely causes for the observed change of low clouds in China.

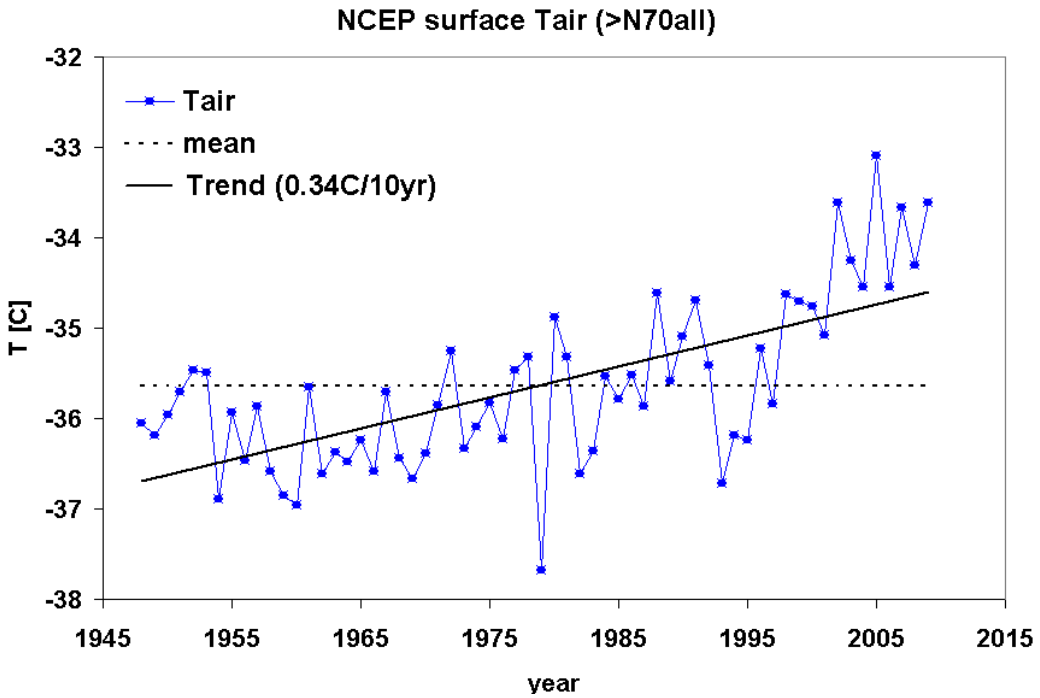

Figure 5.15: Time series of annual mean surface air temperature over the Arctic region (> 70N) from NCEP/NCAR reanalysis data.

The time series of annual mean surface air temperature over the Arctic region (>70) derived from NCEP/NCAR reanalysis data clearly shows the warming over the Arctic (Figure 5.15). The annual mean surface temperature has increased at +0.34°C per decade from 1948 to 2009 and the warming has greatly enhanced during the past two decades starting from 1990 to present at the decadal rate of about 1.3°C. Recent trends in satellite-derived cloud and surface properties for 1982 to 1999 show that the Arctic region north of 60°N has warmed and become cloudier in spring and summer

but has cooled and become less cloudy in winter. On an annual time scale, Arctic surface temperature has increased at a rate of 0.54 per decade, and there is negligible or no trend in cloud fraction due to the cancellation of opposite trends in different seasons [*Wang and Key*, 2003]. *Key et al.* [2008] evaluated the contribution of cloud and radiation anomalies to the 2007 Arctic sea ice extent minimum. They found that over the Western Arctic Ocean, total summertime cloud cover decreased by 16% and downwelling shortwave (longwave) radiative fluxes increases of +32 Wm-2 (-4 Wm-2) from 2006 to 2007 as the results of clearer skies. These radiation differences alone could enhance surface ice melt by 0.3 m, or warm the surface ocean by 2.4 K, which accelerates basal ice melt. The reduced cloudiness is explained by the increased air temperatures and decreased relative humidity associated with an anti-cyclonic atmospheric circulation pattern. Their findings suggest that when sea ice is vulnerably thin, natural year-to-year variations in the summertime atmospheric circulation and associated changes in clouds and shortwave radiation can play in increasingly large role in modulating sea ice extent. At present, it is still unclear to what extent changes in surface temperature and cloud amount in the Arctic are related to large-scale circulation or to local processes (aerosols, evaporation, and shortwave radiation etc.). The study by *Shindell* [2007] showed that Arctic climate well-correlated with the either global or local forcing during boreal summer. During other seasons, the contribution of large-scale dynamics is enhanced and the response of Arctic climate follows the global or Northern Hemisphere extratropical forcing much more closely.

Some sensitivity model experiments can be performed to identify the local or remote effects to the Arctic in the future study by inserting aerosol forcing globally or locally.

Our model simulations suggest that internally mixed absorbing aerosols have large effects on low level clouds over the Arctic, and the strong aerosol semi-direct effect in turn amplifies the surface warming, which might cause the further enhancement of sea ice melting. More studies about the influence of absorbing aerosols on clouds are required to better understand the climate impacts of aerosols. Indirect aerosol effect may have a large impact on climate change and bring more uncertainties. The impacts of aerosols on radiation budget and climate will continue to be of interest because of the complex feedbacks associated with aerosols forcings to the surface and the atmosphere.

References

Ackerman, A. S. and O. B. Toon (1996), Unrealistic desiccation of marine stratocumulus clouds by enhanced solar absorption, *Nature*, 380, 512-515.

Ackerman, A. S., O.B. Toon, D.E. Stevens, A.J. Heymsfield, V. Ramanathan and E.J. Welton (2000), Reduction of tropical cloudiness by soot, *Science*, 288: 1042-1047.

Andreae, M. O., and A. Gelencser (2006), Black carbon or brown carbon? The nature of light-absorbing carbonaceous aerosols, *Atmos Chem Phys*, 6, 3131-3148.

Bohren, C. F., and D. R. Huffman (1983), Absorption and Scattering of Light by Small Particles, John Wiley, Hoboken, N. J.

Bollasian, M., S. Nigam, and K.-M. Lau (2008), Absorbing aerosols and summer monsoon evolution over South Asia: an observational portrayal, *J. Climate*, 21, 3221-3239.

Bonan, G. B., K. W. Oleson, M. Vertenstein, S. Levis, X. Zeng, Y. Dai, R. E. Dickinson, and Z.-L. Yang (2002), The land surface climatology of the Community

Land Model coupled to the NCAR Community Climate Model, *J. Climate*, 15, 3123–3149.

Bond, T. C., G. Habib, and R. W. Bergstrom (2006), Limitations in the enhancement of visible light absorption due to mixing state, *J. Geophys. Res.*, 111, D20211, doi:10.1029/2006JD007315.

Briegleb, B. P., Delta-Eddington approximation for solar radiation in the NCAR Community Climate Model, *J. Geophys. Res.,* 97, 7603–7612, 1992.

Carlson, T. N., and S. G. Benjamin (1980), Radiative heating rates for Saharan dust, *J. Atmos. Sci.*, 37, 193–213.

Chung, C. E. and V. Ramanathan (2006), Weakening of North Indian SST gradients and the monsoon rainfall in India and the Sahel, *J. Climate,* 19, 2036–2045.

Chung, C. E., V. Ramanathan, D. Kim, and I. A. Podgorny (2005), Global anthropogenic aerosol direct forcing derived from satellite and ground-based observations, *J. Geophys. Res.,* 110, D24207, doi:10.1029/2005JD006356.

Collins, W. D., P. J. Rasch, and Others, Description of the NCAR Community Atmosphere Model (CAM 3.0) (2004), Technical Report NCAR/TN-464+STR, National Center for Atmospheric Research, Boulder, Colorado, 210 pp.

Guazzotti, S.A., K.R. Coffee, and K.A. Prather (2001), Continuous measurements of size-resolved particle chemistry during INDOEX-Intensive Field Phase 99, *J. Geophys. Res., 106* (D22), 28607-28627.

Hansen, J., M. Sato, and R. Ruedy (1997), Radiative forcing and climate response. *J. Geophys. Res.,* **102,** 6831–6864.

Hess, M., P. Koepke, and I. Schult (1998), Optical properties of aerosols and clouds: the software package OPAC. *Bull. Am. Meteorol. Soc*., 79, 831–844.

Intergovernmental Panel on Climate Change (IPCC) (2007), Climate change 2007: the scientific basis. In: Solomon, S. (Ed.), Contribution of Working Group I to the Fourth Assessment Report of the Intergovernmental Panel on Climate Change. Cambridge Univ. Press, New York.

Jacobson, M. Z. (2000), A physically-based treatment of elemental carbon optics: Implications for global direct forcing of aerosols, *Geophys. Res. Lett.*, *27*(2), 217–220.

Jacobson, M. Z. (2001), Strong radiative heating due to the mixing state of black carbon in atmospheric aerosols, *N*ature, 409, 695-697.

Johnson, B.T., K.P. Shine, and P.M. Forster (2004), The semi-direct aerosol effect: Impact of absorbing aerosols on marine stratocumulus. *Q. J .R.Meteorol. Soc.*, **130**, 1407–1422.

Kay, J. E., T. L'Ecuyer, A. Gettelman, G. Stephens, and C. O'Dell (2008), The contribution of cloud and radiation anomalies to the 2007 Arctic sea ice extent minimum, *Geophys. Res. Lett.,* 35, L08503, doi:10.1029/2008GL033451.

Klein, S. A., and D. L. Hartmann (1993), The seasonal cycle of low stratiform clouds, *J. Climate*, 6, 1587–1606.

Kim, D., and V. Ramanathan (2008), Solar radiation budget and radiative forcing due to aerosols and clouds, *J. Geophys. Res*., 113, D02203, doi:10.1029/2007JD008434.

Kirchstetter, T. W., T. Novakov, and P. V. Hobbs (2004), Evidence that the spectral dependence of light absorption by aerosols is affected by organic carbon, *J. Geophys. Res.*, 109, D21208, doi:10.1029/2004JD004999.

Lau, K. M., M. K. Kim, and K. M. Kim (2006), Asian summer monsoon anomalies induced by aerosol direct forcing: The role of the Tibetan Plateau, *Climate Dyn.,* 26, 855–864.

Liao, H., and J. H. Seinfeld (1998a), Radiative forcing by mineral dust aerosols: sensitivity to key variables, *J. Geophys. Res.,* 103, 31,637–31,646.

Liao, H., and J. H. Seinfeld (1998b), Effects of clouds on direct aerosol radiative forcing of climate, *J. Geophys. Res.,* 103, 3781– 3788.

Meehl, G. A., J. M. Arblaster, and W. D. Collins (2008), Effects of black carbon aerosols on the Indian monsoon. *J. Climate,* 21, 2869–2882.

Moffet, R. C. and K. A. Prather (2009), In-situ measurements of the mixing state and optical properties of soot with implications for radiative forcing estimates, *Proceedings of the National Academy of Sciences*, 106(29),11872-11877.

Mukai, M., T. Nakajima, and T. Takemura (2008), A study of anthropogenic impacts of the radiation budget and the cloud field in East Asia based on model simulations with GCM, *J. Geophys. Res.,* 113, D12211, doi:10.1029/2007JD009325.

Qian, Y., D. P. Kaiser, L. R. Leung, and M. Xu (2006), More frequent cloud-free sky and less surface solar radiation in China from 1955 to 2000, *Geophys. Res. Lett.,* 33, L01812, doi:10.1029/2005GL024586.

Ramana, M. V., and V. Ramanathan (2006), Abrupt transition from natural to anthropogenic aerosol radiative forcing: Observations at the ABC-Maldives Climate Observatory, *J. Geophys. Res.*, 111, D20207, doi:10.1029/2006JD007063.

Ramana, M.V., V. Ramanathan, D. Kim, G.C. Roberts and C.E. Corrigan (2007), Albedo, Atmospheric Solar Absorption and Heating rate measurements with stacked UAVs, *Quart. J. Roy. Meteor. Soc.*, 133, 1913-1931.

Ramanathan, V. (1976), Radiative transfer within the Earth's troposphere and stratosphere: A simplified radiative-convective model, *J. Atmos. Sci.,* 33, 1330–1346.

Ramanathan, V. et. al (2001a), Indian Ocean EXperiment: An integrated analysis of the climate forcing and effects of the great Indo-Asian haze, *J. Geophys. Res, 106* (D22): 28371-28398.

Ramanathan, V., P. J. Crutzen, J. T. Kiehl and D. Rosenfeld (2001b), Aerosols, Climate, and the Hydrological Cycle, *Science*, 294, 2119-2124.

Ramanathan et al. (2005), Atmospheric brown clouds: Impacts on South Asian climate and hydrological cycle. *Proceedings of the National Academy of Sciences USA,* **102,** 5326–5333.

Ramanathan, V., and P. Downey (1986), A nonisothermal emissivity and absorptivity formulation for water vapor, *J. Geophys. Res.,* 91, 8649–8666.

Ramanathan, V., M. V. Ramana, G. C. Roberts, D. Kim, D., C. E. Corrigan, C. Chung, and D. Winker (2007), Warming trends in Asia amplified by brown cloud solar absorption, *Nature*, 448, 575–578, doi:10.1038/nature06019.

Satheesh, S. K., and V. Ramanathan (2000), Large differences in tropical aerosol forcing at the top of the atmosphere and Earth's surface, *Nature*, 405, 60– 63.

Satheesh, S. K., V. Ramanathan, X. Li-Jones, J. M. Lobert, I. A. Podgorny, J. M. Prospero, B. N. Holben, and N. G. Loeb (1999), A model for the natural and anthropogenic aerosols for the tropical Indian Ocean derived from Indian Ocean Experiment data, *J. Geophys. Res*., 104, 27,421 – 27,440.

Shindell, D., 2007: Local and remote contributions to Arctic warming. *Geophys. Res. Lett.*, **34**, L14704, doi:10.1029/2007GL030221.

Slingo, J. M., The development and verification of a cloud prediction scheme for the ECMWF model (1987), *Q. J. R. Meteorol. Soc.,* 113, 899–927.

Wang, X. and J. Key (2003), Recent trends in Arctic surface, cloud, and radiation properties from space, *Science*, 299(5613), 1725-1728.

Wood, R. and C. Bretherton (2006), On the relationship between stratiform low cloud cover and lower-tropospheric stability, *J. Climate*, 19, 6425-6432.

Xu, K.-M., and S. K. Krueger (1991), Evaluation of cloudiness parameterizations using a cumulus ensemble model, *Mon. Wea. Rev.,* 119, 342–367.

Zhu, A., V. Ramanathan, F. Li, and D. Kim (2007). Dust plumes over the Pacific, India, and Atlantic Oceans: Climatology and radiative impacts, *J. Geophys. Res*., 112, D16208, doi:10.1029/2007JD008427.

Chapter 6

Conclusions

6.1 Summary

The research presented in this dissertation examines the radiative and climate impacts of atmospheric aerosols, with a focus on absorbing carbonaceous aerosols. A unique feature of the present research is that it integrates existing surface, satellite and aircraft observations to develop a consistent aerosol-radiation model.

Chapter 2 presents the climatological distributions and radiative impacts of dust plumes over the Pacific, the Indian and the Atlantic Oceans with the employment of multiple satellite datasets in conjunction with MACR (Monte Carlo Aerosol-Cloud-Radiation) model. Three target regions, namely the Yellow Sea (YS), the Arabian Sea (AS), and the Saharan Coast (SC), are examined for quantitative comparisons of dust properties and their impacts on climate. Twenty year averaged AVHRR (Advanced Very High Resolution Radiometer) AOD (aerosol optical depth) data clearly show the peak dust season for the 3 target regions, March-April-May for YS and June-July-August for AS and SC. GOCART (Georgia Institute of Technology–Goddard Global Ozone Chemistry Aerosol Radiation and Transport) modeled dust AOD fraction and MODIS (MODerate Imaging Spectroradiometer) large mode AOD ratio are adopted to evaluate the dust fraction estimate. SAGE (Stratospheric Aerosol and Gas Experiment) II aerosol extinction coefficient data are used to define the vertical distribution of dust. The elevated dust plumes are detected by subtracting the non-dust season values from

dust season values of SAGE II data, showing extinction peak around ~4 km over AS and SC. Over YS, dust plumes are found presenting multi-layered structure. The SW (shortwave) forcing of dust, although moderated by the LW (longwave) effect, dominates the net effects (SW+LW) of dust plumes. Under clear sky (i.e., cloudless) conditions, dust plumes reduce about 5.9 Wm^{-2}, 17.8 Wm^{-2}, and 14.2 Wm^{-2} regional and seasonal mean radiative flux reaching the surface over YS, AS, and SC, respectively. Of the three regions, dust plumes over AS have the largest effect on atmospheric heating owing to a lower single scattering albedo and the relatively large dust loading. The maximum SW heating occurs over AS with the value around +0.5 K/day inside the dust layer at ~4 km. The LW effect results in strong cooling throughout the dust layer and moderate heating below the dust layer, and dust plumes over SC exert the maximum LW effect on heating rates, with up to -0.5 K/day LW cooling in the free troposphere and about +0.3 K/day warming in the boundary layer. The net heating rate by the dust plumes is the sum of the SW and the LW heating rates. Over SC, large LW cooling inside the dust layer offsets up to 80% SW heating and results in about -0.1 K/day net heating rate change at the height ~5 km over SC. Over AS, the net heating rate change is dominated by SW heating because the maximum LW cooling is less than 60% of the SW heating, which leads to +0.3 K/day net heating inside the dust layer and moderate heating below the dust base. The net heating rate change over YS is the smallest among the three regions, with magnitude within 0.1 K/day.

The mixing state and radiative impacts of light-absorbing aerosol particles over the tropical Indian Ocean is investigated in Chapter 3. The Measurements of aerosol concentration and optical properties from autonomous unmanned aerial vehicles (UAVs) during the Maldives Autonomous UAV Campaign (MAC) were applied to the core-shell mixing model to find the likely mixing state of atmospheric brown clouds. The radiative forcing and heating rate induced by the coated aerosols are estimated by the MACR model. Measured aerosol chemical composition and radiative flux are employed to constrain and validate model results. In the core-shell mixing model, condensation and adsorption of sulfuric acid and organic gases are considered to occur on the surface of light-absorbing particles (LAP), namely black carbon (BC), brown carbon (BB), and mineral dust (DU) during their atmospheric transport. The coating of non-absorbing mixtures of sulfates, organics, nitrate, salt, and water greatly increase the scattering and absorption coefficients of BC, BB, and DU. The contribution of light-absorbing particles to column aerosol optical depth (AOD) increased by about 40%-90% when they are coated by the non-absorbing materials. Coating considerably enhances the absorption of light-absorbing aerosols and contributes to over 20% increase of aerosol radiative forcing at both the top-of-atmosphere and the surface. Coated aerosols trap about 2.4 Wm^{-2} more solar fluxes in the layer from 0.5 to 3.0 km, and lead to extra 0.08 $Kday^{-1}$ heating compared to external mixing.

Detailed investigation of the spectral signature of the aerosol radiative forcing over the tropical Indian Ocean is described in Chapter 4. Using a variety of ground-based measurements of aerosols and shortwave radiation fluxes, remote sensing data,

spectrally-resolved radiative transfer model, and chemical analyses of single particles, the spectral variation of aerosol radiative forcing during the ABC Post-Monsoon Experiment (APMEX) over the tropical Indian Ocean is investigated. The MODerate spectral resolution atmospheric TRANsmittance (MODTRAN) computer code provides accurate simulations of the solar irradiance with a very fine spectral interval. Physically constrained and chemically constrained aerosol models were developed to provide the input parameter of aerosol optical properties for MODTRAN. The spectrally-resolved quantitative measurements of irradiance by ASD are used to validate model results. The comparison results show that both aerosol models can well simulate the spectral pattern of global irradiance with chemically constrained model has better performance than physically constrained model. Model simulations are slightly larger than observations for the band from 400 nm to 500 nm and the overall relative difference is within 10% except for bands with strong gaseous absorption. The spectral signature of aerosol radiative forcing is investigated and the results show that downward global irradiance is decreased throughout the shortwave spectrum as the results of aerosol extinction. Large reduction of incoming solar flux occurs in the visible band with strongest decrease at green channel. Aerosol dimming effect is weak in the gaseous absorption bands where absorption of solar radiation by gases is nearly saturated that the effect of aerosols is relatively small.

The radiative and climate impacts of aerosol mixtures are explored based on model simulations in Chapter 5. The monthly varying three-dimensional aerosol direct radiative forcing is calculated using the MACR model for different aerosol mixing

assumptions. The effect of the absorbing brown carbon, mainly from biomass burning, is evaluated. Numerical experiments are conducted using the NCAR Community Atmosphere Model (CAM) with fixed sea surface temperature. The results in this study clearly indicate that the magnitude of direct aerosol radiative forcing is largely dependent on the mixing state of absorbing particles with other aerosols. Experimental simulations indicate great reduction of low level clouds and lower tropospheric stability (LTS) over the Arctic and China when absorbing aerosols are internally mixed, which in turn amplifies the warming. The effect is relatively weak or negligible when absorbing aerosols are treated as the way most GCM studies have done, externally mixed. The excess heating by absorbing aerosols enhanced the evaporation of low clouds and led to strong semi-direct effects. The decrease of LTS and relative humidity in the lower troposphere is likely the major reasons for the reduction of low clouds over China and the Arctic. The findings of cloud reduction over China and the warming over the Arctic are not inconsistent with observations.

6.2 Avenues for Further Research

The model experiments presented in this dissertation demonstrated that aerosols mixtures play important roles in influencing meteorological variables such as temperature, relative humidity, and most importantly, the low cloud cover. A large burning effect of low clouds by absorbing aerosol mixtures is explored. It is clear that excessive heating by absorbing aerosols warms the air, reduces lower tropospheric stability and relative humidity over land, where water vapor supply is limited, and leads to more rapid detrainment of low clouds. NCAR climate model with simple

cloud parameterizations is able to capture the large semi-direct forcing induced by absorbing aerosol mixtures. Similar results about the burning effect of absorbing aerosols on low level marine clouds were found using cloud-resolving models. Enhanced absorption of solar heating by dark haze can desiccate the stratocumulus cloud layer [*Ackerman and Toon*, 1996] and intensify the dissipation of trade cumulus [*Ackerman et al.*, 2000]. *Johnson et al.* [2004] used a large-eddy model to investigate the semi-direct effect of absorbing aerosols on marine stratocumulus and found that solar heating by absorbing aerosols may lead to a decrease of low cloud cover and liquid water path and cause a positive radiative forcing. The semi-direct effect is proportional to the aerosol absorbing ability (single scattering co-albedo, i.e. 1-SSA). Lower SSA or a higher aerosol optical depth could lead to the complete evaporation of the cloud layer. The sign, magnitude, and relative importance of direct and semi-direct aerosol effects depend essentially on how much absorbing aerosols is within or above the cloudy BL. Aerosol heating within cloud layers reduces cloud fractions, whereas aerosol heating above the cloud layer tends to increase cloud fractions. It seems that for marine stratocumulus, even for moderately absorbing aerosols, the semi-direct forcing may far exceed the direct forcing. Hence, the semi-direct effect could be significantly affected by vertical distribution of absorbing aerosols, or mixing of aerosols, or by the removal of aerosols from BL by wet or dry deposition.

Model simulations suggest that different assumption in aerosol mixing state not only has influence on aerosol radiative forcing; it can also result in different response of climate variables. However, model simulations in this study are the results

using prescribed sea surface temperature, thus the response of ocean to aerosol induced surface dimming is not included. Future study should couple the ocean to fully understand the impact of aerosols on long term climate change. More studies about the influence of absorbing aerosols on clouds are required to better understand the climate impacts of aerosols. Indirect aerosol effect may have a large impact on climate change and bring more uncertainties. The impacts of aerosols on radiation budget and climate will continue to be of interest because of the complex feedbacks associated with aerosols forcings to the surface and the atmosphere.

Reference:

Ackerman, A. S. and O. B. Toon (1996), Unrealistic desiccation of marine stratocumulus clouds by enhanced solar absorption, *Nature*, 380, 512-515.

Ackerman, A. S., O.B. Toon, D.E. Stevens, A.J. Heymsfield, V. Ramanathan and E.J. Welton (2000), Reduction of tropical cloudiness by soot, *Science*, 288: 1042-1047.

Johnson, B.T., K.P. Shine, and P.M. Forster (2004), The semi-direct aerosol effect: Impact of absorbing aerosols on marine stratocumulus. *Q. J .R.Meteorol. Soc.*, **130**, 1407–1422.